EÖTVÖS LORÁND UNIVERSITY
FACULTY OF SCIENCE

Astrophysical sources and fast prediction of gravitational waves:

Radial pulsation of compact stars, surrogate-model representation of signals and their propagation in interstellar medium

---

Doctoral dissertation

submitted to the

Doctoral School of Physics
Particle Physics and Astronomy Program

in partial fulfillment of the requirements for the degree of
Doctor of Philosophy in Physics

Doctoral candidate:
Dániel Barta
Assistant research fellow, Wigner RCP

Doctoral advisor:
Dr. Mátyás Zsolt Vasúth
Senior research fellow, Wigner RCP

Head of the Doctoral School:
Prof. Dr. habil. Jenő Gubicza
Full professor, Eötvös Loránd University

Supervisor of the Doctoral Program:
Prof. Dr. habil. Sándor Katz
Full professor, Eötvös Loránd University

Budapest, 2019

Astrophysical sources and fast prediction of gravitational waves: Radial pulsation of compact stars, surrogate-model representation of signals and their propagation in interstellar medium
Doctoral (Ph.D.) dissertation
DOI: 10.15476/ELTE.2019.230

ORCID iD: 0000-0001-6841-550X

The pieces of research work presented in this dissertation were carried out under the supervision of Dr. Mátyás Zsolt Vasúth, head of Gravitational Physics Research Group at Wigner Research Centre for Physics, Hungarian Academy of Sciences.

Abstract

Keywords: gravitational wave, waveforms, neutron stars, oscillation, dispersion

DOI: 10.15476/ELTE.2019.230

The presented doctoral dissertation covers a range of actively sought fields of research in gravitational-wave astrophysics, divided into three broad topics. With the advent of the era of multi-channel astronomy, the demand both for fast and accurate prediction of theoretical waveforms and for improving models of plausible astrophysical sources has renewed significantly.

I first address the issue of computationally efficient generation of predicted waveform templates. A large number of theoretically predicted waveforms are required by matched-filtering searches for the gravitational-wave signals produced by compact binary coalescence. In order to substantially alleviate the computational burden in gravitational-wave searches and parameter estimation, I propose a novel reduced-order model approach for inspiral waveforms of non-spinning compact binaries that evolve on eccentric orbits. Inspiral waveform templates for spinning compact binaries produced by such a method have proved highly effective and are already available in the LIGO Scientific Collaboration's Algorithms Library (LAL). The inspiral evolution is adequately described by using third-and-a-half post-Newtonian (3.5PN) accurate equations of motion of the binary while the far-zone radiation field is determined by a simultaneous evaluation of analytic waveforms, involving all high-order relativistic contributions up to second-and-a-half (2.5PN) post-Newtonian order beyond the Newtonian order. I provide a singular value decomposition-based reduced-order method in the frequency domain to represent any waveform within the parameter range of the model with optimal accuracy and precision. I construct efficient reduced bases comprized of a relatively small number of the most relevant waveforms over 3-dimensional parameter-space covered by the template bank (total mass $2.15M_\odot \leq M \leq 215M_\odot$, mass ratio $0.01 \leq q \leq 1$, and initial orbital eccentricity $0 \leq e_0 \leq 0.95$). The ROM is designed to predict signals in the frequency band from 10 Hz to 2 kHz for aLIGO and aVirgo design sensitivity. Beside moderating the data reduction, finer sampling of fiducial templates improves the accuracy of surrogates. Considerable increase in the speedup from several hundreds to thousands can be achieved by evaluating surrogates for low-mass systems especially when combined with high-eccentricity.

Binary neutron-star mergers are among the most promising sources of multi-channel astronomy. For this reason, events accompanying oscillations of neutron stars provide invaluable insight into the inner structure of neutron stars. Energetic explosive events associated with gamma-ray bursts or X-ray radiation perturb these stars, and the resulting dynamical behaviour may eventually be deduced from both electromagnetic and gravitational observations. Observations from the current and future missions of space-based radio telescopes will impose stricter constraints on plausible equation of states by yielding the mass and radius of a few stars to $\sim 5\%$ precision. Therefrom, the next chapter is dedicated to presenting my variational formulation of the linearized dynamical equations governing small adiabatic radial oscillations of neutron stars. The interior structure, that relies on accurate stellar models, may be probed by the frequency spectrum of neutrons-star oscillations. These oscillations occur when a star is perturbed away from its dynamical equilibrium and a restoring force tries to return it back to that equilibrium state. The dynamical equations are derived by taking into consideration those effects of viscosity and thermal conductivity of neutron-star matter which directly determine the minimum period of observable pulsars. The period of stellar oscillations for non-relativistic stars is in the range of minutes, whilst for neutron stars the periods are much shorter, typically range from 0.2 to about 0.9 milliseconds. A variational principle is applied to determine the eigenfunctions with a discrete set of complex eigenvalues. The real and imaginary parts of eigenvalues represent the squared natural frequencies and relaxation time of radial oscillations of non-rotating neutron stars, respectively. Moreover, I provide a suitable framework which may be supplemented with various potential species of cold-nuclear-matter models to compute the spectra of the normalized eigenfrequencies with a certain numerical precision. I provide a qualitative estimation of the rate at which viscosity and thermal conductivity drain the kinetic energy of radial oscillation mode in reasonably homogeneous neutron stars, without relying on explicit numerical computations.

Potentially detectable gravitational-wave signals are expected to be of extragalactic origin. Therefore, their sources are likely to be obscured by dust or gas in addition to the Milky Way's stellar halo through which the gravitational waves have to pass on their way to our ground-based detectors. The improving sensitivity of second-generation laser-interferometric detectors and envisaged plans for even more sophisticated instruments have inspired me to investigate the propagation of locally plane, small-amplitude, monochromatic gravitational waves through cold compressible interstellar gas, in order to provide a more accurate picture of expected waveforms for direct detection. The quasi-isothermal gas is concentrated in a giant molecular cloud held together by self-gravitation. Gravitational waves can be treated as linearized perturbations on the background spacetime. The perturbated field equations that govern the gas dynamics and describe the gravitational-wave–matter interaction are decoupled asymptotically for monochromatic high-frequency waves to a set of partial differential equations of different orders through a second-order Wentzel–Kramers–Brillouin method. Three distinct degenerate modes of polarization are revealed, corresponding to gravitational and sound waves propagating along null geodesics of the background spacetime and a zero-frequency mode that corresponds to non-propagating density and vorticity perturbations of the dispersive medium. I have shown that the transport equation for the gravitational-wave amplitudes in post-geometrical optics provides numerical solutions for the frequency shift of gravitational waves that are expressed by varying sinusoidal components of Fourier series. The decrease in frequency is driven by energy dissipation via interaction of gravitational waves with interstellar matter. The decrease is significantly smaller than the magnitude of the original frequency and too small to be detectable by present second- and planned third-generation detectors. The frequency-shift exhibits a power-law relationship between original and decreased frequencies and I examined it particularly for the transient signal GW150914.

Absztrakt

Kulcsszavak: gravitációs hullám, hullámforma, neutroncsillag, oszcilláció, diszperzió

DOI: 10.15476/ELTE.2019.230

A doktori értekezés a gravitációshullám-asztrofizika aktívan kutatott területei közül három átfogó témakört ölel fel. A többcsatornás csillagászat korszakának kezdetével jelentősen megnőtt az igény mind az elméleti hullámformák gyors és pontos előállítása, mind pedig a valószínűsíthető asztrofizikai források modelljeinek továbbfejlesztése iránt.

Először az elméleti hullámformasablonok számítási szempontból hatékony előállításának kérdésével foglalkozom. A kompakt kettős rendszerek összeolvadásából származó gravitációshullám-jelek célzott keresése és a rendszer asztrofizikai paramétereinek becslése során nagyszámú elméleti hullámforma szűrőként történő használatára van szükség. Annak érdekében, hogy a számítógépes erőforrások igénybevételét jelentősen csökkentsem a jelkeresés és paraméterbecslés során, ún. „csökkentett rendű modelleket" (ROM: reduced-order model) alkalmazok elliptikus pályán keringő kompakt kettős rendszerek által sugárzott gravitációs hullámok előállítására. Ezek a modellek rendkívül hatékonynak bizonyultak gyorsan forgó komponensekből álló kompakt kettős rendszerek hullámformáinak előállítására és elérhetőek a LIGO Tudományos Együttműködés adatelemzési algoritmusainak gyűjteményében (LAL). A befelé spirálozó kompakt kettős rendszerek fejlődésének megfelelő leírására egy negyedfél rendű poszt-newtoni közelítésben (3,5 PN) megadott mozgásegyenleteket használok, amivel egyidejűleg történik a sugárzási tér meghatározása analitikus hullámformák segítségével, melyek a Newton-féle rendet követő harmadfél rendig (2,5 PN) megjelenő minden relativisztikus járulékot tartalmaznak. Egy szinguláris értékek szerinti felbontáson (SVD) alapuló dimenziócsökkentési vagy jellemzőszelekciós eljárást (ROM) mutatok be, amivel a frekvenciatérben ábrázolt hullámforma-gyűjtemény sokdimenziós címkézett adatpontjait úgy transzformáljuk egy alacsonyabb dimenziós altér tengelyeire, hogy nagy pontossággal reprezentálható marad az eredeti adat (kiinduló hullámformák adatmátrixa) és bármely más hullámforma alacsonyabb rangú közelítése a gyűjtemény által lefedett paramétertartományban. Az adat varianciáját legjobban megőrző alacsonyabb dimenziós projekciót úgy kapjuk, hogy a projekciós mátrixot a legnagyobb sajátértékhez tartozó sajátvektorból képezzük (a közelítés eltérését Frobenius-normában mérjük), és hogy az eltérő osztályú pontok minél kevésbé keveredjenek az új altérben. A redukált bázist viszonylag kisszámú leglényegesebb hullámformából képzem. A vizsgálat az aLIGO és aVirgo második generációs földi interferometrikus gravitációshullám-detektorok érzékenysége szempontjából lényeges 10 Hz és 2 kHz frekvenciatartományba eső $2.15M_\odot \leq M \leq 215M_\odot$ össztömegű; $0.01 \leq q \leq 1$ tömegarányú; és $0 \leq e_0 \leq 0.95$ kezdeti pályaexcentricitással rendelkező konfigurációk háromdimenziós paraméterterét fedte le. A helyettesítő hullámformamodellek pontosságát növelheti a mérsékeltebb adatcsökkentés mellett a kiindulási hullámformasablonok finomabb mintavételezése (finomabb frekvenciafelbontás). Jelentős gyorsulás érhető el a hullámformaszámítás során, amely néhány száztól több ezerszeres mértékű is lehet, különösen alacsony tömegű és magas pályaexcentricitású kompakt kettős rendszerek helyettesítő hullámformáinak kiértékelése során.

Az összeolvadó neutroncsillagok a többcsatornás csillagászat legígéretesebb forrásai közé tartoznak. Ezért a neutroncsillagok rezgéseit kísérő események felbecsülhetetlen értékű betekintést engednek a neutroncsillagok belső szerkezetébe. A gamma-kitörésekhez vagy röntgensugárzáshoz

kapcsolódó nagyenergiájú események zavarokat okoznak ezekben a csillagokban, és az ebből adódó dinamikus viselkedés mind elektromágneses, mind gravitációs megfigyelésekből kinyerhető. A jelenleg működő és tervezett rádiócsillagászati űrtávcsövek megfigyelései szigorúbb korlátozásokat fognak kiszabni az elképzelhető állapotegyenletekre azáltal, hogy néhány neutroncsillag tömegét és sugarát $\sim 5\%$-os pontossággal meghatározzák. A következő fejezetet tehát a linearizált dinamikai egyenletek variációs módszerek segítségével történő határozásának szenteltem. Ezek az egyenletek szabályozzák a neutroncsillagok adiabatikus radiális pulzációját (melyet azonban nemadiabatikus folyamatok gerjesztenek). A neutroncsillag belső szerkezete, amelyet pontosan megadott csillagmodellek határoznak meg, az alaprezgéseinek frekvenciaspektrumán keresztül feltérképezhetővé válik. Ezek a csillagrezgések akkor fordulnak elő, amikor egy zavar kimozdítja a csillagot dinamikus egyensúlyából, egy visszatérítő erő pedig megpróbálja helyreállítani az egyensúlyi állapotot. A dinamikai egyenleteket a neutroncsillag anyagának transzportjelenségeinek (viszkozitás és hővezetés) figyelembevételével határozzuk meg; ezek közvetlenül meghatározzák a megfigyelhető pulzárok minimális periódusát. A nemrelativisztikus csillagok rezgésének periódusideje perces nagyságrendű. Ezzel szemben a neutroncsillagoknál sokkal rövidebb, jellemzően 0,2 és 0,9 milliszekundum közé eső periódusidő mérhető. A sajátértékek valós és képzetes része a nemforgó neutroncsillagok radiális rezgéseit jellemző csillapítatlan sajátfrekvenciák négyzetének, illetve relaxációs idő inverz négyzetének felel meg. Konzisztens elméleti keretet biztosítok, amely a hideg sűrű maganyagot leíró különféle potenciális modellekkel kiegészítve lehetővé teszi az egyes modellekhez tartozó normalizált sajátfrekvenciák spektrumának adott numerikus pontosságú kiszámítását. Azonfelül nagyságrendi becslést adok arra, hogy meglehetősen homogén anyag esetén a neutroncsillag anyagának viszkozitása és hővezetése milyen mértékben csapolja meg a radiális rezgés energiáját anélkül, hogy explicit numerikus számításokra támaszkodnék.

A potenciálisan észlelhető gravitációshullám-jelek várhatóan extragalaktikus eredetűek. Ezért valószínűleg forrásaikat a csillagközi por és gáz fedi el, ezenfelül a Tejút halóján áthaladva a hullámok hosszú utat tesznek meg a földi detektorokig. A második generációs lézer-interferometrikus detektorok érzékenységének javulása és a kilátásba helyezett még fejlettebb műszerek arra ösztönöztek, hogy vizsgáljam meg a lokálisan sík, kis amplitúdójú, monokromatikus gravitációs hullámok terjedését hideg összenyomható csillagközi gázban annak érdekében, hogy pontosabb képet kapjunk a közvetlen detektálásra várható hullámformákról. A kvázi-izotermikus gáz egy óriás molekuláris felhőben koncentrálódik, amelyet a saját gravitációja tart össze. A gravitációs hullámok az óriás molekuláris felhő által kialakított „háttér” téridő linearizált perturbációiként kezelhetőek. A másodrendű Wentzel–Kramers–Brillouin-eljárás aszimptotikusan rendenként szétcsatolja a perturbált téregyenleteket – amelyek irányítják a gáz dinamikáját és leírják a gravitációs hullám–anyag kölcsönhatást – monokromatikus magasfrekvenciás hullámok parciális differenciálegyenletek rendszerére. Három különféle degenerált polarizációs mód jelenik meg, amelyek a „háttér” téridő fényszerű geodetikus görbék mentén terjedő gravitációs és hanghullámoknak, valamint az anyagi közeg nullfrekvenciás sűrűség- és örvényességperturbációinak felelnek meg. Megmutattam, hogy a gravitációs hullám amplitúdóinak transzportegyenlete posztgeometriai optikai közelítésben megoldásokat biztosít a Fourier-sorba fejtett gravitációs hullám komponenseinek frekvenciaeltolódására. A frekvenciacsökkenés a gravitációs hullámok csillagközi anyaggal történő kölcsönhatása során fellépő energiaveszteség következménye. A csökkenés lényegesen kisebb az eredeti frekvencia nagyságrendjénél; túl kicsi ahhoz, hogy a jelenleg működő második, valamint tervezett harmadik generációs detektorokkal kimutatható legyen. A frekvenciaeltolódás hatványfüggést mutat az eredeti frekvenciákkal, és ezt megvizsgáltam speciálisan a GW150914 tranziens jelre.

Eötvös Loránd University

Declaration form for disclosure of doctoral thesis

I. **The data of the doctoral thesis**

Name of the author: Dániel Barta

MTMT-identifier: 10039723

Title and subtitle of the doctoral thesis: “Astrophysical sources and fast prediction of gravitational waves” (title proper) “Radial pulsation of compact stars, surrogate-model representation of signals and their propagation in interstellar medium” (subtitle)

DOI-identifier: 10.15476/ELTE.2019.230

Name of the doctoral school: Doctoral School of Physics

Name of the doctoral programme: Particle Physics and Astronomy

Name and scientific degree of the supervisor: Dr. Mátyás Zsolt Vasúth, Ph.D.

Workplace of the supervisor: Wigner Research Centre for Physics

II. **Declarations**

1. As the author of the doctoral thesis
   a) I agree to public disclosure of my doctoral thesis after obtaining a doctoral degree in the storage of ELTE Digital Institutional Repository. I authorize Éva Bíró, the administrator of the Office of Doctoral Administration and International Relations at the Faculty of Sciences to upload the thesis and the abstract to ELTE Digital Institutional Repository, and I authorize the administrator to fill all the declarations that are required in this procedure;
   b) I request in case the doctoral thesis contains qualified data pertaining to national security, to disclose the doctoral thesis publicly to the University Library and the ELTE Digital Institutional Repository ensuing the lapse of the period of the qualification process;
   c) I request to defer public disclosure to the University Library and the ELTE Digital Institutional Repository, in case there is a publishing contract concluded during the doctoral procedure or up until the award of the degree. However, the bibliographical data of the work shall be accessible to the public. If the publication of the doctoral thesis will not be carried out within a year from the award of the degree subject to the publishing contract, I agree to the public disclosure of the doctoral thesis and abstract to the University Library and the ELTE Digital Institutional Repository.

2. As the author of the doctoral thesis, I declare that
    a) the doctoral thesis and abstract uploaded to the ELTE Digital Institutional Repository are entirely the result of my own intellectual work and as far as I know, I did not infringe anyone's intellectual property rights;
    b) the printed version of the doctoral thesis and the abstract are identical with the doctoral thesis files (texts and diagrams) submitted on electronic device.

3. As the author of the doctoral thesis, I agree to the inspection of the thesis and the abstract by uploading them to a plagiarism checker software.

Budapest, September 4, 2019

Barta Dániel

Signature of the author

Contents

List of Figures

List of Tables

List of abbreviations

AGN Active galactic nucleus. viii, ix, 96

aLIGO Advanced LIGO. viii–x, 3, 5–8, 11, 27, 42, 52, 93, 94

aVirgo Advanced Virgo. viii, 3, 6, 8, 11, 42, 52

BBH Binary black hole. ix, 11, 12, 31–33, 41, 53, 96

BH Black hole. ix, x, 12, 13, 33

BNS Binary neutron star. ix, x, 8, 33, 41, 42, 52, 53, 96

CBC Compact binary coalescence. ix, xi, 3, 12, 28, 32, 52, 93

CMB Cosmic microwave background. viii

CNRS Centre national de la recherche scientifique. 6

COBE Cosmic Background Explorer. viii

EGO European Gravitational Observatory. 6

EM Electromagnetic. viii, 2, 13, 56, 79

EOS Equation of state. xii, 55–62, 68, 69, 73, 80, 83, 96

FOM Full-order model. 33, 44, 46, 53

GMC Giant molecular cloud. 78, 80, 81, 83, 84, 87, 94, 95

GW Gravitational wave. iii, viii–xii, 2, 4, 5, 8, 9, 12, 13, 23–27, 29, 31–33, 38, 40, 42, 52–54, 78–80, 86, 90, 91, 93, 95, 96

GWTC-1 1st GW-transient catalogue of compact binary mergers. xi, 1, 12

iLIGO Initial LIGO. 7, 8

IMR Inspiral-merger-ringdown. xi, 52, 54

INFN Istituto Nazionale di Fisica Nucleare. 6

ISCO Innermost stable circular orbit. 30, 34, 42, 49, 52

iVirgo Initial Virgo. 7

KAGRA Kamioka Gravitational Wave Detector. 3, 6, 8

LAL LSC Algorithms Library. 52

LIGO Laser Interferometer Gravitational-Wave Observatory. viii, x, xi, 1, 3, 6, 9, 96

LISA Laser Interferometer Space Antenna. 9

LOFT Large Observatory for X-ray Timing. ix, 56

LSC LIGO Scientific Collaboration. xi, 6, 12, 52, 93

LSO Last stable orbit. 34

NICER Neutron Star Interior Composition Explorer. ix, 56

NR Numerical relativity. 2, 29, 32, 33, 49, 52, 54, 55, 57, 77

NS Neutron star. ix, x, 33, 56, 58, 59, 68, 96

NSF National Science Foundation. 6

ODE Ordinary differential equation. xii, 30, 67, 74, 81, 88, 89, 95

PDE Partial differential equations. xii, 66, 88, 89, 91, 95

PN Post-Newtonian. x, xi, 2, 3, 33, 34

PSD Power spectral density. 48, 94

ROM Reduced-order model. 31, 33, 39, 42, 47, 48, 50–54

SDSS Sloan Digital Sky Survey. viii

SEOBNR aligned-Spin Effective-One-Body Numerical Relativity. 52

SLEVP Sturm–Liouville eigenvalue problem. 55, 75

SNR Signal-to-noise ratio. 11, 12, 32, 93

SV Singular value. 43–45, 53

SVD Singular-value decomposition. 33, 42–44, 46, 47, 53

WKB Wentzel–Kramers–Brillouin. 79, 88, 90, 95

WMAP Wilkinson Microwave Anisotropy Probe. viii

Preface

The first direct detection of gravitational waves (designated 'GW150914'), made on September 14, 2015 by LIGO (Laser Interferometer Gravitational-Wave Observatory), was a significant milestone in the history of astrophysics, which led to the birth of an entirely new field of observational astronomy; the gravitational-wave astronomy. Gravitational-wave detections provides astronomy with a revolutionary new tool for probing the universe through ripples in spacetime, in addition to more conventional means of observation of EM (Electromagnetic) radiation. The increased sensitivity of second-generation laser-interferometric detectors operated by the Europe-based aVirgo (Advanced Virgo) and the US-based aLIGO (Advanced LIGO) provided us the much-anticipated joint detection of a GW signal (GW170817) and EM radiation (GRB 170817A) from a binary of colliding neutron stars for the first time. The brief gamma-ray burst from the collisions was recorded on August 17, 2017 by ESA's INTEGRAL and NASA's FERMI gamma-ray satellites only 1.7 sec after the LIGO. Due to the tremendous technological advances, the number of observed events is exploding. The first catalogue of GW transient events (GWTC-1), released on Dec 1, 2018, contains the properties of a total of 11 confirmed events discovered during the first and second observing runs of the global network of advanced gravitational-wave detectors.

Our fundamental understanding of the Universe has predominantly been relying on observations of EM radiation, emitted by various types of astrophysical sources across the EM spectrum. The early second half of the 20th century was marked by the emergence of new types of astronomy (radio, infrared, X-ray and gamma-ray) by which astronomy was transformed from a purely optical science to a multi-wavelength discipline. Pulsars and quasars were discovered in the 1960s to be strong sources of radio waves, and in 1964 the accidental discovery of the CMB (Cosmic microwave background) in microwave region of the radio spectrum implied a compelling evidence of the Big Bang origin of the universe. In infrared band, spectral lines and features of cold dust in the interstellar medium of galaxies are most prominent. Higher energy or shorter wavelength photons are studied by ultraviolet (for hot young stars and evolution of galaxies), X-ray (for AGN (Active galactic nucleus)s, supernova remnants) and gamma-ray astronomy (for distant high-energy objects, blazars, hypernovae). The following decades witnessed humanity's first space exploration and the technological advances enabled both ground- and space-based experiments of improved precision measurements, such as the measurements of CMB anisotropies by COBE (Cosmic Background Explorer) and WMAP (Wilkinson Microwave Anisotropy Probe), and the high-precision estimation of Hubble's constant using photometric redshift catalogues based on SDSS (Sloan Digital Sky Survey). Therefore, neutron star oscillations may impact on a range of observations, involving in particular radio and X-ray timing and gravitational waves. The possibility that radial oscillations of neutron stars give rise to oscillations observed within radio subpulses of pulsars was proposed by V. Boriakoff [6] in 1976. X-ray and γ-ray burst events have been generally associated with neutron stars by many authors e.g. [7]. Periodicities have been observed in X-ray bursts, which has raised considerable interest in radial [8] and other types [9] of neutron-star oscillations since the early 1980s. Bursters exhibit periodic and rapid increases in luminosity (typically a factor of 10 or greater) when an enormous amount of energy deposited in oscillation modes is released in a short period of time through heat outflow via neutrino emission. [10] Physically, some mass from the stellar interior is drawn toward the surface where the hydrogen fuses to helium which accumulates until it fuses in a burst, producing X-rays. After the subsequent emission of thermal photon from the surface, the crust thermally relaxes toward equilibrium with the core. X-ray observations from the recently lunched NICER (Neutron Star Interior Composition Explorer) mission [11] and from the upcoming LOFT (Large Observatory for X-ray Timing) mission [12] will yield the mass and radius of a few stars up to $\sim 5\%$ precision. The observations of CBC (Compact binary coalescence) events by gravitational-wave detectors such as the transient signal GW170817 will also dramatically improve our understanding of ultra-dense matter in neutron stars. Further interest in the study has been stimulated by [13], where γ-ray bursts were assumed to originate as results of collisions between strange stars at cosmological distances. Even though radial oscillations of strange stars are expected to be damped rapidly [14], such strange stars during their short time-scales are likely to be promising targets for multi-messenger observations. For most stellar models, the periods (typically ranging from 0.2 to about 0.9 milliseconds) depend on the stellar model and its central density [15], while the relaxation time is in the range of $0.1 - 0.3$ seconds. Therefore, the study of oscillation spectra and relaxation times of neutron stars could be very valuable as their dynamical behaviour may eventually be deduced from observations.

CBCs such as stellar-mass BBH (Binary black hole)s and BNS (Binary neutron star)s, are among the most promising GWs sources for ground-based GW detectors. [16]. Binaries that evolved through typical main sequence evolution [17] are expected to shed their formation eccentricities over time due to gravitational radiation reaction. For this reason, isolated compact binaries are commonly assumed to move on quasicircular orbits by the time they spiral into the sensitive frequency band of terrestrial GW observatories. [18, 19] Some relatively young sources, nevertheless, which had too short time for the gravitational radiation reaction to completely circularize their orbits retain some residual eccentricity. [20] Therefore, CBC inspirals with non-negligible orbital eccentricities are plausible sources. [18] Some results [21, 22] support the qualitative conclusion that neglecting residual orbital eccentricities (even small ones) in CBCs may seriously deteriorate matched-filter detection performance. A number of possible astrophysical scenarios and mechanisms allow the formation of observationally relevant eccentric ultracompact binaries (cf. [23–25]). Short-period CBCs may form by dynamical capture in dense stellar enviroments, present in both galactic central regions and globular clusters, or by tidal capture of compact object by NS (Neutron star)s; this phenomenon is described in great detail in [26–28]. Stable hierarchical triple star-systems may form in globular clusters where multi-body interactions are involved. It has been estimated that $\sim 30\%$ of binaries formed in systems where the Kozai resonance increased the eccentricity of the inner binary will have initial eccentricities $e_0 > 0.1$ when they enter the frequency window of the aLIGO. [29] The great majority ($\sim 90\%$) of stellar-mass BH (Black hole) binaries formed by scattering in AGN containing a supermassive BH have $e_0 > 0.9$, where e_0 denotes the initial eccentricity of the binary by the time it enters the lower part of the frequency band of detectors. [27] Roughly $0.1-10$ eccentric inspiral events per year up to redshift $z \sim 0.2$ are anticipated to be discovered by LIGO-type observatories. [23] One of the key goals of GW observatories is to measure the intrinsic parameters of coalescing BNSs. Moreover, Favata (2014) pointed out that neglecting initial eccentricities $e_0 \gtrsim 0.002$ causes systematic errors that exceed statistical errors in aLIGO measurements. [30] Since the phasing of the GW signal is significantly more important for parameter estimation, and eccentricity modifies the phasing beginning at 1.5PN (Post-Newtonian) orders, eccentricity corrections to the PN phase have to be included at leading order.

Motivation and academic engagement

On the advent of the multi-channel astronomy, the demand both for *computationally efficient generation of predicted waveforms* (in Chapter 2) and for theoretical investigation of plausible astrophysical sources, such as BNS or BH–NS systems, has renewed significantly. The potential to observe BNS and BH–NS coalescence events motivated us to study the *NS oscillations* (in Chapter 3) and investigate their *thermal relaxation at the neutrino cooling stage* that directly determine a minimum period of observable pulsars. They provide us with unique insights into the physics of the extremely dense and cold nuclear matter, which cannot be reached in terrestrial experiments. The ever-increasing sensitivity of instruments prompts us to discover, gradually reduce and eventually eliminate potential new effects that may lead to the degradation of signal detectability, such as *interaction of gravitational waves with matter* (in Chapter 4). The presented doctoral dissertation covers a wide range of actively sought fields of research which can be divided into three major topics, accordingly.

The pieces of academic research set out in the doctoral dissertation were conducted at Wigner Research Centre for Physics in the position of junior research fellow from 2013, then as assistant research fellow since 2016. I was enrolled in the Particle Physics and Astronomy Doctoral Program of the Doctoral School of Physics at Eötvös Loránd University from 2013 to 2016. The Gravitational Physics Research Group, led by my supervisor, Dr. Mátyás Vasúth, is dedicated to the study of gravitational phenomena in nature, covering a wide range of subjects in numerical and post-Newtonian general relativity, and as a member of Virgo Collaboration it is engaged in gravitational-wave experiments and developing related algorithms. I have also got involved in the collaborative effort of the broader gravitational-wave science community to pursue groundbreaking discoveries in the field of gravitational-wave astrophysics. In the autumn of 2015, the Virgo Membership Committee approved my nomination for addition to the author list of joint LSC–Virgo publications, which consists of a narrower group of members (currently about 1,200 people). In behalf of my membership, I have appeared as co-author on over 70 peer-reviewed research articles as of today. In 2016, together with the entire discovery team from LIGO Scientific Collaboration and Virgo Collaboration, as one of the authors of the GW150914 announcement paper, I was awarded with the *Special Breakthrough Prize in Fundamental Physics* and the *Gruber Prize in Cosmology* for the first detection of gravitational waves.

In April 2014, I carried out a short-term scientific mission (STSM) at Cardiff University, United Kingdom in the framework of NewCompStar program (COST Action MP1304), where Prof. Bangalore Sathyaprakash and Dr. Michael Pürrer with expertise on reduced-order models, have assisted me on constructing computationally efficient waveform templates. In April 2018, I was supported by PHAROS program (COST Action CA16214) to undertake a study aimed at investigating radial pulsations of neutron stars under the supervision of Prof. Kostas Kokkotas, Director of Institute for Astronomy and Astrophysics at University of Tübingen, Germany. In 2019, I was awarded two research grants within the framework of OzGrav International Visitor Funding Program and of the National Talent Scholarship ("Nemzeti Tehetség Program – Nemzet Fiatal Tehetségeiért Ösztöndíj" in Hungarian, NTP-NFTÖ-18), supported by the Australian Research Council and by the Hungarian Ministry of Human Capacities, respectively. They provided me with the opportunity to carry out a research at Monash University, Australia, to assess the utilization of phenomenological waveforms that include very late IMR (Inspiral-merger-ringdown) phases of the CBCs. Dr. Eric Thrane, Data Theme Leader for OzGrav who supervised my work at Monash University supported my membership in LSC (LIGO Scientific Collaboration) and in the ARC Centre of Excellence for Gravitational Wave Discovery (OzGrav).

Structure and components of the dissertation

The body of my dissertation is divided into four chapters, according to their respective subjects. These main chapters are preceded by a preface which explains the underlying motivation for each subject and highlights the links between them in the context of contemporary gravitational-wave research.

Chapter 1 is intended to provide a brief overview of the essential scientific background and basic concepts that are required for the understanding of the pieces of academic research set out in the presented doctoral dissertation. In Sec. 1.1, I begin with a brief account of major historical milestones of the combined theoretical and technological development in gravitational-wave research that led to the discovery of gravitational waves. The discussion in Sec. 1.2 provides a brief overview of the development of Weber-type resonant-mass detectors and type of LIGO-type laser-interferometric detectors. It is intended to cover the most relevant issues of instrumentation, noise sources, strain sensitivities and mission development, including the status of currently operational and upcoming gravitational-wave detectors across the globe. Sec. 1.3 summarizes observations of gravitational waves, including the first indirect evidence presented by PSR B1913+16, followed by direct observations of gravitational waves which constitute part of the first GWTC-1 (1st GW-transient catalogue of compact binary mergers). After reviewing mathematical notation and conventions in Sec. 1.4, the necessary mathematical preliminaries of pseudo-Riemannian geometry are presented which lay the conceptual foundations for clear and intuitive discussion of my own research discussed in the following chapters. The linearized weak-field equations and the corresponding linear plane-waves solution in the transverse-traceless gauge are then derived in Sec. 1.5.

Chapter 2 focuses on the issue of generating gravitational waveforms for non-spinning eccentric compact binaries with reduced computational cost. Sec. 2.1 reviews the development of ROM-based models in GW data analysis. Sec. 2.2 starts with the description of the procedure for generating fiducial PN waveforms by CBwaves, with respect to the statistics of the cost of computing individual waveforms to estimate the total cost of building template banks. Sec. 2.3 proposes the simplest strategy (regular spacing) for template placement in the intrinsic parameter space, followed by the representation of the fiducial waveform templates on a common, finely sampled and regularly spaced frequency grid. Sec. 2.4 gives a general description of my approach to construct efficient ROM assembled from the reduced bases and their characteristic features, particularly the truncation error. Sec. 2.5 is dedicated to assessing the overall performance of ROM building, including the accuracy of the surrogate model and its computational cost relative to that of the fiducial model. Sec. 2.6 contains the summary of this chapter, including the limitations of the research and an outlook for future development.

Chapter 3 is dedicated to discourse radial pulsations of relativistic stellar models for dissipative fluids. Sec. 3.1 places the subject of relativistic stellar oscillations in context. Sec. 3.2 presents a collection of tabulated EOS (Equation of state)s for four nucleonic and three non-nucleonic matter models I examined. Then one-piece and piecewise-polytropic EOSs are discussed, together with hybrid models that extend the validity of polytropic description to heating and cooling processes. Sec. 3.3 presents the basic equations of hydrodynamics of perfect fluids and of dissipative fluids in Eckart frame where the equations of thermal evolution of pulsating neutron stars include radiative transfer. In Sec. 3.4, the Einstein field equations and the generalized Tolman–Oppenheimer–Volkoff equation are expressed through a pair of effective variables that incorporate time-dependent dissipative contributions of the neutron-star matter. In Sec. 3.5, I present a variational method to formulate a lowest-order asymptotic approximation of infinitesimal adiabatic radial oscillations. Sec. 3.5.3 outlines equilibrium stellar models through a local adiabatic index which may be regarded as constant near the centre, but in general, varies, depending on the dynamical regime. Sec. 3.6 deals with the second-order linear ODE (Ordinary differential equation) of radial pulsations that were derived from the perturbation equations. Sec. 3.6.1 discusses the regular Sturm–Liouville eigenvalue problem for the natural frequencies of oscillation, imposed by the aforementioned pulsation equation. Sec. 3.6.2 addresses the characteristic time-scale for the relaxation of dissipation-damped radial oscillations. Lastly, the principal results established in this paper are summarized in Sec. 3.7.

Chapter 4 addresses the issue of the interaction of gravitational waves with interstellar matter, in order to provide a more accurate picture of expected waveforms for direct detection. Sec. 4.1 presents a brief review of previously published studies in the literature that were engaged in studying the propagation of gravitational waves through interstellar matter. Sec. 4.2 first discusses the background with physical properties of typical giant molecular clouds, then its perturbations in detail. In Sec. 4.3 these perturbed quantities yield the field equations governing the gas dynamics and express the interaction of GWs with matter. Sec. 4.4 presents the Wentzel–Kramers–Brillouin method for finding approximate solutions to the perturbed field equations. In this context, in Sec. 4.4.1, the field equations decoupled asymptotically for locally plane high-frequency monochromatic waves to a set of second-order homogeneous linear PDE (Partial differential equations)s of different orders of magnitude. In Sec. 4.4.2 the transport equation for the first-order secondary amplitudes which depend on the density in geometrical-optics limit are formulated, and subsequently solved in Sec. 4.5.1 for varying sinusoidal components of Fourier series. In Sec. 4.5.2 first a match-filtering technique is used to correlate the transient GW signal 'GW150914' with the corresponding signal affected by the interaction with matter. Then I bring to light for what kind of possible GW-sources the effect of interaction is expected to be powerful enough to be taken into consideration in GW data analysis. Conclusions, remarks and limitations are given in Sec. 4.6.

Acknowledgments

To begin with, I would like to thank my doctoral advisor, Dr. Mátyás Vasúth, and my former co-advisor during and prior to my graduate studies, Dr. Péter Raffai, with whose instructions I have learned the basics of general theory of relativity and I have acquired an adequate familiarity with gravitational waves. I am most grateful to Dr. Mátyás Vasúth for his constructive comments and critical remarks, which have helped me tremendously, not just in improving the quality of my research papers, but throughout the preparation of my dissertation. All the scientific results presented in this dissertation were achieved under his helpful guidance. His guidance often gave me the impetus to keep my major goals in mind while preparing this dissertation. With the hope that the bumpy road of gravitational-wave research that we have travelled so far continues, I wish to express my earnest appreciation once more for proposing the approval of my membership in Virgo Collaboration and for all the precious time and energy he has devoted to my work throughout my scientific career.

Prof. Péter Lévai deserves special thanks for granting me the opportunity to work as a junior researcher in the intellectually challenging and supportive environment of the Wigner Research Centre for Physics during my doctoral studies. I am profoundly indebted to him for allowing me to extend the period of my employment beyond the term of my junior research fellowship for further three years in the position of assistant research fellow. I also owe many thanks to colleagues at the Department of Theoretical Physics; particularly to Dr. Gergely Barnaföldi, Dr. Péter Ván and Dr. Balázs Mikóczi for many thought-provoking conversations and technical assistance that greatly helped me in dealing with problematic issues in relation to neutron stars, relativistic thermodynamics and post-Newtonian waveforms. I had the privilege to have Dr. Gyula Fodor and Dr. Zoltán Keresztes as preliminary examiners of the draft of my dissertation and as appointed opponents for the preliminary defence of my dissertation at my home institute. They have provided me with valuable comments and suggestions that have significantly improved the quality and consistency of this dissertation.

My doctoral research also greatly benefited from the help and support of Prof. Bangalore Sathyaprakash and Dr. Michael Pürrer during my research stay at Cardiff University, United Kingdom where I explored the critical issues related to reducing the computational complexity of inspiral-waveform construction by model-order reduction. I would also like to gratefully acknowledge the expert assistance of Prof. Kostas Kokkotas during my research stay in April 2018 at the University of Tübingen, Germany where I investigated numerical methods for radial-mode oscillations of neutron stars. I wish to express my most sincere gratitude towards Dr. Eric Thrane for supporting my membership in LIGO Scientific Collaboration and for his generous hospitality that provided me with the opportunity to carry out a research visit from April to June 2019 at Monash University, Australia to assess the utilization of phenomenological IMR waveforms in parameter estimation that include orbital eccentricity. Last but not least, I am also deeply grateful to my family for their continued support and encouragement throughout my academic progress.

Chapter 1

Introduction to gravitational-wave astronomy

This chapter is intended to provide readers with a review of the essential scientific background and basic concepts needed to understand the pieces of academic research set out in the presented doctoral dissertation. In Sec. 1.1, mostly based on [31], I begin with a brief account of major historical milestones of the combined theoretical and technological development in gravitational-wave research that led to the discovery of gravitational waves. The discussion in Sec. 1.2 provides a brief overview of the development of Weber-type resonant-mass detectors and type of LIGO-type laser-interferometric detectors. It is intended to cover the most relevant issues of instrumentation, noise sources, strain sensitivities and mission development, including the status of currently operational and upcoming gravitational-wave detectors across the globe. Sec. 1.3 summarizes observations of gravitational waves including first indirect evidence presented by PSR B1913+16, followed by direct observations of gravitational waves which constitute part of the GWTC-1. After reviewing mathematical notation and conventions in Sec. 1.4, the necessary mathematical preliminaries of pseudo-Riemannian geometry are presented which lay the conceptual foundations for clear and intuitive discussion of my own research discussed in the following chapters. The linearized weak-field equations and the corresponding linear plane-waves solution in the transverse-traceless gauge are then derived in Sec. 1.5. The discourse of Sections 1.4 and 1.5 is mostly based on the content of comprehensive introductory textbooks [32–34].

1.1 A brief history of gravitational-wave research

The way for Albert Einstein's special theory of relativity was paved by Hendrik Antoon Lorentz [35], who postulated the concept of so-called Lorentz transformation (1.14) in 1904 to explain the invariance of the source-free Maxwell equations under such transformations. In 1905, Henri Poincaré [36] explicitly formulated that the new spacetime transformation emitted by Lorentz applies not only to the electromagnetic, but all forces in nature. The existence of gravitational waves was first proposed by Henri Poincaré as early as June 5, 1905 and subsequently predicted in 1916 by Albert Einstein [37] on the basis of his gravitational-field equations (1.24) in a weak-field approximation (cf. the linearization in more detail in Sec. 1.5). The first attempt to define a solution for polarized plane gravitational waves (1.53) not only in the linearized Einstein theory, but in the full theory was made by Albert Einstein and Nathan Rosen [38] in 1937, who, however, argued that such waves could not exist because the metric would have to contain certain physical singularities.[1] In 1952 Yvonne Choquet-Bruhat [39] provided a proof of the well-posedness of the Cauchy problem for the Einstein equations, but until 1957 broad consensus has not been reached among the scientific community about the physical reality of gravitational waves.

The decisive *Conference on the Role of Gravitation in Physics* held at Chapel Hill on 18–23 January 1957 brought about a dramatic change of opinion. The discovery of a singularity-free solution of a plane gravitational wave that carries energy was announced by Bondi [40] in his Nature paper. In fact, the first attempt at giving a purely geometric definition of GWs was made by Felix Pirani who submitted his paper [41] just a few months before the Chapel Hill conference. He argued that a spacetime containing gravitational radiation should be algebraically special and it should appear as a discontinuity in the Riemann tensor. In Bondi's earlier paper, and the subsequent paper written by Bondi, Pirani, and Robinson [42], plane GWs were defined to be non-flat solutions of the vacuum Einstein equations which admit as much symmetry as do plane electromagnetic waves and inferred that such waves transport energy. Analogous to the changing dipole moment of charge that is necessary for the emission of electromagnetic radiation, gravitational radiation is emitted by time-varying mass quadrupole moment of the source (1.77). But unlike EM radiation, the lowest order of gravitational radiation is quadrupolar and the amplitudes of gravitational radiation from astrophysical sources were expected to be prohibitively small, which questioned even the existence of gravitational waves for decades.[43] Polarized plane gravitational waves (1.53), represented by transverse waves of spatial strain that propagate at speed of light, are perturbative vacuum solutions to the linearized weak-field equations (1.46).[2] Shortly after, Robinson and Trautman [44] found the first class of exact solutions of the full system of Einstein equations in 1962 which, as demonstrated in [45], satisfies Trautman's boundary for spatially confined gravitational sources and thus describing GWs with closed fronts coming from confined sources. In conclusion, the Bondi–Pirani–Robinson papers [40–42] and the Trautman–Robinson papers [44, 45], which were all published at the turn of the 1950s and 1960s, brought about an unprecedented rate of development in the theory of gravitational radiation and provided a firm theoretical foundation for further research and experiments.

The discovery of the first known binary pulsar system, designated PSR1913+16, by Hulse and Taylor [46] in 1974 and the subsequent observation of its pulse-arrival times by Taylor and Weisberg [47] in 1982 provided the first firm observational evidence for the existence of gravitational waves. The groundbreaking discovery and analysis of PSR1913+16 earned them the 1993 Nobel Prize in Physics and led to the recognition that direct observations of gravitational waves would offer the potential of new insight into some of the most extreme, compact objects in the universe. For further details about PSR1913+16, cf. Sec. 1.3.1. The developement of NR (Numerical relativity) methods begins with linearized theory and the PN approximation (cf. 1.5.6). PN approximation (in first-order) was first put into use by Einstein [37] for calculating relativistic corrections to the

---

[1] Later, it was revealed by H. Robertson that the Rosen's argument was invalid because the singularities were induced by a wrong choice of coordinates and the solution may in fact be interpreted as a cylindrical wave.

[2] The amount by which the ripples of the perturbation stretches and contracts measurements of space is referred to as the 'strain'.

perihelion precession of Mercury's orbit in 1915. However, the systematic study of PN approximations was, infact, conducted in the 1960s by the seminal works of Chandrasekhar [48] and co-workers. Numerical methods are used among other things, to predict the gravitational waves emanating from CBCs (cf. Sec. 2.2.1).

1.2 Gravitational-wave observatories and data analysis

This section gives a brief overview of gravitational-wave observatories (or gravitational-wave detectors) devised to measure the subtle effects of stretching and compressing of space that are caused by passing gravitational waves. Sec. 1.2.1 draws the reader's attention to the earlier, Weber-type resonant-mass detectors which were only sensitive to narrow ranges of frequencies and to a small portions of the sky, yet far less expensive than interferometric ones. Sec. 1.2.2 first discusses the basic idea and implementation of using laser interferometry for the measurement of gravitational radiation. Next, I give a brief review of the development of LIGO-type ground-based laser-interferometric gravitational-wave detectors, including the latest technological advancements and instrumental limit of detection. The section is concluded with a presentation of currently operational laser-interferometric gravitational-wave detectors across the globe and a plausible timeline for future detectors over the coming years.

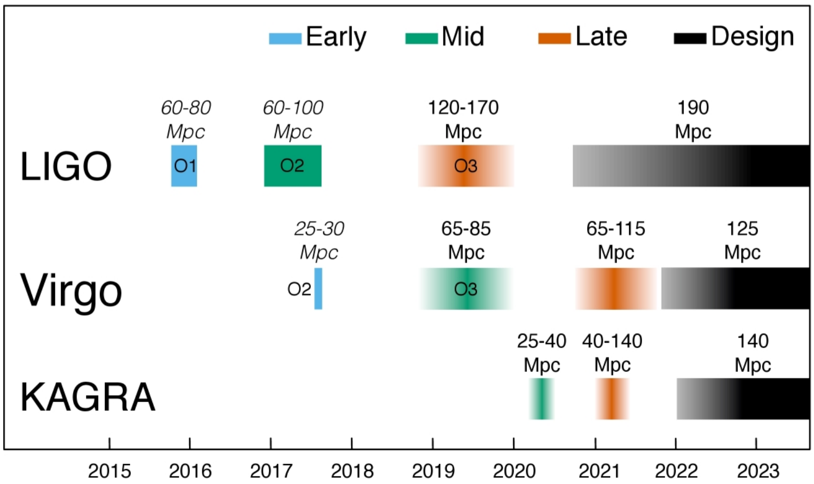

Figure 1.1: A plausible timeline for the evolution of horizon distance for observing runs of aLIGO, aVirgo and KAGRA (Kamioka Gravitational Wave Detector) detector over the coming years. The coloured bars show the observing runs, with achieved sensitivities in O1, O2 and O3, and the expected sensitivities for future runs (as shown in Fig. 1.5). There is significant uncertainty in the start and end times of the planned observing runs, especially for those further in the future, and these could move forward or backwards relative to what is shown above. Uncertainty in start or finish dates is represented by shading. The break between O3 and O4 will last at least 18 months. O3 is expected to finish by June 30, 2020 at the latest. The O4 run is planned to last for one calendar year. I indicate a range of potential sensitivities for aLIGO during O4 depending on which upgrades and improvements are made after O3. The most significant driver of the aLIGO range in O4 is from the implementation of frequency-dependent squeezing. (Original figure, courtesy of the KAGRA Collaboration, the LIGO Scientific Collaboration, and the Virgo Collaboration [49].)

1.2.1 Early measurements with resonant-mass detectors

The experimental search for gravitational waves began in the 1960s with Joseph Weber. In 1960 his paper [50] discussed the possibility of direct detection of GWs and stated that GW luminosity of binary black-hole coalescences could be as high as c^5/G, or about $10^{23} L_\odot$. In 1966 Weber and his students at the University of Maryland constructed the first resonant-mass detector or 'Weber bar'. [51] These cylinders consisted of multiple aluminium cylinders (2 meters in length, 1 meter in diameter and each weighted 1.2 tons) which were held at room temperature and isolated from vibrations in a vacuum chamber. They vibrated at a resonance frequency of 1660 Hz and were designed to be massive enough to be set in motion by supposedly weak GWs and the piezoelectric sensors had to be extremely sensitive as well, capable of detecting a change in the cylinders' length of about 10^{-16} meters. [52] Although Weber began publishing papers in 1968 with evidence claiming that he had detected GWs with one such resonant bar, the results of his experiments were largely discredited by others who all failed to replicate the positive results. Weber-type detectors as the earliest type of resonant-mass detector were dominant in 1960s and 1970s and many were built around the world.

The second generation of resonant-mass detectors emerged in the 1980s and 1990s. They were cooled to cryogenic temperatures with superconducting transducers and, as a result of their upgraded design, they achieved at least 6 orders of magnitude greater flux sensitivity than the original Weber-type detectors. [53] The five detectors – ALLERGO (Louisiana, US), AURIGA (Padua, Italy), EXPLORER (CERN, Switzerland), NAUTILUS (Rome, Italy) and NIOBE (Perth, Australia) – have been almost continuously searching for impulsive events since 1997 and as part of a global network for International Gravitational Event Collaboration (IGEC), they have been providing mutual data access. [51] The third generation of resonant-mass detectors is represented by two cryogenic spherical GW antennas, the MiniGRAIL (Leiden, Netherlands) and the Mário Schenberg (São Paulo, Brazil) that were built in the 2000s as downsized versions of the original proposals (others were cancelled). NAUTILUS, AURIGA and the two spherical antennas are still active, but most resonant-mass detectors have been decommissioned in favour of interferometric detectors.

1.2.2 Modern measurements with interferometric detectors

The idea of using laser interferometry for the measurement of gravitational radiation was first suggested in the early 1960s by Soviet scientists Mikhail Gertsenshtein and Vladislav Pustovoit. [55] The basic idea behind laser interferometry is to split laser beam from a single source into two sub-beams that travel in different optical paths, which are then combined again to produce interference. In classical Michelson–Morley-type laser interferometers designed for gravitational-wave detection, the sub-beams travel down orthogonal arms, bounce off mirrors, and then return to recombine. Normally the travel time is the same in each sub-beam, hence the light recombines constructively. However, interference occurs when a passing GW changes the relative length of the optical cavities in the interferometer (or equivalently, the proper travel time of photons) resulting in a strain

$$h = \Delta L/L, \tag{1.1}$$

where ΔL is the difference in path lengths L along the two arms of the interferometer. [56] For the typically-used, infrared lasers of wavelength $\lambda \sim 1\,\mu\text{m}$, and interferometer

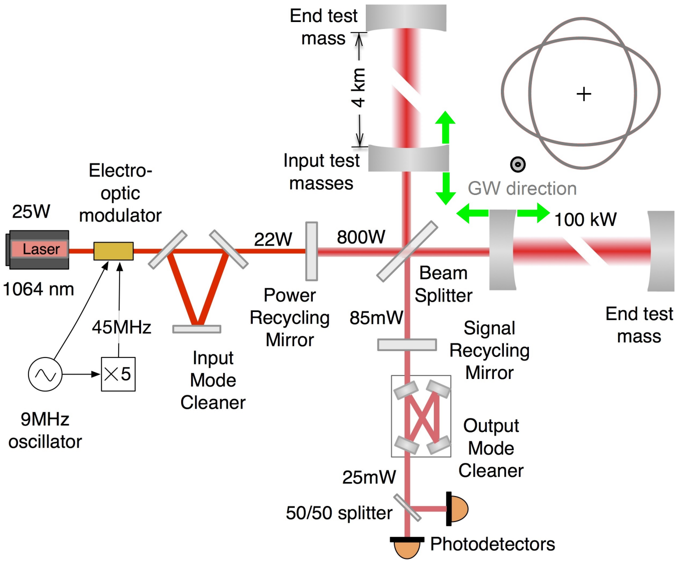

Figure 1.2: A simplified schematic diagram of a Michelson interferometer with annotations showing the optical power used during O1 run in aLIGO detectors. The interferometer is enhanced by two 4-km-long resonant arm cavities, which increase the optical power in the arms by a factor of $G_{\text{arm}} \simeq 270$. The diagram illustrates a laser beam being split into two sub-beams that travel down orthogonal arms, bounce off mirrors, and then return to recombine. Since the interferometer is operated near a dark fringe, all but a small fraction of the light is directed back towards the laser. The Nd:YAG laser, with wavelength $\lambda = 1064$ nm, is capable of producing power up to 180 W, but only 22 W were used in O1. A suspended, triangular Fabry–Pérot optical cavity serves as an input mode cleaner to clean up the spatial profile of the laser beam, suppress input beam jitter, clean polarization, and help stabilize the laser frequency (modulated at radio frequencies 9 and 45 MHz). The power recycling mirror between the beam splitter and the read-out photosensors resonates this light again to increase the power incident on the beamsplitter by a factor of $\simeq 40$, improving the shot noise sensing limit and filtering laser noises. On the antisymmetric side, the signal recycling mirror is used to broaden the response of the detector beyond the linewidth of the arm cavities. The output mode cleaner at the antisymmetric port removes excess spatial and frequency components of the laser light before the signal is detected by the main photodetectors. Faraday isolators suppress reflected beams while electro-optic modulators add radio frequency-sidebands to the laser light for the locking of laser beams to optical cavities. (Based partly on a figure courtesy of the LIGO Scientific Collaboration. [54])

arms of length $L = 4$ km, the minimum detectable strain is $h \sim \lambda/L \sim 3 \times 10^{-10}$. The schematic illustration of the specialized versions of Michelson interferometer applied in the instrumental design of GW detectors is shown in Fig. 1.2. Although the concept of using laser interferometry was conceived the early 1960s, its realization came only in the late 1960s and early 1970s through the pioneering work of Rainer Weiss at MIT and Kip Thorne and Ronald Drever at Caltech. The idea was put into practice by Rainer Weiss, who published an analysis of laser-interferometer performance in 1967 [57], demonstrating that its sensitivity is limited only by photon-shot noise at high frequencies. In 1972, Weiss identified all the fundamental noise sources that can cause movement in the optics. [58] He conceived the original idea of interferometric detectors with L-shaped arms, at 90° angles to each other would be optimal for GW detections. A passing GW would slightly stretch one arm as it would squeeze the other. In the late 1970s, Kip Thorne triggered the creation of an experimental gravitational-wave group at Caltech, led by Ronald Drever and Stan Whitcomb. The subsequent construction of Weiss's 1.5-meter-long prototype at MIT and Drever's and Whitcomb's 40-meter-long prototype interferometer at Caltech was funded by the US NSF (National Science Foundation).

Following the success of the first prototypes, Weiss was funded by NSF to design and lead a technical and cost study for the first generation of several-kilometer-long interferometers. Caltech and MIT submitted proposal to NSF in 1989 for the joint design and building of two 4-km-long and one 2-km-long laser interferometers in the United States at two sites (cf. Fig. 1.3); L1 in Livingston, Louisiana and H1 and H2 in Hanford, Washington under the joint leadership of Drever, Weiss and Thorne. To operate these facilities at both sites, the LSC was created in 1997 under the leadership of Barry Barish, and later joined by a number of universities and research institutions (mostly US-based), including Hungarian research groups from *Eötvös Loránd University* and *University of Szeged*. The first European-based interferometric instrument, GEO600 of just 600 metres arm length was built in a German-British partnership in 1995, in Sarstedt (near Hanover, Germany: see Fig. 1.3) as a downsized version of the original proposal of a 3-kilometer-long interferometer. However, in 1994 the French CNRS (Centre national de la recherche scientifique) and the Italian INFN (Istituto Nazionale di Fisica Nucleare) set up a project as well to design and construct the 3-km-long Virgo interferometric detector in the vicinity of Cascina (near Pisa, Italy: see Fig. 1.3). In 2000, CNRS and INFN created the EGO (European Gravitational Observatory) consortium that is responsible for the maintenance and operation of the instrument. The Virgo Collaboration was later joined by *Wigner Research Centre for Physics* (Hungary), NIKHEF (the Netherlands), POLGRAW (Poland) and University of Valencia (Spain).

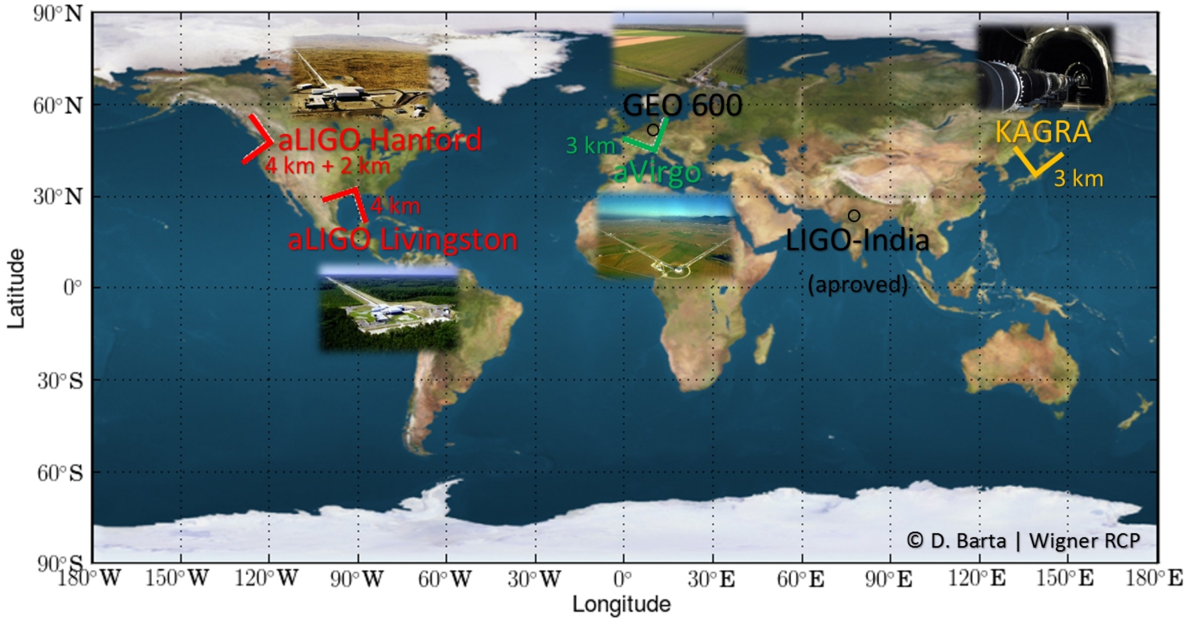

Figure 1.3: Geographical locations and orientations of current and future laser-interferometric gravitational-wave detectors across the globe. The GEO600 detector is currently taking data; the aLIGO detectors at Hanford and Livingston and aVirgo are expected to begin taking data in 2015; KAGRA should operate in its full optical configuration starting around 2018; and LIGO-India around 2020. LIGO-India is contingent on final approvals and funding, and its exact location has not yet been determined. (Based partly on a figure courtesy of the Virgo Collaboration.[59])

The first-generation laser-interferometric detectors; iLIGO (Initial LIGO) and iVirgo (Initial Virgo) commenced several data-taking periods from 2002 to 2010 and from 2007 to 2011, respectively. The 6th science run (S6) of the two iLIGO detectors that occurred from July 2009 through October 2010 were conducted in coincidence with iVirgo detector's 2nd and 3rd science runs (VSR2, VSR3). Although the sensitivity of iLIGO increased in a wide frequency band over four orders of magnitude larger than Weber's original instrument and reached its primary design specification of a detectable strain of 2×10^{-23} Hz$^{-1/2}$ at 200 Hz, no gravitational wave signals were detected at this stage. [54] The era of first-generation instruments in iLIGO came to an end in 2010, at which point it was disassembled to make way for new and improved instruments which were designed to be 10 times more sensitive than their predecessor, and promised to increase the volume of the observable universe by a factor of 1000. Upgraded components for the aLIGO detectors (shown in Fig. 1.2) were installed in the existing facilities from 2008 to 2014. [60] These upgrades included an increase in the laser power to reduce quantum noise, larger and heavier mirrors to reduce thermal and radiation pressure noise, better suspension fibers for the mirrors to reduce suspension thermal noise, among many other improvements. [31] The design levels of the aforementioned sources of noise limiting the sensitivity of the two aLIGO detectors are shown in Fig. 1.4.

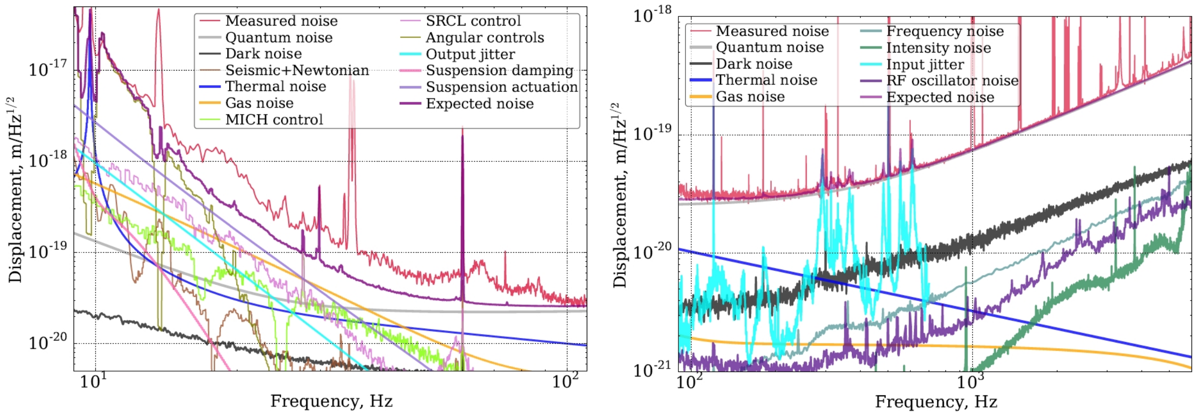

(a) aLIGO Livingston Observatory **(b)** aLIGO Hanford Observatory

Figure 1.4: The design levels of numerous noise sources that limit the sensitivity of the two aLIGO detectors at low frequencies. The strain sensitivities are similar between the two sites. Panel (a) shows the low-frequency curves for L1, whereas panel (b) shows the high-frequency curves for H1 detector. Quantum noise is the sum of the quantum radiation pressure noise and shot noise. Dark noise refers to electronic noise in the signal chain with no light incident on the readout photodetectors. Thermal noise is the sum of suspension and coating thermal noises. Gas noise is the sum of squeezed film damping and beam tube gas phase noises. The coupling of the residual motion of the Michelson (MICH) and signal-recycling cavity (SRCL) degrees of freedom to gravitational wave channel is reduced by a feedforward-cancellation technique. At low frequencies, there is currently a significant gap between the measured strain noise and the root-square sum of investigated noises. At high frequencies, the sensitivity is limited by shot noise and input beam jitter. (Original figure, courtesy of the LIGO Scientific Collaboration. [54])

The newly-installed aLIGO was commissioned from mid-2014 to mid-2015 with a sensitivity roughly 3–4 times greater in the frequency range between 10 Hz and 10 kHz than that of iLIGO's last science run. Around 100 Hz, the strain sensitivity was 8 ×

10^{-23} Hz$^{-1/2}$, which resulted in an astrophysical reach $\simeq 4.1$ and $\simeq 3.5$ times greater than that of the iLIGO detectors: The sky location and source orientation-averaged range was 1.3 Gpc for a $30M_\odot + 30M_\odot$ BNS, whereas for a BNS star system the range was 70–80 Mpc. [54] The target strain sensitivities of advanced detectors anticipated for future runs are shown as bands in Fig. 1.5. All these improvements have culminated in the discovery of a series of GW transient events during the observation runs O1 and O2 between 2015 to 2017 that marked the opening of the era of gravitational-wave astronomy. [61] For further details about GW transient events discovered during the first observation runs of advanced detectors, cf. Sec. 1.3.2.

(a) Advanced LIGO **(b)** Advanced Virgo

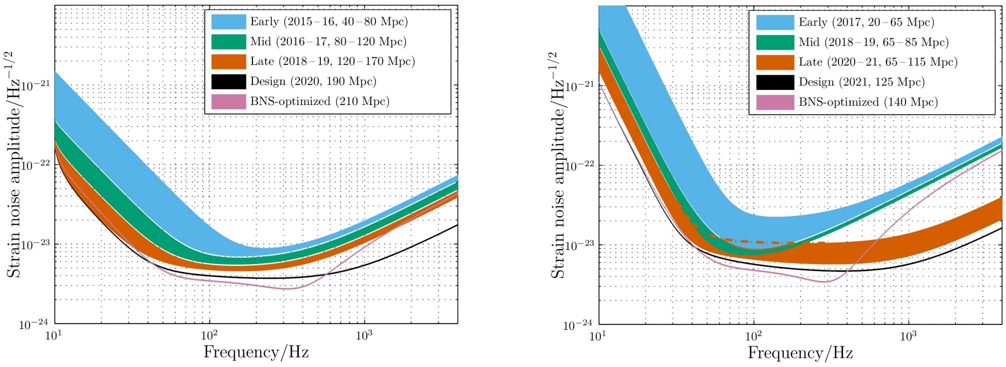

(c) KAGRA

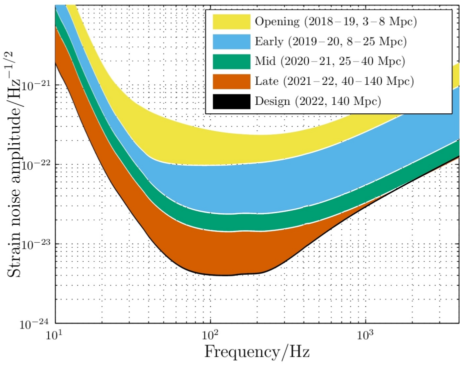

Figure 1.5: The target strain sensitivities of aLIGO (*top left*), aVirgo (*top right*) and KAGRA (*bottom*) as a function of frequency. The quoted range is for a $1.4M_\odot + 1.4M_\odot$ BNS merger. The BNS range (in Mpc) achieved in past observing runs and anticipated for future runs is shown as bands. The O1 aLIGO curve is taken from the Hanford detector, the O2 aLIGO curve comes from Livingston. In each case these had the better performance for that observing run. The O3 curves for aLIGO and aVirgo reflect recent performance. Detailed planning for the post-O3 to O4 period, shown in Fig. 1.1, is now in progress and may result in changes to both target sensitivities for O4 and the start date for this run. The the BNS curve for KAGRA may be realized by detuning the signal recycling cavity to significantly improve the BNS range to 155 Mpc once design sensitivity is reached. (Original figure, courtesy of the KAGRA Collaboration, the LIGO Scientific Collaboration, and the Virgo Collaboration. [49])

Current operating facilities in the global network include the twin aLIGO facilities in the United States and the aVirgo in Europe. KAGRA, an underground cryogenic interferometer built in Japan (Kamioka mine near Hida, Gifu Prefecture) is coming online by the end of 2019 to join the campaign of aLIGO and aVirgo. The coming years will also see the arrival of a third LIGO detector located in India (near Aundha Nagnath, Hingoli District, Maharashtra), which is expected to be operational around 2022. Geographical locations and orientations of current and future laser-interferometric gravitational-wave detectors across the globe are listed in Table 1.1 and shown in Fig. 1.3. Furthermore, the plans to design third-generation observatories, such as the Einstein Telescope [62] or Cosmic Explorer [63], with another factor of 10 improvement in sensitivity, are already on the way. It is also possible that for some sources, there could be multiband GW observations. [49] The space-borne LISA (Laser Interferometer Space Antenna) could provide early warning and sky localization, as well as additional information on system parameters and formation mechanisms. [24, 25] Building multiple GW observatories around the globe will increase the confidence of a detection by observing the signal by independent observatories with uncorrelated noise. Operating them together is also helpful in locating the sources of GW signals more accurately and determining the source parameters with higher precision. [64]

Detector	**Latitude** (ϕ)	**Longitude** (λ)	**Orientation** (γ)	ζ
LIGO Hanford	$46°27'19''$ N	$119°24'28''$ W	$171°$	$90°$
LIGO Livingston	$30°33'46''$ N	$90°46'27''$ W	$242°$	$90°$
GEO600	$52°15'$ N	$9°48'36''$ E	$68°46'48''$	$94°19'48''$
Virgo	$43°37'53''$ N	$10°30'16''$ E	$115°36'$	$90°$
KAGRA	$36°25'26''$ N	$137°19'11''$ E	$75°$	$90°$
LIGO-India	$19°32'24''$ N	$77°2'26''$ E	$58°12' + k\times 90°$	$90°$

Table 1.1: Geographical locations and orientations of currently operational and future laser-interferometric gravitational-wave detectors across the globe. The angles ϕ and λ are the geodetic latitude and longitude, respectively, of the detector's site. The angle γ determines the orientation of the interferometer arms with respect to local geographical directions and it is measured counter-clockwise from the East to the bisector of the interferometer arms. The angle ζ is the angle between the interferometer arms. The geographical locations and orientation angles are based on Refs. [65, 66].

1.3 Observations of gravitational waves

I begin with a discussion of the observations of gravitational-wave events with the first indirect observational evidence of gravitational waves in Sec. 1.3.1. Next, I review a series of directly observed GW events, commenced with the detection of GW150914.

1.3.1 Hulse–Taylor binary pulsar

A number of experiments have provided indirect evidence, notably the observation of binary pulsars. The binary-pulsar system PSR1913+16 was certainly not the first discovered pulsar, but it was the first observed binary-pulsar system which evolves precisely matching the general relativistic predictions of energy loss through gravitational-wave emission. In 1974 Russell Hulse and Joseph Taylor [46] detected pulsed radio emissions from this system using the Arecibo Observatory's 305m radio telescope in Puerto Rico. Subsequent observations of its pulse-arrival times, taken between September 1974 and March 1981, by Taylor and Weisberg, [47] verified that the measured decay of the orbital parameters in the system is in precise agreement with the rate at which the orbital period should decay as kinetic energy is lost from the system through gravitational radiation, according to Einstein's general theory of relativity. The precise agreement provided the first compelling observational evidence for the existence of gravitational waves. The ratio of observed to predicted rate of orbital decay was calculated to be $\dot{P}_{\rm b}^{\rm intr}/\dot{P}_{\rm b}^{\rm GR} = 0.997 \pm 0.002$ at the time. (Now $\dot{P}_{\rm b}^{\rm intr}/\dot{P}_{\rm b}^{\rm GR} = 0.9983 \pm 0.0016$, cf. Table 1.2). The importance of gravitational waves is highlighted by the very fact that even this indirect evidence for their existence earned Hulse and Taylor the Nobel Prize in 1993. Taylor and co-workers monitored PSR1913+16 for 20 years to further confirm that the system lost energy exactly as predicted. [64] Its detailed features were deducted from observations of the pulse-arrival times and the Doppler effect. Fig. 1.6 summarizes the comparsion between the observed change in the epoch of periastron of measurement and the corresponding general relativistic prediction. Since the discovery of PSR B1913+16, several other binary-pulsar systems with gravitational radiation-induced orbital decay have been observed, albeit with somewhat less precision than PSR B1913+16. See the published measurements of $\dot{P}_{\rm b}^{\rm intr}/\dot{P}_{\rm b}^{\rm GR}$ for 10 such pulsars in Table 1.2.

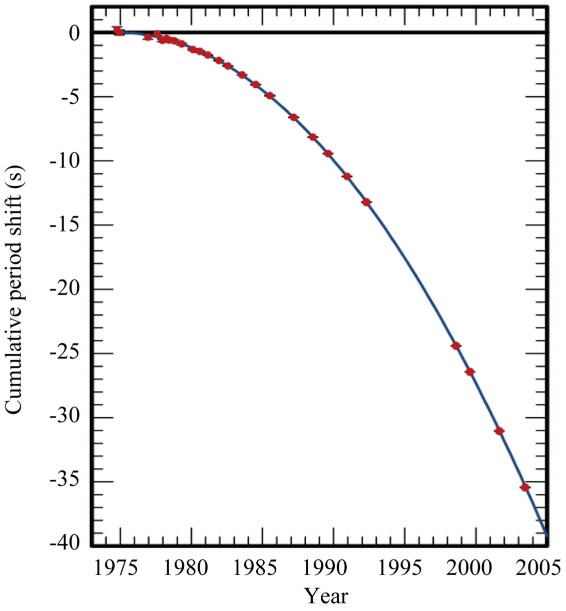

Figure 1.6: Orbital decay of PSR B1913+16 as a function of time. The parabola represents the orbital phase shift predicted for gravitational emission according to general relativity. The data points, with error bars too small to show, indicate the observed change in the epoch of periastron. (Original figure, courtesy of J. M. Weisberg. [67])

PSR	$\dot{P}_{\rm b}^{\rm intr}/\dot{P}_{\rm b}^{\rm GR}$
J0348+0432	1.05 ± 0.18
J0737-3039	1.003 ± 0.014
J1141-6545	1.04 ± 0.06
B1534+12	0.91 ± 0.06
J1738+0333	0.94 ± 0.13
J1756-2251	1.08 ± 0.03
J1906+0746	1.01 ± 0.05
B1913+16	0.9983 ± 0.0016
B2127+11C	1.00 ± 0.03

Table 1.2: Comparison of gravitational radiation-induced orbital decay with the orbital decay predicted by general relativity in 10 binary PRSs. (For further details and references, please, see Ref. [67].)

1.3.2 GW events and source parameters from observation runs O1 and O2

Event	$m_1/M_\odot$	$m_2/M_\odot$	$\mathcal{M}/M_\odot$	$\xi_{\rm eff}$	$M_{\rm f}/M_\odot$	$a_{\rm f}$	$E_{\rm rad}/(M_\odot c^2)$	$\ell_{\rm peak}/({\rm erg s}^{-1})$	$d_L/{\rm Mpc}$	z	$\Delta\Omega/{\rm deg}^2$
GW150914	$35.6^{+4.8}_{-3.0}$	$30.6^{+3.0}_{-4.4}$	$28.6^{+1.6}_{-1.5}$	$-0.01^{+0.12}_{-0.13}$	$63.1^{+3.3}_{-3.0}$	$0.69^{+0.05}_{-0.04}$	$3.1^{+0.4}_{-0.4}$	$3.6^{+0.4}_{-0.4} \times 10^{56}$	430^{+150}_{-170}	$0.09^{+0.03}_{-0.03}$	179
GW151012	$23.3^{+14.0}_{-5.5}$	$13.6^{+4.1}_{-4.8}$	$15.2^{+2.0}_{-1.1}$	$0.04^{+0.28}_{-0.19}$	$35.7^{+9.9}_{-3.8}$	$0.67^{+0.13}_{-0.11}$	$1.5^{+0.5}_{-0.5}$	$3.2^{+0.8}_{-1.7} \times 10^{56}$	1060^{+540}_{-480}	$0.21^{+0.09}_{-0.09}$	1555
GW151226	$13.7^{+8.8}_{-3.2}$	$7.7^{+2.2}_{-2.6}$	$8.9^{+0.3}_{-0.3}$	$0.18^{+0.20}_{-0.12}$	$20.5^{+6.4}_{-1.5}$	$0.74^{+0.07}_{-0.05}$	$1.0^{+0.1}_{-0.2}$	$3.4^{+0.7}_{.1.7} \times 10^{56}$	440^{+180}_{-190}	$0.09^{+0.04}_{-0.04}$	1033
GW170104	$31.0^{+7.2}_{-5.6}$	$20.1^{+4.9}_{-4.5}$	$21.5^{+2.1}_{-1.7}$	$-0.04^{+0.17}_{-0.20}$	$49.1^{+5.2}_{-3.9}$	$0.66^{+0.08}_{-0.10}$	$2.2^{+0.5}_{-0.5}$	$3.3^{+0.6}_{-0.9} \times 10^{56}$	960^{+430}_{-410}	$0.19^{+0.07}_{-0.08}$	924
GW170608	$10.9^{+5.3}_{-1.7}$	$7.6^{+1.3}_{-2.1}$	$7.9^{+0.2}_{-0.2}$	$0.03^{+0.19}_{-0.07}$	$17.8^{+3.2}_{-0.7}$	$0.69^{+0.04}_{-0.04}$	$0.9^{+0.0}_{-0.1}$	$3.5^{+0.4}_{-1.3} \times 10^{56}$	320^{+120}_{-110}	$0.07^{+0.02}_{-0.02}$	396
GW170729	$50.6^{+16.6}_{-10.2}$	$34.3^{+9.1}_{-10.1}$	$35.7^{+6.5}_{-4.7}$	$0.36^{+0.21}_{-0.25}$	$80.3^{+14.6}_{-10.2}$	$0.81^{+0.07}_{-0.13}$	$4.8^{+1.7}_{-1.7}$	$4.2^{+0.9}_{-1.5} \times 10^{56}$	2750^{+1350}_{-1320}	$0.48^{+0.19}_{-0.20}$	1033
GW170809	$35.2^{+8.3}_{-6.0}$	$23.8^{+5.2}_{-5.1}$	$25.0^{+2.1}_{-1.6}$	$0.07^{+0.16}_{-0.16}$	$56.4^{+5.2}_{-3.7}$	$0.70^{+0.08}_{-0.09}$	$2.7^{+0.6}_{-0.6}$	$3.5^{+0.6}_{-0.9} \times 10^{56}$	990^{+320}_{-380}	$0.20^{+0.05}_{-0.07}$	340
GW170814	$30.7^{+5.7}_{-3.0}$	$25.3^{+2.9}_{-4.1}$	$24.2^{+1.4}_{-1.1}$	$0.07^{+0.12}_{-0.11}$	$53.4^{+3.2}_{-2.4}$	$0.72^{+0.07}_{-0.05}$	$2.7^{+0.4}_{-0.3}$	$3.7^{+0.4}_{-0.5} \times 10^{56}$	580^{+160}_{-210}	$0.12^{+0.03}_{-0.04}$	87
GW170817	$1.46 + {}^{0.12}_{-0.10}$	$1.27^{+0.09}_{-0.09}$	$1.186^{+0.001}_{-0.001}$	$0.00^{+0.02}_{-0.01}$	≤ 2.8	≤ 0.89	≥ 0.04	$\geq 0.1 \times 10^{56}$	40^{+10}_{-10}	$0.01^{+0.00}_{-0.00}$	16
GW170818	$35.5^{+7.5}_{-4.7}$	$26.8^{+4.3}_{-5.2}$	$26.7^{+2.1}_{-1.7}$	$-0.09^{+0.18}_{-0.21}$	$59.8^{+4.8}_{-3.8}$	$0.67^{+0.07}_{-0.08}$	$2.7^{+0.5}_{-0.5}$	$3.4^{+0.5}_{-0.7} \times 10^{56}$	1020^{+430}_{-360}	$0.20^{+0.07}_{-0.07}$	39
GW170823	$39.6^{+10.0}_{-6.6}$	$29.4^{+6.3}_{-7.1}$	$29.3^{+4.2}_{-3.2}$	$0.08^{+0.20}_{-0.22}$	$65.6^{+9.4}_{-6.6}$	$0.71^{+0.08}_{-0.10}$	$3.3^{+0.9}_{-0.8}$	$3.6^{+0.6}_{-0.9} \times 10^{56}$	1850^{+840}_{-840}	$0.34^{+0.13}_{-0.14}$	1651

Table 1.3: Selected source parameters of the 11 confident detections. The columns show source frame component masses m_i and chirp mass $\mathcal{M}$, dimensionless effective aligned spin $\xi_{\rm eff}$, final source frame mass $M_{\rm f}$, final spin $a_{\rm f}$, radiated energy $E_{\rm rad}$, peak luminosity $\ell_{\rm peak}$, luminosity distance d_L, redshift z and sky localization $\Delta\Omega/{\rm deg}^2$. Median values with 90% credible intervals include statistical errors, and systematic errors from averaging the results of two waveform models for BBHs. The sky localization is the area of the 90% credible region. For BBH events, the redshift was calculated from the luminosity distance and assumed cosmology. (Original table, courtesy of the LIGO Scientific Collaboration and the Virgo Collaboration. [61])

Just a few days after the start of the first science run (O1), on September 14, 2015, the aLIGO detectors recorded an interference pattern associated with a gravitational-wave transient which was emitted from a BBH system of chirp mass $\mathcal{M} = 28.2^{+1.8}_{-1.7}\, M_\odot$ (cf. definition in (1.6)) at a luminosity distance $d_L = 440^{+160}_{-180}$ Mpc. [68] The signal, designated 'GW150914' [69], was so loud[3] that the probability of a false alarm was much smaller than 10^{-7}. [31] The direct observation of the first signal was shortly followed by the identification of another 10 confirmed signals over the period of aLIGO's first two observation runs (O1, September 2015 to January 2016) and (O2, November 2016 to August 2017) to which aVirgo has joined in August 2017. A third observation run (O3) began on April 1, 2019 from which a large number of candidate events were recorded (a total number of 22

---

[3] The level of signal relative to the level of background noise, measured by the SNR (Signal-to-noise ratio), was much larger than 5σ.

candidate events to September 2019). This section will briefly discuss the first series of confirmed GW events, shown in Fig. 1.7, that constitute the first GW-transient catalogue of CBCs (GWTC-1) [61], and the properties of their sources. From O1, two confident detections of signals from BBH mergers were made: GW150914 [70] and GW151226 [71]. Additionally, a third trigger has appeared in the O1 catalog of binary black holes which was later relabel as GW151012 [72] after its assessment. Following the reanalysis of O1 with the O2 pipelines, GW150914 remained the highest SNR in O1 data sets, behind only the binary neutron star inspiral GW170817 [73] and no new GW events were discovered. [61] From O2, four additional BBH merger events; GW170729, GW170809, GW170818 and GW170823 were reported by Ref. [61]: GW170729, GW170809, GW170818 and GW170823.

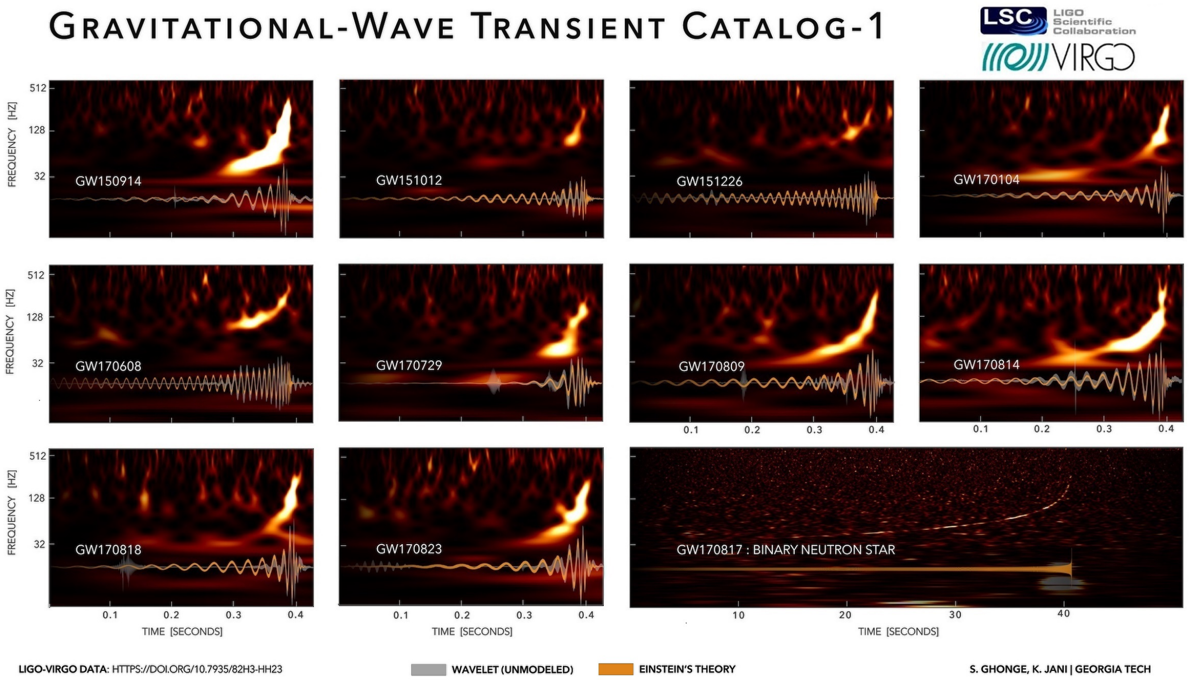

Figure 1.7: Time-frequency maps and reconstructed signal waveforms for the eleven GW events in GWTC-1. (Original figure, courtesy of LSC–Virgo Collaboration, S. Ghonge and K. Jani. [61])

The GW signals emitted from CBCs depend on *intrinsic parameters* that specifically delineate emitted waveform (1.76) and the general relativistic two-body dynamics (1.75) in the binary and on *extrinsic parameters* that encode the position of the source in relation to the detector network. Thus, an isolated compact binary undergoing quasi-circular inspiral is uniquely described by the mass m_i, spin vector $\vec{S}_i$ and electric charge Q_i of its components that are intrinsic to the source. Note that the electric charge of astrophysical BHs is supposed to be negligible. Seven additional extrinsic parameters are required to define the sky location (right ascension α and declination δ), luminosity distance d_L, the orbital inclination ι and polarization angle ψ, the time t_c and phase ϕ_c at coalescence that are extrinsic to the source. For more information about polarizations and sky location, cf. Sec. 1.5.5. Parameter estimation for the sky locations of confirmed GW events from observation runs O1 and O2 are shown in Fig. 1.8. For more details, see references in [61]. If the spins have a component in the orbital plane, then the binary's orbital angular

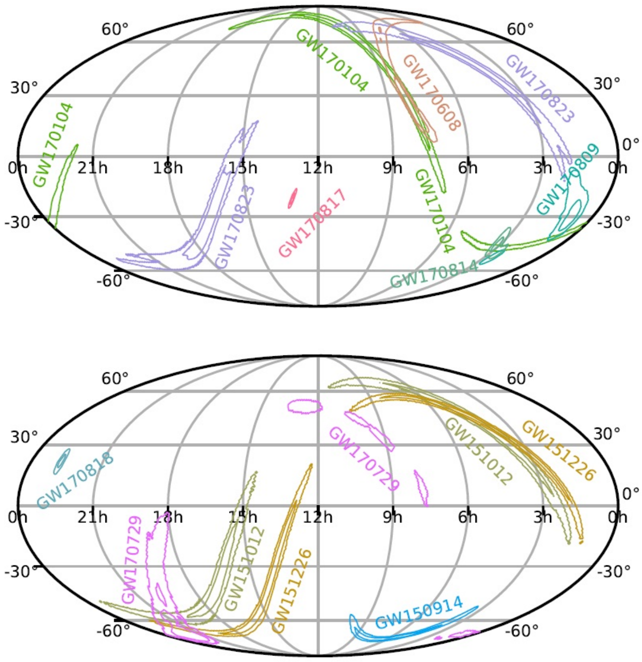

Figure 1.8: Parameter estimation for the sky locations of confirmed GW events from observation runs O1 and O2 in a Mollweide projection. The probable position of the source is shown in equatorial coordinates (right ascension is measured in hours, and declination is measured in degrees). 50% and 90% credible regions of posterior probability sky areas for the GW events. *Top panel*: Confidently detected O2 GW events (GW170817, GW170104, GW170823, GW170608, GW170809, GW170814) for which alerts were sent to EM observers. *Bottom panel*: O1 events (GW150914, GW151226, GW151012), along with O2 events (GW170729, GW170818) not previously released to EM observers. (Original figure, courtesy of the LIGO Scientific Collaboration and the Virgo Collaboration. [61])

momentum $\vec{L}$ and its spin vectors precess [74, 75] around the total angular momentum

$$\vec{J} = \vec{L} + \vec{S}_1 + \vec{S}_2. \tag{1.2}$$

For precessing binaries the orbital angular momentum vector $\vec{L}$ is not a stable direction, and it is preferable to describe the source inclination by the angle θ_{JN} between the total angular momentum $\vec{J}$ and the line of sight vector $\vec{N}$ instead of the orbital inclination angle ι between $\vec{L}$ and $\vec{N}$ [76]. Frequency-dependent quantities such as spin vectors, and derived quantities as ξ_p were quoted by Ref. [61] at a GW reference frequency $f_{\text{ref}} = 20$ Hz. The dimensionless spin vectors and spin magnitudes are defined by

$$\vec{\xi}_i = c\vec{S}_i/(Gm_i^2), \quad a_i = c|\vec{S}_i|/(Gm_i^2), \tag{1.3}$$

respectively, on the grounds that the maximum spin a Kerr BH of mass m may reach is Gm^2/c. The effective aligned spin that represents the dominant spin effect is written as a simple mass-weighted linear combination of the spins [77] projected onto the Newtonian angular momentum $\hat{L}_N$, which is normal to the orbital plane ($\hat{L} = \hat{L}_N$ for aligned-spin binaries)

$$\xi_{\text{eff}} = \frac{(m_1\vec{\xi}_1 + m_2\vec{\xi}_2)\hat{L}_N}{M}, \tag{1.4}$$

where m_1 is defined to be the mass of the larger component of the binary, such that $m_1 \geq m_2$, and

$$M = m_1 + m_2 \tag{1.5}$$

is the total mass of the binary. Throughout the inspiral ξ_{eff} is approximately conserved [78] and the phase evolution depends at leading order on the chirp mass [79],

$$\mathcal{M} = \frac{(m_1 m_2)^{3/5}}{M^{1/5}}, \tag{1.6}$$

which is also the best measured parameter for low-mass systems dominated by the inspiral [80]. The mass ratio

$$q = \frac{m_2}{m_1} \leq 1, \tag{1.7}$$

and effective aligned spin ξ_{eff} appear in the phasing at higher orders [78]. One may also find it useful 0to introduce the reduced mass and the symmetric mass ratio by

$$\mu = m_1 m_2 / M, \quad \eta = \mu / M, \tag{1.8}$$

respectively.

1.4 Fundamentals of spacetimes on pseudo-Riemannian manifolds

In this section, first the mathematical notation and conventions used in the present dissertation are discussed. Next, I summarize the necessary mathematical preliminaries of pseudo-Riemannian geometry which lay the conceptual foundations for clear and intuitive discussion of my own research discussed in the following chapters. The discourse in this section is mostly based on the content of comprehensive introductory textbooks [32–34].

1.4.1 Mathematical notation and conventions

Throughout the dissertation, I shall use 'geometrized' units, in which the speed of light c in vacuum and the gravitational constant G are set to unity by an appropriate choice of units so that the Einstein constant becomes $\kappa \equiv 8\pi G/c^3 = 8\pi$. However, for convenience of the reader, G and c have been restored in those formulae that are compared to their respective Newtonian counterpart. Table A.1 that provides conversion factors for 'geometrized' units into SI units is found in Appendix A.2. Spatial coordinates are labeled with Latin indices a, $b \ldots$, whereas the ones belonging to 4-vectors and tensors are labeled with Greek indices α, $\beta \ldots$. I conventionally denote time coordinate by the index 0, while spatial coordinates are denoted by indices running from 1 to 3. According to Einstein's notational convention, I am summing over all of the possible values of that index variable which occurs twice in a single term, once in an upper and once in a lower position. Lower indices stand for covariant quantities, upper ones for contravariant ones, whereas both in a single term denote mixed variance. Symmetrization of indices is indicated by ( ). The metric signature is chosen as $(-+++)$ according to the Pauli space-like convention. Partial derivatives are denoted by ∂_μ or a comma, single and repeated covariant derivatives by ∇_μ, $\nabla_{\mu\nu}$ or by a semicolon. Any variable with overhead hat (e.g. $\hat{q}$) represents the linearized perturbation of its corresponding 'background' quantity (e.g. q). In the present dissertation, common homogeneous relations which fall into various types according to their specific properties are denoted by the following symbols: Symbols based on equality relations in a broader sense comprise $=$ for equality, $\equiv$ for equality by definition, $\approx$ for approximate equality, $\propto$ for proportionality, $\sim$ for asymptotic equivalency or for same order of magnitude. Furthermore, the following types of inequalities include $<$ or $>$ for strict inequality, $\leq$ or $\geq$ for not-strict inequality (not greater/less than), $\ll$ or $\gg$ for asymptotic comparison (i.e. much less/greater than).

1.4.2 Fundamental definitions and concepts

A principal premise of general relativity is that a spacetime can be modeled by a 4-dimensional pseudo-Riemannian manifold, more specifically, a Lorentzian manifold (which is a pseudo-Riemannian manifold of Lorentzian signature). A pseudo-Riemannian spacetime $(\mathcal{M}, g)$ is a differentiable manifold $\mathcal{M}$ endowed with an everywhere non-degenerate, second-degree, smooth and symmetric metric tensor field g. Let the components of a vector $\boldsymbol{x} \in \mathbb{R}^4$ given on $\mathcal{M}$ by local coordinates

$$\{x^\mu : \mu \in [0,3] \subset \mathbb{N}\}, \tag{1.9}$$

then any tangent vector, denoted by $\mathbf{u} = u^\mu e_\mu$, defines the local basis of the tangent space to $\mathcal{M}$ at each point $\boldsymbol{x} \in \mathcal{M}$ by

$$\{e^\mu = \partial/\partial x^\mu : \mu \in [0,3] \subset \mathbb{N}\}. \tag{1.10}$$

The metric tensor can be written in the form

$$g = g_{\mu\nu} dx^\mu \otimes dx^\nu \quad \text{where} \quad g_{\mu\nu} \equiv e_\mu e_\nu. \tag{1.11}$$

(1.11) is a linear combination of tensor products of one-form gradients of local coordinates (1.9), where the coefficients $g_{\mu\nu}$ are a set of 16 real-valued functions. In order for the metric to be symmetric, 10 of its coefficients are independent. The non-degeneracy of $g_{\mu\nu}$ means that this matrix is non-singular (i.e. has non-vanishing determinant), while the Lorentzian signature of g implies that the matrix $g_{\mu\nu}$ of the metric tensor has one positive and three negative $(+---)$ eigenvalues (or the other way around $(-+++)$). In a 4-dimensional flat spacetime, the metric tensor is named after Hermann Minkowski and written as

$$\eta_{\mu\nu} \equiv \mathrm{diag}[+1,-1,-1,-1] \equiv \begin{pmatrix} 1 & 0 & 0 & 0 \\ 0 & -1 & 0 & 0 \\ 0 & 0 & -1 & 0 \\ 0 & 0 & 0 & -1 \end{pmatrix}, \tag{1.12}$$

with the signature of our choice. Most importantly, the Minkowski spacetime $(\mathcal{M}, \eta)$ is the mathematical setting in which Einstein's theory of special relativity is most conveniently formulated. This metric is Lorentz invariant, in other words, it transforms under a change of coordinates

$$x^\mu \to x^{\mu'} = \Lambda^{\mu'}{}_{\nu} x^\nu \tag{1.13}$$

as $\eta_{\mu'\nu'} = \Lambda^{\alpha}{}_{\mu'} \eta_{\alpha\beta} \Lambda^{\beta}{}_{\nu'}$ which is the defining property of a Lorentz transformation:

$$\Lambda^\mu{}_\nu \equiv \frac{\partial x^{\mu'}}{\partial x^\nu} \equiv \begin{pmatrix} \gamma & \beta\gamma & 0 & 0 \\ -\beta\gamma & \gamma & 0 & 0 \\ 0 & 0 & 1 & 0 \\ 0 & 0 & 0 & 1 \end{pmatrix}, \tag{1.14}$$

where $\beta = v/c$ and $\gamma = (1-\beta^2)^{-1/2}$ are notations from classical electrodynamics for fractional speed and for the Lorentz factor, respectively. A particular Minkowski diagram of Fig. 1.9 illustrates some properties of Lorentz transformations relating events in two inertial frames of reference, where an observer stationary at the event $(0,0)$ makes a change of velocity along the x-axis. With the quantities dx^μ in (1.11) being regarded as

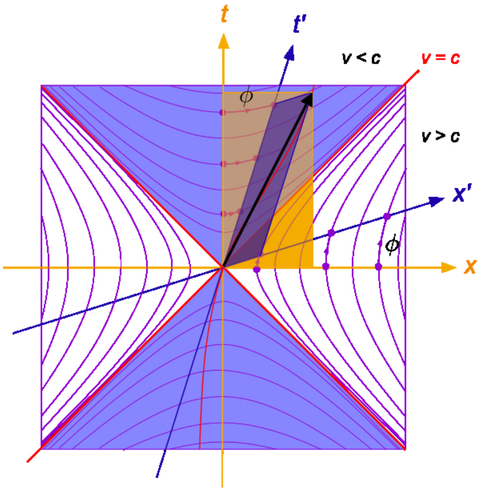

Figure 1.9: Minkowski diagram with resting frame (x,t), moving frame (x',t'), light cone, and hyperbolas indicating the surfaces of transitivity of the orthochronous Lorentz transformations. In 4-dimensional spacetime, they are represented by hyperboloids of two sheets inside the light cone and one-sheeted hyperboloids outside the light cone together with the past and future light cones themselves and, separately, the origin. (Original figure, courtesy of M. P. Hobson *et al.* [34].)

the components of an infinitesimal coordinate displacement four-vector (1.9), the metric determines the invariant square of an infinitesimal line element (also often referred to as ‘spacetime interval’) that measures the separation between two arbitrarily close events in spacetime. The line element is conventionally denoted by

$$ds^2 = g_{\mu\nu} dx^\mu \otimes dx^\nu \tag{1.15}$$

and indicates the causal structure of spacetime. In Minkowski spacetime, the Lorentz transformations (1.14) preserve the spacetime interval between any two events. Unlike Riemannian manifolds with positive-definite metrics, an indefinite signature allows any tangent vector $\mathbf{u}$ in (1.10) to be classified into *timelike*, *null* or *spacelike*, shown in Fig. 1.9. Accordingly, the spacetime interval (1.15) is

- *timelike* and can be physically traversed only by a massive object when $ds^2 < 0$. $\sqrt{|ds^2|}$ acts as an incremental proper time;
- *lightlike* and can only be traversed by light when $ds^2 = 0$;
- *spacelike* and cannot be traversed when $ds^2 > 0$, since they connect events that are outside each other’s light cones. $\sqrt{|ds^2|}$ acts as an incremental proper length.

For a tangent vector field $\mathbf{u} = \{u^\mu e_\mu\}$ in eq. (1.10), the covariant derivative $\nabla_\mu \mathbf{u}$ is defined by

$$\nabla_\mu u^\nu = \partial_\mu u^\nu + \Gamma^\nu_{\rho\mu} u^\rho, \tag{1.16}$$

where ∇_μ denotes the covariant derivative along tangent vectors of the manifold. Determined by how the tangent space is attached to the cotangent space by the metric tensor, the Christoffel symbols of the second kind (also known as metric connection coefficients)

$$\Gamma^{\mu}{}_{\alpha\beta} \equiv \frac{1}{2} g^{\mu\sigma} \left(\frac{\partial g_{\sigma\beta}}{\partial x^{\alpha}} + \frac{\partial g_{\sigma\alpha}}{\partial x^{\beta}} - \frac{\partial g_{\alpha\beta}}{\partial x^{\sigma}} \right) \tag{1.17}$$

are constructed from the metric tensor (1.11) and its first partial derivatives and represented by an $4 \times 4 \times 4$ array of real number and provide a concrete representation of the connection of pseudo-Riemannian geometry in terms of coordinates on the manifold $\mathcal{M}$. They are symmetric in the two lower indices and represents the change in the local basis (1.10) at each point $\boldsymbol{x} \in \mathcal{M}$ through

$$\frac{\partial e^{\alpha}}{\partial x^{\nu}} = -\Gamma^{\mu}{}_{\alpha\beta} e^{\beta}. \tag{1.18}$$

In general relativity, the world line of a freely moving or falling particle is given by the geodesic equation of motion

$$\frac{d^2 x^{\mu}}{ds^2} + \Gamma^{\mu}{}_{\alpha\beta} \frac{dx^{\alpha}}{ds} \frac{dx^{\beta}}{ds} = 0, \tag{1.19}$$

where s is an affine parameter of motion (e.g. the proper time). The Riemann curvature tensor, containing linear in the second-order derivatives of the metric tensor, is formally given by

$$R^{\rho}{}_{\sigma\mu\nu} = \nabla_{\mu} \Gamma^{\rho}{}_{\nu\sigma} - \nabla_{\nu} \Gamma^{\rho}{}_{\mu\sigma} + \Gamma^{\rho}{}_{\mu\lambda} \Gamma^{\lambda}{}_{\nu\sigma} - \Gamma^{\rho}{}_{\nu\lambda} \Gamma^{\lambda}{}_{\mu\sigma}, \tag{1.20}$$

which measures intrinsic curvature of any manifold $\mathcal{M}$ equipped with an affine connection (1.17). The Ricci curvature tensor is formed by the contraction of the first and third indices of the Riemann tensor, and it is written in a more compact form

$$R_{\mu\nu} = R_{\mu\nu} \equiv R^{\sigma}{}_{\mu\sigma\nu} = g^{\sigma\rho} R^{\sigma}{}_{\sigma\mu\rho\nu}. \tag{1.21}$$

By further contraction of indices, the Ricci scalar is called into being as

$$R \equiv g^{\sigma\rho} R_{\sigma\rho}. \tag{1.22}$$

The Ricci curvature tensor and another rank-2 tensor, known as the Einstein tensor, defined by

$$G_{\mu\nu} \equiv R_{\mu\nu} - \frac{1}{2} R g_{\mu\nu} \tag{1.23}$$

stand in dual relationship; they are the trace reverse of each other. Finally, Einstein's gravitational-field equations

$$G_{\mu\nu} = \kappa T_{\mu\nu} \tag{1.24}$$

allows us to relate local curvature of the spacetime, incorporated in $G_{\mu\nu}$, to its source, the stress–energy tensor $T_{\mu\nu}$ which represents the energy and momentum present in the spacetime and $\kappa \equiv 8\pi G/c^3$ is the Einstein constant. – To read more about the stress–energy tensor, please read Sec. 3.3 and Ref. [34, p. 176–201]. – Thus the Einstein equations (1.24) constitute the mathematical setting for the description of the gravitational field and of the chrono-geometrical structure of the spacetime, where the metric tensor determines the invariant line element (1.15), and acts also as a dynamical variable describing the gravitational field. The high degree of non-linearity in eqs. (1.24) implies that exact solutions is analytically unattainable for arbitrary matter distribution. Therefore there is no complete solution for a spacetime with compact binary objects in it but approximate solutions can be found in the case of weak fields. A pair of commonly used approximations found in the dissertation are the following:

- *Linearized gravity* is a perturbative approximation in the week-field regime which involves expansions in a small parameter which express orders of deviations of the metric from the Minkowski metric. (Appears in Sec. 1.5 and Sec. 4.3);
- *Post-Newtonian expansion* is a week-field and slow-motion approximation expanded in small parameters which express orders of deviations from Newton's law of universal gravitation. (Appears in Sec. 1.5.6 and Sec. 2.2).

In addition, special types of exact solutions of the Einstein equations (1.24) can be found in the dissertation by imposing simplifying assumptions. Such simplifying assumptions on the metrics exhibiting symmetries of the spacetime are the following:

- Spherical symmetry is a characteristic feature of some exact solutions, especially the *Schwarzschild solution* and the *Reissner–Nordström solution*. (Appears in Sec. 3.4 and Sec. 4.2.1);
- Axially symmetry is a characteristic feature of *Kerr solution* which describes the empty spacetime around a rotating uncharged axially-symmetric black hole with a quasi-spherical event horizon. (Not used in the dissertation).

Simplifying assumptions on the intended physical interpretation of the stress–energy tensor comprise the following solutions:

- *Dissipative-fluid solution* often employed as general stellar models where viscous flow and heat transfer is present. (Appears in Sec. 3.3.2);
- *Perfect-fluid solution* is used to model idealized distributions of matter, such as the interior of a star or an isotropic universe. It has vanishing viscous shear and heat flux, therefore it is completely characterized by their rest-mass density and isotropic pressure. (Appears in Sec. 3.3.1 and Sec. 4.2.1);
- *Dust solution* is a pressureless perfect fluid often used as cosmological models for matter-dominated epoch. Its constituent particles locally move in concert and interact with each other only gravitationally. (Appears in Sec. 4.3 and Sec. 4.4.2);
- *Vacuum solution* describes regions in which no matter or non-gravitational fields are present. (Appears in Sec. 1.5.4 and Sec. 4.4.2).

1.5 Linearized gravitational-field equations and gravitational waves

As discussed in Sections 1.1 and 1.2, as a result of the astronomical distances to their respective sources, the amplitude of the gravitational waves (expressed by 'strain' (1.1), a dimensionless parameter) when measured by observatories on Earth are predicted to be extremely small. Far away from the source of gravitational radiation, the weak gravitational field can be approximated by a region of asymptotically flat spacetime that is described by the metric tensor

$$g_{\mu\nu} = \eta_{\mu\nu} + h_{\mu\nu}, \tag{1.25}$$

where the small linear disturbance of the Minkowski metric $\eta_{\mu\nu}$ is represented by a dimensionless strain $|h_{\mu\nu}| \ll 1$ and the first and higher partial derivatives of $h_{\mu\nu}$ are also small. Throughout such a region of spacetime, any coordinate system $\{x^\mu : \mu \in [0,3] \subset \mathbb{N}\}$ which allows the metric tensor to be expressed in a close-to-Minkowski form is called quasi-Minkowskian. In Sec. 1.5.2, the mathematical labour of producing the linearized form of the Einstein field equations (1.24) is greatly simplified by the adoption of quasi-Minkowsian coordinates.

1.5.1 Linear coordinate transformations

Quasi-Minkowskian systems may be related to each other by two different classes of coordinate transformations; the global Lorentz transformations and infinitesimal coordinate transformations. Based on (1.13), let us first consider *global Lorentz transformations* which were already introduced in (1.13) by the following change of coordinates:

$$x'^\mu = \Lambda^\mu{}_\nu x^\nu, \tag{1.26}$$

where the matrix elements $\Lambda^\mu{}_\nu$ are constant everywhere and correspond to (1.14). The metric coefficients transform as

$$g'_{\mu\nu} = \frac{\partial x^\rho}{\partial x'^\mu}\frac{\partial x^\sigma}{\partial x'^\nu} g_{\rho\sigma} = \Lambda^\rho{}_\mu \Lambda^\sigma{}_\nu (\eta_{\rho\sigma} + h_{\rho\sigma}) = \eta_{\mu\nu} + \Lambda^\rho{}_\mu \Lambda^\sigma{}_\nu h_{\rho\sigma}, \tag{1.27}$$

where $\eta_{\mu\nu} = \Lambda^\rho{}_\mu \Lambda^\sigma{}_\nu \eta_{\rho\sigma}$. Thus, $g'_{\mu\nu}$ is also of the form (1.25), with

$$h'_{\mu\nu} = \Lambda^\rho{}_\mu \Lambda^\sigma{}_\nu h_{\rho\sigma}. \tag{1.28}$$

Moreover, it is apparent from this expression that, under a Lorentz transformation, $h_{\mu\nu}$ itself transforms like contravariant tensor components in Minkowski spacetime $(\mathcal{M}, \eta)$. [34, pp. 468] Ref. [34, pp. 468] explains that the above property suggests a convenient alternative viewpoint when describing weak gravitational fields. Instead of considering a slightly curved spacetime representing the general-relativistic weak field, one may consider $h_{\mu\nu}$ simply as a symmetric tensor field of rank 2 defined on the flat Minkowski background spacetime in Cartesian inertial coordinates.

The other type of coordinate transformations, *infinitesimal coordinate transformations* is expressed by

$$x'^\mu = x^\mu + \xi^\mu(x), \tag{1.29}$$

where $\xi^\mu(x)$ are four arbitrary functions of position of the same order of smallness as $h_{\mu\nu}$. Infinitesimal transformations of this sort make tiny changes in the forms of all scalar, vector and tensor fields, but these can be ignored in all quantities except the metric, where tiny deviations from $\eta_{\mu\nu}$ contain all the information about gravity. From (1.29), one has

$$\frac{\partial x'^\mu}{\partial x^\nu} = \delta^\mu_\nu + \partial_\nu \xi^\mu, \tag{1.30}$$

and, working to first order in small quantities, it is straightforward to show that the inverse transformation is given by[4]

$$\frac{\partial x^{\mu}}{\partial x'^{\nu}} = \delta^{\mu}_{\nu} - \partial_{\nu}\xi^{\mu}. \tag{1.31}$$

Thus, again working to first order in small quantities, the metric transforms as follows:

$$g'_{\mu\nu} = \frac{\partial x^{\rho}}{\partial x'^{\mu}}\frac{\partial x^{\sigma}}{\partial x'^{\nu}}g_{\mu\nu} = (\delta^{\rho}_{\mu} - \partial_{\mu}\xi^{\rho})(\delta^{\sigma}_{\nu} - \partial_{\nu}\xi^{\sigma})(\eta_{\rho\sigma} + h_{\rho\sigma}) = \eta_{\mu\nu} + h_{\mu\nu} - \partial_{\mu}\xi_{\nu} - \partial_{\nu}\xi_{\mu}, \tag{1.32}$$

where $\xi_{\mu} = \eta_{\mu\nu}\xi^{\nu}$ was defined. Hence, one sees that $g'_{\mu\nu}$ is also of the form (1.25), the new metric perturbation functions being related to the old ones via

$$h'_{\mu\nu} = h_{\mu\nu} - \partial_{\mu}\xi_{\nu} - \partial_{\nu}\xi_{\mu}. \tag{1.33}$$

If one adopts the viewpoint in which $h_{\mu\nu}$ is considered as a tensor field defined on the flat Minkowski background spacetime, then (1.33) can be considered as analogous to a gauge transformation in electromagnetism. From (1.33), it is clear that if $h_{\mu\nu}$ is a solution to the linearized gravitational-field equations (cf. eq. (1.53)), then the same physical situation is also described by

$$h^{\text{new}}_{\mu\nu} = h_{\mu\nu} - \partial_{\mu}\xi_{\nu} - \partial_{\nu}\xi_{\mu}. \tag{1.34}$$

In this interpretation, however, (1.33) is viewed as a gauge transformation rather than a coordinate transformation.

1.5.2 The linearized gravitational field equations

To obtain the linearized form of the Einstein's gravitational field equations (1.24), one needs to produce the linearized expression for the Riemann tensor $R^{\sigma}{}_{\mu\nu\rho}$; the corresponding expressions for the Ricci tensor $R_{\mu\nu}$ and the Ricci scalar R then follow by the contraction of indices.

To perform this task, first the linearized form of the connection coefficients (1.17) is obtained as

$$\Gamma^{\sigma}{}_{\mu\nu} = \frac{1}{2}\eta^{\sigma\rho}(\partial_{\nu}h_{\rho\mu} + \partial_{\mu}h_{\rho\nu} - \partial_{\rho}h_{\mu\nu}) = \frac{1}{2}(\partial_{\nu}h^{\sigma}_{\mu} + \partial_{\mu}h^{\sigma}_{\nu} - \partial^{\sigma}h_{\mu\nu}), \tag{1.35}$$

where only the linear terms of the metric perturbation $h_{\mu\nu}$ were kept and the notation $\partial^{\sigma} \equiv \eta^{\sigma\rho}\partial_{\rho}$ was introduced. One may now substitute (1.35) directly into the expression (1.21) for the Riemann tensor where The last two terms on the right-hand side are products of connection coefficients and so will clearly be second order in $h_{\mu\nu}$; they will therefore be ignored. Hence, to first order, one has

$$R^{\sigma}{}_{\mu\nu\rho} = \frac{1}{2}(\partial_{\nu}\partial_{\mu}h^{\sigma}_{\rho} + \partial_{\rho}\partial^{\sigma}h_{\mu\nu} - \partial_{\rho}\partial^{\sigma}h_{\mu\nu} - \partial_{\rho}\partial_{\nu}h^{\sigma}_{\nu}), \tag{1.36}$$

which is easily shown to be invariant to a gauge transformation of the form (1.34). The linearized Ricci tensor is obtained by contracting the above expression for $R^{\sigma}{}_{\mu\nu\rho}$ on its first and last indices.

$$R_{\mu\nu} = \frac{1}{2}(\partial_{\nu}\partial_{\mu}h + \Box^{2}h_{\mu\nu} - \partial_{\nu}\partial_{\rho}h^{\rho}_{\mu} - \partial_{\mu}\partial_{\rho}h^{\rho}_{\nu}), \tag{1.37}$$

---

[4] Note that, for the remainder of this chapter, the common symbol for equality '=' will be used to indicate equality up to first order in small quantities as well as exact equality.

where the trace $h \equiv h^{\rho}_{\rho}$ and the d'Alembertian operator $\Box^2 \equiv \partial_\rho \partial^\rho$ were defined. The Ricci scalar is obtained by a further contraction, giving

$$R = \eta^{\mu\nu} R_{\mu\nu} = \Box^2 h - \partial_\rho \partial_\sigma h^{\rho\sigma}. \tag{1.38}$$

Substituting the expressions (1.37) and (1.38) into the gravitational-field equations one obtains the linearized form as

$$\partial_\nu \partial_\mu h + \Box^2 h_{\mu\nu} - \partial_\nu \partial_\rho h^{\rho}_{\mu} - \partial_\rho \partial_\mu h^{\rho}_{\nu} - \eta_{\mu\nu}(\Box^2 h - \partial_\rho \partial_\sigma h^{\sigma\rho}) = -2\kappa T_{\mu\nu}. \tag{1.39}$$

The number of terms on the left-hand side of the field equations has clearly increased in the linearization process. This can be simplified somewhat by defining the 'trace reverse' of $h_{\mu\nu}$, which is given by

$$\bar{h}_{\mu\nu} \equiv h_{\mu\nu} - \frac{1}{2}\eta_{\mu\nu} h. \tag{1.40}$$

On contracting indices one finds that $\bar{h} = -h$. On substituting these expressions into (1.39), the field equations become

$$\Box^2 \bar{h}_{\mu\nu} + \eta_{\mu\nu} \partial_\rho \partial_\sigma \bar{h}^{\rho\sigma} - \partial_\nu \partial_\rho \bar{h}^{\rho}_{\mu} - \partial_\mu \partial_\rho \bar{h}^{\rho}_{\nu} = -2\kappa T_{\mu\nu}. \tag{1.41}$$

These are the basic field equations of linearized general relativity and are valid whenever the metric takes the form (1.25). Unless otherwise stated, for the remainder of this chapter I will adopt the viewpoint that $h_{\mu\nu}$ is simply a symmetric tensor field (under global Lorentz transformations) defined in quasi-Cartesian coordinates on a flat Minkowski background spacetime.

1.5.3 Linearized field equations in Lorenz gauge

The field equations (1.41) can be simplified further by making use of the gauge transformation (1.34). Denoting the gauge-transformed field by $h'_{\mu\nu}$ for convenience, the components of its trace-reverse transform as

$$\bar{h}'^{\mu\nu} = \bar{h}^{\mu\nu} - \partial^\mu \xi^\nu - \partial^\nu \xi^\mu + \eta^{\mu\nu} \partial_\sigma \xi^\sigma, \tag{1.42}$$

and hence one concludes that

$$\partial^\rho \bar{h}'^{\mu\nu} = \partial^\nu \bar{h}^{\mu\nu} - \Box^2 \xi^\mu. \tag{1.43}$$

Therefore, if one chooses the functions $\xi^\mu(\boldsymbol{x})$ so that they satisfy

$$\Box^2 \xi^\mu = \partial_\nu \bar{h}^{\mu\nu} \tag{1.44}$$

then one has $\partial_\nu \bar{h}'^{\mu\nu} = 0$. The importance of this result is that, in this new gauge, each of the last three terms on the left-hand side of (1.41) vanishes. Thus, the field equations in the new gauge become

$$\Box^2 \bar{h}'_{\mu\nu} = -2\kappa T'_{\mu\nu}. \tag{1.45}$$

The linearized field equations may be written in the form of inhomogeneous at d'Alembertian equations, [81, pp. 21]

$$\Box^2 \bar{h}_{\mu\nu} = -2\kappa T_{\mu\nu}, \tag{1.46}$$

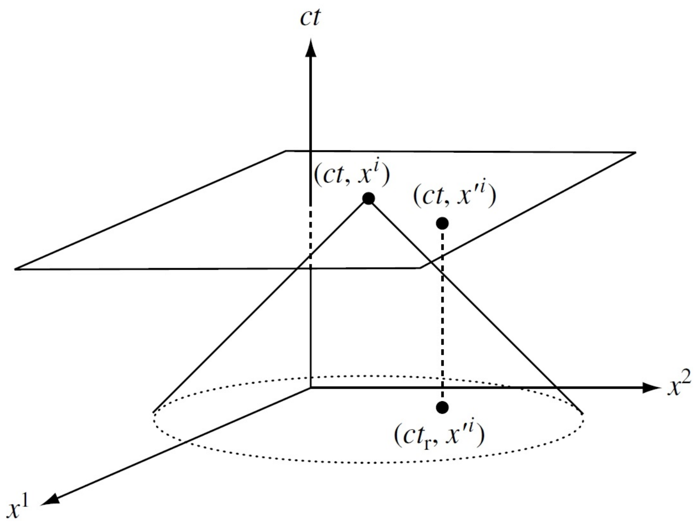

Figure 1.10: The disturbance in the gravitational field at the event $(ct,\, x^i)$ is the sum of the influences of the energy and momentum sources at the points $(ct,\, x'^i)$ on the past lightcone. (Original figure, courtesy of M. P. Hobson *et al.* [34].)

provided that the $\bar{h}_{\mu\nu}$ satisfy the *Lorenz gauge condition* (also referred to as *harmonic gauge*)

$$\partial_\nu \bar{h}^{\mu\nu} = 0. \tag{1.47}$$

The constrains (1.44) and (1.47) on the functions $\xi^\mu(\boldsymbol{x})$ require

$$\Box^2 \xi^\mu = 0 \tag{1.48}$$

to hold to preserve the Lorenz gauge condition by any further gauge transformation of the form (1.34). A suitable transformation, which satisfies the condition (1.48), is given by

$$\xi^\mu = \epsilon^\mu \exp(ik_\rho x^\rho), \tag{1.49}$$

where the ϵ^μ are constants and k_ρ are components of the 4-wavevector (1.54). In the presence of some non-zero stress–energy tensor $T^{\mu\nu}$, the general solution to the linearized field equations (1.46) in harmonic coordinates is most easily obtained by using a Green's function in the form

$$\bar{h}^{\mu\nu}(\vec{x}, t) = -\frac{4G}{c^4} \iiint \frac{d^3\vec{x}'}{|\vec{x} - \vec{x}'|} T^{\mu\nu}\left(\vec{x}',\, t - \frac{|\vec{x} - \vec{x}'|}{c}\right), \tag{1.50}$$

extending over the whole three-dimensional space $\mathbb{R}^3$. In the interests of brevity, the lengthy calculation presented in [34, pp. 475–478] is not repeated here. It is apparent that the solution at the event $(\vec{x}, t)$ depends not only on the data on the light cone where $(\vec{x} - \vec{x}')^2 = c^2t^2$ but also on data that are interior to that cone. [81, pp. 22] Illustrated by Figure 1.10, this region of spacetime is the intersection of the past lightcone of the field point with the world tube of the source at the *retarded times* t_r defined by

$$t_r = t - \frac{|\vec{x} - \vec{x}'|}{c}. \tag{1.51}$$

1.5.4 Plane waves as vacuum solutions of the linearized field equations

In empty space, the linearized field equations (1.46) reduce to the wave equation

$$\Box^2 \bar{h}^{\mu\nu} = 0, \tag{1.52}$$

with the attendant gauge condition (1.47). Obviously, the wave equation (1.52) has plane-wave solutions of the form

$$\bar{h}^{\mu\nu} = A^{\mu\nu} \exp(i k_\rho x^\rho), \tag{1.53}$$

where $A^{\mu\nu}$ are constant complex components of a symmetric amplitude tensor. The $k^\mu \equiv \eta^{\mu\nu} k_\nu$ are constant real components of the 4-wavevector, conventionally to denoted by

$$[k^\mu] = (\omega/c, \vec{k}), \tag{1.54}$$

where $\vec{k}$ is the spatial 3-wavevector in the direction of propagation and ω is the angular frequency of the wave. It is convenient to consider a plane GW propagating in the x^3-direction, in which case the components of the 4-wavevector are

$$[k^\mu] = (\omega/c, 0, 0, \omega/c). \tag{1.55}$$

Substituting the plane-wave solutions (1.53) into the wave equation (1.52) and using the fact that $\partial_\rho \bar{h}^{\mu\nu} = k_\rho \bar{h}^{\mu\nu}$, one finds that

$$\Box^2 \bar{h}^{\mu\nu} = \eta^{\rho\sigma} \partial_\rho \partial_\sigma \bar{h}^{\mu\nu} = \eta^{\rho\sigma} k_\rho k_\sigma \bar{h}^{\mu\nu} = 0. \tag{1.56}$$

This can only be satisfied if

$$k^\sigma k_\sigma = 0, \tag{1.57}$$

i.e. the vector $\vec{k}$ must be null or lightlike vector (cf. Sec. 1.4.2). The nullity of $\boldsymbol{k}$ implies that

$$\omega^2 = c^2 \vec{k}^2, \tag{1.58}$$

and so both the group and phase velocity of a gravitational wave are equal to the speed of light. Since the linearized Einstein equations only take the simple form (1.52) in the Lorenz gauge, one must also take into account the gauge condition (1.47). On substituting into the latter the plane-wave form (1.53), as a consequence the gauge condition is satisfied, provided that one obeys the additional constraint

$$A^{\mu\nu} k_\nu = 0. \tag{1.59}$$

Thus any plane wave of the form (1.53) is a valid solution of the linearized vacuum field equations in the Lorenz gauge, provided that the vector k^μ satisfies (1.57–1.59). Since the vacuum field equations are linear, any solution of them may be written as a superposition of such plane-wave solutions of the form

$$\bar{h}^{\mu\nu}(x) = \int A^{\mu\nu}(\vec{k}) \exp(i k_\rho x^\rho) d^3\vec{k}, \tag{1.60}$$

where the integral is taken over all values of $\vec{k}$. Physical solutions corresponding to propagating plane waves in empty space are represented by the real part of the plane-wave solutions (1.53):

$$\bar{h}^{\mu\nu} = A^{\mu\nu} \exp(i k_\rho x^\rho) + (A^{\mu\nu})^* \exp(-i k_\rho x^\rho) \tag{1.61}$$

as a superposition of two plane waves of the form (1.53). Under the residual gauge transfomation allowed by (1.48), the amplitude tensor transforms as

$$\bar{A}'^{\mu\nu} = A^{\mu\nu} - \epsilon^{\mu} k^{\nu} - \epsilon^{\nu} k^{\mu} + i\eta^{\mu\nu}\epsilon^{\rho} k_{\rho} \tag{1.62}$$

when the expression (1.49) is substituted for ξ^{μ} into the transformation law (1.42) for the trace-reverse tensor $\bar{h}'^{\mu\nu}$, which is assumed to be of the form (1.53). The symmetry of the amplitude tensor, together with the four Lorenz-gauge conditions (1.59) for a four-wavevector (1.55), implies that $A^{\mu 3} = A^{\mu 0}$. Therefrom the number of independent components in the amplitude matrix reduces to six.

1.5.5 Polarization states and effect of passing gravitational waves

In the frame of Einstein's general theory of relativity, the freedom to make a further gauge transformation may further reduce the number of independent components in the amplitude matrix from six to just two. [82] Accordingly, in Einstein's theory of general relativity, which is based on the concept of metric tensor, GWs have two 'tensor' polarizations, denoted by + and × and any possible plane gravitational waves travelling in the z-direction may be obtained in the form

$$h_{\mu\nu}^{(TT)} = \begin{pmatrix} 0 & 0 & 0 & 0 \\ 0 & A_{+}^{(TT)} & A_{\times}^{(TT)} & 0 \\ 0 & A_{\times}^{(TT)} & -A_{+}^{(TT)} & 0 \\ 0 & 0 & 0 & 0 \end{pmatrix} \exp[i(k_g z - \omega_g t)] \tag{1.63}$$

by superposing arbitrary amplitudes and relative phases of these two polarization modes in the new *transverse-traceless gauge*, denoted by 'TT'. k_g and ω_g are wave number and angular frequency of the GWs, respectively.[5]

More general metric theories[6], however, predict the existence of up to four additional modes (called 'vector' and 'scalar' polarizations), to the full complement of six polarization modes of GW. [83] The 'monochromatic components' of amplitude tensor (1.64) can be conveniently written in the form of

$$A_{\mu\nu} = \begin{pmatrix} 0 & 0 & 0 & 0 \\ 0 & A_{+} + A_b & A_{\times} & A_x \\ 0 & A_{\times} & A_b - A_{+} & A_y \\ 0 & A_x & A_y & \sqrt{2}A_l \end{pmatrix}. \tag{1.64}$$

The full metric perturbation due to a gravitational wave from a direction $\hat{\Omega}$ can be written as a sum over all polarization modes

$$h_{ij}(t - \hat{\Omega}) = \sum_{A} h^{A}(t - \hat{\Omega} \cdot \vec{x}) e_{ij}^{A}(\hat{\Omega}), \tag{1.65}$$

where A labels the six possible polarization modes: the +- and ×-type tensor modes, the x- and y-type vector modes, the breathing and longitudinal scalar modes, respectively. [56] The metric perturbation for each mode can be written in terms of a plane wave

---

[5] Provided that the all components of the GWs have the same propagating velocity (the speed of light).

[6] Alternative or modified theories of gravity, such as Horndeski's theory, Brans–Dicke theory or $f(R)$ gravity, are either straightforward alternatives to or generalizations of Einstein's general theory of relativity.

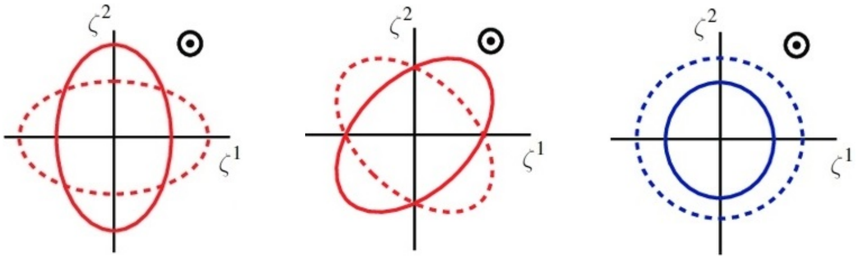

(a) 'plus'-type transverse mode (tensor)

(b) 'cross'-type transverse mode (tensor)

(c) 'breathing'-type transverse mode (scalar)

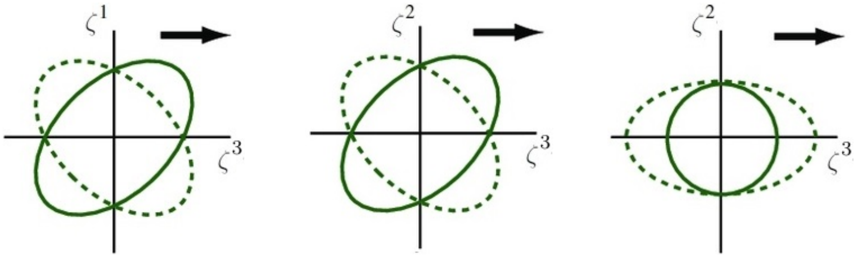

(d) 'x'-type longitudinal mode (vector)

(e) 'y'-type longitudinal mode (vector)

(f) 'l'-type longitudial mode (scalar)

Figure 1.11: Illustration of the displacement the six polarization modes for gravitational waves permitted in any metric theory of gravity induce on a set of circularly arranged test particles. The initial configuration of test particles is represented by solid and doted lines, respectively, at the moments of different phases by π. The ellipses (or circles) illustrate the effect of a passing gravitational wave, the circled dot and the arrow represent the direction of propagation. Transverse polarization modes are shown in (a), (b), and (c), where the wave propagates out of the plane; longitudinal polarization modes are shown in (d), (e), and (f), where the wave propagates in the plane. In Einstein's general theory of relativity, only 'plus' and 'cross'-type polarization modes are present; in massless scalar–tensor gravity, (c) may also be present. (Figure is adapted from [34, pp. 506–507] and [84].)

expansion,

$$h^A(t,\, \vec{x}) = \int_{-\infty}^{\infty} df \int_{S^2} d\hat{\Omega} \exp\left[i2\pi f(t-\hat{\Omega})\right] \tilde{h}^A(f,\, \hat{\Omega}) e^A_{ij}(\hat{\Omega}), \tag{1.66}$$

where f is the frequency of the gravitational waves, $\vec{k} = 2\pi f \hat{\Omega}$ corresponds to the wave vector (1.55), $\hat{\Omega}$ is a unit vector (1.69) that points in the direction of GW propagation, and e^A_{ij} is the Ath polarization tensor represented by [84]

$$\begin{gathered} e^{+}_{ij} = \begin{pmatrix} 1 & 0 & 0 \\ 0 & -1 & 0 \\ 0 & 0 & 0 \end{pmatrix}, \quad e^{\times}_{ij} = \begin{pmatrix} 0 & 1 & 0 \\ 1 & 0 & 0 \\ 0 & 0 & 0 \end{pmatrix}, \\ e^{x}_{ij} = \begin{pmatrix} 0 & 0 & 1 \\ 0 & 0 & 0 \\ 1 & 0 & 0 \end{pmatrix}, \quad e^{y}_{ij} = \begin{pmatrix} 0 & 0 & 0 \\ 0 & 0 & 1 \\ 0 & 1 & 0 \end{pmatrix}, \\ e^{b}_{ij} = \begin{pmatrix} 1 & 0 & 0 \\ 0 & 1 & 0 \\ 0 & 0 & 0 \end{pmatrix}, \quad e^{l}_{ij} = \sqrt{2} \begin{pmatrix} 0 & 0 & 0 \\ 0 & 0 & 0 \\ 0 & 0 & 1 \end{pmatrix}. \end{gathered} \tag{1.67}$$

Three of them are transverse to the direction of propagation, with two 'tensor' modes (+-type and ×-type) representing quadrupolar deformations, and one 'scalar' mode (b-type) representing a monopolar 'breathing' deformation. Other three modes are longitudinal, with one being an axially symmetric stretching 'scalar' mode (l-type) in the propagation direction, and one quadrupolar 'vector' mode (x-type and y-type) in each of the two orthogonal planes containing the propagation direction. Figure 1.11 illustrates the effect of the six polarization modes on a set of circularly arranged test particles. Einstein's general theory of relativity predicts only the first two transverse quadrupolar modes (a) and (b) independently of the source; these modes correspond to the waveforms h_+ and $h_\times$ discussed in eq. (1.63) (note the $\cos 2\phi$ and $\sin 2\phi$ dependences of the displacements). [82]

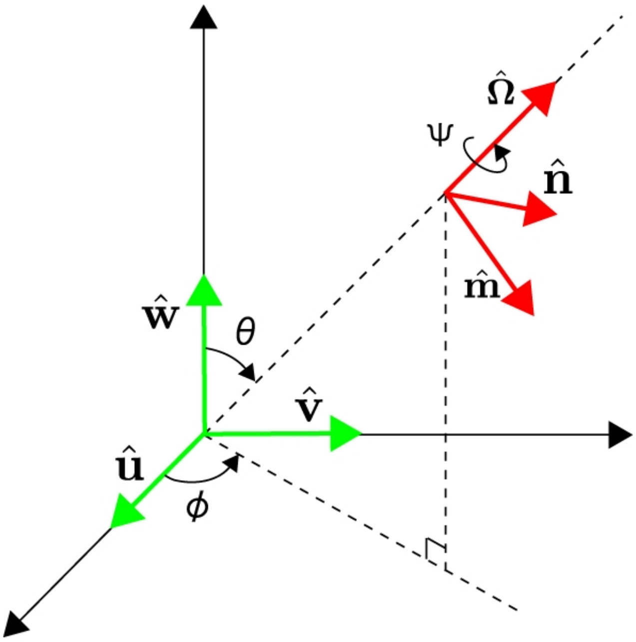

Figure 1.12: The Euler angles (θ, ϕ, ψ) are adapted to describe the orientation of the detector frame ($\hat{x}$, $\hat{y}$, $\hat{z}$) with respect to the frame of GW propagation ($\hat{m}$, $\hat{n}$, $\hat{\Omega}$). (Original figure, courtesy of N. Yunes & X. Siemens [56].)

Let us consider a frame with unit vectors $\hat{x} = (1, 0, 0)$, $\hat{y} = (0, 1, 0)$, $\hat{z} = (0, 0, 1)$ in the direction of the x, y, and z axes fixed to the detector's frame, shown in Figure 1.12. Relative to the detector, a coordinate system of the gravitational wave is given by their coordinates as

$$\begin{aligned} \hat{x}' &= (\cos\theta\cos\phi, \cos\theta\sin\phi, -\sin\theta) \\ \hat{y}' &= (-\sin\phi, \cos\phi, 0) \\ \hat{z}' &= (\sin\theta\cos\phi, \sin\theta\sin\phi, \cos\theta), \end{aligned} \tag{1.68}$$

where the two sets of coordinates may be related to one another through rotation by angles (θ, ϕ). [56] One still has the freedom to perform the third elemental rotation by the angle ψ about the propagation direction of gravitational wave, which is expressed by

$$\begin{aligned} \hat{m} &= \hat{x}'\cos\psi - \hat{y}'\sin\psi \\ \hat{n} &= -\hat{x}'\sin\psi + \hat{y}'\cos\psi \\ \hat{\Omega} &= \hat{z}'. \end{aligned} \tag{1.69}$$

The detector's frame is also shown in Fig. 1.12 with respect to the rotated frame of GW propagation ($\hat{m}$, $\hat{n}$, $\hat{\Omega}$). One may use the unit vectors ($\hat{m}$, $\hat{n}$, $\hat{\Omega}$) to generalize the polarization tensors (1.67) to a wave coming from a direction $\hat{\Omega}$ as follows [56]

$$\begin{aligned} e_{ij}^{+} &= (\hat{m}\otimes\hat{m}-\hat{n}\otimes\hat{n}), \quad & e_{ij}^{\times} &= (\hat{m}\otimes\hat{n}+\hat{n}\otimes\hat{m}), \\ e_{ij}^{x} &= (\hat{m}\otimes\hat{\Omega}+\hat{\Omega}\otimes\hat{m}), \quad & e_{ij}^{y} &= (\hat{n}\otimes\hat{\Omega}+\hat{\Omega}\otimes\hat{n}), \\ e_{ij}^{b} &= (\hat{m}\otimes\hat{m}+\hat{n}\otimes\hat{n}), \quad & e_{ij}^{l} &= \hat{\Omega}\otimes\hat{\Omega}. \end{aligned} \tag{1.70}$$

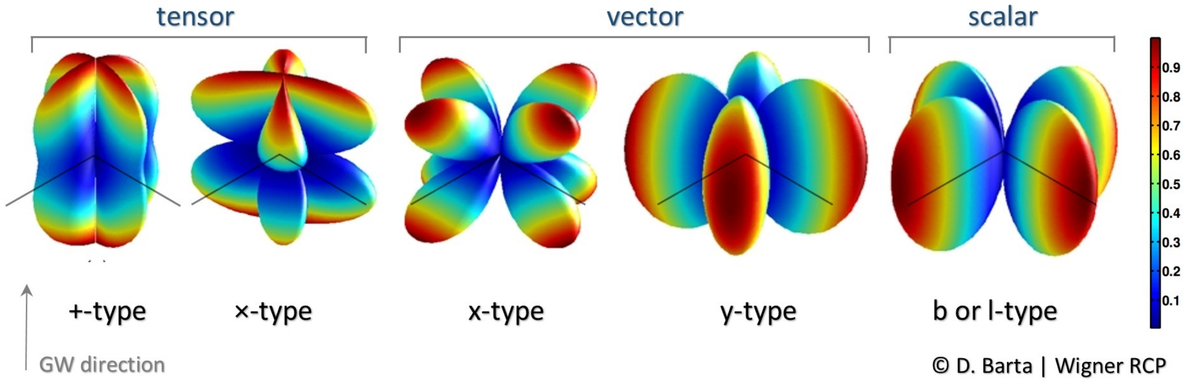

Figure 1.13: Antenna patterns for Michelson interferometer strain response (cf. eqs. (1.73)) evaluated in the small-antenna limit with $\phi = 0$. Panels from left to right show the antenna pattern response functions for the +-type and ×-type tensor modes ($|F_+|$ and $|F_\times|$), the x-type and y-type vector modes ($|F_x|$ and $|F_y|$), and the b-type and l-type scalar modes ($|F_b|$ and $|F_l|$ up to a sign, it is the same for both breathing and longitudinal). Colour indicates the strength of the response with red being the strongest and blue being the weakest. The black lines near the centre give the orientation of the interferometer arms which point in the $\hat{x}$ and $\hat{y}$ directions. (Based partly on a figure courtesy of N. Yunes & X. Siemens [56].)

For aLIGO and aVirgo, the arms are perpendicular so that the antenna pattern response can be written as the difference of projection of the polarization tensor onto each of the interferometer arms,

$$F^{A}(\hat{\Omega},\psi) = \frac{1}{2}(\hat{x}^{i}\hat{x}^{j}-\hat{y}^{i}\hat{y}^{j})e_{ij}^{A}(\hat{\Omega},\psi). \tag{1.71}$$

This means that the strain measured by an interferometer due to a gravitational wave from direction $\hat{\Omega}$ and polarization angle ψ takes the form

$$h(t) = \sum_{A} h_{A}(t-\hat{\Omega}\cdot x)F^{A}(\hat{\Omega},\psi). \tag{1.72}$$

Explicitly, the antenna pattern functions are, [82]

$$\begin{aligned}
F^{+}(\theta,\phi,\psi) &= \frac{1}{2}(1+\cos^2\theta)\cos 2\phi\cos 2\psi - \cos\theta\sin 2\phi\sin 2\psi \\
F^{\times}(\theta,\phi,\psi) &= -\frac{1}{2}(1+\cos^2\theta)\cos 2\phi\sin 2\psi - \cos\theta\sin 2\phi\cos 2\psi \\
F^{x}(\theta,\phi,\psi) &= \sin\theta(\cos\theta\cos 2\phi\cos\psi - \sin 2\phi\sin\psi) \\
F^{y}(\theta,\phi,\psi) &= -\sin\theta(\cos\theta\cos 2\phi\sin\psi + \sin 2\phi\cos\psi) \\
F^{b}(\theta,\phi) &= -\frac{1}{2}\sin^2\theta\cos 2\phi \\
F^{l}(\theta,\phi) &= \frac{1}{2}\sin^2\theta\cos 2\phi.
\end{aligned} \tag{1.73}$$

The dependence on the polarization angles ψ reveals that the $+$-type and $\times$-type polarizations are spin-2 tensor modes, the x-type and y-type polarizations are spin-1 vector modes, and the b-type and l-type polarizations are spin-0 scalar modes. Note that for interferometers, the antenna pattern responses of the scalar modes are degenerate. Figure 1.13 shows the antenna patterns for the various polarizations given in eqs. (1.73) with $\psi = 0$.

1.5.6 Post-Newtonian equations of motion and gravitational waveform

Post-Newtonian expansions are approximate solutions of the Einstein field equations (1.24) in weak-gravitational-field and slow-motion regime, expanded to any specified order in a small parameter

$$\epsilon \sim \frac{v^2}{c^2} \sim \frac{G}{c^2}\frac{M}{r} \tag{1.74}$$

which express orders of deviations from Newton's law of universal gravitation and provide a powerful formalism for modeling CBCs during the inspiral phase, when the orbital speed of the binary v is much smaller than the speed of light c. [29] A PN expansions of order $\mathcal{O}(\epsilon^n)$ to the Newtonian expression of gravity is said to be of $(n/2)$PN order.

In the PN formalism, the spacetime is assumed to be split into the near and wave zones. The field equations (1.24) for the perturbed Minkowski metric (1.12) are solved numerically by *CBwaves* in both regions. A fourth-order Runge–Kutta (RK4) method with adaptive step-size control is carred out to numerically solve for the 3PN-accurate near-field radiative dynamics for the relative two-body equation of motion written as

$$\boldsymbol{a} = \frac{d\boldsymbol{v}}{dt} = \frac{M}{r}\left(-\hat{\boldsymbol{n}} + \boldsymbol{A}_{1\mathrm{PN}} + \boldsymbol{A}_{2\mathrm{PN}} + \boldsymbol{A}_{2.5\mathrm{PN}} + \boldsymbol{A}_{3\mathrm{PN}} + \boldsymbol{A}_{3.5\mathrm{PN}} + \ldots\right) \tag{1.75}$$

at each time $t > t_0$, where t_0 is the time of arrival of the signal at the detector; $r = |\boldsymbol{x}_1 - \boldsymbol{x}_2|$ is the separation, $\boldsymbol{v} = \boldsymbol{v}_1 - \boldsymbol{v}_2$ is the orbital velocity, $\hat{\boldsymbol{n}} = (\boldsymbol{x}_1 - \boldsymbol{x}_2)/r$ is the mean motion, and M is the total mass (1.5), and μ is the reduced mass (1.8) of the compact binary system that consists of two components of mass m_1 and m_2. The far-zone radiation field, decomposed as [75]

$$h_{\mu\nu} = \frac{2G\mu}{c^4 d_L}(Q_{\mu\nu} + P^{0.5}Q_{\mu\nu} + PQ_{\mu\nu} + PQ_{ij}^{\mathrm{SO}} + P^{1.5}Q_{\mu\nu} + P^{1.5}Q_{ij}^{\mathrm{SO}} + P^2Q_{\mu\nu} + P^2Q_{\mu\nu}^{\mathrm{SS}}), \tag{1.76}$$

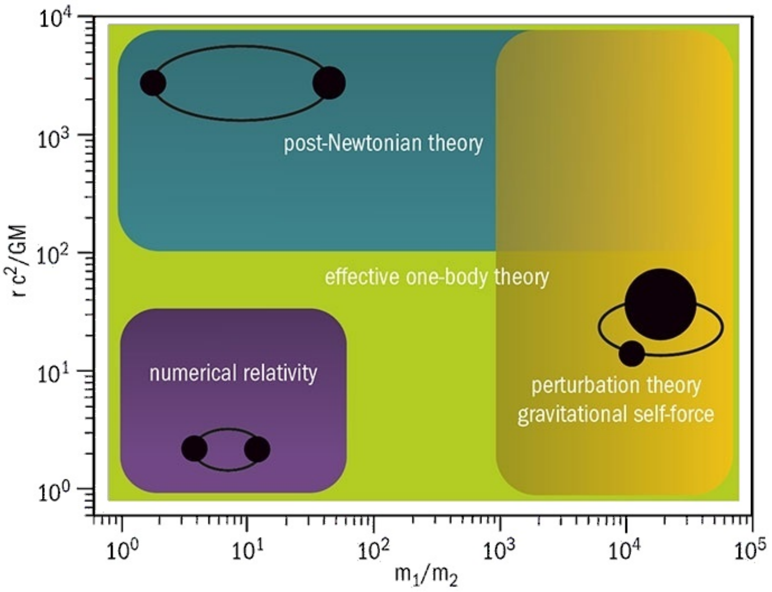

Figure 1.14: Range of validity of the main analytical and NR methods to solve the two-body equation of motion. The horizontal axis shows the binary mass ratio, while the vertical axis shows the radial separation between the two black holes in the binary. (Original figure, courtesy of A. Buonanno & B.S. Sathyaprakash [85].)

is determined in harmonic coordinates (1.47) by a simultaneous evaluation of orbital elements (ϕ, r, $\hat{\boldsymbol{n}}$) for the relative two-body equation of motion (1.75), where d_L is the luminosity distance (typically a few Mpc) to the GW source. The leading term Q_{ij} is the Newtonian mass quadrupole moment that leads to the so-called ‘quadrupole formula’

$$h_{\mu\nu}(t,\, \boldsymbol{x}) = \frac{2}{d_L}\ddot{I}_{\mu\nu}(t - d_L) \tag{1.77}$$

where $\ddot{I}_{\mu\nu}$ is the quadrupole moment of the source. $P^{0.5}Q_{ij}$, $P^{1.5}Q_{ij}$, $P^{2}Q_{ij}$ are higher-order relativistic corrections up to 2PN order beyond the Newtonian term, while PQ^{SO}_{ij}, $P^{1.5}Q^{\mathrm{SO}}_{ij}$, $P^{2}Q^{\mathrm{SS}}_{ij}$ are corrections arising from spin–orbit and spin–spin effects, respectively. The notation $A_{n\mathrm{PN}}$ and P^n indicates that the term is $\mathcal{O}(\epsilon^n)$ relative to the Newtonian term $-\hat{\boldsymbol{n}}$ and $Q_{\mu\nu}$, respectively. Here, for brevity, I will not repeat the lengthy PN coefficients for P^n. They are written out explicitly in the appendix of Ref. [86]. Nor will I quote all relativistic corrections $A_{n\mathrm{PN}}$ to the acceleration – they are written out explicitly in Ref. [87] – but only the 1PN corrections and the leading radiation-reaction terms at 2.5PN order:

$$\begin{aligned} \boldsymbol{A}_{1\mathrm{PN}} &= \left[(4+2\eta)\frac{M}{r} - (1+3\eta)v^2 + \frac{3}{2}\eta\dot{r}^2\right]\hat{\boldsymbol{n}} + (4-2\eta)\dot{r}\boldsymbol{v}, \\ \boldsymbol{A}_{2.5\mathrm{PN}} &= \frac{8}{5}\frac{M}{r}\eta\left[\left(3v^2 + \frac{17}{3}\frac{M}{r}\right)\dot{r}\hat{\boldsymbol{n}} - \left(v^2 + 3\frac{m}{r}\right)\boldsymbol{v}\right]. \end{aligned} \tag{1.78}$$

The radiation-reaction acceleration is expressed in the so-called Damour–Deruelle gauge. Radiative orbital dynamics involving all possible correction terms up the 3PN order beyond the Newtonian term are sufficient to analyze the orbit and evolution of the binary pulsar (cf. the Hulse–Taylor binary pulsar in Sec. 1.3.1) and they are written out explicitly in terms of unperturbed mean motion $\hat{\boldsymbol{n}}$ and orbital eccentricity e in Ref. [25]. The secular evolution is treated adiabatically, assuming that the timescales of the shrinkage of orbits (due to gravitational energy radiation $\dot{E}$) and the precession (due to angular momentum flux $\dot{J}$) are much longer than that of the orbital period. Consequently, the functions $(\dot{\boldsymbol{x}}_{\mathrm{1PN}}, \dot{e}_{\mathrm{1PN}} \ldots)$ in the equations derived from $\dot{E}$ and $\dot{J}$ depend only on the eccentricity e, and not on eccentric anomaly u. Hence, the adiabatic evolution equations for $\boldsymbol{x} \equiv (M\omega)^{2/3}$ and e form a closed system, and can be solved independently of Kepler's equation. Given initial conditions $\boldsymbol{x}(0)$ and $e(0)$, one can solve the system of ODEs numerically to obtain $\boldsymbol{x}(t)$ and $e(t)$. The integration of the equations of motion is terminated at the ISCO (Innermost stable circular orbit), which is located at

$$r_{\mathrm{ISCO}} = 6GM/c^2 \tag{1.79}$$

in Schwarzschild spacetime (for a non-spinning sources). The orbital angular frequency at the ISCO is

$$f_{\mathrm{ISCO}} = c^3/(6\sqrt{6}\pi GM), \tag{1.80}$$

which marks the end of the inspiral phase. It ought to be noted that the PN equations of motion applied in the computation are a series expansion of corrections to the acceleration of the binary components. Whole-order terms in the series represent conservative, relativistic corrections, and half-order terms represent dissipative corrections. [88]

It is critical to point out that the PN approximation can not be reliably applied when higher-order corrections to the equations of motions become comparable in magnitude to lower-order corrections. Levin, McWilliams, and Contreras argue in Ref. [88] that the PN expansion breaks down in the strong-field regime when 3.5PN order term becomes larger than preceding terms and drives the binary system to larger separation. The range of validity of the PN approximation is illustrated in Fig. 1.14.

Chapter 2

Fast prediction of eccentric inspirals using reduced-order models

The present piece of research is a response to the growing demand for computationally-efficient generation of eccentric waveform families in gravitational-wave searches. To the extent of our knowledge, surrogate model building for this particular family of waveforms has not yet been tested. ROM (Reduced-order model) techniques have proved exceedingly efficient for other models (such as for aligned-spin BBHs), thus, one may anticipate similar benefits of extremely large speedups in the time-consuming process of generating eccentric waveform. My aim is to give a proof-of-principle demonstration of its exceptional potential and to offer a novel and practical way to dramatically accelerate parameter estimations.

The introductory Sec. 2.1 delineates the issue of cost in gravitational waveforms generation and reviews the development of ROM-based models in response to the computational demand for cheaper methods. Sec. 2.2 deals with the procedure for generating fiducial PN waveforms by *CBwaves*, with respect to the statistics of the cost of computing individual waveforms to estimate the total cost of building template banks. Sec. 2.3 proposes the simplest strategy (regular spacing) for template placement in the intrinsic parameter space, followed by the representation of the fiducial waveform templates on a common, finely sampled and regularly spaced frequency grid. Sec. 2.4 gives a general description of my approach to construct efficient ROM assembled from the reduced bases and of its characteristic features, particularly the truncation error. Sec. 2.5 is dedicated to assess the overall performance of the ROM, including the accuracy of the surrogate model and its computational cost relative to that of the fiducial model. Conclusions, remarks, limitations and an outlook for future research will be given in Sec. 2.6.

2.1 Computational complexity in the multi-dimensional parameter space

As it has been discussed in Sec. 1.3.2, GW sources can be described by a set of eight *intrinsic* and seven additional *extrinsic parameters* $\boldsymbol{\lambda} = \boldsymbol{\lambda}_{\text{intrinsic}} + \boldsymbol{\lambda}_{\text{extrinsic}}$, associated with the astrophysical model of their respective sources. The earlier are intrinsic to the source (the mass m_i, spin vector $\vec{S}_i$ and electric charge Q_i of its components) while the extrinsic parameters are those which depend on the relative location of the source with respect to the detector (right ascension α and declination δ of the sky location, luminosity distance d_L, the orbital inclination ι and polarization angle ψ, the time t_c and phase ϕ_c at coalescence). Each template has a specific set of values for its parameters which are hereinafter collectively referred to as *model parameters*. A collection of points in a *p-dimensional parameter space*, provided that p is the number of model parameters, is called a *template bank* (or *template grid*). [89] A template bank generated with *minimal match* Γ_m could contain a large number of templates that scales as $L \sim (1-\Gamma_m)^{-p/2}$. The number of templates L required for correlations grows rapidly with p and the number of GW cycles L_{cyc}. [90] A fully coherent GW search for a CBC with $p = 8$ parameters lasting for $L_{\mathrm{cyc}} = 10^5$ cycles would require as much as $L = 10^{40}$ waveform model evaluations. [91]

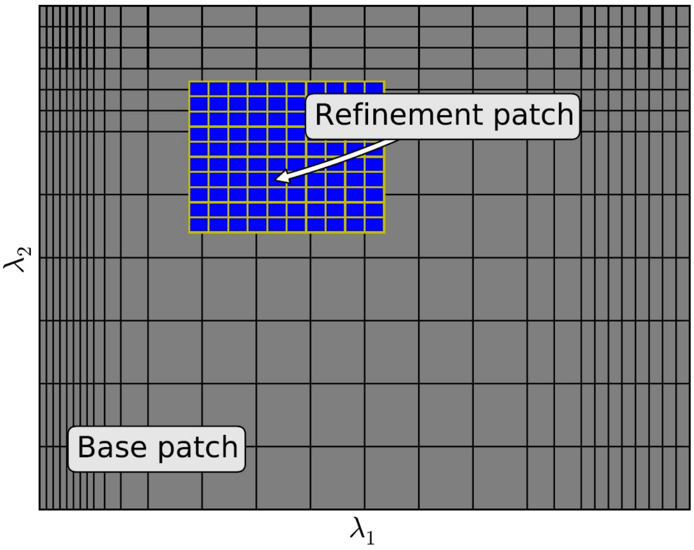

Figure 2.1: A schematic illustration of a tensor product grid on a base patch covering the entire domain of interest in model parameters λ_1, λ_2 and a refinement patch. (Original figure, courtesy of M. Pürrer. [92])

Over the last three decades methods have been developed for setting up template banks which minimize the computational cost in GW searches without degrading the signal detectability, measured by the *signal-to-noise ratio* (SNR). [93–95] Since the 1990s a method most feasible for small-dimensional parameter space ($p = 2$, 3, or 4 at most) has been popular to address the problem of *template placement* by associating the parameter space with a positive-definite metric space. In this geometric framework, the metric measures the fractional loss in squared SNR of a predicted signal (at one point in the parameter space) filtered through the optimal waveform template corresponding to a nearby point in the parameter space. [96] In 2009 a template placement algorithm was developed that is suitable for any number of dimensions, provided that the metric distance between two points in the parameter space is large or well-defined. [97] A schematic illustration of a template tensor product grid with refinement patch is shown in Fig. 2.1. Beside the issue of ensembling sufficiently large template banks, *parameter estimation* (PE) carries a number of challenges unique to large data sets. The exploration of the parameter space of BBHs relies on numerical relativity (NR) simulations of the field equations to discover how such mergers evolve. [98] Even a very coarse survey of the parameter space would require an enormous number, typically $L = 10^6 - 10^7$ [99], of expensive NR simulations which impose a computationally insuperable obstacle. The required number is in fact subtantially greater than the combined number of all simulations ever performed by each and every NR group [100, 101]. Consequently, techniques which can estimate the astrophysical parameters fast and accurately are needed to overcome this computational bottleneck. [102]

Reduced-order modeling or *model order reduction* is a practical mathematical tool to extract the fundamental features of a computationally demanding high-order model through exploiting only a reduced set of information. Investigations [103–106] over the last few years have revealed that GW templates exhibit significant redundancy in the parameter space, suggesting that the amount of information required to represent a fiducial waveform model is appreciably smaller than commonly anticipated. The reduction of information content is achieved through expressing the essential information by means of only a remarkably few, reduced number of representative waveforms $r \ll L$ to construct a *reduced-order model* (ROM) also known as a *surrogate model.* ROMs provide compressed approximations of any selected waveforms within the same physical model. They are projection-based techniques that aim to lower the computational complexity in the simulations by mapping the original FOM (Full-order model) onto an appropriate subspace of much lower dimension spanned by a *reduced-order basis.* To find these representative waveforms that constitutes the reduced basis several methods, including SVD (Singular-value decomposition) and *greedy* methods have been proposed, usually combined with the *empirical interpolation method* (EIM). [103, 107] SVD-based methods have been applied in Refs. [105, 106, 108] to interpolate time-domain inspiral waveforms. I am going to provide an effcient (fast and accurate) representations of approximated waveforms for any desired parameter values within the model by using the information provided by only r ROM waveforms instead of the total number L. [105, 109] The SVD-based approach to significantly accelerate PE process used in Ref. [110] is to directly interpolate the likelihood function over a significant portion of the parameter space. Moreover there is yet another method, presented in Refs. [98, 111], that defines special *reduced-order quadrature* (ROQ) rules to assist in fast likelihood evaluation.

2.2 Fiducial waveform models

Current searches for GWs from NS and stellar-mass BH binaries use restricted stationary-phase approximations to the Fourier transform of 3.5PN-accurate circular inspiral-only waveforms, such as spin-aligned *TaylorF2* or *SpinTaylorT4*. [29] The first part of this section describes a procedure for constructing PN non-spinning eccentric inspiral waveforms by *CBwaves* model in the time domain. The second part deals with the statistics of the cost of computing individual time-domain (TD) waveforms, drawn from a relatively large number of sample points in a finite-sample distribution.

2.2.1 Construction of eccentric post-Newtonian waveform templates

Stellar-mass BBHs and BNSs in the inspiral regime are adequately described by high-order *Post-Newtonian* (PN) waveform templates. For more details about the PN framework, please recall Sec. 1.5.6. Therefore, I construct PN templates by making use of the *CBwaves* software, developed by the Virgo Group at Wigner RCP with the intent of providing an efficient computational tool capable of generating gravitational-waveform templates produced by generic spinning binary configurations moving on eccentric closed or open orbit within the applied PN framework. A detailed examination of the software's performance is given in Ref. [86]. The source release and binary packages supported both on x86 and x86_64 platforms are available at the group's website [112]. The range of validity for the PN approximation in the late inspiral phase has been examined in Ref. [86] by CBwaves simulations through PN expansion parameter ϵ, which was introduced in (1.74) and found to be below the critical upper bound $\epsilon \sim 0.08 - 0.1$. Therefore, the equations of motion shall be cut off at the radial separation $r \approx 10GM/c^2$, in accordance with Ref. [88], well outside the radius of Schwarzschild ISCO (1.79). As a consequence, the highest orbital frequency [113]

$$f_{\mathrm{LSO}} = c^3[(1 - e_{\mathrm{LSO}}^2)/(6 - 2e_{\mathrm{LSO}})]^{3/2}(\pi GM)^{-1} \tag{2.1}$$

at the LSO (Last stable orbit) for nonrotating eccentric sources is less than the orbital frequency at the ISCO (1.80) if e_{LSO}, associated with the residual orbital eccentricity at the end of inspiral phase, exceeds 1/3.

Fig. 2.2 demonstrates that the integration run-time t_{int} depends sensitively both on the initial eccentricity and on the disparity of components' masses (m_1, m_2) in a binary system. The t_{int} increases exponentially with decreasing total mass M. The mass disparity, defined by $\bar{q} \equiv 1-q$, allows better comparability with e_0 than q itself, considering that t_{int} asymptotically increases – faster than with decreasing M – towards infinity as either e_0 (left panel) or $\bar{q}$ (right panel) tends to 1. The physical interpretation of these competing trends is very simple:

1. The lighter the components of the binary are, the longer it takes for them to gradually descend onto their ISCO through a sequence of increasingly circular orbits. [114]

2. The more eccentric the orbit was initially, the longer it takes to shed its residual eccentricity over many orbital periods. [18]

3. Among different configurations of equal total mass, the one with the largest mass disparity has the longest inspiral time for harbouring the lightest component. [114]

At the high total-mass region on Fig. 2.2, the influence of first trend grows comparable to that of the last two to reverse the trend of decreasing integration run-time. Fig. 2.4 shows the influence of M and q on the length of integration run-time t_{int} from a different aspect. Excluding the red and yellow dots, each point in the coloured triangular region is assigned to a hue level running from dark to light as the value of t_{int} increases on a logarithmic scale. The dark blue 'basin' represents the region where M and q simultaneously lower the value of t_{int} to its minimum. Isoclines running in parallel are connecting points at which t_{int} has the same value, therefore they are associated with horizontal lines in Fig. 2.2 (b). The influence of growing q becoming comparable to and gradually greater than that of M accounts also for the drift from the linear rising trend in the curvature of isoclines that occurs at the high-q region on Fig. 2.4. Although Fig. 2.4 suggests that over 85% of the waveform templates of initial eccentricity $e_0 = 0$ are computed up to 10 seconds, in fact, only 4.6% of all waveform templates require less then 10 seconds to integrate, as demonstrated in Fig. 2.3. Out of a total of 1800, only those 120 templates are shown in Fig. 2.4 that are located in the $e_0 = 0$ plane. Still, the figure illustrates well that in the same e_0-plane the frequency of templates with little t_{int} is extremely high compared to that of templates with large t_{int}, regardless of the value e_0.

In the next section I shall give a quantitative description of the summary statistics computed from the relative frequency of occurrence (or empirical probability) of the integration time-runs.

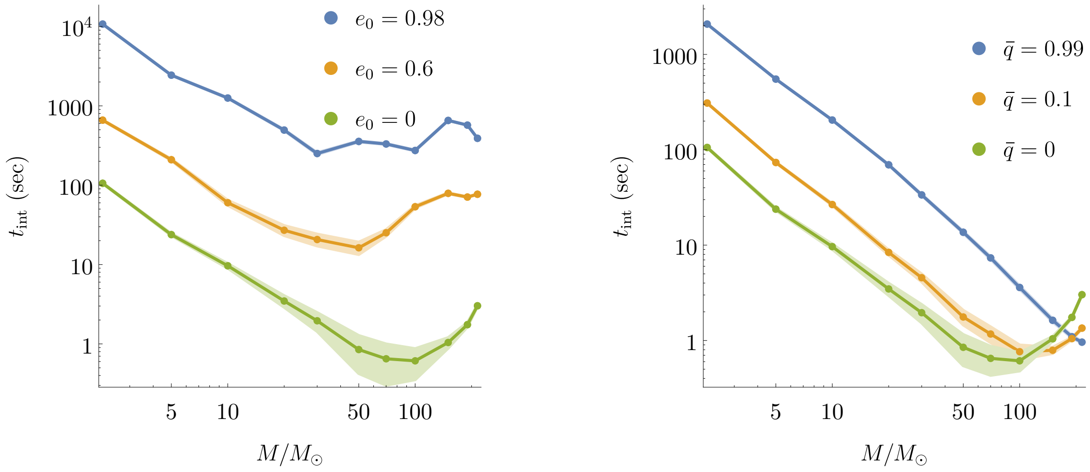

(a) Integration run-times for equal-mass systems ($\bar{q} = 0$).

(b) Integration run-times for systems on circular orbit ($e_0 = 0$).

Figure 2.2: The integration run-time t_{int} increases exponentially with decreasing total mass M. With increasing initial eccentricity e_0 (left panel) or mass disparity $\bar{q}$ (right panel), t_{int} grows asymptotically at a significantly faster rate than with decreasing M. The integration time of those template waveforms that enter a detector's sensitivity band at a frequency of 10 Hz has been measured 20 times, each at 11 distinct values of $M \in [2.15M_\odot, 215M_\odot]$ for three distinct values of initial eccentricity; $e_0 = \{0, 0.7, 0.98\}$ and mass disparity; $\bar{q} = \{0, 0.1, 0.99\}$ represented by blue, orange and green dots, respectively. The template waveforms were generated at a uniform sampling frequency 16.384 kHz. Around each median curve of corresponding t_{int} values, the shaded bands represent their respective 95% point-wise confidence band.

2.2.2 Probability distribution of integration run-times

Let $\mathbb{T} = \{t_1^{\text{int}}, t_2^{\text{int}}, \ldots, t_L^{\text{int}}\}$ be a univariate independent and identically distributed (IID) finite data sample drawn from the probability (or relative frequency) distribution of the *discrete* random variable $t \in \mathbb{T}$ while a discrete set of L time-domain input waveforms

$$\boldsymbol{h}(t) \equiv \{h(t; \lambda_l)\}_{l=1}^{L} \tag{2.2}$$

is computed at each parameter point λ_l (cf. Sec. 2.3.1) by evaluating Eq. (1.76) at a distance $D = \mu$ simultaneously with the integration of the equations of motions at 3PN order that requires integration run-times t_l^{int}.

Since I do not make any prior assumption about the probability distribution, I shall use a non-parametric model where the *statistical measures* are determined by the finite data sample $\mathbb{T}$. In statistics, kernel density estimation (KDE) is a fundamental data-smoothing technique that provides a non-parametric estimate, based on observed data $\mathbb{T}$, of an unobservable underlying probability density function (PDF) of the *continuous* random variable $\inf \mathbb{T} \leq t \leq \sup \mathbb{T}$. A PDF, denoted by $\mathscr{f}_t$ and illustrated in Fig. 2.3, is a non-negative Lebesgue-integrable function that defines the cumulative distribution function (CDF) of a real-valued random variable t, evaluated at a value t' as

$$\mathscr{F}_t[t'] \equiv \Pr[t \leq t'] = \int_{-\infty}^{t'} \mathscr{f}_t[\tau] d\tau. \tag{2.3}$$

It represents the probability that the random variable t, with the expected value given by

$$E[t] = \int_{-\infty}^{\infty} t' d\mathscr{F}_t[t'], \tag{2.4}$$

takes on a value less than or equal to t' and its kernel density estimator is

$$\hat{\mathscr{f}}_h[t] = \frac{1}{Lh} \sum_{l=1}^{L} K \left[\frac{t - t_l^{\text{int}}}{h} \right], \tag{2.5}$$

where $K \geq 0$ is a symmetric kernel with total integral normalized to unity and $h > 0$ is the bandwidth (or smoothing parameter). One might intuitively choose h as small as the data sample $\mathbb{T}$ allows; however, there is always a trade-off between the bias of the estimator and its variance. Another option is the use of adaptive bandwidth kernel estimators in which the bandwidth changes as a function of t.

A specific quantitative measure of the probability distribution is the n-th moment

$$\mu_n \equiv E[(t - c)^n] \tag{2.6}$$

of the continuous random variable t about some central value c (e.g. the mean, denoted by μ) where E is the expected value of t defined by Eq. (2.4). The graphical representation of the most common measures of central tendency (mean, median, mode) is depicted on Fig. 2.3 with solid, dashed and dotted red lines, respectively. The PDF rapidly increases with the random variable t up to a point at $t = 0.81653$ sec. From then onwards this monotone increase slows down and eventually comes to a halt at $t = 4.438$ sec, which marks the *mode*, i.e. the most frequent value in the distribution. The *median* which represents the value separating the higher half of the probability distribution from the lower half is located at $t = 20.615$ sec. The *mean* which represents the first moment of the PDF ($\mu \equiv \mu_1$ in Eq. (2.6)) is situated at $t = 77.499$ sec.

The central tendency of distributions is typically contrasted with its dispersion that measures the extent to which a distribution stretched or squeezed. Common measures of statistical dispersion are the variance and standard deviation: The *variance* of t is the second central moment, given by (2.6) as $\text{Var}[t] \equiv E[(t - \mu)^2]$ and the *standard deviation* is its square root, denoted by σ. For the given distribution $\sigma = 266.885$ sec. Finally, the shape (or asymmetry) of probability distributions is quantitatively measured by the third and fourth central moments, called *skewness* and *kurtosis* and denoted by $\text{Skew}[t] \equiv E[(t - \mu)^3/\sigma^3] = 18.56$ and $\text{Kurt}[t] \equiv E[(t - \mu)^4/\sigma^4] = 490.04$, respectively.

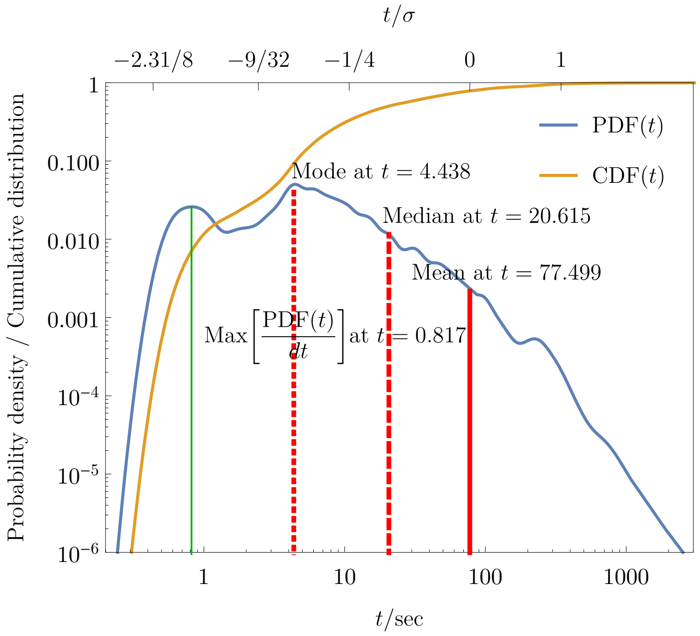

Figure 2.3: PDF denoted by $\mathscr{f}_t(t)$ (blue line) and CDF by $\mathscr{F}_t(t)$ (orange line) are displayed as functions of the random variable $t \in [\inf \mathbb{T}, \sup \mathbb{T}]$, corresponding to t_{int}-values, which is measured in seconds on the lower horizontal axis and in standard deviation ($\sigma = 266.885$ sec) round the mean value of t on the upper horizontal axis. The smooth KDE with adaptive bandwidth is based on the data sample $\mathbb{T}$ collected from the integration run-times of $L = 1800$ waveform templates that were generated in the parameter space Ω, described in Sec. 2.3.1. The location of the *mode*, the *median* and the *arithmetic mean* are illustrated by dotted, dashed, and solid red lines, respectively in ascending order of their locations. This order of the measures of central tendency is a characteristic feature of right-skewed (positive skewness) distributions.

2.3 Template placement and common frequency grid

Let us now discuss the placement of a grid of TD waveform templates in a compact parameter space, followed by the generation of a sequence of frequency-domain (FD) templates on a common finely sampled uniform frequency grid. The TD waveforms are Fourier transformed and split into their amplitude and phase parts. These functions are accurately represented on a sparse frequency grid with only $\mathcal{O}(10^4)$ nodes, with a sampling frequency recorded well above the Nyquist frequency of the shortest time-series in the template bank.

2.3.1 Template placement in an associated 3-dimensional parameter space

The set of input waveforms (2.2) is computed by *CBwaves*, described in Sec. 2.2.1, at corresponding parameter points

$$\boldsymbol{\lambda} \equiv \{\lambda_l \in \Omega\}_{l=1}^{L} \tag{2.7}$$

in a compact p-dimensional parameter space $\Omega \subset \mathbb{R}^p$, where p is the number of model parameters. I restricted this study to a feasible 3-dimensional parameter space consisting of totally ordered one-dimenstional sets of values of corresponding model parameters

$(m_1,\, m_2,\, e)$ that define a sparse grid of points

$$\boldsymbol{\lambda} \equiv \boldsymbol{m}_1 \otimes \boldsymbol{m}_2 \otimes \boldsymbol{e} = \{(m_i, m_j, e_k) : i \in [0, i_{\max}]; j \in [i, i_{\max}]; k \in [0, k_{\max}]\} \tag{2.8}$$

covering the desired parameter range in the particular model involved. Owing to the invariance of input waveforms under exchange of the components' masses $(m_1,\, m_2)$, the values of the 2-dimensional index pair $(i,\, j)$ are constrained to a triangular sub-region in the positive quadrants where $i \leq j$. Considering that the waveform templates span a 3-dimensional parameter space, each template is successively placed into a single vector (2.2) as indexed by

$$l \equiv \left[\left(i_{\max} - \frac{i-1}{2}\right) i + j\right] k_{\max} + k + 1 \tag{2.9}$$

in the range of values $1 \leq l \leq L$. This flat index corresponds to the position of templates in the parameter space. The total number of templates in the set is then expressed as

$$L = \left[(2 i_{\max} + 1)^2 - 2\right] k_{\max}/8 + 1. \tag{2.10}$$

It is desirable to work with a dense grid of short waveforms encompassing the late inspiral phase to make a better coverage of the selected region of the parameter space. For the sake of simplicity, templates are sampled at equidistant parameter combinations within the region. Nevertheless, using a template placement algorithm that is based on a template-space metric over the parameter space makes a far more efficient coverage. [115, 116] Generally, the algorithms that use geometrical techniques concentrate more points near the boundaries of the region and at lower mass-ratios.

The set of initial eccentricity $\{e_k : 1 \leq k \leq k_{\max}\}$ is chosen to cover the entire interval $[0,\, 0.95]$ and the mass ratio (1.7) is allowed to range between equal mass at $q = 1$ and relatively extreme systems at $q \approx 0.01$ with total mass $M/M_\odot \in [2.15, 215]$. In terms of the symmetric mass ratio (1.8) the model covers approximately $\eta \in [0.01, 0.25]$. Fig. 2.4 shows the placement of those $L = 120$ templates (red dots) that are situated in the $k = 0$ plane section of the parameter space Ω, out of a total of 1800 templates, and are collected in $\boldsymbol{h}(t)$. These templates are confined within a triangular region with a boundary $\partial\Omega$ (thick gray line).

2.3.2 Production of frequency-domain waveforms

For optimal orientation all time-domain waveforms in Eq. (2.2), composed of their two fundamental polarizations h_+ and $h_\times$ in the dominant $\ell = m = 2$ mode are represented by complex-valued GW strain amplitudes

$$h_n(\lambda_l) \equiv h_+(t_n; \lambda_l) - i h_\times(t_n; \lambda_l) \tag{2.11}$$

at N equidistant grid points

$$\{t_n = n\Delta t\}_{n \in [0, N-1]} \tag{2.12}$$

as elements of a finite sequence of N regularly spaced samples of the complex-valued TD waveforms $\{h_0(\lambda_l),\, h_1(\lambda_l),\, \ldots,\, h_{N-1}(\lambda_l)\}$. The sequence is converted by a *fast Fourier transform* (FFT), denoted by a linear operator $\mathscr{F} : h \rightarrow \tilde{h}$, into an other equivalent-length sequence of regularly spaced samples

$$\{\tilde{h}_k(\lambda_l)\}_{k \in [-N/2, N/2-1]} = \mathscr{F}\{h_n(\lambda_l)\}_{n \in [0, N-1]} \tag{2.13}$$

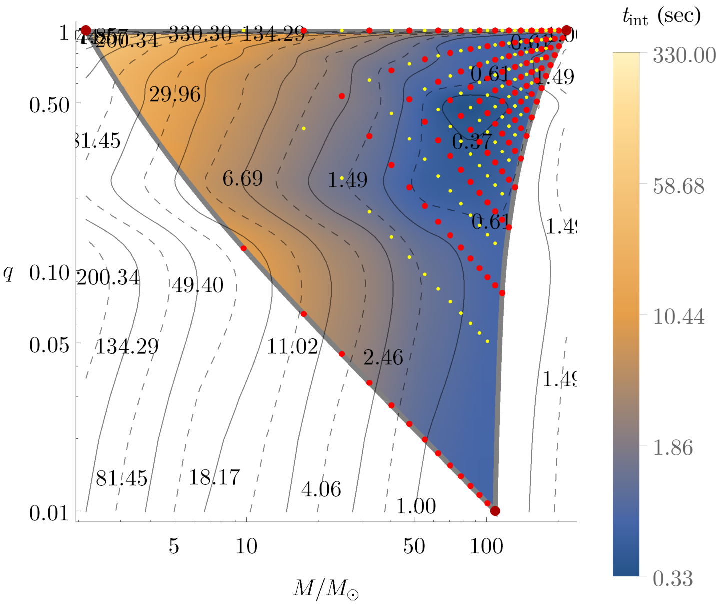

Figure 2.4: The template bank $\boldsymbol{h}(t)$ of $L = 1800$ waveform templates was set up over a domain $\{(M,\, q,\, e_0) | M \in [2.15 M_\odot, 215 M_\odot],\, q \in [0.01, 1],\, e_0 \in [0, 0.95]\} \subset \Omega$ by computing Eq. (2.2) with uniform grid spacings $\{\Delta M = 14.19 M_\odot,\, \Delta q = 0.06,\, \Delta e_0 = 0.063\}$. Red points, confined within a triangular region with a boundary $\partial\Omega$ (thick gray line), represet the parameter points of those 120 input waveforms that are situated in the $k = 0$ plane section of the parameter space Ω. In order to measure the accuracy of the ROM of waveforms, Eq. (2.34) is evaluated at equidistant parameter points (yellow points) from their respective nearest basis-waveform neighbours. Each background point in the coloured triangular region is assigned to a hue level running from dark to light as the value of the integration run-time t_{int} increases on a logarithmic scale. t_{int} increases exponentially with decreasing total mass M and grows asymptotically at a significantly faster rate with increasing mass disparity $\bar{q}$. The dark blue 'basin', where the great majority of template waveforms are concentrated, represents the region where M and q simultaneously lower the value of t_{int} to its minimum. Isoclines (thin gray curves) running in parallel are connecting points at which t_{int} has the same value. A drift from the linear rise in the curvature of isoclines occurs at the high-q region, where the influence of growing q becomes comparable to and gradually greater than that of M.

evaluated at the same N equidistant frequency grid points $\{f_{-N/2}, \ldots, f_0, \ldots, f_{N/2-1}\}$ considering that ROM construction, to be discussed in Sec. 2.4, will require a set of values that reside in the same grid points over all the waveforms in the template bank.

1. This is achieved by having the length of all frequency series truncated to that of the shortest waveform in time, denoted by

$$T = t_{N-1} - t_0. \tag{2.14}$$

   This particular waveform is associated with the highest mass, lowest eccentricity configuration ($i = i_{\max}$, $j = i_{\max}$, $k = 0$) in the template bank and its position in the parameter space, given by Eq. (2.9), is $l_{\mathrm{short}} = (i_{\max} + 3) i_{\max} k_{\max}/2 + 1$.

2. Another possible way, used by [92, 117], to adjust the frequency series to the same length is to make the shorter-length waveforms of sufficient length by extending them with other templates such as TaylorF2.

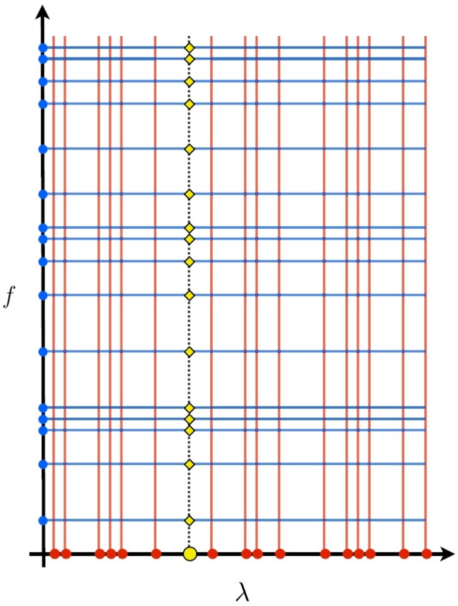

Figure 2.5: A schematic illustration of the method for building and evaluating the surrogate model over a common frequency grid. The red dots show the selection of parameter points for building the reduced basis, the blue dots show the associated empirical nodes in time from which a waveform can be reconstructed by interpolation with high accuracy, and the blue lines indicate a fit for the waveform's parametric dependence at each empirical time. (Original figure, courtesy of S. E. Field *et al.*. [102])

The Fourier coefficients in Eq. (2.13), given by

$$\tilde{h}_k(\lambda_l) \equiv \sum_{n=0}^{N-1} h_n(\lambda_l) e^{-2\pi i k n/N}, \quad k \in [0, N-1], \tag{2.15}$$

are complex-valued functions of the frequency f_k which encodes both the amplitude and the phase,

$$\tilde{h}^{(A)}_{kl} = \sqrt{\mathrm{Re}[\tilde{h}_k(\lambda_l)]^2 + \mathrm{Im}[\tilde{h}_k(\lambda_l)]^2/N}, \quad \tilde{h}^{(\phi)}_{kl} = -i \ln\left(\tilde{h}_k(\lambda_l)/|\tilde{h}_k(\lambda_l)|\right), \tag{2.16}$$

respectively. In this interpretation, $\tilde{h}_k(\lambda_l)$ corresponds to the cross-correlation of the time sequence $h_n(\lambda_l)$ and an N-periodic complex sinusoid $e^{2\pi i k n/N}$ at a frequency point $f_k \equiv k/N$ that represents k cycles of the sinusoid. Therefore, Eq. (2.15) acts in place of a *matched filter* for that frequency. (To read more about matched-filters, please read Sec. 4.5.2) Now, the sequence of frequency-domain waveforms (2.13) can be re-expressed as 'chirps' in a simple form

$$\{\tilde{h}_k(\lambda_l)\} = \{\tilde{h}^{(A)}_{kl} \exp(i\Lambda \tilde{h}^{(\phi)}_{kl})\} \tag{2.17}$$

where the oscillation degree Λ is a large number. The behaviour of GWs in the late inspiral phase is highly oscillatory, but the amplitude and the phase themselves are smoothly varying functions of frequency. [118] It will thus be more expedient to perform high-accuracy parametric fits of the phase and amplitude given by (2.16) rather than of the complex waveform (2.11) itself. The preprocessed amplitudes and phases are collected in the columns of separate template matrices $\{\mathcal{H}^{(A)}, \mathcal{H}^{(\phi)}\} \in \mathbb{R}^{N\times L}$,

$$\mathcal{H} = (\tilde{h})_{kl} \in \mathbb{C}^{N\times L} \tag{2.18}$$

where the amplitude or phase labels have been dropped for brevity and where L is the total number of templates, and each template $\tilde{h}_l(f_k)$ is given on a common freqency grid of length N. I will represent the waveforms at a large number of frequency points so that $N \gtrsim L$. A schematic illustration of building templates over a common frequency grid is shown in Fig. 2.5.

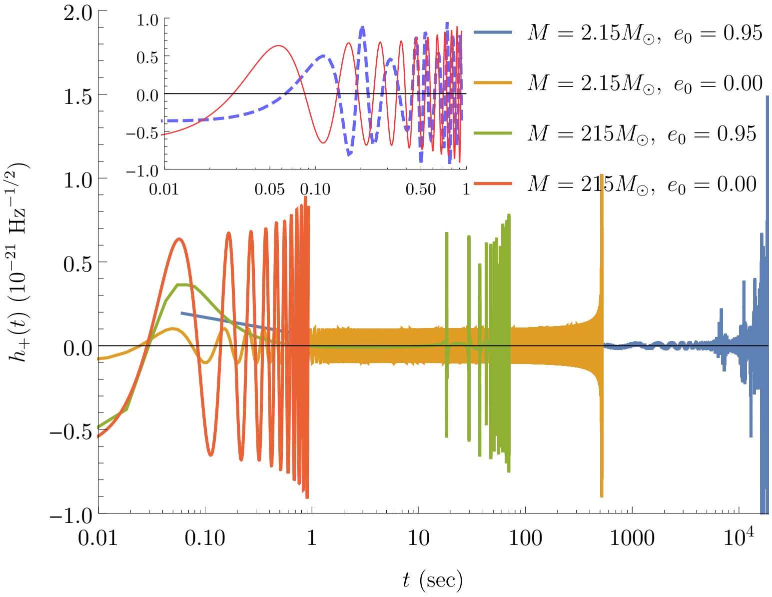

Figure 2.6: The panels illustrate the inspiral evolution of equal-mass BBH/BNS systems ($\bar{q} = 0$) starting at a Keplerian mean orbital frequency of 5 Hz at a distance $D = \mu$. The four most distinct template waveforms were generated by *CBwaves* at a uniform sampling frequency of 16.384 kHz with extreme values of total mass $M = \{2.15M_\odot, 215M_\odot\}$ and initial eccentricity $e_0 = \{0.00, 0.95\}$ in the investigated parameter space Ω. (See large red points on Fig. 2.4.) The top inset panel presents the last $N = 15,000$ points of the longest waveform (blue) projected onto an equal number of points of the shortest waveform (red).

2.3.3 Definition of a regularly spaced high-resolution frequency grid

Provided that T in (2.14) is the longest time length, the time spacing is defined as

$$\Delta t = T/(N-1) \tag{2.19}$$

by Eqs. (2.12) and (2.14). The time spacing and the number of time steps N in the grid (2.12) are chosen such that the FD waveforms (2.17) are sampled at a rate of f_s and cover a suitable and well-resolved frequency range $[f_\mathrm{low}, f_\mathrm{high}]$.

1. The lower limit of the frequency range f_low is specified by the low-frequency cutoff of the detector noise spectrum which is close $f_\mathrm{cutoff} = 10$ Hz for advanced detectors design.

2. The upper limit f_{high} is determined to be at $f_{\text{ISCO}} = 2.045$ kHz by the ISCO frequency (1.80) for the lowest total mass configuration of interest $M = 2.15 M_\odot$.

The Nyquist criterion requires the sampling frequency to be at least twice the highest frequency contained in the signal to avoid aliasing. Thus, the smallest sufficient sampling frequency is $f_s = 4096$ samples per second for being the first power of 2 to meet the criterion. Note that the typical sampling rate being used by aLIGO and aVirgo observatories in ongoing searches for GWs is at 2048 Hz. [119] Instead, an equidistant grid with $N = 4000$ grid points is sampled at $f_s = 16.384$ kHz in the frequency band $Mf \in [0.0001, 0.0216]$ in geometrized units ($G = c = 1$). The conversion factors for 'geometrized' units into SI units are listed in Table A.1. The total mass M is expressed in units of geometrized solar mass by $M_\odot[\text{s}] = G/c^3 \times M_\odot[\text{kg}] \approx 4.93 \times 10^{-6}$ sec. At the time resolution $\Delta t = 1/f_s \approx 4.59M$ which corresponds to a Nyquist frequency

$$f_{\text{Ny}} = f_s/2 \approx 2.03 \times 10^{-32} M^{-1}, \tag{2.20}$$

a waveform long enough for the BNS system of total mass $M = 2.15 M_\odot$ down to $f_{\text{low}} = 2.48 \times 10^{-35} M^{-1}$ is given and is about $T = (N-1)\Delta t \approx 1.83 \times 10^4 M$ long in time. The spacing in frequency domain is

$$\Delta f = 2 f_{\text{Ny}}/N, \tag{2.21}$$

so the power will be either in positive or negative frequencies, depending on conventions and only half of the FFT should be considered. Combining this with the relations (2.19–2.20), one has

$$\Delta f = \frac{N-1}{N}\frac{1}{T} \approx 5.45 \times 10^{-5} M^{-1}. \tag{2.22}$$

Only half of the points in the FFT spectrum are unique, the rest are symmetrically redundant. Thus, the points of negative frequencies contain no new information on the periodicity of the random number sequence. Which amounts to swapping the left and right half of the result of the transform.

2.4 SVD-based reduced-order surrogate model building

In this section I summarize some of the characteristic features of SVD that are especially useful for reduced-order modeling and discuss my approach to construct a compressed approximate representation of a collection of fiducial waveforms at the cost of truncation error. Next, projection coefficients of the waveforms are determined in terms of the reduced basis. In conclusion, the ROM is assembled from the reduced basis and projection coefficients interpolated over the parameter space. My procedure follows the well-established strategy that has been pursued by Pürrer and by Cannon for building frequency-domain ROMs. [92, 105, 106, 117]

2.4.1 Singular values and truncation error

Formally, the decomposition of the template matrix $\mathcal{H} \in \mathbb{C}^{N \times L}$ in Eq. (2.18) is expressed by a factorization of the form

$$\mathcal{H} = V \Sigma U^\dagger, \tag{2.23}$$

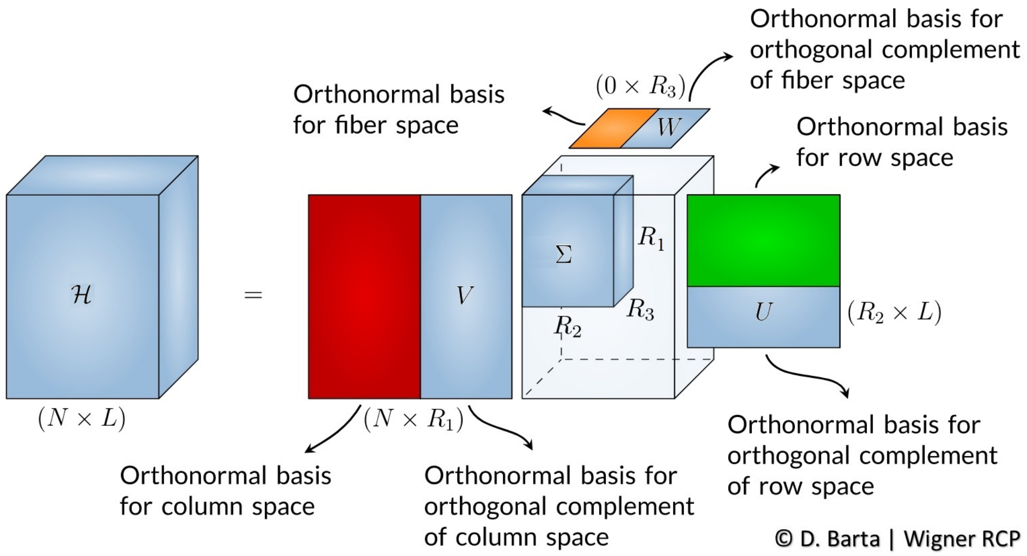

Figure 2.7: Illustration of the multilinear SVD of a multilinear rank-(R_1, R_2, R_3) tensor of a 3-mode and the different spaces.

where the complex unitary matrices

$$V = [\boldsymbol{v}_1|\dots|\boldsymbol{v}_L] \in \mathbb{R}^{L\times L}, \quad U = [\boldsymbol{u}_1|\dots|\boldsymbol{u}_N] \in \mathbb{R}^{N\times N} \tag{2.24}$$

are orthogonal sets of non-zero eigenvectors of the non-negative self-adjoint operators $\mathcal{H}^\dagger\mathcal{H}$ and $\mathcal{H}\mathcal{H}^\dagger$ so that $U^\dagger U = \mathbb{I}$ and $V^\dagger V = \mathbb{I}$. The illustration of SVD of multilinear tensor is shown in Fig. 2.7. The rank–nullity theorem states that the SVD (2.23) provides a decomposition of the range of $\mathcal{H}$. [117] Accordingly, the left-singular vectors (or *eigensamples*) $\{\boldsymbol{v}_i \in V\}$ provide an orthonormal basis

$$\mathrm{range}(\mathcal{H}) = \mathrm{span}\{\boldsymbol{v}_1, \dots, \boldsymbol{v}_R\} \tag{2.25}$$

for the range of $\mathcal{H}$ (columnn space) where the maximal number of linearly independent columns of $\mathcal{H}$ is $R \equiv \mathrm{rank}(\mathcal{H}) \leq L$. In a qualitative sense, each $\boldsymbol{v}_i$ represents a typical waveform pattern. The right-singular vectors (or *eigenfeatures*) $\{\boldsymbol{u}_i \in U\}$ provide a basis for the domain of $\mathcal{H}$ (row space) and represent the evolution of the magnitude of each waveform along the frequency gridpoints. The diagonal entries of the rectangular matrix $\Sigma \in \mathbb{R}^{N\times L}$ correspond to the non-negative real SV (Singular value)s $\sigma_1 \geq \dots \geq \sigma_s \geq 0$ where $s = \min(N, L)$. SVs are roots of eigenvalues of $\mathcal{H}^\dagger\mathcal{H}$ (and of $\mathcal{H}\mathcal{H}^\dagger$) describing the spectrum of the template matrix $\mathcal{H}$, arranged in monotonically decreasing order (cf. Fig. 2.8). If the number of frequency points is significantly larger than the number of waveforms (i.e. $L \ll N$), then a *thin* SVD is a more compact and 'economical' factorization of Eq. (2.23) than the *full-rank* SVD that comprizes all R eigensamples. In practice, low-rank matrices are often contaminated by errors, and for that reason they feature an effective rank R_{eff} smaller than its exact rank R. The *reduced-rank* approximation of the template matrix $\mathcal{H}$ is expressed by

$$\mathcal{H}_r = \sum_{i=1}^{r} \sigma_i \boldsymbol{v}_i \otimes \boldsymbol{u}_i^T, \tag{2.26}$$

which comprises only those $r < R$ singular vectors which correspond to singular values of a significant magnitude. The approximated representation (2.26) of the fiducial template bank $\mathcal{H}$ is the r-th partial sum of the outer-product expansion of the expression (2.23), where r denotes the desired *target rank*. The Eckart–Young theorem [120] implies that the low-rank SVD in Eq. (2.26) provides the optimal rank-r reconstruction of the template matrix

$$\mathcal{H}_r \equiv \underset{\text{rank}(\mathcal{H}'_r)=r}{\text{argmin}} \parallel \mathcal{H} - \mathcal{H}'_r \parallel \tag{2.27}$$

in the least-square sense, where the truncation error of approximated representation (2.26) in both the spectral and Frobenius norm is given by

$$\parallel \mathcal{H} - \mathcal{H}_r \parallel_2 = \sigma_{r+1}(\mathcal{H}), \quad \parallel \mathcal{H} - \mathcal{H}_r \parallel_F = \sqrt{\sum_{i=r+1}^{\min(N,L)} \sigma_i^2(\mathcal{H})}, \tag{2.28}$$

respectively.

Fig. 2.8 shows $\hat{\sigma}_i \equiv \sigma_i/\sigma_1$ on logarithmic scale as a function of the number of SVD components $i = \{1, \ldots, R\}$ involved in the approximated representation. Each $\hat{\sigma}_i$, which describes the relative magnitudes of the corresponding eigenfeatures, is computed from the truncated SVD (2.26) of template matrices with three distinct full-ranks $R = \{550,\ 936,\ 1800\}$ (i.e. total number of templates). The truncation error in the approximation, in accordance with Eq. (2.28), decreases with the number of SVD components retained. The ultimate accuracy (or minimal error) achievable is limited by the total number of templates L that the original template matrix $\mathcal{H}$ contains. The growing rate of decay in the SV spectrum demonstrates that the individual SVD components gradually lose their relevance for being included in the approximation. In this respect, the spectrum has three clearly distinctive regions characterized by the rate at which SVs decrease:

1. *Overreduced* SVD ($k \lesssim 400$) retain insufficient amount of information to construct a representation by the orthonormalization (2.25) with less than relative error of $10^{-5} - 10^{-6}$. The initial steep exponential fall attests that the information contained in the corresponding eigenfeatures is predominantly relevant. In fact, the first few components shown on Fig. 2.9 contain roughly 90% of all the information on the input waveforms, regardless of rank($\mathcal{H}$). Then, SVs decrease at a much lower, yet a slowly increasing rate, practically indistinguishable for different values of full rank R.

2. *Sufficiently reduced* SVDs ($400 \lesssim k \lesssim 500 - 600$) efficiently select the relevant information, so that the relative error of representation (2.39) is kept well-suppressed while the number of SVD components stored in the reduced-rank template matrix is significantly lower than that of the full-rank. The larger the full-rank R is, the more SVD components have to be kept to achieve the same accuracy of representation.

3. *Underreduced* SVDs ($k \gtrsim 500 - 600$) admit the lowest possible truncation errors, limited only by the numerical errors of the FOM or full-rank approximation itelf. However, the accuracy of reconstructed waveform representation improves at a rate much lower than in the preceding regions. The loss of relevant information content due to the reduction of the number of SVD components is inefficiently low compared to the improvement of accuracy.

Choosing an optimal target rank r is highly dependent on the objective. One either desires a highly accurate reconstruction of the fiducial waveform templates, or a very low dimensional representation of the fundamental features in the templates. In the former case r should be chosen close to the *effective rank*, while in the latter case r might be chosen to be much smaller. Fig. 2.8 demonstrates that choosing a target rank $r = 456$ for the smallest among fiducial template matrices will result in a truncation error related to $\hat{\sigma} = 2.66 \times 10^{-15}$ at $r = 456$.

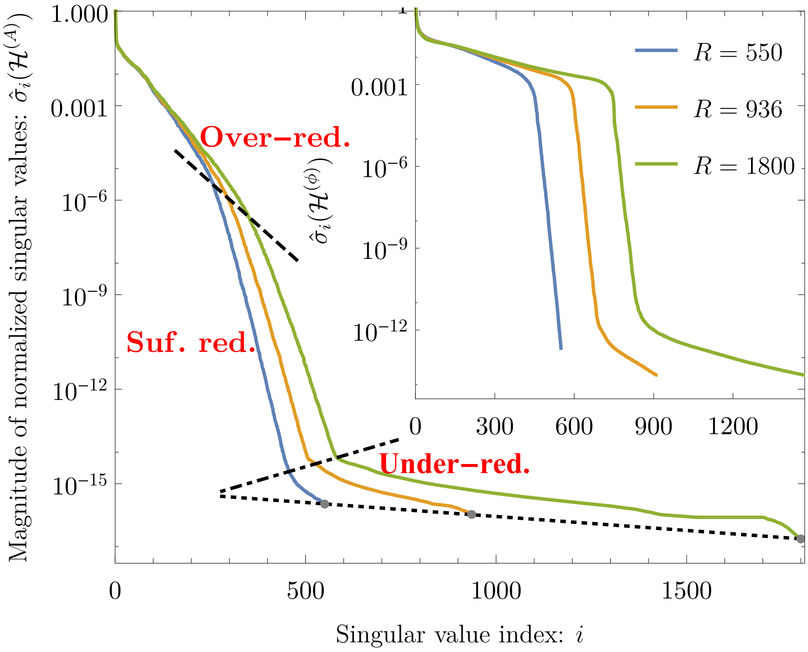

Figure 2.8: Normalized singular-value spectra of the template matrix for full ranks $R = \{550, 936, 1800\}$ are illustrated by blue, orange and green colour, respectively. The horizontal axis represents the index of SVs, while the vertical axis represents the relative variance of SVs. The main panel displays the relative variance of $\hat{\sigma}_i$ of the matrix $\mathcal{H}^{(A)}$ which encodes the amplitude part of waveform templates while the corresponding relative variance of $\hat{\sigma}_i$ for the phase is shown in the top inset. At $r = R - 1$ its infimum, $\hat{\sigma}_r$, falls onto a dotted black line given by $\log \hat{\sigma}_r - \log \sigma_1 \approx -34.8877 - 0.00204394R$. The rate at which the ratio decreases is significantly lower under the dashed black line given by $-6.23703 - 0.0250683R$. Excluding waveforms in the lower section causes less errors by a magnitude much smaller than in the upper section.

2.4.2 Assembly of the surrogate model

The basis for the amplitude or phase space is given in the columns $\mathcal{B}_i$ of the matrix

$$\mathcal{B} \equiv \begin{cases} V_L \in \mathbb{R}^{N \times L}, & \text{if } N > L \\ V \in \mathbb{R}^{N \times N}, & \text{if } N \leq L \end{cases} \tag{2.29}$$

and a full-rank basis is desired. If $N < L$, then the information from L waveforms at N grid points is contained in a basis of dimension N. The reduced basis waveforms only resemble the physical behaviour of frequency domain amplitudes and phases for the first basis function, the higher basis functions are oscillatory (cf. Fig. 2.9). To compress the

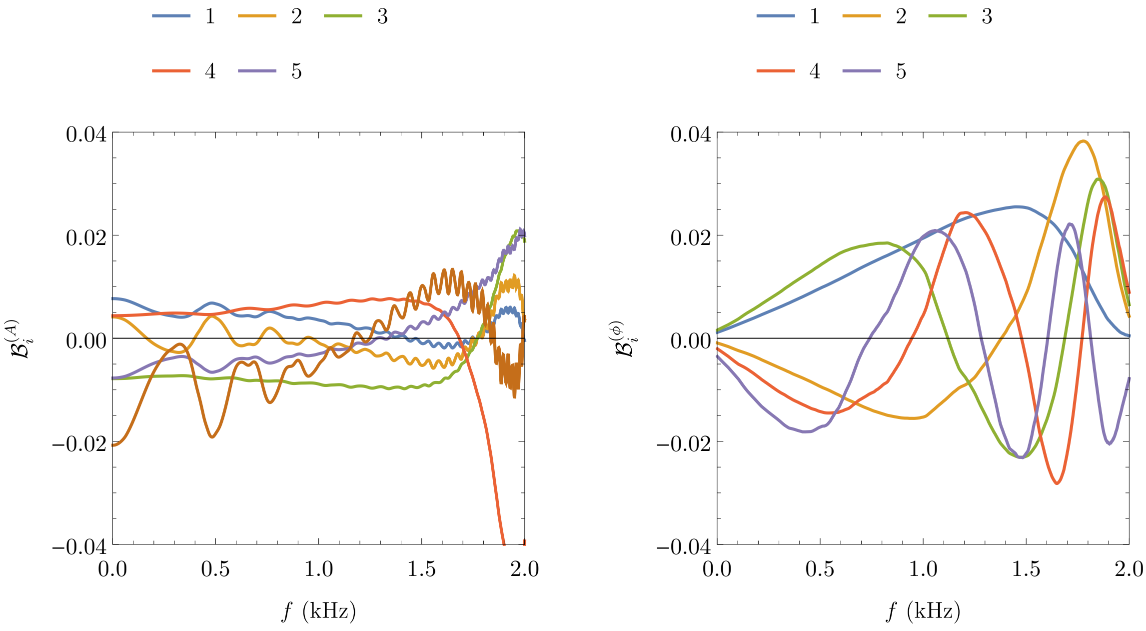

(a) Basis functions for the amplitude modes. **(b)** Basis functions for the phase modes.

Figure 2.9: Reduced basis functions for the first 5 amplitude and phase SVD modes are represented at $N = 4000$ grid points in the frequency domain. The basis functions become increasingly oscillatory as their index i increases.

model, a *reduced basis* of rank r is selected from the FOM or full-rank basis (2.25) in the form

$$\mathcal{B}_r = V_r = [\boldsymbol{v}_1|\dots|\boldsymbol{v}_r] \in \mathbb{R}^{N\times r} \text{ for } r < R \leq N. \tag{2.30}$$

For any r the columns of V_r are optimal orthonormal basis for the starting waveforms. Notice that $\mathcal{B}_r \subset \mathcal{B}_{r+1}$, which demonstrates the underlying hierarchical nature of the generated template banks. [117] Fig. 2.10 may serve as an illustration of the underlying sparsity of the selected basis in the parameter space. The identification of parameter values associated with the basis waveforms selected by SVD from the FOM is not that straightforward as a greedy algorithm would pick values that parameters take. Nevertheless, it may safely be said that a very small part of the parameter space volume is covered; the parameter points are heavily concentrated at low-mass and low-eccentricity values.

Hereafter the label r on the rank-r reduced basis will be dropped for brevity. The projection coefficient vectors $\vec{\mu}$ are computed from the reduced bases $\mathcal{B}^{(A)}$ and $\mathcal{B}^{(\phi)}$ for any given input waveform $\tilde{h} \in \mathbb{R}^N$ as follows

$$\vec{\mu}(\tilde{h}) \equiv \mathcal{B}^T\tilde{h} \in \mathbb{R}^r, \tag{2.31}$$

where the labels referring to amplitude or phase were dropped for brevity. The projection coefficient vectors for all waveform templates are packed in the matrices $\mathcal{M}^{(A)}$ and $\mathcal{M}^{(\phi)}$ with entries

$$\mathcal{M}_{kl} = \mu_k(\tilde{h}_l) = (\mathcal{B}^T\mathcal{H})_{kl} \in \mathbb{R}^{r\times L}. \tag{2.32}$$

By the comparison with Eq. (2.23), one may concede that $\mathcal{M} = \mathcal{B}^T\mathcal{H} = -\Sigma U^T$ for a full-rank basis $\mathcal{B} = V$. It follows that the projection coefficient matrices are ordered in the same way as the individual waveforms in $\mathcal{H}$. To undo the packing of the waveforms in the matrices $\mathcal{M}$ I partition the linear index l that enumerates the waveforms in $\mathcal{H}$ and obtain a tensor

$$\mathcal{M}_{k,l_q,l_e} = \mu_k(\tilde{h}_{(l_q,l_e)}) \in \mathbb{R}^{r\times L_q\times L_e}. \tag{2.33}$$

To complete the model the projection coefficient vectors are defined at any position in the chosen parameter space by suitable interpolants $I[\mathcal{M}](\lambda) \in \mathbb{R}^r$ for the amplitude and phase coefficient tensors $\mathcal{M}^{(A)}$, $\mathcal{M}^{(\phi)}$. For each input waveform one has two corresponding r-vectors of projection coefficients (for amplitude and phase) that are interpolated over the parameter space. The frequency-domain ROM representation of waveform templates is then constructed in the form

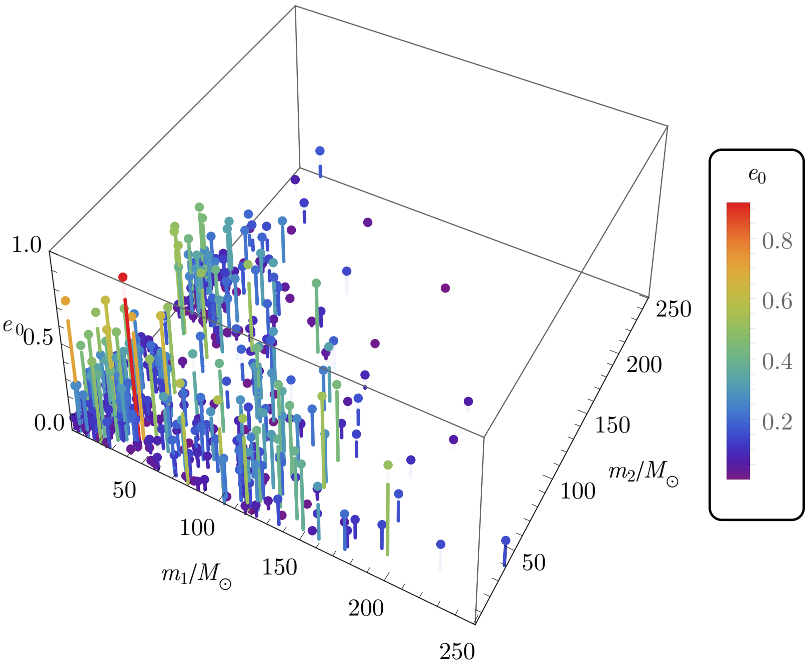

Figure 2.10: The SVD-based reduced-basis parameter choices in the 3-dimensional parameter space (m_1, m_2, e_0). Comparing the positions of the retained $r = 600$ templates to the placement of the original $R = 1800$ template shown in Fig. 2.4, it becomes clear that primarily those parameters are selected that are associated with low-mass and low-eccentricity systems. Only a small fraction of the whole volume of the parameter space is covered.

$$\tilde{h}_{\mathrm{S}}(\lambda; f) \equiv A_0(\lambda) I_f[\mathcal{B}^{(A)} \cdot I[\mathcal{M}^{(A)}](\lambda)] \exp\{i I_f[\mathcal{B}^{(\Phi)} \cdot I[\mathcal{M}^{(\Phi)}](\lambda)]\}, \tag{2.34}$$

where $\cdot$ denotes matrix multiplication, $I_f[\cdot]$ interpolates vectors in frequency on a suitable grid, and $A_0(\lambda)$ is an amplitude prefactor which is stored before the SVD takes place and an interpolant is computed over the parameter space.

2.5 Accuracy and speedup for surrogate model predictions

Once a ROM is built, any surrogate waveform can be evaluated as a sum of reduced basis elements with incremental errors within the parameter range covered in the particular model. The main criteria for a successful ROM are that it facilitates data analysis applications that were infeasible with the fiducial waveform model and that it represents waveforms accurately. [92] This section is dedicated to appraise the overall performance of the ROM building discussed in Sec. 2.4. The first part of this section assesses the accuracy of surrogate model predictions in terms of the match between the surrogate model and the fiducial model. In the second part an overview of the computational efficiency of the ROM is provided with respect to computational complexity and cost relative to the cost of the fiducial model.

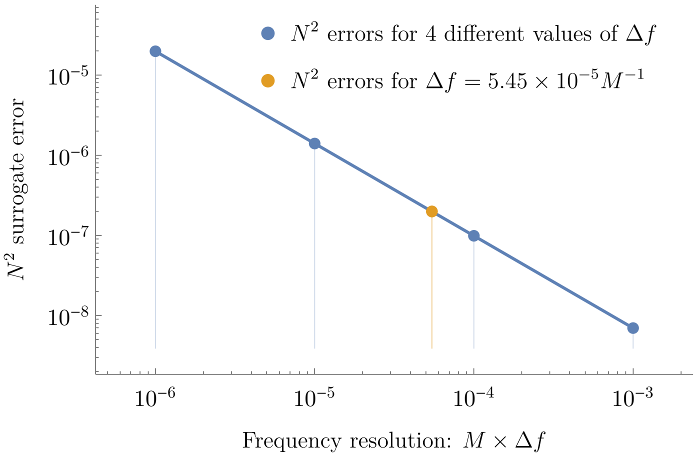

Figure 2.11: The linear trend in the change of surrogate error (2.37) as a function of the resolution of the frequency grid. Higher resolution of sampling times (i.e. lower resolution for sampling frequencies) result lesser uncertainty in estimating the amplitudes and phases. Surrogate error $\Delta\tilde{h}^2 = 1.98 \times 10^{-7}$ is marked with an orange point for a frequency-grid spacing $\Delta f = 5.45 \times 10^{-5} M^{-1}$ which was obtained in Eq. (2.22). The value of surrogate error corresponds to the mean relative error of the amplitude $\Delta\tilde{h}^{(A)} \approx 4 \times 10^{-14}$ shown in Fig. 2.12.

2.5.1 Reconstruction errors

The overlap integral of two normalized waveforms, say, of a fiducial *CBwaves* waveform h_{CB} and its surrogate model prediction h_{S}, is given by the *mismatch* (or *unfaithfulness*) between the two waveforms and is defined as the normalized inner product (2.36) maximized over time and phase shifts

$$\mathcal{M} \equiv 1 - \max_{t_0,\phi_0} \frac{\langle h_{\mathrm{CB}}, h_{\mathrm{S}} \rangle}{\|h_{\mathrm{CB}}\| \|h_{\mathrm{S}}\|} \tag{2.35}$$

with an inherited norm given by $\|h\|^2 \equiv \langle h, h \rangle$. A natural inner product between the two waveforms is given by the complex scalar product

$$\langle \tilde{h}_{\mathrm{CB}}, \tilde{h}_{\mathrm{S}} \rangle \equiv 4\,\mathrm{Re} \int_{f_{\mathrm{low}}}^{f_{\mathrm{high}}} \frac{\tilde{h}_{\mathrm{CB}}(f), \tilde{h}^*_{\mathrm{S}}(f)}{S_{\tilde{h}}(f)} df \tag{2.36}$$

where the tilde denotes Fourier transformation given in Eq. (2.13), $\tilde{h}^*_{\mathrm{S}}(f)$ is the complex conjugate of $\tilde{h}_{\mathrm{S}}(f)$, $S_{\tilde{h}}(f)$ is the one-sided PSD (Power spectral density) of the detector noise and f_{low}, f_{high} are suitable cutoff frequencies for detector sensitivity. The low-frequency cutoff depends on the PSD and is at 10 Hz for advanced detectors design. The high-frequency cutoff is at 2.045 kHz, which is the ISCO frequency of the lowest total-mass configuration in my fiducial model, discussed in Sec. 2.3.3.

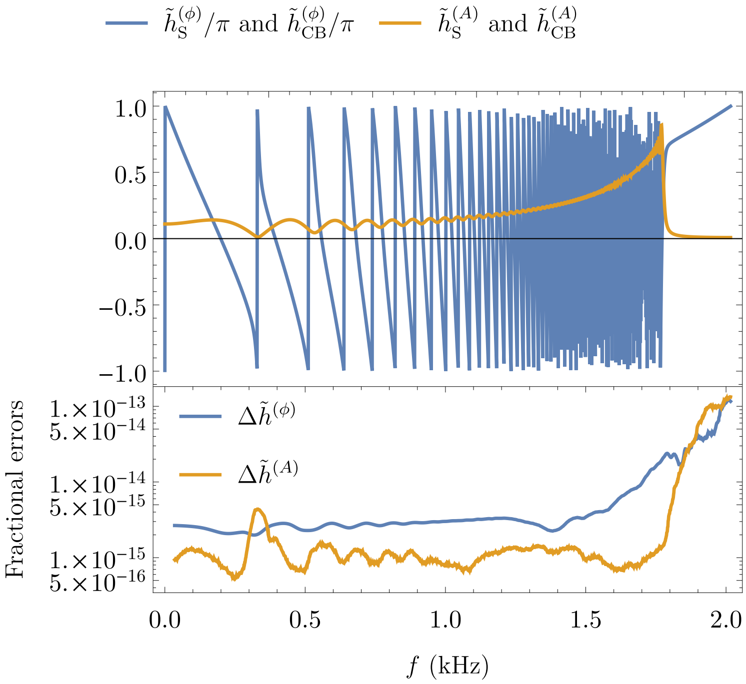

Figure 2.12: *Top panel:* The amplitude and the phase part of the waveform associated with $l = 1$. There is visual agreement among the fiducial *CBwaves* waveform and its surrogate prediction throughout the entire frequency range. *Bottom panel:* The relative errors (2.39) with moving average of 50 points, defined by Eq. (2.39), in the amplitude and the phase difference between the fiducial waveform and its surrogate model prediction. The differences are smaller than the errors intrinsic to the surrogate model itself, as well as those of state-of-the-art NR simulations.

A discrete version of the normed difference between a fiducial waveform and its surrogate is what one may actually measure:

$$\Delta\tilde{h}^2(\lambda) = f_s \sum_{k=0}^{N-1} \left| |\tilde{h}_{\rm CB}(f_k;\lambda) - \tilde{h}_{\rm S}(f_k;\lambda) \right|^2, \tag{2.37}$$

where f_s is the sampling frequency discussed in Sec. 2.3.3. The square of the normed difference between two waveforms, referred to as the *surrogate error*, is directly related to their overlap (2.36). It is the dominant source of error in the surrogate model that translates directly into errors in the fits of the parameters for building the surrogate. [102] Fig. 2.11 shows the linear correlation of the surrogate error in Eq. (2.37) with the time spacing Δf in the regularly spaced grids (2.12–2.13). The surrogate model gradually converges to the fiducial one at finer time scales (i.e. larger sampling frequencies). Other errors of interest are the pointwise ones (separately for the amplitude and phase). They are encoded in the lth surrogate model prediction (2.34) as

$$\tilde{h}_{\rm S}^{(A)}(f_k;\lambda_l) \equiv I_f[\mathcal{B}^{(A)} \cdot I[\mathcal{M}^{(A)}](\lambda_l)], \quad \tilde{h}_{\rm S}^{(\phi)}(f_k;\lambda_l) \equiv I_f[\mathcal{B}^{(\Phi)} \cdot I[\mathcal{M}^{(\Phi)}](\lambda_l)], \tag{2.38}$$

respectively. The *relative errors* in approximating the amplitude and phase of a fiducial waveform by its surrogate model prediction is then expressed by

$$\Delta\tilde{h}^{(A)}(f_k;\lambda_l) = \left|1 - \tilde{h}^{(A)}_{\mathrm{S}}(f_k;\lambda_l)/\tilde{h}^{(A)}_{\mathrm{CB}}(f_k;\lambda_l)\right|, \quad \Delta\tilde{h}^{(\phi)}(f_k;\lambda_l) = \left|1 - \tilde{h}^{(\phi)}_{\mathrm{S}}(f_k;\lambda_l)/\tilde{h}^{(\phi)}_{\mathrm{CB}}(f_k;\lambda_l)\right|, \tag{2.39}$$

where the amplitude and phase parts of fiducial waveforms, $\tilde{h}^{(A)}_{\mathrm{CB}}(f_k;\lambda_l)$ and $\tilde{h}^{(\phi)}_{\mathrm{CB}}(f_k;\lambda_l)$, respectively, are given by Eq. (2.16) on N discrete frequency points f_k.

Fig. 2.12 shows a comparison between the surrogate and fiducial model, using the template assigned to $l = 1$. The top panel shows that the fiducial and surrogate waveforms are visually indistinguishable. The bottom panel demonstrates that both amplitude and phase pointwise errors (2.39) increase with frequency. Nevertheless, the errors are indeed as small as predicted on Fig. 2.8. A moving average of 50 points was used to smooth out short-term fluctuations in the error and highlight longer-term trends. Fig. 2.5 shows a schematic illustration of building surrogate models over a common frequency grid.

2.5.2 Computational cost and speedup for surrogate model predictions

Apart from the requirements for accuracy or reliability, a ROM building is considered efficient if it generates cost-efficient surrogate models. The major advantage of using surrogate model predictions in lieu of actual waveform evaluations is their significantly reduced resource consumption. Now I discuss the computational cost, in terms of *operation counts* and *run-time*, of ROM building and present the desired *speedup* that can be achieved when evaluating surrogate models.

As described in Sec. 2.4.2, the complete surrogate model (2.34) is assembled with the evaluation of r projection coefficients $\mu_l(f)$ given in (2.31) and $2r$ fitting functions $\{\tilde{h}^{(A)}_l(\lambda)\}^r_{l=1}$ and $\{\tilde{h}^{(\phi)}_l(\lambda)\}^r_{l=1}$ given in (2.38). In order to construct a surrogate model for some parameter λ, one only needs to evaluate each of those $2r$ fitting functions at λ_0, recover the r complex values $\{\tilde{h}^{(A)}_l(\lambda_0)\exp[-i\tilde{h}^{(\phi)}_l(\lambda_0)]\}^r_{l=1}$, and perform the summation over the index l. Each $\mu_l(f)$ is a complex-valued frequency series with N samples. Therefore, the total operation count to evaluate the surrogate model at each λ_0 is $(2r-1)N$ plus the cost to evaluate the fitting functions. [102] The entire process of constructing a small, efficient ROM which is comprized of only $r = 550$ waveform templates sampled at $N = 4000$ grid points requires the execution of approximately 4.4×10^6 operations (excluding the cost of evaluating the fitting functions).

The notion of 'speedup', in this terminology, is the number that evaluates the relative performance of generating the same waveforms on the same processor by the execution of CBwaves code and of the surrogate model. More specifically, I test the acceleration of waveform generation by measures on the length of time required to perform each computational process. Let as note that the time which was denoted by t_{int} and was referred to as 'integration run-time' in Sec. 2.2.1 is actually the execution time during which the processor is actively working on my computations. It is referred to as CPU time (or run-time) and will be denoted by t_{CPU}. In contrast, the actual elapsed real time accounts for the whole duration from when the computational process was started

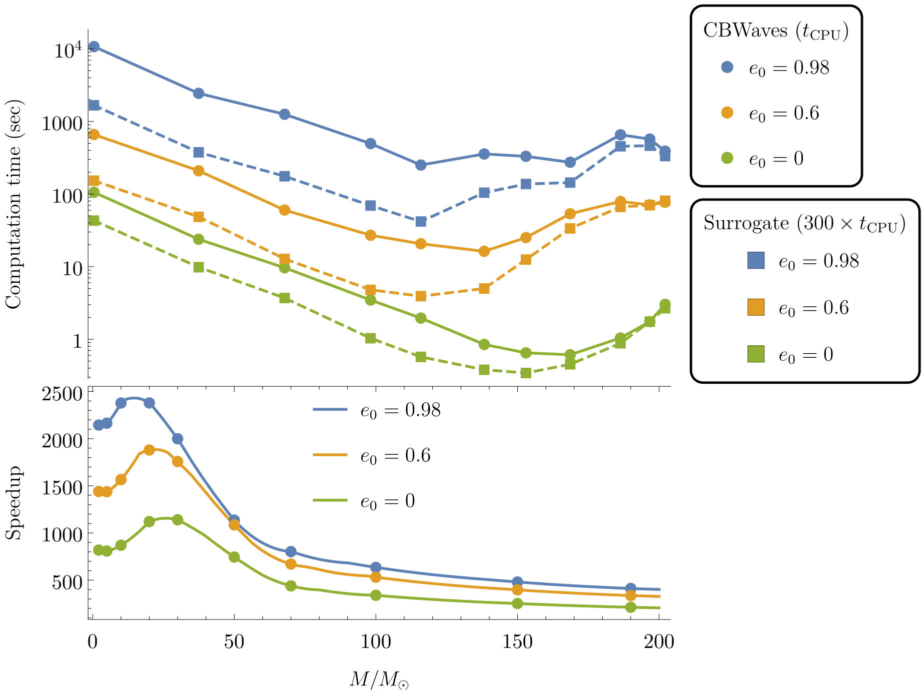

Figure 2.13: *Top panel:* Computational time $t_{\rm CPU}$ to generate fiducial waveforms by CBwaves code (dots; connected by solid lines) against the cost of evaluating corresponding surrogates by ROM (rectangles; connected by dashed lines). The computational time was measured for three different initial eccentricities of equal-mass configurations, each associated with different colours. *Bottom panel:* The speedup in evaluating the surrogate model is several thousand times faster around $10-50\ M_\odot$ than generating CBwaves waveforms. For high total mass the speedup falls off to several hundreds. The speedup is roughly twice as great for configurations having extremely high initial eccentricity at $e_0 = 0.98$ (blue line) as for circular ones at $e_0 = 0$ (green line).

until the time it terminated. The difference between the two can arise from architecture and run-time dependent factors such as waiting for input/output operations (e.g. saving waveform templates). Consequently, the elapsed real time is greater than or equal to the CPU time.

Fig. 2.13 shows (on top) the computation time or CPU time for CBwaves waveforms (solid lines) against corresponding surrogate waveforms (dashed lines) as a function of total mass of the binary system. The total mass M is measured in the same 11 points as in Fig. 2.2 for three different initial eccentricities ($e_0 = \{0.98, 0.6, 0\}$) of equal-mass configurations, each associated with different colours. The computation time $t_{\rm CPU}$ for surrogates is multiplied by a factor of 300 in order to shift the curves close to their respective CBwaves counterparts and enable visual comparison. The bottom panel demonstrates that surrogates are several thousand times faster around $10 - 50\ M_\odot$ to evaluate as compared to the cost of generating CBwaves waveforms. The speedup falls off to several hundreds as the total mass increases. Moreover, the speedup grows when the initial eccentricity e_0 is increased in much the same way as with the mass disparity $\bar{q}$ (cf. Fig. 6 in [92]). The speedup is roughly twice as great for configurations having extremely high initial eccentricity ($e_0 = 0.98$) as for circular ones ($e_0 = 0$). The resemblance of the influence of e_0 and $\bar{q}$ on the speedup can be attributed to their asymptotical nature as it had been pointed out earlier in Sec. 2.2.1. It is also evident that the speedup culminates when waveforms for configurations of very low total mass and very high eccentricity are generated. Such waveforms are prohibitively expensive to generate with CBwaves in contrast to surrogates that are generated at the same cost, regardless of the parameters of the configuration.

Let us note that successive versions of SEOBNR (aligned-Spin Effective-One-Body Numerical Relativity) ROMs have been developed and put to use within LAL (LSC Algorithms Library) (LSC Algorithms Library) to shorten data analysis applications carried out since the first observation runs have begun. [121] It has been shown in [102, 103] that the cost of evaluating the surrogate model is linear in the number of samples N (cf. Fig. 2.11 where the surrogate error depends on the sampling rate). Depending on the sampling rate, the speedup is between 2 and almost 4 orders of magnitude. The speedup in evaluating surrogate models compared to generating NR waveforms with the LAL analysis routines is crucial for searches and theoretical parameter estimations. SEOBNR (aligned-Spin Effective-One-Body Numerical Relativity), IMRPhenomD (IMR Phenomenological Model 'D') and PhenSpinTaylorRD waveform approximants are among the best available GW models for generic spinning, compact binaries. In comparison with my results, the speedup achieved at the typical rate of 2.048 kHz used by aLIGO and aVirgo observatories is roughly 2300. [119]

2.6 Summary of ROM-based predictions, limitations and an outlook

The primary goals of the present research have been to propose a potential extension of the ROM techniques to alleviate the computational burden of constructing waveform templates for coalescing compact binaries with any residual orbital eccentricity and to validate the applicability of ROMs to this particular family of waveforms. ROMs have been applied to several waveform families (SEOBNR, IMRPhenomP and PhenSpinTaylorRD) in LAL routines for gravitational-wave data analysis. [103–109] The aforementioned waveform families provide efficient descriptions of gravitational waves emitted during the late IMR stages of compact binary systems, but only in the zero-eccentricity limit. The major motivation for extending the scope of application beyond the zero-eccentricity limit is based on the ground, referred to in Sec. 2.1, that the great majority of compact objects formed in dense stellar environments retain some non-negligible eccentricity when entering the frequency band of ground-based GW detectors [18, 19], as well as the impact of eccentricity on the accuracy of parameter estimation for BNSs [30].

My approach to construct frequency-domain ROMs has been predominantly based on the method outlined in Refs. [92, 117] (cf. Sec. 2.4). Input waveforms comprised in the ROM are Fourier transformed and split into their amplitude and phase parts (cf. Sec. 2.3.2). These functions are accuretely represented on a common, finely sampled and regularly spaced frequency grid defined in Sec. 2.3.3 with only $N = 4000$ equidistant nodes, with a sampling frequency recorded well above the required Nyquist frequency, at $f_s = 16.384$ kHz. Fig. 2.11 demonstrates that, beside the degree of model order reduction, the accuracy of surrogate-waveform representation relies on the sampling frequency. The upper and lower limits of frequency contained in the grid are determined from the ISCO frequency for the lowest total-mass configuration of interest (which is roughly 2 kHz in this study) and the low-frequency cutoff of the detector noise spectrum (which is close to 10 Hz for aLIGO design). The ROM is designed to be capable of producing surrogates for GWs from CBCs of total mass between $2.15M_\odot$ and $215M_\odot$, thereby covering the entire total-mass range of stellar-mass BBH/BNS systems of interest for ground-based GW detectors. The mass ratio is allowed to range between equal mass at $q = 1$ and relatively high mass-ratio at $q \approx 0.01$ while the initial orbital eccentricity changes over a relatively wide range of values from $e_0 = 0$ (circular orbits) up to $e_0 = 0.95$ (highly eccentric orbits). Configurations with both low total-mass and high mass-ratio would imply component masses well below $1M_{\odot}$, which, of course, are excluded as inconceivable astrophysical sources. Despite the fact that the investigation has been restricted to a feasible 3-dimensional subset of the full 8-dimensional parameter space of GW signals (cf. Fig. 2.4), the conclusions of Sec. 2.4, in agreement with that of Refs. [92, 102–104, 117], suggest that a full representation of the 8-parameter space might actually be achievable with a relatively compact reduced basis (cf. Ref. [102]). Template placement algorithms based on template-space metric (such as in Ref. [115, 116]) make admittedly far more effective coverage of the parameter space than the uniform spacings used in this study. As a matter of fact, Fig. 2.10 illustrates that the large majority of parameters of the selected templates constituting the reduced basis are concentrated along the axes of the parameter space.

The reduced bases were built separately for the input amplitude and phase (cf. Fig. 2.9) by the decomposition of template matrices that comprise 550, 936, and 1800 input waveforms, respectively. The projection coefficients for corresponding input waveforms projected onto their reduced bases were calculated as functions of the model parameters (M, q, e_0) and were interpolated by tensor product cubic lines over the parameter space. Finally, the ROM which preserves fundamental features of the original FOM is assembled from its constituent parts. Fig. 2.8 demonstrates the underlying hierarchical nature of the generated template banks and indicates that the truncation error in the approximated representation of surrogates decreases with the number of SVD components retained, characterized by a rate at which SVs decrease. Extremely little ($r \lesssim 400$) or large number ($r \gtrsim 500-600$) of SVD components retained are equally poor choices because the amount of information is either insufficient to construct accurate representations or excessively large compared to the achieved accuracy. An effective rank is chosen preferentially from a ROM which posess the lowest SV with the smallest possible number of components retained (in the presented case $r = 456$). The first part of Sec. 2.5 assess the error of surrogate model predictions for waveforms that were originally not present in the original template bank, with special regard to the impact of frequency on the reconstruction error. To that end, reference waveforms were generated by CBwaves in all the intersection points right between the grid poinst of the original template bank (cf. the yellow in Fig. 2.4). Finally, the surrogates were evaluated in the corresponding parameter-space points for comparison and the relative error was measured along all the $N = 4000$ frequency points. The bottom panel of Fig. 2.12 attests that the relative error of the approximated representation is consistent with the error estimates derived from the singular values ($\Delta\tilde{h}^{(A)} \approx 10^{-15}$, $\Delta\tilde{h}^{(\phi)} \approx 10^{-13}$) over a large portion of the frequency range, but larger than expected at around the starting frequency ($\Delta\tilde{h}^{(A)} \approx 10^{-13}$, $\Delta\tilde{h}^{(\phi)} \approx 10^{-13}$). The figure indicates that the relative error of the amplitude and phase increases with the frequency. My results provide clear examples of the construction and use of ROMs for eccentric inspiral waveforms.

My results also provide strong evidence that large increases in the speed of computation are obtained through the use of ROMs. Fig. 2.2 has exposed that the cost of computing input waveforms increases exponentially as the total mass decreases, but rises asymptotically at an even faster rate than the initial eccentricity or mass disparity increase. In contrast to the cost of EOB waveform (complete IMR) generation that rises steeply as the starting frequency is decreased (cf. Ref. [92]), the cost of CBwaves waveform (inspiral-only) generation rises more gradually. The cost of input waveform generation varies considerably in the region of parameter space (M, q, e_0) explored and depicted in Fig. 2.4, but Fig. 2.3 has revealed that only a surprisingly small fraction of waveforms of high-eccentricity and high-mass-disparity configurations are actually responsible for the prohibitively large time-consumption of integrating a large number of 3PN-accurate equation of motion over the investigated range of parameters. As discussed in the second part of Sec. 2.5 (based on Ref. [117]), the cost of generating surrogate waveforms (shown in the top panel of Fig. 2.13) comprises a constant cost of the spline interpolation at each frequency point and a cost of performing the interpolations of coefficients over the parameter space. The speedup in evaluating the surrogate model, shown in the bottom panel of Fig. 2.13, is 2–3 orders of magnitude faster than generating corresponding CBwaves waveforms overall, reaching a factor of several thousand around 10–50 $M_\odot$.

Finally, the method presented in this chapter is limited to building surrogate models of inspiral-only PN input waveforms for the reason that eccentric binaries circularize in the last few cycles before the merger. Nevertheless, composite waveforms that fully cover all the IMR phases can be constructed as prescribed in Ref. [92, 117] by matching the inspiral and NR waveforms of merger stages in either the time or frequency domain and then fitting this ‘hybrid’ waveform to the ring-down part, described by damped exponentials. The gap between the initial part of the waveform and its final ring-down part, described by damped exponentials, is bridged by a phenomenological phase. The practical implementations of ‘hybrid’ waveforms that comprise eccentric inspirals will be left for future work. I anticipate substantial speedup factors to come for predicting NR waveforms with a surrogate model compared to the expensive NR simulations for the same parameters. Developing an efficient template placement technique (such as in Ref. [115, 116]) for better coverage of the parameter space and an adaptive sampling technique in the frequency domain are critical factors in the operational efficiency of ROMs and have been left for future work. All these ultimately leading to computationally feasible and successful exploration of the full 8-dimensional parameter space of GW signals.

Chapter 3

Radial pulsations of relativistic stellar models for dissipative fluids

This chapter is dedicated to present my results of my latest papers [4, 5] on the radial oscillations of neutron stars affected by the viscosity and thermal conductivity of neutron-star matter. Here, in addition to providing a comprehensive review of the basic theory of relativistic stellar pulsations, I present an analytical formulation of the dynamical equations that governs the radial mode of linear adiabatic stellar oscillations through a perturbation scheme. I prove that, similarly to the non-dissipative case, the pulsation equation expressed by a set of effective variables which involve dissipative terms, can be recast in a self-adjoint form. In contrast to the common non-dissipative case, the associated SLEVP (Sturm–Liouville eigenvalue problem) is generalized for a discrete set of eigenfunctions with complex eigenvalues which correspond to the squared frequencies of the oscillation modes and the imaginary part corresponds to the damped solution. However, the main novelty of this approach is the ability to directly relate the damping ratio of oscillations to the expressions $\mathcal{S}_1$ and $\mathcal{S}_2$, which stem from the viscous and heat-conductive contributions to the stress–energy tensor, without relying on explicit NR computations. The scale of relaxation time, directly related to the damping ratio, is identical to approximate solution for the time-scale of energy dissipation given by [122] in an alternative way. The usefulness of my analytical approximation method is evidently restricted to providing qualitative and ‘order-of-magnitude’ information about the dissipative time-scales in (3.104) rather than a precise one.

Conversely, the numerical solution of the eigenvalue problem has yet to be published in my next paper [5]. There SLEVP for the radial oscillation modes of stars is converted to a system of finite difference equations where I implement a second-order accurate differencing scheme so the resulting system of finite difference equations emerges as a tridiagonal matrix eigenvalue problem. In a manner similar to the approach of Kokkotas and Ruoff [123], I compute the four lowest-frequency radial-oscillation modes of neutron stars constructed from various potential EOSs of cold-nuclear-matter considered by Özel and Freire [124]. The algorithm yields zero-frequency modes at the maxima and minima of the mass curves while the equilibrium adiabatic index characterizes the stiffness of the EOS at a given density. Finally, I evaluate the rate at which viscosity and thermal conductivity drain energy from the radial oscillation mode.

3.1 Context of relativistic asteroseismology

3.1.1 Astrophysical motivation for relativistic stellar oscillations

Neutron stars provide us with unique insights into the physics of the extremely dense and cold nuclear matter, which cannot be reached in terrestrial experiments. The central density of a neutron star is expected to reach up to several times of the nuclear saturation density ($n_0 \simeq 0.16\ \mathrm{fm}^{-3}$). The constraints on the properties of matter at supernuclear densities (cf. [125] and references therein) and relatively low temperatures (compared to particle collisions producing comparable energy densities) rely heavily on observations of macroscopic equilibrium parameters (masses, radii, moments of inertia, etc.) of NSs. Attention has focused especially on measurements of the stellar mass M and circumferential radius R of these stars which depend significantly on their respective EOS (e.g., the relation between the pressure and the total energy density). [124, 126, 127] The recent discovery of NS with mass as high as $M \approx 2.01 M_\odot$ (e.g., PSR J1614-2230 has $M = 1.927 \pm 0.017 M_\odot$ [128] and PSR J0348+0432 with mass $M = 2.01 \pm 0.04 M_\odot$ [129] has ruled out several EOSs, as shown in Fig 3.3. Due to the tremendous advances in the measurements, precise masses for ~ 35 currently known NSs range from 1.17 to 2.01 $M_\odot$. Also more than a dozen radii are known in the 9.9-11.2 km range, but current estimates for radii are still dominated by systematic errors [130, 131]. One major class of EM observations comprises X-ray and γ-ray burst phenomena. These events are clearly explosive in nature and have been generally associated with neutron stars by many authors (cf. e.g., [7]). These explosive events perturb the associated neutron stars, and the resulting dynamical behaviour may eventually be deduced from such observations. X-ray observations from the recently launched NICER mission ([11]) and from the upcoming LOFT mission [12, 132] will impose stricter constraints on plausible EOSs by yielding the mass and radius of a few stars to $\sim 5\%$ precision. EOS predictions as well have become more reliable due to precision measurements of nucleon-nucleon interactions, detailed calculations of binding energies of light nuclei and cold nuclear matter which constrain three-body forces, inclusion of relativistic effects, improved many-body and Monte Carlo methods. [133]

The interior structure of stars is probed by asteroseismology using the frequency of seismic waves rippling throughout the star. The frequencies of NS oscillations that relies on accurate stellar models are matched to the observed frequencies. The period of stellar oscillations for non-relativistic stars are in the range of minutes, whilst for neutron stars the periods are much shorter, typically range from 0.2 to about 0.9 milliseconds. [15] These oscillations occur when a star is perturbed away from its dynamical equilibrium and a restoring force tries to return it back to that equilibrium state. Among the various types of oscillation modes, I focus on the fundamental modes (f-modes) of non-rotating NSs where the pressure provides the dominant restoring force that produces radial oscillations. Pulsation in radial modes are the simplest and generally the largest amplitude stellar pulsations, where the displacement is purely radial and spherically symmetric. Provided that there is no stationary surface between the centre and the surface of the star, an oscillation can be called the fundamental radial mode. [134, p. 55] Moreover, knowledge of f-modes of non-rotating stars also provides estimates for the f-mode properties of slowly rotating stars, for the case of uniform rotation [135] and also for differential rotation [136].

3.1.2 Theoretical development in relativistic stellar oscillations

Theoretical interest in the dynamical stability of relativistic stars has arisen since 1964 from the seminal works of S. Chandrasekhar, R.F. Tooper and J.M. Bardeen [137–141] and a general stability criterion was formalized in the 1970s by J. L. Friedman and B. F. Schutz [142]. The stability of spherically symmetric stars under radial adiabatic perturbations has been extensively studied and reported in the literature (e.g [8, 9, 143–145]). Induced by the small radial perturbations, dynamical instability will intervene by radial oscillation before the star contracts. Several techniques for obtaining spectra of oscillation modes have been developed for various stellar equilibrium models, mostly with zero-temperature EOS. Although, these studies mostly investigated for zero-temperature EOS stellar models, proto-NS with finite-temperature EOS [146] and strange stars [145, 147] were also studied. I have applied Chandrasekhar's linear varational method [137, 138] to formulate the variational principle which forms the basis for determining the characteristic eigenfrequencies and relaxation times of radial oscillations.

The first exhaustive compilation of radial modes for various zero-temperature EOS was presented by Glass & Lindblom in [8]. Although their equations were correct, the numerical results for the oscillation frequencies were flawed as it was later pointed out by Väth & Chanmugam in [145]. Väth & Chanmugam computed the frequencies of radial oscillation for six EOSs and verified their own results invoking the argument [143] that a correct NR algorithm must yield a zero-frequency mode at that specific central density that corresponds to the maximal-mass configuration for the particular EOS. Stars on the high-density side of this maximal-mass instability point are unstable and eventually collapse. Kokkotas & Ruoff emphasized in [123] that the above mentioned test is only applicable when a constant local adiabatic index is used both in the equilibrium stellar model and its perturbation equations. In general, a variable adiabatic index can be employed that depends on the dynamical regime regulated by a more complicated EOS. Kokkotas & Ruoff re-examined earlier studies of radial oscillation modes for the most common EOSs and corrected the values of eigenfrequencies found by Glass & Lindblom in [8]. Moreover, their survey included six additional EOSs that were more recent at the time (cf. [123] and references therein).

Concurrently, the conversion of kinetic energy into heat and effects of viscosity on stellar pulsations in general has been addressed first by [148–150]. Properties of transport coefficients (bulk viscosity, shear viscosity, thermal conductivity) in neutron stars have been studied more in detail by a number of recent of works [151–154]. The density and temperature dependence of shear viscosity and of bulk viscosity in the crust and in the core, respectively, have been described for different EOSs of neutron stars by [151]. Thermal conductivity and shear viscosity of nuclear matter arising from nucleon-nucleon interaction in non-superfluid neutron-star cores were considered by [152], whereas those arising from the collisions among phonons in superfluid neutron stars were considered by [154]. An extension of [152] for different nucleon-nucleon potentials and different three-body forces in [153] found that the nucleon contribution dominates the thermal conductivity, but the shear viscosity is dominated by leptons. The most up-to-date review of the transport properties and the underlying reaction rates of dense hadronic and quark matter in the crust and the core of neutron stars is found in [155].

3.2 Equation of state and chosen models

Internal structure and macroscopic properties of NSs are strongly correlated with the EOS of dense matter, even though the exact EOS remains exceedingly uncertain especially at high densities. Although, the latest discovery of high-mass NSs PSR J1614-2230 [128] and PSR J0348+0432 [129] has ruled out several EOSs, suggesting that the maximal mass for NSs has to be larger than $M \sim 2M_{\odot}$ for a given EOS, but the number of candidate models with maximal mass below this limit is still considerably large.

In NS cores, the temperature of matter is far below the Fermi energy of its constituent particles and its particular thermodynamic state at $T \simeq 0$ is accurately described by the isentropic one-parameter EOS

$$p = p(\rho),\ \epsilon = \epsilon(\rho), \tag{3.1}$$

relating the pressure p and energy density ϵ to the rest-mass density ρ which exceeds nuclear density [156]

$$\rho_{\mathrm{nuc}} \simeq 2.3 \times 10^{14}\ \mathrm{g/cm}^3. \tag{3.2}$$

In fact, densities in the cores are expected to be as large as $\rho \sim 5-10\rho_0$, where the nuclear matter at saturation (i.e. at the minimum of the energy per nucleon) has the density $\rho_0 \simeq 2.8 \times 10^{14}\ \mathrm{g/cm}^3$ or $n_0 \simeq 0.16\ \mathrm{fm}^{-3}$, where the baryon-number density is related to the baryon-mass density as $n_B = \rho_B/m_u$ and $m_u = 931.494$ MeV is the atomic mass unit. Given that neutrons geometrically overlap at $\rho \sim 4\rho_0$ and with increasing overlap between nucleons, transitions to non-nucleonic states of matter are expected. [124] It is possible for ultra-dense matter to contain hyperon, pion or kaon condensates. [157] Some of the possibilities considered to date also include free quarks or colour superconducting phases. [158]

3.2.1 Tabulated nuclear-theory-based EOS models

With the intention of covering a wide range of potential types of representative EOSs and generation methods, here I consider four EOSs of cold nucleonic matter (i.e. the hypothetical components composed of neutrons, protons, electrons, and muons) and I follow the widespread naming convention of Refs. [124, 126, 127]:

- *APR4* was derived of a variational method with modern nuclear potentials [159];
- *MPA1* was derived of a relativistic Brueckner–Hartree–Fock theory [160];
- *MS1* was derived of a relativistic mean-field theory [161];
- *SLy* was derived of a potential method [162].

and I also include three EOS of non-nucleonic state (i.e. the hypothetical components composed of hybrid nucleon–hyperon–quark matter):

- *H4* was derived of a relativistic mean-field theory including effects of hyperons [157];
- *ALF1* is a hybrid EOS which describes a APR4 nuclear matter for a low density and a colour–flavor-locked quark matter for a high density with the transition density is $3\rho_0$ where $\rho_0 \simeq 2.8 \times 10^{14}\ \mathrm{g/cm}^3$. [158];

Abbr.	**Constituents**	$M_{\rm max}/M_\odot$	$R_{1.4}$/km	**Ref.**
APR4	Nucleons	2.22	11.13	[160]
MPA1	Nucleons	2.47	12.08	[160]
MS1	Nucleons	2.78	14.77	[161]
SLy	Nucleons	2.06	11.45	[162]
H4	Nuc., Σ, Λ	2.04	13.57	[157]
ALF1	u, d, s quarks	1.50	9.63	[158]
SQM1	Nuc., s quarks	1.56	8.89	[163]

Table 3.1: Nucleonic and hybrid nucleon–hyperon–quark matter models based on different microphysics. The upper 4 models correspond to nucleonic, the lower 3 models involve non-nucleonic states of matter, such as kaon condensates or hyperons. $M_{\rm max}$ and $R_{1.4}$ are the maximal mass of spherical NSs in units of $M_\odot$ (also marked in Fig. 3.3 by the symbols $\diamond$) and the circumferential radius of $1.4M_\odot$ NSs in units of km for a given EOS, respectively.

- *SQM1* is a hybrid EOS which describes relativistic non-interacting gas mixed with strange quark matter [163].

Provided that the above considered EOSs is described by piecewise-polytropes with $n = 3$ pieces as in Sec 3.2.2, the following densities are determined at the boundary of two neighbouring pieces: $\rho_1 \simeq 10^{14}$ g/cm^3, $\rho_2 \simeq 5.012\times10^{14}$ g/cm^3, $\rho_3 \simeq \times10^{15}$ g/cm^3. ALF1 has the lowest pressure among the above considered EOSs and, thus, making it the softest one. APR4, MPA1 and Sly have also relatively small pressure as in the case of ALF1 for a low-density region $\rho_1 \leq \rho \leq \rho_3$, but for $\rho_2 \lesssim \rho \leq \rho_3$, the pressure is higher than that for ALF1. Thus, for $\rho < \rho_3$, which NSs of canonical mass 1.3 – $1.4M_\odot$ have, these EOSs are soft as far as the canonical neutron stars are concerned. It is worthy of note that for a relatively small value of p_2, the adiabatic index, as illustrated in Fig. 3.2, is as large as $\Gamma_2 \sim 3$, owing to that the maximal mass of NS has to be $M_{\rm max} \lesssim 2M_\odot$ for a given EOS. Thus, an EOS that is soft at $\rho = \rho_2$ has to be in general stiff for $\rho \gtrsim \rho_3$. Although MPA1 has pressure that even exceeds that of H4 for a high-density region $\rho \gtrsim \rho_3$. By contrast, H4 and MS1 have pressure higher than the rest for $\rho \lesssim \rho_3$, although the EOSs become softer for a high-density region $\rho \gtrsim \rho_3$. In particular, MS1 has extremely high pressure among many other EOSs for $\rho \lesssim \rho_3$, and on that account, it is the stiffest EOS. All the distinguishing feature mentioned above are reflected in Fig. 3.1, which display the pressure in NS as a function of the baryon-number density or of rest-mass density. Table 3.1 lists the constituent particles, the maximal mass and circumferential radius of neutron stars of total mass $1.4M_\odot$, associated with the representative EOS, respectively.

3.2.2 One-piece and piecewise-polytropic EOS

Although the tabulated EOSs listed in Table (3.1) are more realistic, they are too complicated to illustrate some fundamental features. A very common closed-form EOS is the polytropic one,

$$p = K\rho^\Gamma, \tag{3.3}$$

which describes a non-interacting, degenerate matter. In general, the ‘polytropic constant’ $K = K(s)$ depends on the entropy, however, the degenerated matter dynamics in zero-temperature approximation can be modeled as an adiabatic flow with a constant K.

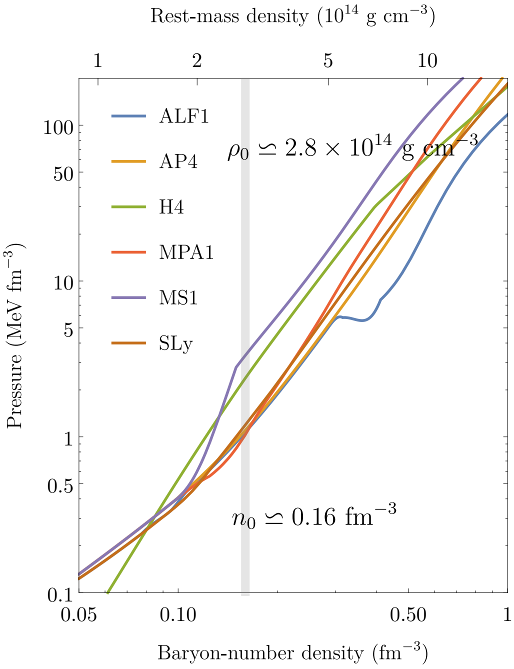

Figure 3.1: Pressure in compact stars as a function of the baryon-number density or of rest-mass density for some nucleonic and hybrid nucleon–hyperon–quark matter models based on different microphysics. The nuclear saturation density $n_0 \simeq 0.16$ fm^{-3} is denoted by a shaded gray line. The range of pressures at n_0 is approximately a factor of 1 to 3 MeV fm^{-3}. The pressures and number density series were reproduced from Ref. [124].

(For more details on K, cf. A.11.) The internal energy is given by the first law of thermodinamics for adiabatic process ($\delta Q = 0$), which can be integrated to obtain

$$\epsilon = \rho + \frac{1}{\Gamma - 1} K \rho^{\Gamma} = \rho + \frac{1}{\Gamma - 1} p, \tag{3.4}$$

where $\lim_{\rho \to 0} \epsilon/\rho = 1$ was imposed. [139] With the adiabatic assumption, eqs. (3.3–3.4) represent a barotropic fluid where the pressure is just a function of ρ. The adiabatic index Γ_1, defined by

$$\Gamma_1 = \frac{d \log p}{d \log \rho} = \frac{\epsilon + p}{p} \frac{dp}{d\epsilon}, \tag{3.5}$$

is an important dimensionless parameter characterizing the stiffness of the EOS (3.3) at a given density. [164, p. 190] For instance, a non-relativistic degenerate Fermi gas is reasonably well described by a polytropic EOS that scales as $p \propto \rho^{5/3}$, and for highly relativistic degenerate Fermi gases, $p \propto \rho^{4/3}$. Generally, Γ_1 depends on the dynamical regime given by ρ and ϵ as shown in Fig. 3.2 for the EOSs listed in Table 3.1. The EOS (3.3) must satisfy the following two conditions. The first, thermodynamic stability, requires the EOS be monotonic ($dp/d\rho \geq 0$ and $dp/d\epsilon \geq 0$), and therefore Γ must be positive. The second, causality requires the speed of sound c_s be less than the speed of light:

$$c_s^2 = \left. \frac{dp}{d\epsilon} \right|_s \leq 1. \tag{3.6}$$

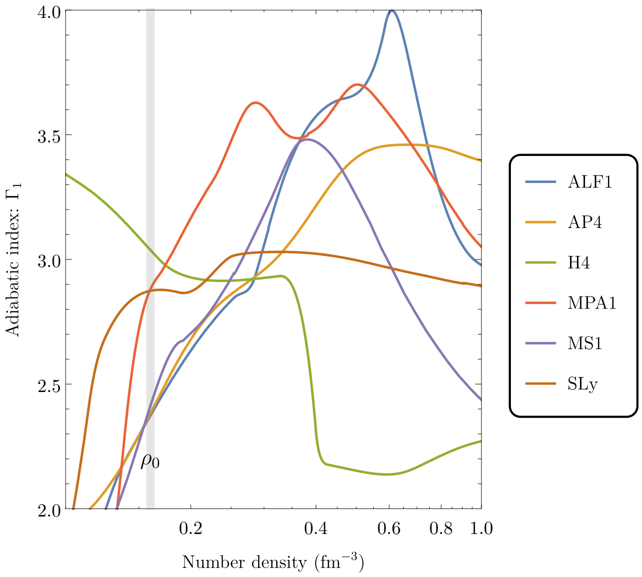

Figure 3.2: The effective adiabatic index $\Gamma(\epsilon)$ function of the energy density ϵ (including the rest-mass density ρ contribution) for the set of candidate EOS models considered in Table 3.1. The average value of the exponent $\Gamma_1 = d\log p/d\log n_B \simeq 2$ holds for nucleonic EOSs in the vicinity of nuclear saturation density $n_0 \simeq 0.16$ fm^{-3}, denoted by a shaded gray line.

Therefore, eqs. (3.5–3.6) bound the average value of adiabatic index as

$$\bar{\Gamma}_1 = \frac{\epsilon + p}{p} c_s^2 \geq \frac{4}{3} \tag{3.7}$$

within a dynamically stable star. [165] For spherical stars in Newtonian gravity, $\Gamma_1 < 4/3$ is a sufficient condition for dynamical stability, however, in the stronger gravity of general relativity, even models with the stiffest EOS become unstable for some value $R/M > 9/8$. The more rigorous constrain on Γ_1 for a star to be stable against radial perturbation

$$\Gamma_1 < \frac{4}{3} + K\frac{4M}{R}, \tag{3.8}$$

where K is positive and of order of unity. For dynamical oscillations of neutron stars, the adiabatic index Γ_1 does not coincide with the polytropic one Γ.

Read et al. [127] demonstrated that a piecewise-polytropic EOS with three pieces ($n = 3$) above the nuclear density approximately reproduces most properties of the representative EOS listed in Table 3.1. These nuclear-theory-based EOSs at high density are modeled with a small number of parameters and the expression for pressure (3.3) is written in a parameterized form as

$$p(\rho) = K_i \rho^{\Gamma_i} \quad \text{for} \quad \rho_i \leq \rho < \rho_{i+1} \quad (0 \leq i \leq n), \tag{3.9}$$

where n is the number of the pieces used to parameterize a EOS at high-density, ρ_i is the rest-mass density at the boundary of two neighbouring $(i-1)$-th and i-th pieces, K_i is the polytropic constant for the i-th piece, and Γ_i is the adiabatic index for the i-th piece. Here, $\rho_0 = 0$, ρ_1 denotes a nuclear density evaluated in eq. (3.2), and $\rho_{n+1} \to \infty$. Other parameters (ρ_i; K_i; Γ_i) are determined by fitting with a nuclear-theory-based EOS.

Requiring the continuity of the pressure at each ρ_i, $2n$ free parameters, say $(K_i; \Gamma_i)$, determine the EOS completely.

Hotokezaka et al. [166] showed the free parameters the free parameters can be determined the following way: First, the EOS below the nuclear density ρ_1 is fixed by the parameters $\Gamma_0 = 1.35692395$ and $K_0/c^2 = 3.99873692 \times 10^{-8}$ $(\mathrm{g/cm}^3)^{1-\Gamma_0}$. The EOS for the nuclear matter was determined in [127] as follows: ρ_2 was fixed to be $\rho_2 \simeq 5.012 \times 10^{14}$ g/cm^3, and p_2 at $\rho = \rho_2$ was chosen as a free parameter. The reason is that p_2 is closely related to the radius and deformability of neutron stars [126]. Namely, p_2 primarily determines the stiffness of an EOS. Second, ρ_3 was fixed to be $\rho_3 \simeq \times 10^{15}$ g/cm^3. With these choices, the set of free parameters becomes $(p_2; \Gamma_1; \Gamma_2; \Gamma_3)$. These four parameters are determined by a fitting procedure (cf. [127]). With the given set of values $(\rho_1; K_1; \Gamma_1; p_2)$ are subsequently determined by

$$K_1 = p_2 \rho_2^{-\Gamma_1} \quad \text{and} \quad \rho_1 = (K_0/K_1)^{1/(\Gamma_1 - \Gamma_0)}. \tag{3.10}$$

By the same method, K_2 and K_3 are determined from

$$K_2 \rho_2^{\Gamma_2} = K_1 \rho_2^{\Gamma_1}; \quad K_3 \rho_3^{\Gamma_3} = K_2 \rho_3^{\Gamma_2}. \tag{3.11}$$

3.2.3 Hybrid EOS for heating and cooling processes

One of the most serious drawbacks of the polytropic EOS is that, although (3.3) is a good approximation for a ‘cold’ star, there are extremely energetic processes, like the merger of stars or accretion from a disk, which can increase enormously the temperature and a simple polytrope will not provide a physical description. A more realistic EOS in closed form can be obtained by a combination of the polytripic EOS to describe the cold part and an ideal EOS for the thermal one, allowing for fluid heating due to shocks. Thy hybrid EOS is given by

$$p = K\rho^\Gamma + (\Gamma_{\mathrm{th}} - 1)\rho\epsilon_{\mathrm{th}} \tag{3.12}$$

with an adiabatic thermal index Γ_{th} that can be different from the adiabatic cold index Γ. The internal energy can be split into a thermal and a cold part,

$$\epsilon = \epsilon_{\mathrm{th}} + \epsilon_{\mathrm{cold}}. \tag{3.13}$$

The total internal energy density ϵ can be obtained from the evolution of the conserved quantities, whilst the cold part is described by (3.4), leading to the explicit expression

$$p = K\frac{\Gamma - \Gamma_{\mathrm{th}}}{\Gamma - 1}\rho^\Gamma + (\Gamma_{\mathrm{th}} - 1)\rho\epsilon_{\mathrm{th}}. \tag{3.14}$$

It is possible to extend this approach by using a collection of continous piecewise-polytropes (3.9) in hybrid EOSs, which in turn allows an accurate match with any tabulated nuclear-theory-based EOSs at high density.

3.3 Stress–energy tensor and equations of thermal evolution

The general-relativistic hydrodynamic equations for a generic fluid involve the equations of motion that are given by the conservation of rest mass and by the conservation of energy and momentum:

$$\nabla_\mu J^\mu = 0, \tag{3.15}$$

$$\nabla_\mu T^{\mu\nu} = 0, \tag{3.16}$$

respectively, and the second law of thermodynamics

$$\nabla_\mu S^\mu \geq 0 \tag{3.17}$$

that are relativistically consistent. Although the perfect-fluid approximation disregards scenarios when dissipation and energy fluxes are present, it works well for most fluids under generic conditions. However, it loses its validity when thermodynamic (i.e microscopic) time-scales are comparable to the dynamic (i.e. macroscopic) ones and thus when assumption of local thermodynamic equilibrium breaks down. The requisite extension of perfect-fluid description that accounts for dissipative terms and energy fluxes is non-perfect fluid. In general, one can assume the rest-mass density current and stress–energy tensor as the linear combination of two contributions:

$$J^\mu = J^\mu_{\text{PF}} + J^\mu_{\text{NPF}}, \quad T^{\mu\nu} = T^{\mu\nu}_{\text{PF}} + T^{\mu\nu}_{\text{NPF}}, \tag{3.18}$$

where the indices "PF" and "NPF" refer to the perfect and non-perfect fluid contributions, respectively.

3.3.1 Stress–energy tensor for perfect fluids

For a system which consists of perfect fluid with total-energy density ϵ, isotropic pressure p and covariant metric elements $g_{\mu\nu}$ corresponding to the antecedent line element (4.24), one shall have

$$J^{\text{PF}}_\mu = \rho u_\mu, \quad T^{\text{PF}}_{\mu\nu} = (\epsilon + p) u_\mu u_\nu - p g_{\mu\nu}, \tag{3.19}$$

where the spatial components of fluid four-velocity u_μ are zeros. Normalized to $u^\mu u_\mu = 1$, it becomes

$$u_\mu = (e^{\nu/2},\ 0,\ 0,\ 0). \tag{3.20}$$

By construction, the quantity ϵ introduced above in eq. (3.19) represents the total-energy density of the fluid, given by

$$\epsilon = \rho(1 + \varepsilon), \tag{3.21}$$

which consists of both the rest-mass density of the fluid ρ and the specific internal-energy density ε, internal-energy density per unit rest mass or which in this case represents the thermal motion of the constituent fluid particles. [167, p. 98] Finally, the specific enthalpy h is defined by

$$h = \frac{p + \epsilon}{\rho} = 1 + \varepsilon + \frac{p}{\rho}. \tag{3.22}$$

Now, recognizing that in a non-relativistic regime $\varepsilon \ll c^2$ (i.e., the energy density of the fluid is essentially given by the rest-mass density) and $p/\rho \ll c^2$ (i.e., the pressure contribution to the energy density is negligible), the Newtonian limit of the specific enthalpy is given by

$$h = 1 + \varepsilon + \frac{p}{\rho} \to 1. \tag{3.23}$$

Note that there are two natural ways to define four-velocity u^μ. One option, given by Eckart, uses a unit timelike vector $\boldsymbol{u}_{\text{N}}$ parallel to $\boldsymbol{J}$, whereas the other, suggested by

Landau, defines a unit timelike vector $\boldsymbol{u}_{\rm E}$ parallel to $\boldsymbol{T} \cdot \boldsymbol{u}_{\rm E}$. However, these two vectors are identical for a perfect fluid and parallel to entropy current $\boldsymbol{S}$. The (maximum) entropy principle (3.17) implies a strict equality for perfect fluids, whose entropy current is then given simply as $S^\mu = s\rho u^\mu$. However, for relation (3.17) to be strictly non-zero, the entropy current must have an additional contribution from dissipative parts (first-order theories) with non-zero divergence such that

$$S^\mu = s\rho u^\mu + Q^\mu/T, \tag{3.24}$$

where the temperature T, deduced from the first law of thermodynamics, is given by

$$T = \frac{1}{\rho}\left(\frac{\partial \epsilon}{\partial s}\right)_\rho \tag{3.25}$$

and $[Q^\mu] = [0, \vec{Q}]$ are the components of the heat-flux four-vector (3.32) that describes the rate of energy flow per unit area along each spatial coordinate axis within the Eckart frame.

3.3.2 Stress–energy tensor for dissipative fluids

Neutrino emission processes are supposed to be the main sources of energy loss in the stellar core in the later stages of stellar evolution. For this reason, the equations of relativistic fluid dynamics to describe energy–momentum conservation are written as

$$T^{\alpha\beta}_{;\beta} = -Q_\nu u^\alpha, \tag{3.26}$$

where Q_ν is the total neutrino emissivity of all processes outlined in Table 3.2, and $T^{\alpha\beta}$ is the full stress–energy tensor for dissipative fluids. It is possible to write the dissipative contributions $T^{\mu\nu}_{\rm NPF}$ to the full stress–energy tensor as the sum of a viscous stress tensor $T^{\alpha\beta}_{\rm visc}$ and a heat-flow tensor $T^{\alpha\beta}_{\rm heat}$ that accounts for the generation of energy fluxes. Therefore, the full stress–energy tensor can be further decomposed into the form of

$$T^{\alpha\beta} = T^{\alpha\beta}_{\rm PF} + T^{\alpha\beta}_{\rm visc} + T^{\alpha\beta}_{\rm heat}, \tag{3.27}$$

where

$$\begin{aligned} T^{\alpha\beta}_{\rm PF} &= (\epsilon + p)u^\alpha u^\beta + p h^{\alpha\beta}, \\ T^{\alpha\beta}_{\rm heat} &= Q^\alpha u^\beta + Q^\beta u^\alpha, \\ T^{\alpha\beta}_{\rm visc} &= -\zeta\Theta h^{\alpha\beta} - 2\eta\sigma^{\alpha\beta} \end{aligned} \tag{3.28}$$

are the perfect fluid, heat-flux and viscosity stress–energy tensors, respectively. [168] Note that despite its causality and stability problems [169], the above description of stress–energy tensor has been widely used in Eckart's theory of relativistic irreversible thermodynamics [170]. The p and ϵ are the isotropic pressure and energy density, appearing in eq. (3.1), as measured by a comoving observer with velocity u^α which satisfies $u^\alpha u_\alpha = 1$ with $u^0 > 0$, and

$$h^{\alpha\beta} = g^{\alpha\beta} + u^\alpha u^\beta \tag{3.29}$$

is the standard projection tensor onto 3-space normal to flow. The symmetric trace-free spatial shear tensor is defined as

$$\sigma^{\alpha\beta} = \frac{1}{2}\left(u^\alpha_{;\mu} h^{\mu\beta} + u^\beta_{;\mu} h^{\mu\alpha}\right) - \frac{1}{3}\Theta h^{\alpha\beta} \tag{3.30}$$

and expansion scalar (or dilatation rate)

$$\Theta = u^{\alpha}_{;\alpha} \tag{3.31}$$

is associated with the convergence (or divergence) of the fluid world lines. The heat-flux density in eqs. (3.26–3.28) written as

$$Q^{\alpha} = -\kappa h^{\alpha\beta}\left(T_{,\beta} - T a_{\beta}\right) \tag{3.32}$$

is a spacelike vector, $Q^{\alpha}u_{\alpha} = 0$, which describes the flow of thermal energy per unit of area along spatial coordinate axis x^{α} per unit of time. The first term in eq. (3.32) corresponds to the non-relativistic Fourier's law of heat conduction, the second term takes into account the relativistic effect of isothermal heat flux due to the inertia of energy with $a_{\beta} = u^{\gamma}u_{\beta;\gamma}$ being the acceleration of fluid. The negative sign indicates that heat flows from higher to lower temperature regions.

In eqs. (3.28) and (3.32), η, ζ, and κ are collectively called transport coefficients (or dissipation coefficients). The bulk viscosity coefficient ζ defines the resistance of the medium to gradual uniform compression or expansion; and κ is non-negative and accounts for the thermal conductivity, respectively. [167] The shear (also called as 'common' or 'dynamic') viscosity coefficient η describes the fluid's resistance to gradual shear deformation and it is assumed to be equal to the electron shear viscosity η_e in the stellar core. The shear viscosity of neutrons and of protons (which is even smaller cf. [171]) can be neglected for the reason that it depends strongly on the nuclear interaction model and the many-body theory. [151]

3.3.3 Equations of thermal evolution of neutron stars

The thermal balance equation for a pulsating neutron star will be derived taking into account three dissipation mechanisms: the shear viscosity in the core, the non-equilibrium beta-processes in the core and heat conduction. The internal structure of neutron stars can be regarded as temperature-independent. After thermal relaxation, the redshifted temperature $\tilde{T}(t) \equiv T(r,t)e^{\nu/2}$ becomes constant throughout the interior. The relativistic equations of thermal evolution include the flux and energy equations [172]:

$$\begin{aligned} \frac{L_r}{4\pi r^2} &= -\kappa\sqrt{1-\frac{2m}{r}}\,e^{\nu/2}\frac{\partial}{\partial r}(Te^{\nu/2}), \\ \frac{1}{4\pi r^2 e^{\nu}}\sqrt{1-\frac{2m}{r}}\frac{\partial}{\partial r}(L_r e^{\nu}) &= -Q_{\nu} - \frac{C_v}{e^{\nu/2}}\frac{\partial T}{\partial t}, \end{aligned} \tag{3.33}$$

where the gravitational mass $m(r)$ and the metric function $\nu(r)$ are determined by the equilibrium stellar model (3.37). C_v is the specific heat capacity, κ is the thermal conductivity, T is the local temperature. The first equation is the general relativistic definition of the local photon luminosity L_r, due to the non-neutrino heat flux Q_{γ} transported through a sphere of radius r. The second equation expresses how the photon luminosity varies with the neutrino emissivity Q_{ν}.

Process	**Reaction**	**Heat flux** [erg cm^{-3}s^{-1}]	**Local luminosity** [erg s^{-1}]
Direct Urca	$n \to p + e + \bar{\nu}_e$ $p + e \to n + \nu_e$	$Q \sim 3 \times 10^{27} T_9^8$	$L_\nu \sim 10^{46} T_9^8$
Modified Urca	$n + N \to p + e + N + \bar{\nu}_e$ $p + e + N \to n + e + N + \nu_e$	$Q \sim 10^{20-22} T_9^8$	$L_\nu \sim 10^{38-40} T_9^8$
Bresmmstrahlung	$N + N \to N + N + \nu + \bar{\nu}$	$Q \sim 10^{18-20} T_9^8$	$L_\nu \sim 10^{36-38} T_9^8$

Table 3.2: Possible mechanisms of neutron star cooling by various neutrino-emission processes due to nucleon-nucleon collisions assumed to take part in the core. The modified Urca process has the neutron and the proton branch, each including a direct and an inverse where $N = n$ or p, respectively. (Original table, courtesy of Y. Lim. [173])

3.4 Equilibrium stellar model and quasistatic approximation

Let us consider a static spherically symmetric star, described by the Schwarzschild metric

$$ds^2 = e^\nu dt^2 - e^\lambda dr^2 - r^2 d\Omega^2, \tag{3.34}$$

where t and r are the time and radial coordinates, $d\Omega$ is a solid angle element in a spherical frame with the origin at the stellar centre and

$$\nu = \nu(t, r), \quad \lambda = \lambda(t, r) \tag{3.35}$$

are the metric functions which depend only on the temporal and radial coordinates $(t,\, r)$. The later function is often replaced by the expression

$$e^\lambda = (1 - 2m/r)^{-1}, \tag{3.36}$$

where the m is the gravitational mass contained within the radius r. It is convenient to replace the physical variables for energy density ϵ and for isotropic pressure p by corresponding effective variables

$$\bar{\epsilon} = \epsilon + (T_1^{\mathrm{NPF}})^0{}_0, \quad \bar{p} = p - (T_1^{\mathrm{NPF}})^1{}_1 \tag{3.37}$$

that incorporate time-dependent dissipative contributions of the stress–energy tensor (3.28). So that Einstein field equations

$$G^\nu{}_\mu = 8\pi T^\nu{}_\mu, \tag{3.38}$$

upon satisfying the metric (3.34), provide five PDEs for each of the non-vanishing mixed-variance components of the stress–energy tensor, of which the four distinct ones are

$$8\pi\bar{\epsilon} = e^{-\lambda}\left(\frac{\lambda'}{r} - \frac{1}{r^2}\right) + \frac{1}{r^2} \tag{3.39a}$$

$$8\pi\bar{p} = e^{-\lambda}\left(\frac{\nu'}{r} + \frac{1}{r^2}\right) - \frac{1}{r^2} \tag{3.39b}$$

$$8\pi\tilde{p} = e^{-\lambda}\left(\frac{\nu''}{2} - \frac{\lambda'\nu'}{4} + \frac{\nu'^2}{4} + \frac{\nu' - \lambda'}{2r}\right) + \frac{e^{-\nu}}{4}\left(2\ddot{\lambda} + \dot{\lambda}(\dot{\lambda} - \dot{\nu})\right) \tag{3.39c}$$

$$8\pi T^1_0 = e^{-\lambda}\dot{\lambda}/r, \tag{3.39d}$$

where $\tilde{p} = \bar{p} - {T_{\mathrm{NPF}}}^1_1 + {T_{\mathrm{NPF}}}^2_2$ and overdots and primes denote partial differentiation with respect to t and r, respectively. Another equation is proportional to (3.39c), thus it is needless to consider it separately. The effective variables ($\bar{\rho}$, $\bar{p}$) satisfy the same Einstein field equations in the quasi-static regime as the corresponding physical variables (ρ, p) that take account of the contribution of $T^{\mu\nu}_{\mathrm{NPF}}$ to p and ϵ in eq. (3.21). Therefore, the effective and physical variables share the same radial dependence. [174] Owing to the fact that (3.39a) involves only λ and ρ, it becomes

$$m' = 4\pi r^2 \rho, \tag{3.40}$$

once the new radial-dependent variable $m(r)$ from (3.36) has been introduced. Similarly,

$$\nu = \nu_0 + \int_0^R \frac{2(4\pi r^3 p + m)}{r(r-2m)} dr. \tag{3.41}$$

Suppose that the radius extends to R, from (3.40) it is evident that the integral of the effective rest-mass density over the stellar interior

$$m(R) = 4\pi \int_0^R \rho(r) r^2 dr \tag{3.42}$$

can be interpreted as the 'gravitational mass' of the system which includes all contributions to the relativistic mass (rest mass, internal energy, and the negative gravitational binding energy). However, integrating the total energy-density over the proper volume

$$dV_0 = \sqrt{\det(\gamma_{ij})} dx^3 = 4\pi e^{\lambda/2} r^2 dr, \tag{3.43}$$

where the curvature of 3-space has been taken account of through λ, one obtains the mass

$$\bar{m}(R) = 4\pi \int_0^R \rho(r) e^{\lambda/2} r^2 dr \tag{3.44}$$

that represents the sum of rest mass and internal energy. The difference between the two arises as a result of the mutual attraction of the fluid elements, called the binding energy, which is given by

$$E_B = \bar{m}(R) - m(R) > 0 \tag{3.45}$$

and exhibits the amount of energy required to disassemble a whole system into separate elements.

It is convenient not to use eq. (3.39c) directly, but instead substracting it from (3.39b). It can be replaced by the first-order ODE

$$\bar{p}' + \tfrac{1}{2}(\bar{\rho} + \bar{p})\nu' = \frac{2({T_{\mathrm{NPF}}}^1_1 - {T_{\mathrm{NPF}}}^2_2)}{r} + \frac{e^{-\nu}}{16\pi}\left(2\ddot{\lambda} + \dot{\lambda}(\dot{\lambda} - \dot{\nu})\right), \tag{3.46}$$

which stands for the condition for hydrostatic equilibrium, provided that the right-hand side of the equation is zero (cf. (3.59)). The first term on the right-hand side recovered from eq. (3.27) is simply the result of

$$(g_{11} T^{11}_{\mathrm{NPF}} - g_{22} T^{22}_{\mathrm{NPF}}) = \frac{1}{4}\eta e^{-\nu/2} r \dot{\lambda} \tag{3.47}$$

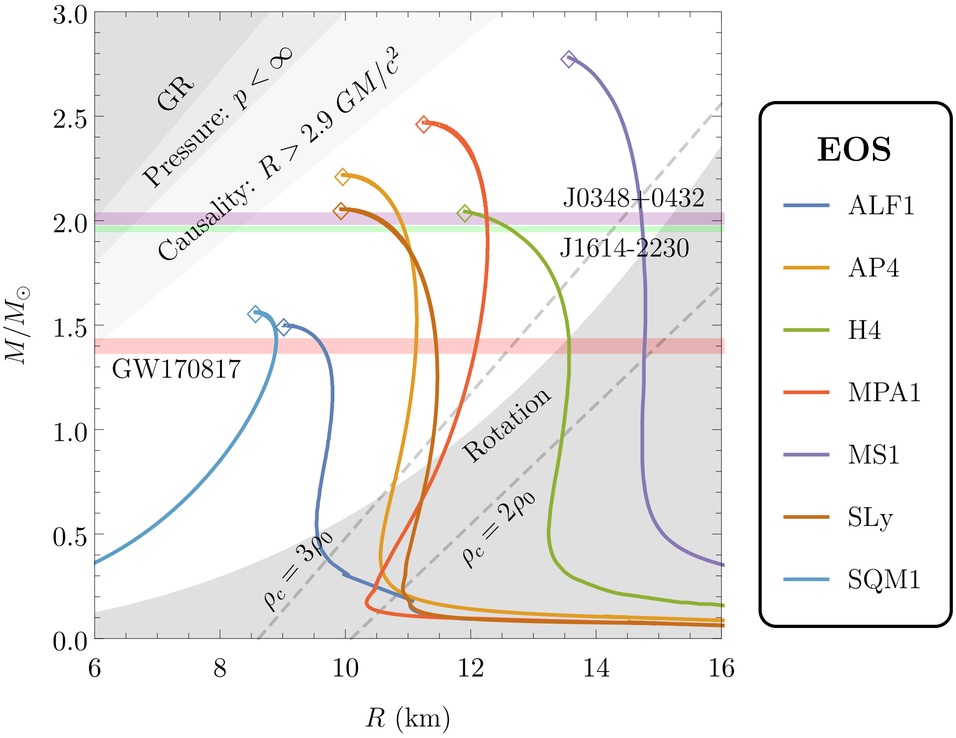

Figure 3.3: Typical M–R relations for non-spinning neutron-star models corresponding to the realistic EOSs displayed on p–n plane in Fig. 3.1. M–R curves for typical nucleonic EOSs (AP4, MPA1, MS1, SLy) are shown as light-coloured curves, blue curves refer to self-bound quark stars (ALF1, SQM1), and the green line to a strange star model (H4). The symbols $\diamond$ mark the maximal mass models. Most EOSs involving non-nucleonic matter, such as kaon condensates or hyperons, tend to predict an upper limit around $2.01 M_\odot$ for the maximal mass of neutron stars. The purple and the green bands indicate the rapidly rotating neutron stars in millisecond pulsars, catalogued as PSR J1614-2230 [128] and J0348+0432 [129], with the highest-known mass of $1.97 \pm 0.04\ M_\odot$ and $2.01 \pm 0.04\ M_\odot$, respectively. The light red band shows the interval of total binary NS masses inferred from gravitational-wave signal GW170817 (cf. Sec. 1.3.2). The dashed gray lines refer to stars whose central density ρ_c is double or triple of the nuclear saturation density ρ_0, respectively. The upper left areas of different shades of grayscale refer to regions of the M–R plane excluded by general relativity (GR) constraint for $R > 2GM/c^2$, by finite pressure for $R > 2.25GM/c^2$, and by causality for $R > 2.9GM/c^2$. The lower shaded area indicates the region bounded by the realistic mass-shedding limit $R/10\ \text{km} < \mathcal{C}^{2/3}(M/M_\odot)^{1/3}(f_K/1\ \text{kHz})$ for the highest-known Keplerian frequency, $f_K \simeq 716$ Hz, for the uniformly rotating neutron star PSR J1748-2446ad. The deviation of $\mathcal{C}$ from its Newtonian value of 1.838 depends, in GR, (as computed by [175]) on the neutron star interior mass distribution. For a hadronic EOS, $\mathcal{C} = 1.08$, whilst for a strange star with a crust, $\mathcal{C} \simeq 1.15$.

recovered from eq. (3.27). After the elimination of ν', one obtains the generalized Tolman–Oppenheimer–Volkoff (TOV) equation

$$\bar{p}' + \frac{(\bar{\rho} + \bar{p})(4\pi r^3 \bar{p} + m)}{r(r-2m)} = \frac{e^{-\nu}}{16\pi}\left(2\ddot{\lambda} + \dot{\lambda}(\dot{\lambda} - \dot{\nu} + 8\pi e^{\nu/2}\eta)\right) \tag{3.48}$$

for non-perfect fluids. Let us note that the non-zero terms on the left-hand side of eq. (3.48) are not contradictory to conservation of energy and momentum in (3.15–3.16). It will be shown that a set of two equations (3.59) takes over its role; one describing the hydrostatic equilibrium and another describing the perturbation-induced departure from the equilibrium configuration. When supplemented with an EOS (3.1), relating some fundamental thermodynamical quantities such as $\bar{\epsilon}$ and $\bar{p}$, eq. (3.48) completely determines the structure of spherically symmetric stars of isotropic material in equilibrium as shown in Fig. 3.3.

3.5 Infinitesimal radial oscillations

Let us suppose an equilibrium configuration of non-perfect fluid governed by the eqs. (3.39) is subject to a small linear perturbation that does not violate its spherical symmetry. Let δ hereafter denote a small ratio between the scale of variation of the perturbed variables and the correspondig ones in unperturbed configuration. Any quantity associated with the unperturbed equilibrium state is denoted by the subscript '0', whereas those that represent perturbations are equipped with the subscript '1'. In respect to such a perturbation, motions in the radial directions arise. While formulating the equations governing the perturbed state, I shall ignore all quantities which are of the second or higher orders in motions. Consequently, the four-velocity of a fluid element will be expressed as

$$u_\mu = (-e^{\nu_0/2},\, e^{\lambda_0 - \nu_0/2}\delta v_1,\, 0,\, 0), \tag{3.49}$$

where

$$\delta v_1 = dr/dt \tag{3.50}$$

is the radial velocity with respect to the time coordinate t.

3.5.1 Perturbation equations for stellar oscillations

One way to describe perturbations is the 'microscopic' point of view where the observer follows individual fluid particles as they move through space and time. [176] It is convenient to introduce a displacement field ξ_1 (in our case, a scalar field) in the Lagrangian representation defined by

$$\frac{\partial \xi_1}{\partial t} = v_1 + \frac{(T_1^{\mathrm{NPF}})^1_{\ 0}}{\bar{p}_0 + \bar{\epsilon}_0}, \tag{3.51}$$

which connects fluid elements in the equilibrium with corresponding ones in the perturbed configration. There is yet another, 'macroscopic' way of looking at the perturbations. [177] In the Eulerian representation of fluid motion, I simply consider changes in the variables (λ, ν, ϵ, p) at a fluid element fixed in space and time. [178] This means that

$$\lambda = \lambda_0 + \delta\lambda_1, \quad \nu = \nu_0 + \delta\nu_1, \quad \epsilon = \epsilon_0 + \delta\epsilon_1, \quad p = p_0 + \delta p_1, \tag{3.52}$$

where the linear perturbations ($\delta\lambda_1$, $\delta\nu_1, \delta\epsilon_1$, δp_1) are Euler changes. In this manner, I retain only those terms of the full stress–energy tensor (3.27) that do not involve second or higher orders in δ. The PF and NPF parts of the tensor assume the form of

$$(T_{\mathrm{PF}})^{\mu}_{\ \nu} = \begin{pmatrix} \epsilon_0 + \delta\epsilon_1 & (p_0 + \epsilon_0)\delta v_1 & 0 & 0 \\ -e^{\lambda_0 - \nu_0}(p_0 + \epsilon_0)\delta v_1 & -p_0 - \delta p_1 & 0 & 0 \\ 0 & 0 & -p_0 - \delta p_1 & 0 \\ 0 & 0 & 0 & -p_0 - \delta p_1 \end{pmatrix} \tag{3.53a}$$

$$(T_{\mathrm{NPF}})^{\mu}_{\ \nu} = \begin{pmatrix} \delta(T_1^{\mathrm{NPF}})^0_{\ 0} & (T_0^{\mathrm{NPF}})^1_{\ 0} + \delta(T_1^{\mathrm{NPF}})^1_{\ 0} & 0 & 0 \\ (T_0^{\mathrm{NPF}})^0_{\ 1} + \delta(T_1^{\mathrm{NPF}})^0_{\ 1} & \delta(T_1^{\mathrm{NPF}})^1_{\ 1} & 0 & 0 \\ 0 & 0 & \delta(T_1^{\mathrm{NPF}})^2_{\ 2} & 0 \\ 0 & 0 & 0 & \delta(T_1^{\mathrm{NPF}})^3_{\ 3} \end{pmatrix}, \tag{3.53b}$$

respectively. Notice that in eq. (3.53a), the off-diagonal elements are the only elements where the leading-order terms are absent, whereas in eq. (3.53b) the leading-order terms are present only in these very same elements (cf. Appendix). In view of the above, field equations (3.39a) and (3.39b) hold true if the pair of static metric potentials (λ_0, ν_0) is replaced by (λ, ν). The corresponding linearized equations governing the perturbations are, thus,

$$\frac{\partial}{\partial r}\left(re^{-\lambda_0}\delta\lambda_1\right) = -8\pi r^2 \delta\bar{\epsilon}_1 \tag{3.54}$$

and

$$\frac{\partial}{\partial r}\delta\nu_1 + \frac{\mathrm{d}\nu_0}{\mathrm{d}r}\delta\lambda_1 = \delta\lambda_1 - 8\pi e^{\lambda_0} r^3 \delta\bar{p}_1. \tag{3.55}$$

The appropriately linearized form of eqs. (3.39d) and (3.16), respectively,

$$\frac{\partial}{\partial t}\delta\lambda_1 = 8\pi e^{\lambda_0} r \left[(p_0 + \epsilon_0)\delta v_1 + \delta(T_1^{\mathrm{NPF}})^1_{\ 0}\right] \tag{3.56}$$

and

$$\begin{aligned} &p_0' + \tfrac{1}{2}(p_0 + \epsilon_0)\nu_0' + e^{\lambda_0 - \nu_0}(p_0 + \epsilon_0)\delta\dot{v}_1 + (\delta p_1 - \delta(T_1^{\mathrm{NPF}})^1_{\ 1})' + \tfrac{1}{2}(p_0 + \epsilon_0)\delta\nu_1' \\ &+\tfrac{1}{2}\left(\delta p_1 + \delta\epsilon_1 + \delta(T_1^{\mathrm{NPF}})^0_{\ 0} - \delta(T_1^{\mathrm{NPF}})^1_{\ 1}\right)\nu_0' - \tfrac{1}{2}(T_0^{\mathrm{NPF}})^0_{\ 1}(\delta\dot{\lambda}_1 + \delta\dot{\nu}_1) \\ &-\delta(\dot{T}_1^{\mathrm{NPF}})^0_{\ 1} + (\delta(T_1^{\mathrm{NPF}})^2_{\ 2} + \delta(T_1^{\mathrm{NPF}})^3_{\ 3} - 2\delta(T_1^{\mathrm{NPF}})^1_{\ 1})/r = 0 \end{aligned} \tag{3.57}$$

shall serve in place of the remaining two field equations. At this point one may recall the definitions (3.37) for the effective variables ($\bar{\epsilon}$, $\bar{p}$) and introduce their respective linearized forms ($\bar{\epsilon}_0 + \delta\bar{\epsilon}_1$, $\bar{p}_0 + \delta\bar{p}_1$). Eqs. (3.52–3.53) enable us to identify these new variables easily:

$$\begin{aligned} \bar{\epsilon}_0 &= \epsilon_0, \quad & \bar{\epsilon}_1 &= \epsilon_1 + (T_1^{\mathrm{NPF}})^0_{\ 0} \\ \bar{p}_0 &= p_0, \quad & \bar{p}_1 &= p_1 - (T_1^{\mathrm{NPF}})^1_{\ 1}. \end{aligned} \tag{3.58}$$

Consequently, expressed in these more suitable variables, eq. (3.57) decomposes into a set of two equations

$$\bar{p}_0' + \frac{\bar{p}_0 + \bar{\epsilon}_0}{2}\nu_0' = 0, \quad (\bar{p}_0 + \bar{\epsilon}_0)\left(e^{\lambda_0 - \nu_0}\dot{v}_1 + \frac{\nu_1'}{2}\right) + \bar{p}_1' + \frac{\bar{p}_1 + \bar{\epsilon}_1}{2}\nu_0' = \mathcal{T}, \tag{3.59}$$

where the first equation assumes the role of the constraint (3.48) for hydrostatic equilibrium while the second one governs the dynamics of perturbation-induced departure from the equilibrium configuration. As will be shown later on in Sec. 3.6, fluctuations of the stellar radius exhibit oscillatory behaviour: expansions and contractions in the outer layers as a star pursues to maintain equilibrium. The remaining NPF contributions are gathered on the right-hand side to form the source term

$$\mathcal{T} = \frac{1}{2}(T_0^{\mathrm{NPF}})^0{}_1(\dot{\lambda}_1 + \dot{\nu}_1) + (\dot{T}_1^{\mathrm{NPF}})^0{}_1 - \frac{(T_1^{\mathrm{NPF}})^2{}_2 + (T_1^{\mathrm{NPF}})^3{}_3 - 2(T_1^{\mathrm{NPF}})^1{}_1}{r}, \tag{3.60}$$

which stems from frictional forces in the fluid itself. As such, it is responsible for exponential growth or damping, depending on the friction coefficient.

Now, in the sense of the definition (3.51), the integration of eq. (3.56) yields

$$\frac{e^{-\lambda_0}}{r}\delta\lambda_1 = 8\pi(\bar{p}_0 + \bar{\epsilon}_0)\delta\xi_1 \tag{3.61}$$

or in consideration of the first eq. of (3.59),

$$\delta\lambda_1 = \delta\xi_1 \frac{\mathrm{d}}{\mathrm{d}r}(\lambda_0 + \nu_0). \tag{3.62}$$

Eqs. (3.54) and (3.61) provide

$$\delta\bar{\epsilon}_1 = -\delta\xi_1\frac{\mathrm{d}\bar{\epsilon}_0}{\mathrm{d}r} - \delta\xi_1\frac{\mathrm{d}\bar{p}_0}{\mathrm{d}r} - \frac{1}{r^2}\frac{\partial(r^2\delta\xi_1)}{\partial r}(\bar{p}_0 + \bar{\epsilon}_0). \tag{3.63}$$

Substituting for $d\bar{p}_0/dr$ in the last equation from the first eq. of (3.59), one may also write

$$\delta\bar{\epsilon}_1 = -\delta\xi_1\frac{\mathrm{d}\bar{\epsilon}_0}{\mathrm{d}r} - \frac{e^{\lambda_0/2}}{r^2}\frac{\partial(r^2 e^{-\lambda_0/2}\delta\xi_1)}{\partial r}(\bar{p}_0 + \bar{\epsilon}_0). \tag{3.64}$$

Considering next equation (3.55) and substituting for $\delta\lambda_1$ in accordance with eq. (3.61), one obtains

$$\frac{e^{-\lambda_0}}{r}\frac{\partial}{\partial r}\delta\nu_1 = 8\pi\left[\delta\bar{p}_1 + (\bar{p}_0 + \bar{\epsilon}_0)\left(\frac{\mathrm{d}\nu_0}{\mathrm{d}r} + \frac{1}{r}\right)\delta\xi_1\right] \tag{3.65}$$

or in view of the first eq. of (3.59),

$$(\bar{p}_0 + \bar{\epsilon}_0)\frac{\partial}{\partial r}\delta\nu_1 = \left[\delta\bar{p}_1 + (\bar{p}_0 + \bar{\epsilon}_0)\left(\frac{\mathrm{d}\nu_0}{\mathrm{d}r} + \frac{1}{r}\right)\delta\xi_1\right]\frac{\mathrm{d}}{\mathrm{d}r}(\lambda_0 + \nu_0). \tag{3.66}$$

3.5.2 Damping of stellar oscillations

Suppose that for normal modes of the fluid perturbations ($\delta\lambda_1$, $\delta\nu_1$, $\delta\bar{\epsilon}_1$, $\delta\bar{p}_1$) possess a harmonic time-dependence of the form $\exp(i\Omega t)$ where

$$i\Omega = -1/\tau + i\omega_d \tag{3.67}$$

is a complex characteristic frequency to be determined in Sec. 3.6. Being subject to the damping effect of the dissipative forces, the fluid perturbations oscillate with a damped angular frequency (sometimes called pseudo-frequency)

$$\omega_d = \omega_n\sqrt{1-\zeta^2}, \tag{3.68}$$

related to ω_n which is the natural frequency (or resonant frequency) of the undamped system. The rate at which the normal modes of radial oscillations are damped is characterized by the relaxation time (or damping time)

$$\tau = -1/\omega_n\zeta \tag{3.69}$$

and can be determined from energy-dissipation eq. (3.102). [133] Expressed by the damping ratio ζ, a dimensionless non-negative parameter, the complex characteristic frequency is

$$i\Omega = -\omega_n(\zeta - i\sqrt{1-\zeta^2}). \tag{3.70}$$

The value of ζ prescribes the frequency response and critically determines the dynamical behaviour. The oscillation is undamped ($\zeta = 0$), if the star oscillates with its natural angular frequency ω_n. It is underdamped ($\zeta < 1$) if the star oscillates with a damped frequency ω_d and with the amplitude gradually decreasing with the rate of decay $1/\tau$. It is critically damped ($\zeta = 1$) if the star returns to steady state as quickly as possible without any oscillation.

With the harmonic time-dependence, one may rewrite the second equation of (3.59) in the form

$$\Omega^2 e^{\lambda_0-\nu_0}(\bar{p}_0+\bar{\epsilon}_0)\xi_1 = \bar{p}_1' + \left(\frac{\lambda_0'}{2}+\nu_0'\right) + \frac{\bar{\epsilon}_1\nu_0'}{2} - \frac{\bar{p}_0+\bar{\epsilon}_0}{2}\left(\nu_0'+\frac{1}{r}\right)(\lambda_0'+\nu_0')\xi_1 + i\Omega\mathcal{S}_1, \tag{3.71}$$

where, in accordance with eq. (3.66), $(\bar{p}_0+\bar{\epsilon}_0)\nu_1'$ was substituted for. Also, one may recall that $\bar{\epsilon}_1$ is expressed in terms of ξ_1 and the perturbed variables by eq. (3.63). The additional term $\mathcal{S}_1$ is given by the expression (A.6).

3.5.3 The conservation of baryon number

The continuity equation (3.15) of the rest-mass-density current given as in (3.19) involves the conservation of the baryon number, represented by the condition

$$\nabla_\mu(Nu^\mu) = 0, \tag{3.72}$$

provided that N is the number of constituent baryons per unit volume. Let the covariant derivative be written differently, in the form

$$\frac{\partial}{\partial x^\mu}(Nu^\mu) + (Nu^\mu)\frac{\partial}{\partial x^\mu}\log\sqrt{-g} = 0 \tag{3.73}$$

with the expression $\partial(\log\sqrt{-g})/\partial x^\mu$ being put in the place of the Christoffel symbols corresponding to the metric given in eq. (3.34) and

$$g = e^{\lambda+\nu}r^4\sin^2\theta \tag{3.74}$$

being the determinant of the metric tensor. In the framework of the present linearized theory, it is quite reasonable to define the baryon number by

$$N = N_0 + \delta N_1, \tag{3.75}$$

so that eq. (3.73) endowed with the non-vanishing components of the four-velocity (3.49) emerges as

$$e^{-\nu_0/2}\frac{\partial}{\partial t}\delta N_1+\frac{1}{r^2}\frac{\partial}{\partial r}\left(N_0 r^2 e^{-\nu_0/2}\delta v_1\right)+\frac{1}{2}N_0 e^{-\nu_0/2}\left(\frac{\partial}{\partial t}\delta\lambda_1+\delta v_1\frac{\mathrm{d}}{\mathrm{d}r}(\lambda_0+\nu_0)\right)=0. \tag{3.76}$$

With v_1 replaced by the Lagrangian displacement ξ_1 defined in eq. (3.51), the last equation brings about fluctuations in the baryon number:

$$\delta N_1+\frac{e^{\nu_0/2}}{r^2}\frac{\partial}{\partial r}\left(N_0 r^2 e^{-\nu_0/2}\delta\xi_1\right)+\frac{1}{2}N_0\left(\delta\lambda_1+\delta\xi_1\frac{\mathrm{d}}{\mathrm{d}r}(\lambda_0+\nu_0)\right)=i\Omega^{-1}\mathcal{N}, \tag{3.77}$$

where the second term on the right-hand side vanishes on account of eq. (3.62) and

$$\mathcal{N}=\frac{1}{r^2}e^{\lambda_0+2\nu_0}\frac{\partial}{\partial r}\left(r^2 e^{-(\lambda_0+2\nu_0)/2}N_0\frac{(T_1^{\mathrm{NPF}})^1_{\;0}}{\bar{p}_0+\bar{\epsilon}_0}\right) \tag{3.78}$$

represents the effect of dissipative terms on the baryon-number perturbation. Subsequently, eq. (3.77) reduced significantly and one obtains

$$\delta N_1=-\frac{\mathrm{d}N_0}{\mathrm{d}r}\delta\xi_1-N_0\frac{e^{\nu_0}}{r^2}\frac{\partial}{\partial r}\left(r^2 e^{-\nu_0}\delta\xi_1\right)-i\Omega^{-1}\mathcal{N}. \tag{3.79}$$

Provided that $N\equiv N(\epsilon,\,p)$ is an EOS that corresponds to (3.1), small linear perturbations in the energy density or pressure treated as variation are expected to induce baryon-number perturbations given by

$$\delta\bar{N}_1=\frac{\partial\bar{N}_1}{\partial\bar{\epsilon}_1}\delta\bar{\epsilon}_1+\frac{\partial\bar{N}_1}{\partial\bar{p}_1}\delta\bar{p}_1, \tag{3.80}$$

which in turn yields

$$\delta\bar{p}_1=\left(\frac{\partial\bar{N}_0}{\partial\bar{p}_0}\right)^{-1}\left(\delta\bar{N}_1-\frac{\partial\bar{N}_0}{\partial\bar{\epsilon}_0}\delta\bar{\epsilon}_1\right), \tag{3.81}$$

under the assumption that variables in the perturbed state relate to each other roughly the same way as the corresponding variables in equilibrium, that is $\partial\bar{N}_1/\partial\bar{\epsilon}_1\approx\partial\bar{N}_0/\partial\bar{\epsilon}_0$ and $\partial\bar{N}_1/\partial\bar{p}_1\approx\partial\bar{N}_0/\partial\bar{p}_0$. With $\delta\bar{\epsilon}_1$ and $\delta\bar{N}_1$ given by eqs. (3.63) and (3.79), respectively, eq. (3.81) comes to be

$$\delta\bar{p}_1=-\frac{\mathrm{d}\bar{p}_0}{\mathrm{d}r}\delta\xi_1-\Gamma_1\bar{p}_0\frac{e^{\nu_0}}{r^2}\frac{\partial}{\partial r}\left(r^2 e^{-\nu_0/2}\delta\xi_1\right)-i\Omega^{-1}\left(\frac{\partial\bar{N}_0}{\partial\bar{p}_0}\right)^{-1}\mathcal{S}_2, \tag{3.82}$$

where the dimensionless parameter Γ_1, given by

$$\Gamma_1=\left(\bar{p}_0\frac{\partial\bar{N}_0}{\partial r}\right)^{-1}\left(\bar{N}_0-(\bar{p}_0+\bar{\epsilon}_0)\frac{\partial\bar{N}_0}{\partial\bar{\epsilon}_0}\right), \tag{3.83}$$

is identified with the adiabatic index (3.5) that characterize the stiffness of the EOS at a given density. The average value for the adiabatic index is determined by eq. (3.7) to be greater than or equal to 4/3 within a star that is dynamically stable against infinitesimal radial adiabatic perturbations.

3.6 The pulsation equation and eigenvalue problem

With elimination of $\bar{\epsilon}_1$ and $\bar{p}_1$ from eq. (3.71), through eqs. (3.63) and (3.82), eq. (3.71) may be written as

$$\begin{aligned}\Omega^2 e^{\lambda_0-\nu_0}(\bar{p}_0+\bar{\epsilon}_0)\xi_1 &= \frac{\mathrm{d}}{\mathrm{d}r}(\xi_1\bar{p}_0') - \left(\frac{1}{2}\lambda_0'+\nu_0'\right)\xi_1\bar{p}_0' - \frac{1}{2}(\bar{p}_0+\bar{\epsilon}_0)\left(\nu_0'+\frac{1}{r}\right)(\lambda_0'+\nu_0') \\ &+\frac{\nu_0'}{2r^2}\frac{\mathrm{d}}{\mathrm{d}r}\left[r^2(\bar{p}_0+\bar{\epsilon}_0)\xi_1\right] - e^{-(\lambda_0+2\nu_0)/2}\frac{\mathrm{d}}{\mathrm{d}r}\left[e^{(\lambda_0+3\nu_0)/2}\frac{\Gamma_1\bar{p}_0}{r^2}\frac{\mathrm{d}}{\mathrm{d}r}\left(r^2e^{-\nu_0/2}\xi_1\right)\right] + i(\Omega\mathcal{S}_1-\Omega^{-1}\mathcal{S}_2),\end{aligned} \tag{3.84}$$

where the third and forth terms on the right-hand side are the result of the transformation $\frac{\mathrm{d}f}{\mathrm{d}r}+f\frac{\mathrm{d}g}{\mathrm{d}r}=\exp(-g)\frac{\mathrm{d}}{\mathrm{d}r}\left[f\exp(g)\right]$, which applies to any two functions $(f,\, g)$ of the variable r and $\mathcal{S}_2$ is written out in eq. (A.8) in appendix.

Substituting for $\bar{p}_0'$ from the first eq. of (3.59) and applying the same transformation for the first two terms on the right-hand side of eq. (3.84) allow us to merge them with the next two terms in the expression

$$\frac{1}{2}(\bar{p}_0+\bar{\epsilon}_0)\left(\nu_0''-\frac{1}{2}\lambda_0'\nu_0'-\frac{1}{2}\lambda_0'-\frac{3}{r}\nu_0'\right)\xi_1, \tag{3.85}$$

which (cf. (56) in [137]), in turn, compared with the field equation (3.39c) restricted by equilibrium conditions,

$$8\pi\bar{p}_0 = e^{-\lambda}\left(\frac{\nu_0''}{2}-\frac{\lambda_0'\nu_0'}{4}+\frac{\nu_0'^2}{4}+\frac{\nu_0'-\lambda_0'}{2r}\right), \tag{3.86}$$

is reduced to three terms. Making use of the first eq. of (3.59) once again, the relation (3.84) appreciably reduces to give the pulsation equation

$$\begin{aligned}\Omega^2 e^{\lambda_0-\nu_0}(\bar{p}_0+\bar{\epsilon}_0)\xi_1 &= \left(\frac{4}{r}\frac{\mathrm{d}\bar{p}_0}{\mathrm{d}r}+8\pi e^{\lambda_0}\bar{p}_0(\bar{p}_0+\bar{\epsilon}_0)-\frac{1}{\bar{p}_0+\bar{\epsilon}_0}\left[\frac{\mathrm{d}\bar{p}_0}{\mathrm{d}r}\right]^2\right)\xi_1 \\ &-e^{-(\lambda_0+2\nu_0)/2}\frac{\mathrm{d}}{\mathrm{d}r}\left(e^{(\lambda_0+3\nu_0)/2}\frac{\Gamma_1\bar{p}_0}{r^2}\frac{\mathrm{d}}{\mathrm{d}r}\left[r^2e^{-\nu_0/2}\xi_1\right]\right)+i(\Omega\mathcal{S}_1-\Omega^{-1}\mathcal{S}_2)\end{aligned} \tag{3.87}$$

associated to the class of second-order linear ODEs. Besides this, the definitions (3.67–3.70) make possible the separation of real and imaginary parts of the complex frequency squared:

$$\Omega^2 = \omega_n^2(1-2\zeta^2)+2i\omega_n^2\zeta\sqrt{1-\zeta^2}, \tag{3.88}$$

thus the last term of the right-hand side:

$$i(\Omega\mathcal{S}_1-\Omega^{-1}\mathcal{S}_2) = -\zeta\left(\omega_n\mathcal{S}_1+\omega_n^{-1}\mathcal{S}_2\right)+i\sqrt{1-\zeta^2}\left(\omega_n\mathcal{S}_1-\omega_n^{-1}\mathcal{S}_2\right). \tag{3.89}$$

For positive Ω^2, the characteristic frequency Ω is real and thus, the solution is purely oscillatory. However, for $\Omega^2 < 0$, Ω contains an imaginary part, which corresponds to a damped solution. Since the general solution is a superposition of damped modes, the occurrence of a negative value of Ω^2 corresponds to a secular instability whose growth time is long compared to the dynamical time of radial oscillations. The Harrison–Zel'dovich–Novikov criterion [143] for static stability of compact stars states that the total mass of such stars increases with the central density ρ_0, which implies that $dM(\rho_0)/d\rho_0 \geq 0$ for the stable region where $M(\rho_0)$ is the function of total mass in terms of the central density. For neutron stars this will, indeed, happen for ρ_0 larger than the critical central density ρ_{crit} at which the stellar mass $M(\rho_0)$ as a function of ρ_0 has its maximum. In this case the star will ultimately collapse to a black hole. For $\rho_0 = \rho_{\text{crit}}$ there must be a neutral mode with the corresponding eigenvalue $\omega^2 = 0$. [165]

3.6.1 Eigenfrequencies of radial pulsation

The real part of left-hand side of eq. (3.87) can be equated to the real part of right-hand side, comparably to the imaginary parts. Intrinsically, one can recast it in the so-called homogeneous Sturm–Liouville form

$$\frac{\mathrm{d}}{\mathrm{d}r}\left[\mathcal{P}\frac{\mathrm{d}\chi}{\mathrm{d}r}\right] + \left[\mathcal{Q} + \Lambda_n\mathcal{R}\right]\chi = 0 \tag{3.90}$$

with a free parameter

$$\Lambda_n \equiv (1 - 2\zeta^2)\omega_n^2 \tag{3.91}$$

that denotes the eigenvalues and with a set of coefficient functions

$$\begin{aligned}
\mathcal{P}(r) &= r^{-2}e^{(\lambda_0+3\nu_0)/2}\Gamma_1\bar{p}_0\\
\mathcal{Q}(r) &= r^{-2}e^{(\lambda_0+3\nu_0)/2}\left[\left(\frac{\bar{p}_0'}{\bar{p}_0+\bar{\epsilon}_0} - \frac{4}{r}\right)\bar{p}_0' + 8\pi e^{(\lambda_0+3\nu_0)/2}\bar{p}_0(\bar{p}_0+\bar{\epsilon}_0)\right]\\
\mathcal{R}(r) &= r^{-2}e^{(3\lambda_0+\nu_0)/2}(\bar{p}_0+\bar{\epsilon}_0)
\end{aligned} \tag{3.92}$$

which hail from eq. (3.87), are specified at the outset. The function $\mathcal{R}(r)$ is referred to as weighting function. The normalized Lagrangian displacement defined by

$$\chi \equiv r^2 e^{-\nu_0}\xi_1 \tag{3.93}$$

is a scalar-valued function of the variables $(t,\, r)$. Provided that χ satisfies eq. (3.90), it is called a solution. Solutions of (3.90) are subject to the boundary conditions

$$\chi = 0 \text{ at } r = 0 \quad \text{and} \quad \delta p = 0 \text{ at } r = R. \tag{3.94}$$

Together with the boundary condition (3.94), the pulsation equation (3.90) imposes a Sturm–Liouville eigenvalue problem (SLEVP), which seeks non-trivial solutions only for a countable set of real eigenvalues $\{\Lambda_1, \Lambda_2, \ldots, \Lambda_n\}$. The SLEVP is said to be regular if $\mathcal{P} > 0$ and $\mathcal{R} > 0$ for any $r \in [0,\, R]$, the functions $(\mathcal{P},\, \mathcal{P}',\, \mathcal{Q},\, \mathcal{R},\, \mathcal{S})$ are continuous over the finite interval $[0,\, R]$, and the problem has separated boundary conditions of the form

$$\alpha_1\chi(0) + \alpha_2\chi'(0) = 0 \quad \text{for} \quad \alpha_1^2 + \alpha_2^2 > 0 \tag{3.95a}$$

$$\beta_1\chi(R) + \beta_2\chi'(R) = 0 \quad \text{for} \quad \beta_1^2 + \beta_2^2 > 0. \tag{3.95b}$$

The Sturm–Liouville theory states that the eigenvalues of the regular SLEVP are real and can be arranged in ascending order such that

$$\Lambda_1 < \Lambda_2 < \Lambda_3 < \ldots < \Lambda_n < \ldots \quad \text{where} \quad \lim_{n\to\infty}\Lambda_n = +\infty. \tag{3.96}$$

Corresponding to each eigenvalue Λ_n is a unique (up to a normalization constant) eigenfunction $\chi_n(r)$ which has exactly $n-1$ zeros in $(0,R)$. Moreover, the normalized eigenfunctions form an orthonormal basis

$$\int_R^0 \chi_n(r)\chi_m(r)\mathcal{R}(r)dr = \delta_{mn}, \tag{3.97}$$

where δ_{mn} is the Kronecker delta and to each Λ_n is associated with a single eigenfunction χ_n.

3.6.2 Characteristic relaxation time of radial pulsation

In the Newtonian limit, the kinetic energy contained in these oscillations is given by

$$E_k = \frac{1}{2}\int \rho\delta v_1 \delta v_1^* dV_0, \tag{3.98}$$

an integral over an element of proper volume of fluid dV_0 (cf. eq. (3.43)), where δv_1^* is the complex conjugate of the velocity perturbation δv_1. Associated with the radial displacement $\delta\xi_1 = \delta r/r$, the later is given for radial oscillations by eq. (3.51) as

$$\delta v_1 = i\Omega\left(\delta\xi_1 - \frac{\exp(-\nu_0/2)}{\bar{p}_0+\bar{\epsilon}_0}\left[3\eta\nu_0'\delta\nu_1 - \left(\eta - \frac{1}{4}\kappa T\right)\delta\nu_1'\right]\right), \tag{3.99}$$

where, in accordance with second expression of (A.2), $(\delta T_1^{\mathrm{NPF}})_0^1$ was substituted for. The total energy in an oscillating star consists of kinetic and potential energy which are supposed to equally contribute to the total energy of harmonic oscillations, thus given by $E = 2E_k$. On account of the density, ρ, is reasonably uniform in neutron stars [122], the total energy contained in the oscillation is given as

$$E = \bar{\rho}\omega_n\epsilon^2 R^5 \tag{3.100}$$

by evaluating the integral (3.98) explicitly for an average density $\bar{\rho} = 3M/4\pi R^3$. Being bilinear in the fluid perturbations, E has a time-dependence $\exp[-2\,\mathrm{Im}(\Omega)t]$. [133] Subsequently, its time derivative implies that

$$\frac{\mathrm{d}E}{\mathrm{d}t} = -2\,\mathrm{Im}(\Omega)E, \tag{3.101}$$

which together with the energy-dissipation rate for the stress–energy tensor (3.27) as

$$-\frac{\mathrm{d}E}{\mathrm{d}t} = -\int\left(2\eta\delta\sigma^{\mu\nu}\delta\sigma_{\mu\nu}^* + \zeta(\delta\Theta)^2 + \frac{\kappa}{T}\nabla_\mu\delta T\nabla^\mu\delta T^*\right)dV_0, \tag{3.102}$$

directly determines the dissipative time-scale of small perturbations of the fluid away from the equilibrium state as

$$\tau = -2E/\dot{E}. \tag{3.103}$$

An approximate formula for each dissipative time-scales can be given by evaluating the corresponding dissipation integral (3.102). Cutler & Lindblom [122] have found that the following propotionalities hold for the dissipative time-scales:

$$\frac{1}{\tau_\eta} \sim \frac{\eta}{\rho R^2}, \quad \frac{1}{\tau_\zeta} \sim \frac{\eta}{\rho R^2}, \quad \frac{1}{\tau_\kappa} \sim \frac{\kappa T}{\rho^2 R^4}, \tag{3.104}$$

which reveals that the time-scale of shear viscosity is much shorter than either that of bulk viscosity or thermal conductivity. The imaginary part of the pulsation equation (3.87), together with eqs. (3.88–3.89), yields

$$\zeta_n = \frac{\mathcal{S}_2 - \omega_n^2 \mathcal{S}_1}{2\omega_n^3 (\bar{p}_0 + \bar{\epsilon}_0)\xi_1} e^{\nu_0 - \lambda_0} \tag{3.105}$$

which implies that a unique damping ratio ζ_n corresponds to each eigenfrequency ω_n computed for undamped oscillations. From (3.105), it is evident that higher frequency components die out first. These damping ratios are identical with those associated with the dissipative time-scales (3.104) which, according with (3.69), are obtained from $\zeta_n = \tau_n \omega_n$.

3.7 Summary of dissipation-damped stellar oscillations

A generic formulation of the dynamical equations governing small adiabatic radial oscillations of pulsating relativistic stars has been proposed in this paper through a perturbation scheme that, combined with the equations of viscous thermally-conductive fluids, constitutes an extension of radially pulsating perfect-fluid stellar models. I have proved that, similarly to the regular perfect-fluid case, the stellar pulsation equation (3.87) expressed by a set of effective variables (3.37) which involve dissipative terms, can be recast in a homogenous Sturm–Liouville form (3.90) with separated boundary conditions (3.95). In contrast to the regular perfect-fluid case, the associated eigenvalue problem is generalized for a discrete set of eigenfunctions with complex eigenvalues where the real and imaginary parts of the eigenvalues represent the squared natural frequency and relaxation time (or decay rate) of the oscillation, respectively. In the absence of dissipation, the discrete spectrum consists of real eigenvalues that form a complete set.

The main novelty of this approach is the ability to directly relate the damping ratio of oscillations to the expressions $\mathcal{S}_1$ and $\mathcal{S}_2$ in (A.7–A.8), which stem from the viscous and heat-conductive contributions to the stress–energy tensor, without relying on explicit NR computations. An illustrative example set by [122] for neutron stars with uniform density, allowed us in this paper to estimate the rate at which the viscosity and thermal conductivity of the nuclear matter drains energy from the oscillations. In accordance with the literature, the time-scale of shear viscosity is much shorter than either that of bulk viscosity or thermal conductivity and the imaginary part of the pulsation equation indicate that higher components vanish first from the frequency spectrum. The usefulness of my analytical approximation method is evidently restricted to providing qualitative and ‘order-of-magnitude’ information about the dissipative time-scales in (3.104) rather than a precise one.

Chapter 4

Interaction of gravitational waves with matter

The present piece of research is the result of a comprehensive study that aimed at investigating the dispersion of gravitational waves in interstellar medium. It is dedicated to explore the dumping effect of GMC (Giant molecular cloud)s on GWs, and to provide a more accurate picture of expected waveforms for direct detection. Most papers – referring to the weak interaction – neglect the dispersive character of GWs in a medium as most of the estimates for detection are made under the assumption of GWs following null geodesics even in the presence of matter. The interaction is weak indeed, moreover even the densest nebulæ are extremely thin. Nonetheless, the currently detectable GWs are expected to be of extragalactic origin, their sources are likely to be obscured by dust or gas in addition to the Milky Way's stellar halo through which the gravitational waves have to pass on their way to our ground-based detectors. Following the discovery of a total of 11 confirmed GW transient events (cf. Sec. 1.3.2) during observation runs O1 and O2 (between 2015 and 2017), and a long list of candidate events during O3 in 2019, we witness a progressively dedicated search for new events from various astrophysical sources where the interaction may prove to be relevant.

4.1 Chasing waves and their dispersive nature for half a century

For half a century after Einstein predicted the existence of GWs in 1915, a thorough examination of their dispersive nature seemed to be inconvenient and pointless for the strong reasons above. In their pioneering 1966 papers [179, 180], Steven Hawking and Steven Weinberg investigated the rate at which GWs are damped by a dissipative fluid in the case of a Robertson–Walker background spacetime. They found that the amplitude of a high-frequency gravitational wave is damped in a characteristic time η^{-1}, where η is the fluid's shear viscosity. Although Isaacson [181] dealt with the high-frequency limit of GWs, this work has been of great importance and motivated numerous researches.

In the 1970s several authors (cf. [180, 182–192]) were engaged in studying the propagation of GWs through matter under various simplifying assumptions with different methods of approximations. Their primary concern was not the possible damping influence on the amplitude, but the modification of dispersion relation. The most commonly used two distinct models were a medium composed of deformable molecules with internal structure giving rise to anisotropic pressures or free particles with rare collisions described by kinetic theory. To describe the damping in kinetic theory, the rate of particle collisions has to be addressed giving rise to the imaginary part of the complex index of refraction. The refractive index turned out to be related to the viscosity response function in fluids and crystals. [193] Anile & Breuer provided a formalism for a more accurate description of the transfer equation [188] for polarized gravitational radiation in terms of the Stokes parameters. Anile & Pirronello obtained the transport equation for the amplitude of a GW in a dispersive medium using high-frequency approximation [190]. Additionally, the design of Weber bars and subsequent resonant-mass detectors was an engineering problem of considerable importance since they were thought to be sensitive enough to measure the metric deviations. This problem inspired many to focus on GW refraction in condensed matters. The behaviour of an elastic medium under the influence of GWs was derived firstly in a gauge-independent way in terms of relative strains, and secondly in terms of displacements [189]. However, some authors like Gayer & Kennel in the case of Landau damping reached contradictory conclusions, particularly with respect to the dispersion relation [191]. In the case of a parabolic Friedmann background, Sacchetti & Trevese showed that the presence of matter does not affect the GW propagation at low temperature in the geometrical-optics limit $\mathcal{O}(\eta)$, however a second-order WKB (Wentzel–Kramers–Brillouin) – so-called 'post-geometrical optics' – approximation revealed a plasmalike dispersion relation in the $\mathcal{O}(\eta^2)$, where η was a small parameter [192]. The geometrical-optics description in this chapter is based on that of Thorne who has shown [194] that in realistic astrophysical situations the vacuum approximation to wave propagation is appropriate. He specialized the geometrical-optics laws to propagation through vacuum for simplicity, but a propagation equation that describes the interaction of the waves with matter and with EM fields was also derived. Recently, a study [195] of perfect-fluid perturbations of Kantowski–Sachs models with a positive cosmological constant has concluded that in contrast with the Friedmann case, one of the two gravitational degrees of freedom is coupled to the matter density perturbations, and decouples only in the geometrical optics limit. There, the dynamics is encompassed in six evolution equations, representing forced oscillations and two uncoupled damped oscillator equations.

The most useful papers for the piece of research presentend in this chapter are a series of studies [196–198] published by Ehlers, Prasanna and Breuer either in collaboration or on their own. The first of these works which in some ways reviewed the results of [188], revealed two degenerate modes of polarization (one represented GWs, whereas another one described non-propagating density and vorticity perturbations) by the dispersion relation for small-wavelength, small-amplitude GWs propagating through an arbitrary background dust spacetime. The following paper [197] generalized the background to perfect fluids, through which one more mode for sound waves was identified; all modes, but the doubly degenerate zero-frequency matter mode exhibited propagation along the null geodesics of the background. The work was further extended by Prasanna [198] to include dissipative terms of shear and bulk viscosity in the stress–energy tensor. In order to avoid loss of generality, assumption on symmetry of background had never been initiated. Generality however also entails several disadvantages: due to the lack of specifically detailed background, alterations in the wave's amplitude and frequency cannot be determined. The procedure developed in [196–198] was generalized to curved backgrounds and is largely similar to that of Svítek's approach to the damping of GWs in dust cloud [199]. There the geodesic deviation equation stemmed from the periodic oscillations produced within the molecules by the incoming waves. The oscillations themselves produce GWs that were composed with the original waves propagating through the GMC from a distant source.

4.2 Equilibrium configuration of interstellar clouds

Let us consider an isolated interstellar nebula remote from any other matter, and assume that the hydrostatic pressure is balanced by the GMC's self-gravitation. As seen in eq. (3.42), the 'gravitational mass' of the nebula within a distance r from its centre is given by

$$m(r) = 4\pi \int_0^r r'^2 \rho(r') \mathrm{d}r', \tag{4.1}$$

where ρ denotes the rest-mass density. The most dense and heavy of among nebulae are the GMCs composed by mostly gas and some dust. The typical physical values of cold GMCs are listed in Table 4.1. For the sake of simplicity, assume that the considered medium consists only of cold neutral gas. In this case collisions between these low-energy particles are rare and weak, and have no significant effect on the system. Hence the medium of nebula can be realistically regarded to be composed of an ideal gas. Since the temperature is very small and nearly constant ($10-20$ K for a typical GMC), the polytropic EOS (3.3) reduces to a linear relation of pressure p and density ρ, given by

$$p = c_s^2 \rho. \tag{4.2}$$

As I stated after eq. (3.3), 'polytropic constant' K for the degenerated matter may be regarded as constant and it corresponds to c_s^2, the squared isothermal speed of sound (3.6) within the gaseous medium, and the adiabatic index Γ_1 corresponds to 1. On the basis of the isothermal EOS (4.2) and (4.1), the total mass of the GMC M_R is expressed by the average pressure $\bar{p}$. By the comparsion of these with a given radial pressure distribution $p(r)$, the value of average pressure can be written as

$$\bar{p} = \frac{R^3}{3} \int_0^R p(r) r^2 \mathrm{d}r. \tag{4.3}$$

It is important to state that the following criteria must be met for real physical systems:

Composition:	neutral H_2
Radius:	$R = 70$ pc
Constant temperature:	$T = 10$ K
Average density:	$\bar{\rho} = 3.3475 \times 10^{-15}$ kg/m^3
Radius:	$R = 70$ pc
Total mass:	$M = 0.5433 \times 10^{23}\ M_\odot$

Table 4.1: Typical physical properties of cold GMCs, based on K. Ferrière's results [200].

1. $M_\mathrm{R} \leq M_\mathrm{BE}$ where M_BE refers to the Bonnor–Ebert mass given by $M_\mathrm{BE} = c_\mathrm{BE} c_s^4 p^{-1/2}$, where $c_\mathrm{BE} \simeq 1.18$ is a dimensionless constant (cf. in [201]). This is the largest mass that an isothermal gas sphere embedded in a pressurized medium can have while still remaining in hydrostatic equilibrium.

2. $\rho(r)$, $p(r) > 0$ and $\mathrm{d}\rho/\mathrm{d}r$, $\mathrm{d}p/\mathrm{d}r < 0$ everywhere in the GMC, the maximum of the density and pressure are ρ_0 and p_0 in $r = 0$. On the border of the nebula, the density and pressure distributions must satisfy the boundary conditions

$$\lim_{r\to R} \rho(r) = \lim_{r\to R} p(r) = \lim_{r\to R} \frac{\mathrm{d}\rho}{\mathrm{d}r} = \lim_{r\to R} \frac{\mathrm{d}p}{\mathrm{d}r} = 0. \tag{4.4}$$

   These conditions can be easily justified: the first one expresses the simple fact that the density and pressure disappear, the second one says that they do not change on the border of the GMC. So the matter does not suddenly vanish on the border, but steadily aligns into the environment.

3. As seen in the causal requirement (3.6), the speed of sound c_s in the medium must be at most the speed of light, that is

$$c_s^2 = \frac{\mathrm{d}p}{\mathrm{d}\rho} \leq 1. \tag{4.5}$$

4.2.1 Field equations for the spherically symmetric static cloud

Let us recall the line element (4.24) for stationary spherically symmetric configurations given by

$$ds^2 = -e^{\nu}\mathrm{d}t^2 + e^{\lambda}\mathrm{d}r^2 + r^2(d\vartheta^2 + \sin^2\vartheta \mathrm{d}\varphi^2), \tag{4.6}$$

where the metric functions ν and λ were defined by (3.35). Let us consider a remote and isolated GMC in a region of spacetime of metric tensor (4.6) which is filled with cold perfect fluid. The perfect fluid that constitutes the GMC is described by the stress–energy tensor $T^{\alpha\beta}_{\mathrm{PF}}$ from (3.28) and obeys the gravitational-field equations (1.24) that are written in a form

$$R_{\mu\nu} = \kappa(\rho + p)\left(u_\mu u_\nu + \frac{1}{2}g_{\mu\nu}\right) - \kappa p g_{\mu\nu}, \tag{4.7}$$

where ρ, $p > 0$ are the density and pressure respectively. The normalized 4-velocity of fluid elements u^μ, given in (4.35), satisfies the geodesic equation (1.19) of the form

$$u^\mu \nabla_\mu u^\nu = 0 \tag{4.8}$$

along with the continuity equation

$$u^\mu \nabla_\mu (\rho + p) u^\nu + g^{\mu\nu}\nabla_\mu p = 0. \tag{4.9}$$

The field equations (4.7) yield a set of three ODEs for the rest-mass density ρ, for the radial pressure p_r, and for the angular pressure p_ϑ as

$$\begin{array}{rcl} 8\pi r^2 \rho & = & e^{-\lambda}(r\lambda' - 1) + 1 \\ 8\pi r^2 p_r & = & -e^{-\lambda}(r\nu' + 1) + 1 \\ 32\pi r p_\vartheta & = & -e^{-\lambda}(2r\nu'' - r\lambda'\nu' + r\nu'^2 + 2\nu' - 2\lambda'), \end{array} \tag{4.10}$$

where the prime denotates derivates with respect to the radial coordinate r. This set of ODEs is the static limit of the more general, time-dependent the field equations (3.39). Through the application and modification of the method originally established by Ref. [202], I have shown in Ref. [1] that it is possible to replace eqs. (4.10) by a set of algebraic equations where the integration of one metric function is required, but not of the physical variables ρ and p.

Due to the isotropic configuration, $p \equiv p_r = p_\vartheta$ implies one can require one more field equation

$$r(r\nu' + 2)\frac{\mathrm{d}}{\mathrm{d}r}e^{-\lambda} + (2r^2\nu'' + r^2\nu'^2 - r\nu' - 4)e^{-\lambda} + 4 = 0 \tag{4.11}$$

by extracting the last equation from the second one. Regarding the coefficient of $\mathrm{d}e^{-\lambda}/\mathrm{d}r$, it turns out to be practical to introduce a pair of new variables

$$\alpha = -\lambda' e^{-\lambda}\beta^2 \quad \text{and} \quad \beta = \frac{r\nu'}{2} + 1. \tag{4.12}$$

Then the field equation (4.11) reduces to a second order algebric equation in β, namely

$$2(\alpha + 1)\beta^2 + (r\alpha' + 8\alpha)\beta + 4\alpha = 0. \tag{4.13}$$

For any function α the quadratic equation (4.13) is solved by the real roots

$$\beta_\pm = \frac{8\alpha - r\alpha' \pm \sqrt{(r\alpha' + 8\alpha)^2 - 32\alpha(\alpha + 1)}}{4(\alpha + 1)} \tag{4.14}$$

where the discriminant must be non-negative. The only physically relevant solution is β_+, since its non-positive counterpart always belongs to a non-positive, hence non-physical mass density. The metric functions belonging to β are formally given by the definitions (4.12) as

$$\lambda = \ln\left(\frac{\beta^2}{\alpha}\right) \quad \text{and} \quad \nu = \int_0^r \frac{2(\beta - 1)}{r}\mathrm{d}r + \nu_0, \tag{4.15}$$

where the constant ν_0 determines the scaling of the time coordinate t. One can also calculate the pressure and density

$$\rho = \frac{1 - (r\alpha/\beta^2)'}{8\pi r^2} \quad \text{and} \quad p = \frac{(2\beta - 1)\alpha - \beta^2}{8\pi\beta^2 r^2} \tag{4.16}$$

by substituting functions α and β into the first two field equations of Eq. (4.10). The simple, but still realistic choice for the generating function α is the ratio of two polynomials of the radial coordinate r. The lowest degree form which is physically valid for a compact fluid or gaseous sphere is

$$\alpha = 1 + \frac{A^2 r^2}{1 + Br^2}, \tag{4.17}$$

where A and B are positive constants associated by inverse first and second power of distance dimensions. It is advisable to introduce a further new non-negative real constant $C^2 = 2B/A^2 - 2$ and use it in place of constant B. In order to eliminate the square root appeared in Eq. (4.14) while expressing β, a new radial variable defined by

$$\sinh\xi = 2C\frac{1 + Br^2}{3 + 4Br^2} \tag{4.18}$$

will be introduced. Then the centre gets into $\xi_c = \operatorname{arcsinh}(2C/3)$, and the spatial infinity $\xi_\infty = \operatorname{arcsinh}(C/2)$, and the new variable is restricted by $0 < \xi_\infty \leq \xi \leq \xi_c$. Through (4.17), the generating functions α and β become

$$\alpha = \frac{(C^2 - 4)\sinh\xi + 4C}{(C^2 + 2)\sinh\xi}, \qquad \beta = \frac{C\coth(\xi/2) - 2}{1 + C\tanh(\xi/2)}. \tag{4.19}$$

The equations (4.15) provide the metric functions and the inner Schwarzschild metrics appears to be

$$\mathrm{d}s^2 = -e^{\nu}\mathrm{d}t^2 + \frac{C^2 e^{\lambda}\cosh^2\xi\,\mathrm{d}\xi^2}{4A^2(C^2+2)(2C-3\sinh\xi)(2\sinh\xi - C)^3} + \frac{(2C-3\sinh\xi)(\mathrm{d}\vartheta^2 + \sin^2\vartheta\,\mathrm{d}\varphi^2)}{A^2(C^2+2)(2\sinh\xi - C)} \tag{4.20}$$

by using the charasteric ξ as radial coordinate. The constant A corresponds to a constant conformal transformation of the metrics. From eq. (4.10), both the density and the pressure are expressable by a ratio of two polynomials of hyperbolic function of the radial coordinate ξ.

Moving away from the centre of the GMC due to the conditions (4.4), the pressure monotonously tends to zero at $r = R$, on the border of the GMC. Any choice of constants A and C satisfies the restriction (4.5) on the speed of sound in the medium. One takes $C^2 = 2B/A^2 - 2$ into consideration and assumes $B \ll 1 \ll C$, then p and ρ vanish simultaneously at $r = R$ if and only if $B = 4/R^2$. This restriction implies $A = 8c_s^2/R$. By eliminating the variable ξ via the transformation (4.18), one can formulate the functions of state

$$\rho = \frac{8Br^2 - 3}{4\pi C(4Br^2-1)^{-1}}, \quad p = \frac{2Br^2 - 1}{4\pi C^2(4Br^2-1)^{-1}} \tag{4.21}$$

in terms of polynomials of the natural radial coordinate r, cf. Fig. 4.1a. As it was required, if $B \ll 1 \ll C$ then the EOS is nearly linear for every $r \leq R$, therefore

$$\frac{dp}{d\rho} = \frac{1}{2C}\left(1 + \frac{1}{5 - 16Br^2}\right) = c_s^2 < 1 \tag{4.22}$$

fixes the last constant as $C = 4/c_s^2$. Consequently, they differ from one another only by a constant factor, thus verifying the legitimacy of the isothermal EOS (4.2). In accordance with the literature (cf. Fig. 6. in [203] and [204]), the density and pressure profile is expressed by

$$p = c_{\mathrm{s}}^2\rho, \;\; \rho(r) = \frac{3c_{\mathrm{s}}^2}{16\pi}\left(\frac{16r^2}{R^2} - 1\right)\left(\frac{8r^2}{3R^2} - 1\right). \tag{4.23}$$

Similarly, the metric functions ν and λ, shown in Fig. 4.1b, that are consistent with this profile, are expressed as functions of the radial coordinate r. The line element

$$\mathrm{d}s^2 = -\frac{c_s^2}{4}\left(1 + \frac{c_s^2}{4}\frac{r^2}{R^2}\right)\mathrm{d}t^2 + \exp\left(-\frac{c_s^2}{2}\frac{r^2}{R^2}\right)\mathrm{d}r^2 + r^2(\mathrm{d}\vartheta^2 + \sin^2\vartheta\,\mathrm{d}\varphi^2) \tag{4.24}$$

is immediately obtaind by the insertion of the metric functions into the general form of Schwarzschild metrics (4.6).

4.2.2 Lagrangian function and geodesics of the particles

In the following subsections, the behaviour of massive particles and photons in the Schwarzschild geometry will be briefly reviewed, based on [34]). For the Schwarzschild metrics (4.24) the relativistic Lagrangian function $L = g_{\mu\nu}\dot{x}^{\mu}\dot{x}^{\nu}$ of the particles in the investigated nebula is

$$L = -e^{\nu}\dot{t}^2 + e^{\lambda}\dot{r}^2 + r^2(\dot{\vartheta}^2 + \sin^2\vartheta\,\dot{\varphi}^2) \tag{4.25}$$

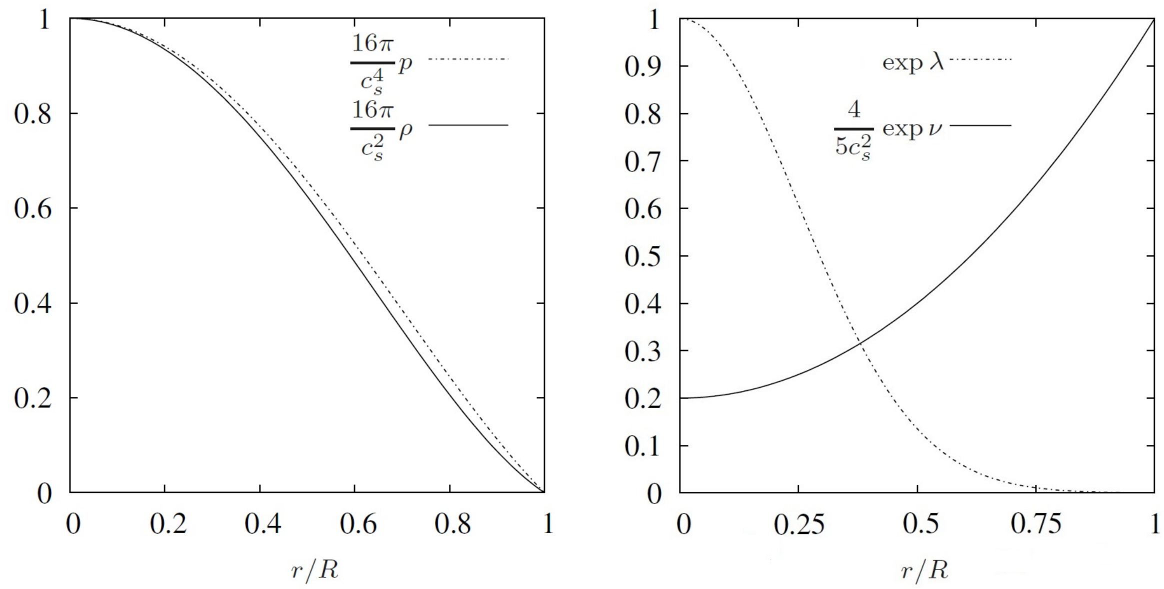

(a) The pressure and density profile in the interval $0 < r/R < 1$, normalized to the central values p_c and ρ_c.

(b) The evolution of the normalized metric functions $\exp\lambda$ and $\exp\nu$ within the interval $0 < r/R < 1$.

Figure 4.1: The profiles of pressure and density consistent with the metric functions $\exp\lambda_+$ and $\exp\nu_+$ within the nebula.

where the dot denotates derivates with respect to the proper time coordinate τ. By substituting this form for L into the Euler–Lagrange equations $\frac{\mathrm{d}}{\mathrm{d}\tau}\left(\frac{\partial L}{\partial \dot{x}^\mu}\right) - \frac{\partial L}{\partial x^\mu} = 0$, result the geodesics equations. Since the eqation for $\mu = 3$ is satisfied by $\vartheta = \pi/2$, it is sufficient to keep only the set of three equations independent of ϑ:

$$\begin{aligned} e^\nu \dot{t} &= L_t \\ \ddot{r} + \frac{1}{2}\frac{\mathrm{d}\lambda}{\mathrm{d}r}\dot{r}^2 + \frac{1}{2}\frac{\mathrm{d}\nu}{\mathrm{d}r}e^{\nu-\lambda}\dot{t}^2 - re^{-\lambda}\dot{\varphi}^2 &= 0 \\ r^2\dot{\varphi} &= L_\varphi \end{aligned} \tag{4.26}$$

The two simplest equations are derived immediately since the Lagrangian is not an explicit function of t or φ. The appearing constants L_t and L_φ proportional to the total energy and the angular momentum of the particles. It is expedient to replace the complicated second equation of Eq. (4.26) by the first integral $g_{\mu\nu}\dot{x}^\mu\dot{x}^\nu = -1$ of the geodesics equations (1.19), since the worldline of a massive partice is timelike. In this case, it takes the form

$$-e^\nu\dot{t}^2 + e^\lambda\dot{r}^2 + \frac{1}{2}r^2\dot{\varphi}^2 = -1. \tag{4.27}$$

By substituting the two original expressions of (4.26) into (4.27), one obtain the combined energy equation

$$\dot{r}^2 + \frac{L_\varphi^2}{r^2}e^{-\lambda} = \left(L_t^2 e^{-\nu} - 1\right)e^{-\lambda} \tag{4.28}$$

for the radial coordinate valid inside the GMC. Outside of the GMC the customary equation $\dot{r}^2 + (1-2M/r)L_\varphi^2/r^2 - 2M/r = (L_t^2 - 1)$ governs the motion of particles. Note that the right-hand side is a constant of motion, $L_t \propto E$ as previously stated. The constant of proportionality is fixed by requiring $E = m_0$ for a particle at rest at $r = \infty$ where m_0 denotes the mass of the particle at rest. Letting $r \to \infty$ and $\dot{r} = 0$ in the equation, $L_t^2 = 1$ thus is required. Hence, one must has $L_t = E/m_0$, where E is the total energy of the particle in its orbit.

The shape of a particle orbit is given by using the last equation of Eq. (4.26) to express $\dot{r}$ in the (4.28) as

$$\frac{\mathrm{d}r}{\mathrm{d}\tau} = \frac{\mathrm{d}r}{\mathrm{d}\varphi}\frac{\mathrm{d}\varphi}{\mathrm{d}\tau} = \frac{L_\varphi}{r^2}\frac{\mathrm{d}r}{\mathrm{d}\varphi}. \tag{4.29}$$

Furthermore, if one parametrizes Eq. (4.27) by $\tilde{r} \equiv 1/r$, one obtains $\left(\frac{\mathrm{d}\tilde{r}}{\mathrm{d}\varphi}\right)^2 + \tilde{r}^2 e^{-\lambda} = \frac{1}{L_\varphi^2}\left(L_t^2 e^{-\nu} - 1\right) e^{-\lambda}$. Finally, the differentiation with respect to φ provides the orbits

$$\frac{\mathrm{d}^2\tilde{r}}{\mathrm{d}\varphi^2} + \tilde{r}e^{-\lambda} = \frac{L_t^2(\nu' + \lambda')e^{-\nu} - \lambda'}{2L_\varphi^2\tilde{r}^2}e^{-\lambda} - \frac{\lambda'}{2}e^{-\lambda} \tag{4.30}$$

for a particle in the equatorial plane $\vartheta = \pi/2$ where the prime denotes derivates with respect to the radial coordinate r. The particle orbits have two special cases, namely the radial motion where $\dot{\varphi} = 0$ and the circular motion where $\dot{r} = 0$. Since the density of the nebula is constant in time, one might ignore the radial motion and focus on investigating the latter motion.

4.2.3 Circular motion on bounded and stabil orbits, velocity of the gas particles

In the equatorial plain for circular motion, one has $r =$ constant, and thus $\dot{r} = \ddot{r} = 0$. This restriction in accordance of (4.29) imposes $\tilde{r}' = \dot{\tilde{r}}/L_\varphi\tilde{r}^2 = 0$; consequently $\tilde{r}''$ is zero too. Setting $\tilde{r} = 1/r =$ constant in the equation of orbits (4.30), one has $L_\varphi^2 = \frac{1}{2}r^3 L_t^2(\nu' + \lambda')\nu' e^{-\nu}$. Beside replacing the differentials of the metrics functions of Eq. (4.24)

$$\frac{\mathrm{d}\lambda}{\mathrm{d}r} = -\frac{c_s^2 r}{R^2} \quad \text{and} \quad \frac{\mathrm{d}\nu}{\mathrm{d}r} = \frac{c_s^2 r}{2R^2}\left(1 + \frac{c_s^2}{4}\frac{r^2}{R^2}\right)^{-1} \tag{4.31}$$

in the energy equation (4.28) in addition to the condition $\dot{r} = 0$, one can identify the constants of motion as

$$L_t = \frac{c_s}{2}\left(1 + \frac{c_s^2 r^2}{4R^2}\right) \quad \text{and} \quad L_\varphi = \frac{c_s}{2}\frac{r^2}{R}. \tag{4.32}$$

It has been shown that $E = L_t m_0$ is the total energy of a particle of rest mass m_0 in a circular of radius r. Subsequently one can circumscribe the bounded orbits by requiring $E < m_0$, so as long as $L_t = 1$. The limits on r for the orbit to be bound is given by $1 = \frac{c_s}{2}\left(1 + \frac{c_s^2 r^2}{4R^2}\right)$, which is satisfied when

$$r = \frac{2R}{c_s}\sqrt{\frac{2}{c_s} - 1}. \tag{4.33}$$

The first and third geodesics equations in Eq. (4.26) immediately show that the components of 4-velocity of a particle are simply

$$[u^\mu] = \left[\frac{2}{c_s}, 0, 0, c_s\frac{r}{2R}\sin\vartheta\right] \tag{4.34}$$

in the coordinate system $(t, r, \vartheta, \varphi)$. The geodesics equations specify the circular trajectory $\varphi(\tau)$ and the orbital period $T = 2\pi/\dot{\varphi}$, which according to (4.32) is $T = 4\pi R/c_s$ by substituting L_φ from (4.32). Although r is not the radius of the orbit, it is readily conceivable that the spatial distance travelled in one complete revolution is $2\pi r$, just as in the Newtonian case. Instead of parametrizing φ in the proper time, one can alternatively describe it by $\mathrm{d}\varphi/\mathrm{d}t = c_s^2/4R$ in terms of coordinate time t. The components of 4-velocity of a particle in the equatorial plain $\vartheta = \pi/2$ are thus given by

$$[u^\mu] = \left[1,\ 0,\ 0,\ \frac{c_{\mathrm{s}}^2}{4}\frac{r}{R}\sin\vartheta\right] \tag{4.35}$$

in the coordinate system $(t, r, \vartheta, \varphi)$ where $\vartheta = \pi/2$ in the equatorial plane. The continuity equation (4.9) requires that

$$u_\mu u^\mu = -\frac{c_{\mathrm{s}}^2}{4} + \mathcal{O}(c_{\mathrm{s}}^4/c^2) \equiv -c_*^2, \tag{4.36}$$

where it is sufficient to keep only the leading order term. Due to symmetry, the connection has only four non-zero components

$$\Gamma^0_{01} = \left(1 + \frac{c_s^2}{4c^2}\frac{r^2}{R^2}\right)^{-1}\frac{c_s^2}{4c^2}\frac{r}{R^2}, \quad \Gamma^1_{00} = \frac{c_s^4}{16c^4}\frac{r}{R^2}\exp\left(\frac{c_s^2}{2c^2}\frac{r^2}{R^2}\right), \quad \Gamma^1_{11} = -\frac{c_s^2}{2c^2}\frac{r}{R^2}, \quad \Gamma^2_{12} = \frac{1}{r}. \tag{4.37}$$

4.3 Linear perturbation of equilibrium configuration

Let some smooth, non-degenerate, symmetrical metric tensor $g_{\mu\nu}$, associated with the line element (4.24), be given on some differentiable mainfold $\mathcal{M}$ which existed before the train of GWs came. Let the 'background' field variables $(g_{\mu\nu},\ u^\mu,\ \rho,\ p)$, as described above, be disturbed by small linear perturbations, denoted with overhead hat as $(\hat{g}_{\mu\nu},\ \hat{u}^\mu,\ \hat{\rho},\ \hat{p})$. According to linearization stability, $(g_{\mu\nu} + \varepsilon\hat{g}_{\mu\nu},\ u^\mu + \varepsilon\hat{u}^\mu,\ \rho + \varepsilon\hat{\rho},\ p + \varepsilon\hat{p})$ will approximate a solution of the linearized equations (4.7–4.8) at the background field. At least in a compact part of spacetime, provided the constant numerical factor $\varepsilon \ll 1$ is sufficiently small.[2] Let ε denote a small ratio between the scale of variation of the perturbed variables and that of the background. Let us associate the strain amplitude of the radiation in with a small linear perturbation $\varepsilon\hat{g}_{\mu\nu}$.

Consequently, the contravariant notions of perturbed quantities of different tensorial order are

$$\hat{g}^{\alpha\beta} = g^{\alpha\rho}g^{\beta\sigma}\hat{g}_{\rho\sigma}, \quad \hat{u}^\alpha = g^{\alpha\beta}\hat{u}_\beta + \hat{g}^{\alpha\beta}u_\beta. \tag{4.38}$$

Let ∇ be the covariant derivative associated with some torsionless and metric-compatible connection $\Gamma^\kappa_{\mu\nu}$, then the perturbation of this connection is a tensor $\hat{\Gamma}^\kappa_{\mu\nu}$ given by

$$\hat{\Gamma}^\gamma_{\alpha\beta} = \frac{1}{2}g^{\gamma\delta}(\nabla_\beta\hat{g}_{\delta\alpha} + \nabla_\alpha\hat{g}_{\delta\beta} - \nabla_\delta\hat{g}_{\alpha\beta}). \tag{4.39}$$

Based on this scheme of work, the Ricci identity implies

$$\hat{R}_{\alpha\beta} = \frac{1}{2}\left(\nabla^{\gamma}_{\alpha}\hat{g}_{\beta\delta} + \nabla^{\delta}_{\beta}\hat{g}_{\alpha\delta} - \nabla^{\delta}_{\delta}\hat{g}_{\alpha\beta} - \nabla_{\alpha\beta}\hat{g}_{\delta\gamma}g^{\delta\gamma}\right). \tag{4.40}$$

Likewise, by retaining only terms of the first order in the linear approximations of eqs. (4.7) and (4.36), one obtains

$$\hat{R}_{\alpha\beta} = \kappa(\hat{\rho}+\hat{p})\left(u_{\alpha}u_{\beta} + \frac{1}{2}g_{\alpha\beta}\right) - \kappa\hat{p}g_{\alpha\beta} + \kappa(\rho+p)\left(2u_{(\alpha}\hat{u}_{\beta)} + \frac{1}{2}\hat{g}_{\alpha\beta}\right) \tag{4.41}$$

and

$$2u^{\alpha}\hat{u}_{\alpha} = \hat{g}_{\alpha\beta}u^{\alpha}u^{\beta}, \tag{4.42}$$

respectively. From these last two equations the perturbation of the remaining quantities can be expressed as

$$\hat{\rho}+\hat{p} = -\left(2\kappa^{-1}\hat{R}_{\alpha\beta} + (\rho+p)\hat{g}_{\alpha\beta}\right)c_{*}^{-2}u^{\alpha}u^{\beta} \tag{4.43}$$

and

$$\hat{u}_{\alpha} = \frac{1}{2}\left(\hat{g}_{\alpha\gamma} - \frac{2\hat{R}_{\beta\gamma} + \kappa(\rho-p)\hat{g}_{\beta\gamma}}{\kappa c_{*}^{4}(\rho+p)}\mathcal{P}^{\beta}_{\alpha}\right)u^{\gamma}. \tag{4.44}$$

Up to this point, my results entirely corresponded to that of Refs. [196, 197]. Now, however, I shall define not a single, but a pair of appropriate tensors

$$\mathcal{P}^{\beta}_{\alpha} \equiv c_{*}^{2}g^{\beta}_{\alpha} + u_{\alpha}u^{\beta}, \quad \mathcal{Q}^{\beta}_{\alpha} \equiv c_{*}^{2}g^{\beta}_{\alpha} - u_{\alpha}u^{\beta} \tag{4.45}$$

which significantly simplify expressions to appear later on. $\mathcal{P}$ projects onto the subspaces of the tangent spaces that are orthogonal to u_{α} whilst to the auxiliary tensor $\mathcal{Q}$ may not carry such evident geometrical meaning. The set of eqs. (4.41–4.44) yields the key equation that drives the spatio-temporal evolution of linearized perturbations. Making use of the preceding notation (4.45), it can be appreciably simplified to

$$\left[\mathcal{P}^{\gamma}_{\alpha}\mathcal{P}^{\delta}_{\beta} - \mathcal{Q}_{\alpha\beta}u^{\gamma}u^{\delta}\right]\left[\hat{R}_{\gamma\delta} + \frac{1}{2}\kappa(\rho-p)\hat{g}_{\gamma\delta}\right] = \kappa c_{*}^{4}(c^{2}\rho - 3p)\hat{g}_{\alpha\beta} + 2\kappa(c_{*}^{2}pu^{\gamma}\hat{u}_{\gamma} - \hat{p})g_{\alpha\beta}. \tag{4.46}$$

It is important to highlight two noteworthy details about the equation:

1. In flat spacetime c_{*} is equal to 1, thus the last term in the right-hand side would perish.

2. If the GMC is assumed to be made of only dust, such terms would vanish just as well where the pressure or its perturbation appear.

In consequence, my result in the flat dust-filled spacetime limit would be identical to the formula (21) in [196]. By its very nature, eq. (4.46) inherently satisfies the conditions (4.8–4.9). However, in deriving (4.46), no restriction on the perturbations has been imposed. In order to eliminate redundant components, one can take the liberty to impose a gauge condition. Conventionally, either the ‘de Donder gauge’ (as in [192]) or the ‘Landau gauge' (as in [196]) have been favoured. The former – also known as harmonic coordinate condition – ultimately requires the product $\Gamma^{\beta}_{\gamma\gamma}\hat{g}_{\alpha\beta}$ to vanish whereas the latter one imposes

$$\hat{g}_{\alpha\beta}u^{\beta} = 0. \tag{4.47}$$

This latter gauge condition is particularly suitable for the fact that the metric perturbation contracts to the unperturbed 4-velocity in several terms of the perturbed field equation. By requiring (4.47) to hold, (4.46) reduces to the form

$$\left[\mathcal{P}^{\gamma}_{\alpha}\mathcal{P}^{\delta}_{\beta} - \mathcal{Q}_{\alpha\beta}u^{\gamma}u^{\delta}\right]\left[g^{\mu}_{(\gamma}\nabla^{\nu}_{\delta)} - g^{\mu}_{\gamma}g^{\nu}_{\delta}\nabla^{\lambda}_{\lambda} - g^{\mu\nu}\nabla_{\gamma\delta}\right]\hat{g}_{\mu\nu} = \kappa c_*^4(\rho - 5p)\hat{g}_{\alpha\beta} - 4\kappa c_*^4\hat{p}g_{\alpha\beta}, \tag{4.48}$$

where the operator on the left-hand side of this formula maps the space of symmetric 'spatial' tensor field into itself. This basic equation restricted by (4.47) is an unconstrained system of six coupled ODEs of second order for six unknown variables. A solution is therefore specified by twelve functions of three variables. Since the restricted gauge freedom consists of four functions, the intrinsic freedom of the perturbation amounts to eight functions corresponding to four degrees of freedom.

4.4 WKB expansions of geometrical optics

4.4.1 WKB approximation for monochromatic high-frequency field perturbations

The set of field equations (4.48) for metric perturbations results a system of coupled linear first-order PDEs. A strategy for finding a unique closed-form analytical solution for arbitrary initial data is based on decoupling the set order by order by small parameter ε. Let a linear parabolic PDE

$$\mathcal{D}(\mathbf{x}, \nabla)\hat{g}_{\mu\nu} = (\mathcal{D}_2^{\alpha\beta}(\mathbf{x})\nabla_{\alpha\beta} + \mathcal{D}_1^{\alpha}(\mathbf{x})\nabla_{\alpha} + \mathcal{D}_0(\mathbf{x}))\hat{g}_{\mu\nu} = 0 \tag{4.49}$$

in $\mathbf{x} \equiv (t, \vec{x})$ be given for some function $\hat{g}_{\mu\nu} : \mathbb{R}^{n\times n} \to \mathbb{R}^{m\times m}$, where $\mathcal{D}_2, \mathcal{D}_1, \mathcal{D}_0 \in \mathbb{R}^{m\times m}$ are matrix-valued, smooth functions with real entries which act on the six-dimensional space of metric perturbations. [2] Geometrical optics emerges as a short-wavelength limit for solutions to the PDE (4.49). Accordingly, let us specialize metric perturbations $\hat{g}_{\mu\nu}$ to locally plane, monochromatic, high-frequency fields. Assuming formal solutions can be locally approximated in a successive procedure by plane wave

$$\hat{g}_{\mu\nu}(\mathbf{x}, \varepsilon) = A_{\mu\nu}(\mathbf{x}, \varepsilon)\exp[i\varepsilon^{-1}\psi(\mathbf{x}, \varepsilon)], \tag{4.50}$$

a WKB ansatz can be constructed, provided that for any $n \in \mathbb{N}$, amplitude $A_{\mu\nu}$ and phase $\varepsilon^{-1}\psi$ take the form of asymptotic series expansions

$$\begin{aligned} A_{\mu\nu}(\mathbf{x}, \varepsilon) &\sim \sum_{n=0}^{\infty}\left(\frac{\varepsilon}{i}\right)^{n} A^{(n)}_{\mu\nu}(\mathbf{x}) \\ \psi(\mathbf{x}, \varepsilon) &\sim \sum_{n=0}^{\infty}\varepsilon^{n}\psi^{(n)}(\mathbf{x}) \end{aligned} \tag{4.51}$$

in the limit $\varepsilon \to 0$. It is evidently expressed that as long as the parameter ε is small, the amplitude varies slowly in comparison with the rapid oscillation of the phase. On account of the gauge-fixing condition (4.47)

$$A^{(n)}_{\mu\nu} u^\nu = 0 \tag{4.52}$$

is required to hold for any non-negative n; in other words, any n-order wave amplitude is transversal to the direction of propagation. The wave covector is defined to be $\varepsilon^{-1} l_\mu$, where

$$l_\mu \equiv \nabla_\mu \psi, \quad k_\mu = \mathcal{P}_{\mu\nu} l^\nu \tag{4.53}$$

and the angular frequency relative to the unperturbed matter flow is $-\varepsilon^{-1} u^\mu l_\mu$ which itself would be denoted by

$$\omega \equiv 2\pi f \equiv -u^\mu l_\mu = -k_0. \tag{4.54}$$

One may re-arrange the expression $\mathcal{D}\left(A_{\mu\nu} \exp[i\psi/\varepsilon]\right)$ after having the ansatz (4.50–4.51) inserted into (4.48) and taken into account the choice of gauge (4.52) by requiring the terms of order $1, \varepsilon, \varepsilon^2, \ldots$ of the resulting formal series

$$\left(\mathcal{L}^{(0)\alpha\beta}_{\ \ \mu\nu} + \frac{\varepsilon}{i} \mathcal{L}^{(1)\alpha\beta}_{\ \ \mu\nu} + \left(\frac{\varepsilon}{i}\right)^2 \mathcal{L}^{(2)\alpha\beta}_{\ \ \mu\nu} \right) \left(A^{(0)}_{\alpha\beta} + \frac{\varepsilon}{i} A^{(1)}_{\alpha\beta} + \ldots \right) = 0 \tag{4.55}$$

to vanish separately. The $\mathcal{L}^{(j)}$ linear differential operators of order j, called the symbols of $\mathcal{D}$ are given by the field equations (4.48) and eq. (4.49) as

$$\begin{aligned}
\mathcal{L}^{(0)\alpha\beta}_{\ \ \mu\nu} \equiv\ & -2\mathcal{P}^{\alpha}{}_{(\mu} l^\beta k_{\nu)} + \mathcal{P}^\alpha_\mu \mathcal{P}^\beta_\nu l^2 + g^{\alpha\beta}(k_\mu k_\nu - \omega^2 \mathcal{Q}_{\mu\nu}) \\
\mathcal{L}^{(1)\alpha\beta}_{\ \ \mu\nu} \equiv\ & -4\mathcal{P}^\gamma_{(\mu}\mathcal{P}^{(\alpha}_{\nu)}(l^{\beta)}\nabla_\gamma + \nabla^{\beta)} l_\gamma) + 2\mathcal{P}^{(\alpha}{}_{(\mu} k_{\nu)} \nabla^{\beta)} + 2\mathcal{P}^{(\alpha}_{(\mu}\mathcal{P}^{\beta)}_{\nu)}(\nabla_{\mathbf{l}} + \theta/2) \\
& +2\omega \mathcal{Q}_{\mu\nu} \nabla^\beta u^\alpha - \mathcal{P}^{\alpha\beta}\left[\mathcal{P}^\gamma_{(\mu}\mathcal{P}^\delta_{\nu)} \nabla_\delta l_\gamma + \mathcal{P}^\gamma{}_{(\mu} k_{\nu)} \nabla_\gamma - \mathcal{Q}_{\mu\nu}(2\omega \nabla_{\mathbf{u}} - u^\gamma \nabla_{\mathbf{u}} l_\gamma)\right] \\
\mathcal{L}^{(2)\alpha\beta}_{\ \ \mu\nu} \equiv\ & \mathcal{P}^\gamma_\mu \mathcal{P}^\delta_\nu (2 g^\alpha_\lambda g^\beta{}_{(\gamma} \nabla_{\delta)} \nabla^\lambda + g^\alpha_\gamma g^\beta_\delta \nabla_\lambda \nabla^\lambda) - 4\kappa c_*^2 \hat{p} g^\alpha_\mu g^\beta_\nu - \kappa c_*^4 (\rho - 5p) g^\alpha_\mu g^\beta_\nu \\
& -g^{\alpha\beta}(\mathcal{P}^\gamma_\mu \mathcal{P}^\delta_\nu - \mathcal{Q}_{\mu\nu} u^\gamma u^\delta) \nabla_{\gamma\delta},
\end{aligned} \tag{4.56}$$

where, in addition to the abbreviations $\theta \equiv \nabla^\mu l_\mu, \nabla_{\mathbf{u}} \equiv u^\mu \nabla_\mu, \nabla_{\mathbf{l}} \equiv l^\mu \nabla_\mu$, the identities (4.53–4.54) were applied. The method of characteristics discovers characteristic curves along which the PDEs in eq. (4.55) reduce to ODEs. Once the ODE for the respective $\mathcal{L}^{(j)}$ symbol is found, it can be solved for the corresponding amplitude $A^{(j)}_{\alpha\beta}$ along the characteristic curves and transformed into a solution for the original PDE.

4.4.2 Geometrical optics and transport equation for amplitudes

It has been shown by Thorne [194] that in realistic astrophysical situations the vacuum approximation to wave propagation is appropriate. Here, the geometrical optics is formulated in terms of ray tracing, i.e. an ODE model. Provided that l^μ is smooth, it corresponds to locally solving the eikonal equation through the method of bicharacteristics. Bicharacteristics of (4.48) or so-called rays along which the amplitudes $A^{(0)}$ are transported are spacetime projections of the solutions of Hamilton's system of ODEs

$$\dot{x}^\mu = \frac{\partial \mathcal{H}}{\partial l_\mu}, \quad \dot{l}^\mu = \frac{\partial \mathcal{H}}{\partial x_\mu}. \tag{4.57}$$

The method is discussed in great detail in Refs. [196, 197]. A lengthy calculation, which I do not repeat here, finally yields the zeroth-order amplitude that shall consist of the following linear combinations of basis vectors $e_{\mu\nu}$:

$$A^{(0)}_{\mu\nu} = \begin{cases} a^{(0)}_{+} e^{+}_{\mu\nu} + a^{(0)}_{\times} e^{\times}_{\mu\nu} & \text{(Mode I: \textit{Gravitational wave})} \\ b^{(0)}_{1} (\mathcal{Q}_{\mu\nu} + e^{3}_{\mu\nu}) & \text{(Mode II: \textit{Sound wave})} \\ C_{(\mu} e^{3}{}_{\nu)} & \text{(Mode III: \textit{Pressure wave})}, \end{cases} \tag{4.58}$$

where $C_\mu = c^{(0)}_1 e^1_\mu + c^{(0)}_2 e^2_\mu + c^{(0)}_3 e^3_\mu$. To put eq. (4.58) in context, one can recognize that the first mode corresponds to an arbitrary plane-wave solution in the standard transverse traceless (TT) gauge, where $(a^{(0)}_{+}, a^{(0)}_{\times})$ are the amplitudes (polarization states) of the two independent components with linear polarization, and $(e^{+}_{\mu\nu}, e^{\times}_{\mu\nu})$ are the corresponding polarization tensors. The second mode partly, and the third mode fully are in the frame orthogonal to u^μ and k^μ. They correspond to sound waves and pressure waves, respectively. For the particular case of dust ($p = 0$) or in case $c_s = 0$, there are no sound waves and second mode degenerates into the longitudinal part of the third one. In case of stiff matter ($p = \rho$), $c_s = 1$, sound waves propagate with the speed of light.

The first-order WKB equation acquired from (4.55) imposes

$$\mathcal{L}^{(0)\alpha\beta}_{\mu\nu} A^{(1)}_{\alpha\beta} + \mathcal{L}^{(1)\alpha\beta}_{\mu\nu} A^{(0)}_{\alpha\beta} = 0 \tag{4.59}$$

to hold for zeroth- and first-order amplitudes. Applying the expressions from (4.56), $\mathcal{L}^{(0)}$ is annulled upon being transvected with either one of polarization tensors given in (4.58). After some manipulation, one gets the pair

$$\begin{aligned} (\nabla_{\mathbf{l}} + \theta/2) a^{(0)}_{+} + \tfrac{1}{2} e^{\mu\nu}_{+} (a^{(0)}_{+} \nabla_{\mathbf{l}} e^{+}_{\mu\nu} + a^{(0)}_{\times} \nabla_{\mathbf{l}} e^{\times}_{\mu\nu}) = 0 \\ (\nabla_{\mathbf{l}} + \theta/2) a^{(0)}_{\times} + \tfrac{1}{2} e^{\mu\nu}_{\times} (a^{(0)}_{+} \nabla_{\mathbf{l}} e^{+}_{\mu\nu} + a^{(0)}_{\times} \nabla_{\mathbf{l}} e^{\times}_{\mu\nu}) = 0, \end{aligned} \tag{4.60}$$

which assert that the pair of polarization states $(a^{(0)}_{+},\, a^{(0)}_{\times})$ are transported along rays bended by the background field. Along each null geodesic ray x^μ with tangent $\dot{x}^\mu = l^\mu$ given in (4.57), the vectors l^μ, u^μ span a timelike two-plane, and basis vectors span its spacelike orthogonal complement. Assuming the basis vectors $(e^\mu_1,\, e^\mu_2)$ are such that they are transported quasi-parallel along the rays, the transport of the amplitudes will be bounded by

$$(\nabla_{\mathbf{l}} + \theta/2) \begin{pmatrix} a^{(0)}_{+} \\ a^{(0)}_{\times} \end{pmatrix} = 0, \tag{4.61}$$

testifying that the change of complex vector $(a^{(0)}_{+},\, a^{(0)}_{\times})$ along the ray consists solely of a rescaling the two 'TT' polarization modes of GWs (1.63) travelling in empty space. Making use of the expression for $\mathcal{L}^{(2)}$ from (4.56), the transport equation for the first-order amplitudes yields

$$\begin{aligned} (\nabla_{\mathbf{l}} + \theta/2) a^{(1)}_{+} = \frac{1}{2} \kappa (\rho - 5p) a^{(0)}_{+} + \frac{1}{2} e^{\alpha\beta}_{+} \big[2(\nabla^\mu \nabla_\alpha + \nabla_\alpha \nabla^\mu) g^\nu_\beta - g^\mu_\alpha g^\nu_\beta \nabla^2 \\ - c_*^{-2} \mathcal{P}^{\mu\nu} \nabla_\alpha \nabla_\beta \big] [a^{(0)}_{+} e^{+}_{\mu\nu} + a^{(0)}_{\times} e^{\times}_{\mu\nu}] \end{aligned} \tag{4.62}$$

and a similar one for $a^{(1)}_{\times}$.

4.5 Numerical solution and application for data analysis

In this section the transport equation is converted into a PDE which is numerically solved and where the first-order amplitudes are assumed to change in a sinusoidal manner over retarded time. However extremely small in value, the frequency shows a decreasing behaviour that can be traced back to the nature of dissipative interaction of the GW with the surrounding matter. From the decomposition of any given signal into varying sinusoidal components by Fourier analysis, I construct the changes in frequency of all the sinusoids for all the frequencies. I shall use the well-established concept of match-filtering technique to correlate the unaltered signal with the signal affected by crossing through the medium. For its importance, the reconstructed time series of the transient GW signal 'GW150914' (cf. Sec. 1.3.2) as a known template is taken into examination. [69, 205] My first priority is to measure the deviation of this signal by an overlap function. Secondly, it is to bring to light in what types of possible GW-sources the effect of interaction is expected to be powerful enough to be taken into account for future examination.

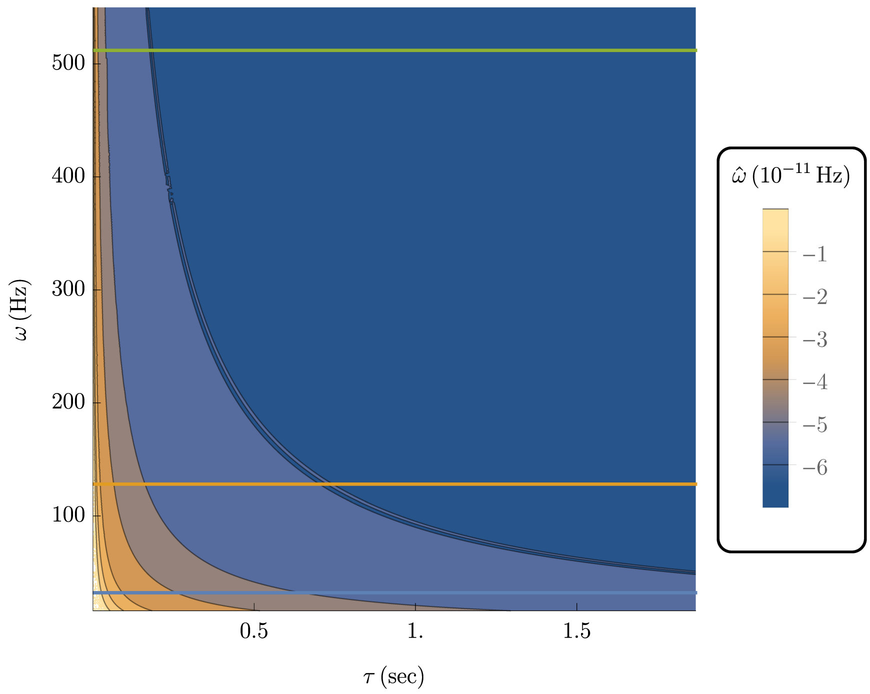

Figure 4.2: Retarded-time dependence of frequency shift $\hat{\omega}$ for plain waves of several discrete values of initial frequency. Higher initial frequencies approach the limiting $\hat{\omega}_{\max}$ exponentially faster.

4.5.1 Numerical solution for the transport equation

Assuming the real part of the zeroth-order amplitude of the plane wave (4.50) travelling in the equatorial plain $\vartheta = \pi/2$ in z-direction to be

$$A^{(0)}_{\mu\nu} = (a^{(0)}_{+} e^{+}_{\mu\nu} + a^{(0)}_{\times} e^{\times}_{\mu\nu}) \sin[t_r \omega], \tag{4.63}$$

with the retarded time obtained from eq. (1.51) as

$$t_r = -e^{\nu(z)}t + e^{\lambda(z)}z/c, \tag{4.64}$$

with the metric potentials e^ν, e^λ correspond to the ones in the line element (4.24), the transport equation (4.62) reduces to the form of

$$\begin{aligned}&\left([64C_2\hat{\omega}^2 + C_1\omega - 2\lambda']a_+^{(0)} + C_0\hat{\omega}a_\times^{(0)}\right)\cos\left(t_r\hat{\omega}\right)\\ &+\left(4[S_2\omega + S_1]\hat{\omega}a_+^{(0)} + 3\lambda'^2 a_\times^{(0)}\right)\sin\left(t_r\hat{\omega}\right) = 2\kappa(\rho - 5p)e^{3\lambda}a_+^{(0)},\end{aligned} \tag{4.65}$$

where primes denote partial differentiation with respect to coordinate z and

$$\begin{aligned} C_2 =&\ e^{2\lambda}(1+z\lambda')^2 + t^2e^{2\nu}\nu'^2 - e^{\lambda+\nu}\left(1 + 2\nu' t\left[1 + z\lambda'\right]\right)\\ C_1 =&\ e^{4\lambda}[\nu' + \lambda'(19 + 11z\lambda' + z\nu') + 8z\lambda'']\\ C_0 =&\ 24\lambda'\left[e^\lambda(1+z\lambda') - t\nu' e^\nu\right] - 24te^{3\lambda+\nu}(3\nu'\lambda' + 9\nu'^2 + 8\nu'')\\ S_2 =&\ e^{5\lambda}(1+z\lambda')^2 - 2te^{4\lambda+\nu}(1+z\lambda')\nu' + e^{3\lambda+2\nu}(1+t^2\nu'^2)\\ S_1 =&\ 16e^\lambda(2\lambda + z\lambda'^2 + z\lambda'') - 16te^\nu(\nu'^2 - \nu'')\end{aligned} \tag{4.66}$$

are functions of $(t,\, z)$ alone. For the sake of the simpler representation of the following results, the coordinate time t is to be replaced by the retarded time t_r. The numerical solution for $\hat{\omega}$ given by (4.65) for any possible values of $(t_r,\, \omega)$ is expected to be negative, owing to the energy dissipation, and to be extremely small compared to the initial frequency ω. Having the eqs. (4.24–4.23) applied for a nebula of radius $R = 50$ pc [1], the maximal decrease in frequency is found to be $\hat{\omega}_{\text{max}} = -6.3956 \times 10^{-11}$ Hz. Here and thereafter the order of magnitude of amplitudes $(a_+^{(0)},\, a_\times^{(0)})$ is set to $\mathcal{O}(10^{-21})$. All the frequency components that constitute the waveform suffer a tiny, gradually decreasing 'redshift-like' change in frequency, denoted by $\hat{\omega}$, that depends on the initial frequency and the position of wavefront. Fig. 4.2 displays the frequency shift $\hat{\omega}$ on a log scale for

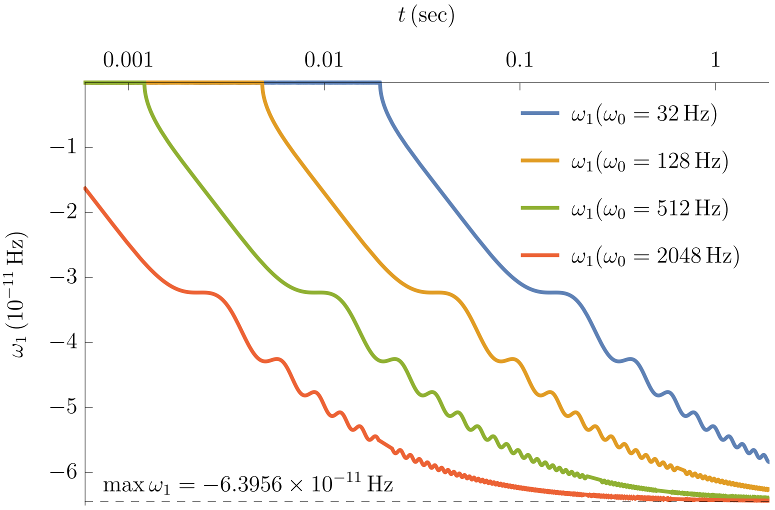

Figure 4.3: Frequency shift in the low-frequency regime. The horizontal lines represent the first three initial frequency values (32 Hz, 128 Hz, 512 Hz) shown in Fig. 4.2 with respective colours.

several discrete values of initial frequency for an arbitrary plane wave (4.63) that lasts for $t_r = 2$ sec. The figure reveals a characteristic distinctive feature of self-similarity of the frequency-shift curves for different initial frequencies. A more detailed figure, Fig. 4.3 demonstrates the frequency shifts that belong to any initial frequency in the (t_r, ω) domain. For the gravitational-wave transient GW150914, the effect is the greatest in the frequency range 100–250 Hz.

4.5.2 Matched filtering techniques for gravitational-wave data analysis

Putative frequency modulated GW signals (also known as '*chirps*') from CBC inspirals will be buried in the noisy data streams of the advanced detectors. Data analysis of targeted search extract any possible signal from the white Gaussian noise by cross-correlating the discrete-time sequences of the detector data against a large set of theoretical waveform templates as *filters*. [110] In signal processing, this technique allows us to efficiently extract faint gravitational-wave signals of known form from a noise-dominated data and the matched filter is obtained as the optimal linear filter for maximizing the SNR in the presence of additive stochastic noise. In a similar way, I investigate the correlation of a theoretically given template waveform (h_1) with the one that have been alterated (h_2) by the interaction with the medium. The technique is based on correlating the output of detectors with waveform templates. The noise-weighted inner product of two time-domain waveforms $h_1(t)$ and $h_2(t)$ is defined by

$$\langle h_1 | h_2 \rangle = 4\Re \int_{f_{\min}}^{f_{\max}} \frac{\tilde{h}_1^*(f)\tilde{h}_2(f)}{S_n(f)}\,\mathrm{d}f, \tag{4.67}$$

where the limits of integration $(f_{\min}, f_{\max})$ correspond to the upper and lower sidebands of the detector. The $S_n(f)$ is the power-spectral density due to instrument noise[205] and $\tilde{h}^*(f)$ is the Fourier transform of the respective time series $h(t)$. The expectation value of the optimal matched filtering to examine differences in waveforms is to measure their overlap $\mathcal{O}$, which is

$$\mathcal{O} = \max_{t_0, \psi_0} \frac{\langle h_1 | h_2 \rangle}{\sqrt{\langle h_1 | h_1 \rangle \langle h_2 | h_2 \rangle}} \equiv 1 - \mathcal{M}. \tag{4.68}$$

The overlap is maximalized over the initial time t_0 and phase ψ_0 of the template waveform. It is also related to the mismatch $\mathcal{M}$ between signal and template. For a straight forward derivation of eqs. (4.67–4.68) cf. [206]. The $S_n(f)$ is the power-spectral density due to instrument noise[205] and $\tilde{h}^*(f)$ is the Fourier transform of the respective time series $h(t)$. The expectation value of the optimal linear filter (or matched filter) is by measure the overlap (4.68) to examine differences in waveforms. The power-spectral density $S_n(f)$ of the detector noise was taken from the average-measured strain-equivalent noise, or sensitivity, of the aLIGO detectors at Hanford (H1) and Livingston (L1) sites (within bandwidth 0.125–8192 Hz) at the time the gravitational-wave event designated 'GW150914' was observed. The template $h_1(f)$ represents the reconstructed time series of the gravitational-wave transient signal that was released for event GW150914 by the LSC and Virgo Collaboration [69, 205]. $h_2(f) \equiv h_1(f + \hat{f})$ denotes the signal $h_1(f)$ altered by the small frequency change $\hat{f}$, where $\hat{f} \equiv \hat{\omega}/2\pi$. The deviation of the altered frequency $\tilde{f} \equiv f + \hat{f}$ from the original frequency f is most prominently observed in the interval

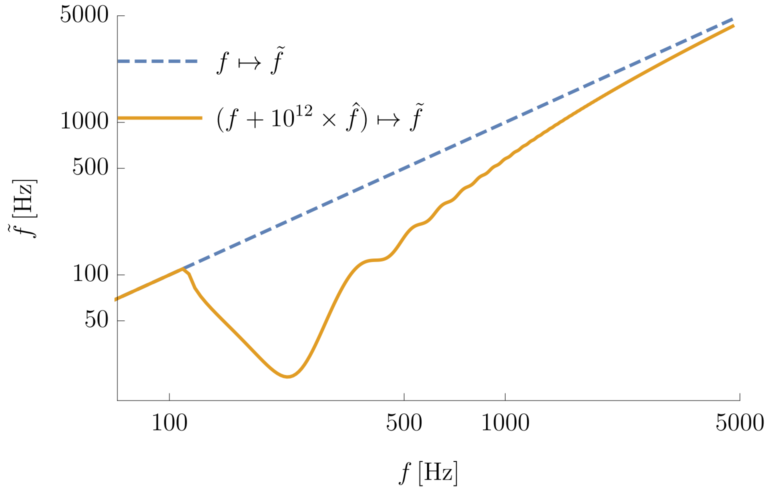

Figure 4.4: The dashed blue line represents the identity map, whereas the solid orange line shows the expected deviation in frequency for transient event GW150914 after it crossed the medium. The frequency shift is very small for the specific system examined here, therefore $\hat{f}$ was amplified by a factor of 10^{12} to better illustrate the nature of this phenomenon.

of 110–380 Hz in the frequency domain, known as super-low frequency. The change of frequency in the entire frequency band, specific for transient event GW150914 is shown in Fig. 4.4. The change is very small for the specific system I examined, therefore $\hat{f}$ was amplified by a factor of 10^{12} to better illustrate its nature in Fig. 4.4. The rapid growth of $\tilde{f}$ starting at $f = 110$ Hz comes to a standstill at a major low peak at $f = 220$ Hz. From that point on, $\tilde{f}$ approaches $\hat{\omega}_{\max}/2\pi$ at a much slower rate. It also comes to one's attention that in the kHz regime, the deviation is nearly comparable with the original frequency f. Due to the non-linear change in frequency, the signal distortion exhibits a complex behaviour. Fig. 4.5 shows the magnitude of the original and the altered signal – where $\hat{f}$ was amplified by a factor of 10^{12} – from GW150914 (h_1 and h_2, respectively) versus the frequency in the band 100–250 Hz.

To measure the actual difference between the original signal and the frequency-altered counterpart, I calculated the overlap (4.68) for Hanford detector's PSD (due to its better sensitivity in low-frequencies compared to $L1$). Consequently, the overlap is $\mathcal{O}_{H1} = 0.970995$ for a signal $h_2(f)$ in which the contribution of $\hat{f}$ was amplified by a factor of 10^{12}. Apart from demonstrational purposes (cf. Figs. 4.4, 4.5) the amplification was required to appropriately increase the numeric working precision which would not have been large enough to suppress numerical errors otherwise. Fig. 4.6 shows the UPEs of $h_1(f)$ and $h_2(f)$ (same as in Fig. 4.5) projected onto sensitivity curves of aLIGO detectors.

4.6 Summary of GW–matter interaction

In order to provide a more accurate picture of expected waveforms for direct detection, I have carried out a general study on the interaction of gravitational waves with matter. I have considered the wave passing through a vast spherical assemblage of cold, compressible gas, called a GMC. Gravitational waves were treated as linearized metric perturbations embedded in an interior Schwarzschild spacetime that belongs to nebula. The perturbed quantities lead to the field equations governing the gas dynamics and de-

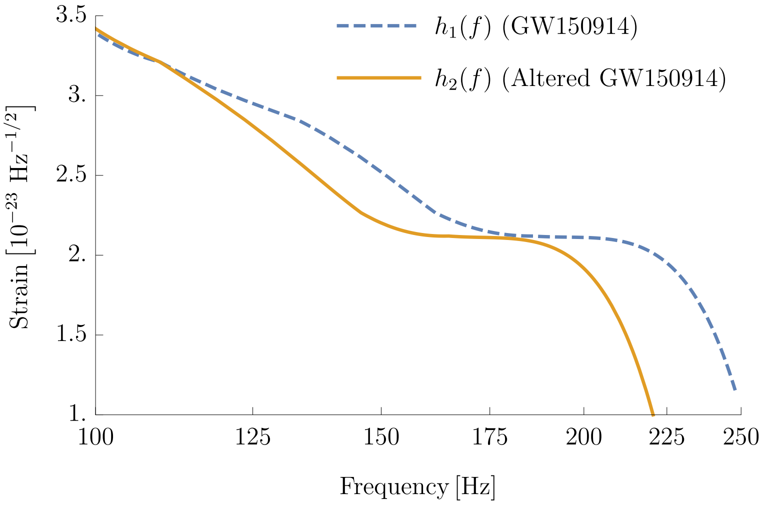

Figure 4.5: The upper peak envelope of the coincident signal in GW150914 $h_1(f)$ (dashed blue line) and its frequency-altered counterpart $h_2(f)$ (solid orange line) in frequency regime above 100 Hz. As in Fig. 4.3, the frequency shift $\hat{f}$ in the argument of h_2 has been amplified by 10^{12}. Both curves are fitted on maxima points by cubic spline interpolation.

scribe the interaction of gravitational waves with matter. The field equations decoupled to a set of PDEs of different orders of magnitude by WKB approximation, assuming the GW-amplitude to relatively slowly vary compared to the rapid oscillation of the phase. In the frame of WKB approximation, the dispersion relation indicates three distinct degenerate modes of polarization. Two of them are regular and correspond to gravitational and sound waves obeying the transport equations along rays (determined via Hamilton's ODEs on characteristic hypersurfaces), whereas the zero-frequency one is singular and represents non-propagating density and vorticity perturbations of the dispersive medium. See corresponding result in Refs. [196–198]. In regular case, the primary amplitudes follow null-characteristics (cf. Sec. 4.4.2), whereas the obtained transport equation of secondary amplitudes depends upon gas density in geometrical-optics limit.

The principal result established in this chapter is the demonstration that in the framework of post-geometrical optics, the transport equation of secondary amplitudes provides numerical solutions for the frequency shift $\hat{f}$. On the grounds that the energy dissipating process is responsible for decreasing frequency, $\hat{f}$ is bound to be negative, yet extremely small compared to the unaltered frequency f.

As an illustrative example, I considered a nebula with a mass assigned to an average-sized GMC, namely $10^5\ M_\odot$ and a diameter of 100 parsecs (typically ranges 5–200 parsecs). Whereas the average density in the solar vicinity is one particle per cubic centimeter, the average density of a GMC is a hundred to a thousand times as great. (See, e.g. Table 1 and the Appendix of [207].) In fact, even in such a dense environment, for any unaltered frequency that falls within the bandwidth of current advanced ground-based detectors the frequency shift still remains so small (ca. 10^{-11} Hz) that its influence is practically untraceable: the resulting mismatch $\mathcal{M}$ between measurement and expectation was barely 2.9005×10^{-14}. Despite the fact that the frequency-shift pattern exhibits a power-law relationship between f and $\hat{f}$, such small changes in the frequency will still remain far below the frequency resolution of third-generation detectors.

For sources in the 1–2 kHz frequency range, the influence of the interaction on the

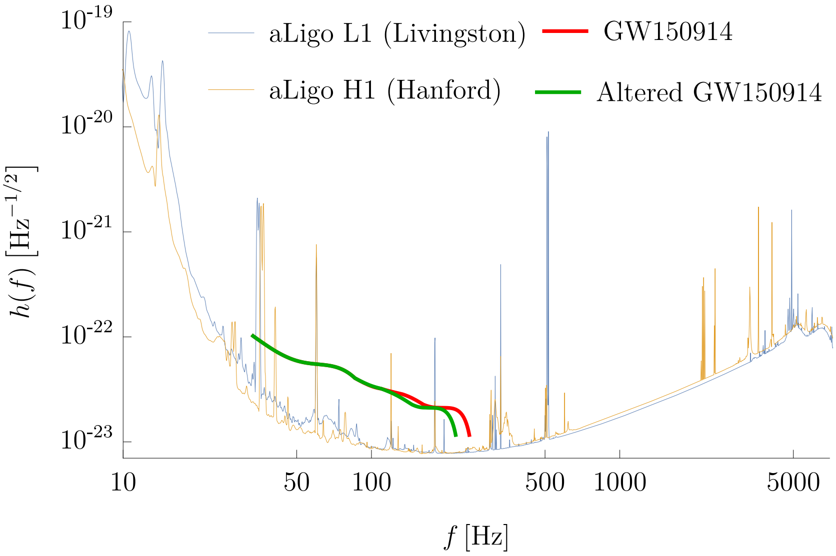

Figure 4.6: The upper peak envelope of GW strain amplitude of the coincident signal in GW150914 $h_1(f)$ (solid red line) and its frequency-altered counterpart $h_2(f)$ (solid green line) are projected onto the sensitivity curve of LIGO detector at Hanford (thin light blue line) in the full bandwidth of the detector. As in Figures 4.4 and 4.5, the frequency change $\hat{f}$ amplified by 10^{12} in the argument of h_2.

signal may increase significantly compared to that of the value on initial frequency of 100–200 Hz. Such high-frequency signals are expected to be emitted from the post-merger phase of low-mass NS mergers such as the GW event GW170817, which originated from a BNS system. [73] The dominant frequency of the post-merger signal from two NSs (each with mass 1.2 $M_\odot$ and with the EOS LS220) was computed at 2.56 kHz by relativistic simulations. [208] It is also noteworthy that mergers of the above-mentioned sources are detectable over much greater distances than those of stellar-mass BBHs such as GW150914, which was emitted from a BBH system of chirp mass $\mathcal{M} = 28.2^{+1.8}_{-1.7}\ M_\odot$ (cf. definition in (1.6)) at a luminosity distance $d_L = 440^{+160}_{-180}$ Mpc. Moreover, even higher frequencies (3–4 kHz) of quasi-periodic signals are expected from the formation of the hypermassive NSs. [68]

Another possibility to significantly ‘boost’ the effect is to increase the density of the environment by taking AGN into consideration. Suppose that an event of dynamical merger occurs in the central region of an AGN and it is observed over its dissipative accretion disk. In this extremely favorable but rare angular position, $\hat{f}$ might be sufficiently large to be measured.

Appendix A

Appendix

A.1 Components of the stress–energy tensor for non-perfect fluids

I will enumerate the non-vanishing components of the NPF stress–energy tensor $(T_{\mathrm{NPF}})^{\mu}_{\ \nu}$ referred in eq. (3.53b). To explicitly evaluate them, the arithmetic operations in eqs. (3.30–3.27) have to performed. The non-vanishing components of the zeroth-order are

$$(T_0^{\mathrm{NPF}})^1_{\ 0} = -e^{\lambda_0-\nu_0}(T_0^{\mathrm{NPF}})^0_{\ 1} = \frac{1}{4}e^{-\nu_0/2}\left[8\kappa T' + (12\eta - \kappa T)\,\nu_0'\right], \tag{A.1}$$

those of the first-order are

$$\begin{aligned} \frac{(T_1^{\mathrm{NPF}})^2_{\ 2} + (T_1^{\mathrm{NPF}})^3_{\ 3} - 2(T_1^{\mathrm{NPF}})^1_{\ 1}}{r} &= \frac{e^{-\nu_0/2}}{r}\left(A_0\upsilon_1 + \eta\dot{\lambda}_1\right) \\ (T_1^{\mathrm{NPF}})^1_{\ 0} = -e^{\lambda_0-\nu_0}(T_1^{\mathrm{NPF}})^0_{\ 1} &= e^{-\nu_0/2}\left[3\eta\nu_0'\nu_1 - \left(\eta - \frac{1}{4}\kappa T\right)\nu_1'\right] \end{aligned} \tag{A.2}$$

with an only radial-dependent coefficient

$$A_0 = \eta\left[\left(1 + 3e^{\nu_0-\lambda_0}\right)\nu_0' - 9\lambda_0' - \frac{2}{r}e^{\lambda_0}\right] + \kappa\left[T\nu_0' - 8T'\right]. \tag{A.3}$$

In view of (A.2), it is evident that to abide by the nature of harmonic time-dependence, a relation of the form

$$(\dot{T}_1^{\mathrm{NPF}})^1_{\ 0} = i\frac{\Omega}{c}(T_1^{\mathrm{NPF}})^1_{\ 0} \tag{A.4}$$

is implied. According to the definition (3.51), this implication requires

$$\dot{\upsilon}_1 = -\frac{\Omega^2}{c^2}\xi_1 - i\frac{\Omega}{c}\frac{(T_1^{\mathrm{NPF}})^1_{\ 0}}{\bar{p}_0 + \bar{\epsilon}_0} \tag{A.5}$$

to hold. In regard to to eq. (A.5), the expression $e^{\lambda_0-\nu_0}(\dot{T}_1^{\mathrm{NPF}})^1_{\ 0}$ is combined with $\mathcal{T}$ given by eq. (3.60) to compose

$$\mathcal{S}_1 = -\frac{1}{2}(T_0^{\mathrm{NPF}})^0_{\ 1}(\dot{\lambda}_1 + \dot{\nu}_1) + \frac{(T_1^{\mathrm{NPF}})^2_{\ 2} + (T_1^{\mathrm{NPF}})^3_{\ 3} - 2(T_1^{\mathrm{NPF}})^1_{\ 1}}{r} \tag{A.6}$$

which first appears in eq. (3.71). Substituted with the set of eqs. (A.1–A.5), the expression unfolds as

$$\mathcal{S}_1 = \frac{e^{-\nu_0/2}}{r}\left(\eta\lambda_1 + A_0\xi_1 - A_0\frac{(T_1^{\mathrm{NPF}})^1_{\ 0}}{\bar{p}_0+\bar{\epsilon}_0}\right) - \frac{1}{2}(T_0^{\mathrm{NPF}})^1_{\ 0}(\lambda_1+\nu_1). \tag{A.7}$$

Next to the $\mathcal{S}_1$, another quantity, expressed by

$$\mathcal{S}_2 = e^{-(\lambda_0+2\nu_0)/2}\frac{\mathrm{d}}{\mathrm{d}r}\left[\frac{e^{\lambda_0+2\nu_0}}{r^2}\left(\frac{\partial\bar{N}_0}{\partial\bar{p}_0}\right)^{-1}\frac{\mathrm{d}}{\mathrm{d}r}\left(r^2e^{-(\lambda_0+2\nu_0)/2}\bar{N}_0\frac{(T_1^{\mathrm{NPF}})^1_{\ 0}}{\bar{p}_0+\bar{\epsilon}_0}\right)\right]. \tag{A.8}$$

appears in different forms the pulsation equation, namely in eqs. (3.87) and (3.84). Together, they constitute the expression $i(\Omega\mathcal{S}_1 - \Omega^{-1}\mathcal{S}_2)$ which represents the source of inhomogenity of the SL equation.

A.2 Geometrized units

Throughout the dissertation, I adopt a system of so-called ‘geometrized’ units, often used in general relativity, in which the base physical units are chosen so that

$$\begin{array}{ll} \text{the speed of light:} & c = 2.9979\times10^{8}\ \mathrm{m/s}, \\ \text{the reduced Planck constant:} & \hbar = 1.0546\times10^{34}\ \mathrm{J\ s}, \\ \text{the electric constant:} & \epsilon_0 = 8.8542\times10^{12}\ \mathrm{A^2\ s^4\ kg^{-1}\ m^{-3}}, \\ \text{the Boltzmann constant:} & k_B = 1.3806\times10^{23}\ \mathrm{J\ K^{-1}} \end{array} \tag{A.9}$$

are all set equal to unity. In this system, every time interval is interpreted as the distance travelled by light during that given time interval. Consequently, physical quantities such as mass, energy, and momentum are identified with the magnitude of a timelike vector and acquire the geometric dimension of length, whereas velocity, force, and power are dimensionless. The desired SI unit of ($\mathrm{kg}^{\alpha}\ \mathrm{m}^{\beta}\ \mathrm{s}^{\gamma}$) can always be recovered from geometrized units of ($\mathrm{m}^{\alpha+\beta+\gamma}$) by multiplying with the conversion factor $G^{-\alpha}c^{2\alpha-\gamma}$. Table A.1 provides conversion factors for some commonly used kinematical variables are listed below where SI units are expressed in corresponding geometrized units.

Variable	SI unit	Geometrized unit	Factor	Geometrized unit → SI unit
mass	kg	m	$G^{-1}c^2$	1 m → 1.3466×10^{27} kg
length	m	m	1	1 m → 1 m
time	s	m	c^{-1}	1 m → 3.3356×10^{-9} s
energy	kg m^2 s^{-2}	m	$G^{-1}c^4$	1 m → 1.2102×10^{44} kg m^2 s^{-2}
energy density	kg m^{-1} s^{-2}	m^{-2}	$G^{-1}c^4$	1 m^{-2} → 1.2102×10^{44} kg m^{-1} s^{-2}
momentum	kg m s^{-1}	m	$G^{-1}c^3$	1 m → 4.0370×10^{35} kg m s^{-1}
angular momen.	kg m^2 s^{-1}	m^2	$G^{-1}c^3$	1 m^2 → 4.037×10^{35} kg m^2 s^{-1}
velocity	m s^{-1}	dimensionless	c	1 → 2.9979×10^{8} m s^{-1}
acceleration	m s^{-2}	m^{-1}	c^2	1 m^{-1} → 8.9875×10^{16} m s^{-2}

Table A.1: Geometrized units for some commonly used kinematical variables. To convert geometrized unit to SI unit, multiply by the factor ($G^{-\alpha}c^{2\alpha-\gamma}$) with appropriate exponents to obtain the units desired. And for the reverse conversion, from SI unit to geometrized unit, divide by the same factor. (For reference, cf. Ref. [209])

Fig. (3.3) exposes that the radius of neutron stars typically varies from about 10 to 14 kilometres. In fact, if kilometres are chosen as the characteristic length scale in the discretized stellar structure models, the total mass, energy-density, and pressure of neutron stars become comparable in geometrized units. For polytropic equations of state (3.3) with arbitrarily chosen value of polytropic index

$$n = (\Gamma_1 - 1)^{-1}, \tag{A.10}$$

the corresponding 'polytropic constant' K is given by

$$K = 2 \times 10^{12}\, G^{\Gamma_1 - 1} c^{4 - 2\Gamma_1} \tag{A.11}$$

in units of $m^{2\Gamma_1 - 2}$ where Γ_1 is the adiabatic index 3.7. In particular, I evaluate models for the following values of K and n: ($n = 1$, $K = 100$ km^2), ($n = 0.8$, $K = 700$ km$^{2.5}$), ($n = 0.5$, , $K = 2 \times 10^5$ km^4).

Bibliography

Publications that form the basis of the dissertation

[1] **D. Barta**. “Relativistic model for cold spherical interstellar gas clouds”. In: *Astron. Nachr.* 334.9 (2013), p. 916. DOI: `10.1002/asna.201211958`. arXiv: `1708.05570 [gr-qc]`.

[2] **D. Barta** and M. Vasúth. “Dispersion of gravitational waves in cold spherical interstellar medium”. In: *Int. J. Mod. Phys. D* 27.4 (2018), p. 1850040. DOI: `10.1142/S0218271818500402`. arXiv: `1708.05576 [gr-qc]`.

[3] **D. Barta** and M. Vasúth. “Fast prediction and evaluation of eccentric inspirals using reduced-order models”. In: *Phys. Rev. D* 97.12 (2018), p. 124011. DOI: `10.1103/PhysRevD.97.124011`. arXiv: `1803.00348 [gr-qc]`.

[4] **D. Barta**. “Effect of viscosity and thermal conductivity on the radial oscillation and relaxation of relativistic stars”. In: *Class. Quantum Grav.* 36.21 (2019), p. 215012. DOI: `10.1088/1361-6382/ab472e`. arXiv: `1904.00907 [gr-qc]`.

[5] **D. Barta**. “Fundamental oscillation modes and thermal relaxation in young neutron stars”. In: *preprint* (2019). In preparation. arXiv: `1908.02808 [gr-qc]`.

Publications of the LSC and Virgo Collaboration

[43] The LIGO Scientific Collaboration, the Virgo Collaboration, including **D. Barta**, et al. “Observation of Gravitational Waves from a Binary Black Hole Merger”. In: *Phys. Rev. Lett.* 116.6 (2016), p. 061102. DOI: `10.1103/PhysRevLett.116.061102`. arXiv: `1602.03837 [gr-qc]`.

[49] The LIGO Scientific Collaboration, the Virgo Collaboration, including **D. Barta**, et al. “Prospects for observing and localizing gravitational-wave transients with Advanced LIGO, Advanced Virgo and KAGRA”. In: *Living Rev. Relativ.* 21.1 (2018), p. 3. DOI: `10.1007/s41114-018-0012-9`.

[54] The LIGO Scientific Collaboration, the Virgo Collaboration, including **D. Barta**, et al. “Sensitivity of the Advanced LIGO detectors at the beginning of gravitational wave astronomy”. In: *Phys. Rev. D* 93.11 (2016), p. 112004. DOI: `10.1103/PhysRevD.93.112004`.

[59] The LIGO Scientific Collaboration, the Virgo Collaboration, including **D. Barta**, et al. "Data analysis challenges in transient gravitational-wave astronomy". In: *American Institute of Physics Conference Series*. Ed. by R. Lahmann et al. Vol. 1535. American Institute of Physics Conference Series. May 2013, pp. 252–259. DOI: `10.1063/1.4807558`. arXiv: `1210.7173 [gr-qc]`.

[61] The LIGO Scientific Collaboration, the Virgo Collaboration, including **D. Barta**, et al. "GWTC-1: A Gravitational-Wave Transient Catalog of Compact Binary Mergers Observed by LIGO and Virgo during the First and Second Observing Runs". In: *Phys. Rev. X* 9.3 (2019), p. 031040. DOI: `10.1103/PhysRevX.9.031040`.

[63] The LIGO Scientific Collaboration, the Virgo Collaboration, including **D. Barta**, et al. "Exploring the sensitivity of next generation gravitational wave detectors". In: *Class. Quant. Grav.* 34.4 (2017), p. 044001. DOI: `10.1088/1361-6382/aa51f4`. arXiv: `1607.08697 [astro-ph]`.

[69] The LIGO Scientific Collaboration, the Virgo Collaboration, including **D. Barta**, et al. "Observation of Gravitational Waves from a Binary Black Hole Merger". In: *Phys. Rev. Lett.* 116 (6 2016), p. 061102. DOI: `10.1103/PhysRevLett.116.061102`.

[70] The LIGO Scientific Collaboration, the Virgo Collaboration, including **D. Barta**, et al. "GW150914: First results from the search for binary black hole coalescence with Advanced LIGO". In: *Phys. Rev. D* 93 (12 2016), p. 122003. DOI: `10.1103/PhysRevD.93.122003`.

[71] The LIGO Scientific Collaboration, the Virgo Collaboration, including **D. Barta**, et al. "GW151226: Observation of Gravitational Waves from a 22-Solar-Mass Binary Black Hole Coalescence". In: *Phys. Rev. Lett.* 116 (24 2016), p. 241103. DOI: `10.1103/PhysRevLett.116.241103`.

[72] The LIGO Scientific Collaboration, the Virgo Collaboration, including **D. Barta**, et al. "Binary Black Hole Mergers in the First Advanced LIGO Observing Run". In: *Phys. Rev. X* 6 (4 2016), p. 041015. DOI: `10.1103/PhysRevX.6.041015`.

[73] The LIGO Scientific Collaboration, the Virgo Collaboration, including **D. Barta**, et al. "GW170817: Observation of Gravitational Waves from a Binary Neutron Star Inspiral". In: *Phys. Rev. Lett.* 119 (16 2017), p. 161101. DOI: `10.1103/PhysRevLett.119.161101`.

[99] The LIGO Scientific Collaboration, the Virgo Collaboration, including **D. Barta**, et al. "Parameter estimation for compact binary coalescence signals with the first generation gravitational-wave detector network". In: *Phys. Rev. D* 88.6 (Sept. 2013), p. 062001. DOI: `10.1103/PhysRevD.88.062001`.

[119] The LIGO Scientific Collaboration, the Virgo Collaboration, including **D. Barta**, et al. "Search for gravitational waves from binary black hole inspiral, merger, and ringdown in LIGO-Virgo data from 2009–2010". In: *Phys. Rev. D* 87.2 (2013), p. 022002. DOI: `10.1103/PhysRevD.87.022002`.

[205] The LIGO Scientific Collaboration, the Virgo Collaboration, including **D. Barta**, et al. In: *Data release for event GW150914* (2016). doi:10.7935/K5MW2F23.

Publications of historical significance

[35] H. Lorentz. “Elektromagnetische verschijnselen in een stelsel dat zich met willekeurige snelheid, kleiner dan die van het licht. (Dutch) [Electromagnetic phenomena in a system moving with any velocity smaller than that of light]”. In: *Proceedings of the Royal Netherlands Academy of Arts and Sciences* 6 (1904), 809–831. DOI: 10.1007/978-94-015-3445-1_5.

[36] H. Poincaré. “Sur la dynamique de l’électron. (French) [On the dynamics of the electron]”. In: *Comptes Rendues de l’Académie des Sciences* 140 (June 1905), 1504–1508. DOI: 10.1007/BF03013466.

[37] A. Einstein. “Näherungsweise Integration der Feldgleichungen der Gravitation. (German) [Approximative integration of the field equations of gravitation]”. In: *Sitzungsberichte der Königlich Preußischen Akademie der Wissenschaften zu Berlin* 1 (June 1916), 688–696. DOI: 10.1007/978-3-662-57411-9_13.

[38] A. Einstein and N. Rosen. “On Gravitational Waves”. In: *J. Franklin Inst.* 223 (Jan. 1937), pp. 43–54. DOI: 10.1016/S0016-0032(37)90583-0.

[39] Y. Fourès-Bruhat (Choquet-Bruhat). “Théorème d’existence pour certains systèmes d’équations aux dérivées partielles non linéaires. (French) [Existence theorem for certain systems of nonlinear partial differential equations]”. In: *Acta Mathematica (Djursholm)* 88.1 (1952), pp. 141–225. DOI: 10.1007/BF02392131.

[40] H. Bondi. “Plane gravitational waves in general relativity”. In: *Nature* 179 (1957), pp. 1072–1073. DOI: 10.1038/1791072a0.

[41] F. Pirani. “Invariant Formulation of Gravitational Radiation Theory”. In: *Phys. Rev.* 105.3 (Feb. 1957), pp. 1089–1099. DOI: 10.1103/PhysRev.105.1089.

[42] H. Bondi, F. A. E. Pirani, and I. Robinson. “Gravitational Waves in General Relativity. III. Exact Plane Waves”. In: *Proc. Roy. Soc. London Ser. A* 251 (June 1959), pp. 519–533. DOI: 10.1098/rspa.1959.0124.

[44] I. Robinson and A. Trautman. “Some spherical gravitational waves in general relativity”. In: *Proc. Roy. Soc. Lond.* A265 (1962), pp. 463–473. DOI: 10.1098/rspa.1962.0036.

[45] Andrzej Trautman. “Radiation and Boundary Conditions in the Theory of Gravitation”. In: *Bull. Acad. Pol. Sci. Ser. Sci. Math. Astron. Phys.* 6.6 (1958), pp. 407–412. arXiv: 1604.03145 [gr-qc].

[46] R. A. Hulse and J. H. Taylor. “Discovery of a pulsar in a binary system”. In: *Astrophys. J. Lett.* 195 (Jan. 1975), pp. L51–L53. DOI: 10.1086/181708.

[47] J. H. Taylor and J. M. Weisberg. “A new test of general relativity - Gravitational radiation and the binary pulsar PSR 1913+16”. In: *Astrophys. J.* 253 (Feb. 1982), pp. 908–920. DOI: 10.1086/159690.

[48] S. Chandrasekhar. “The Post-Newtonian Equations of Hydrodynamics in General Relativity.” In: *Astrophys. J.* 142 (Nov. 1965), p. 1488. DOI: 10.1086/148432.

[50] J. Weber. “Detection and Generation of Gravitational Waves”. In: *Phys. Rev.* 117.1 (Jan. 1960), pp. 306–313. DOI: 10.1139/cjp-2016-0615.

[55] M. E. Gertsenshtein and V. I. Pustovoit. “К вопросу об обнаружении гравитачионных волн малых частотстатья. (Russian) [On the detection of low-frequency gravitational waves]”. In: *Sov. Phys. JETP* 43.2 (Feb. 1962), pp. 605–607.

[57] R. Weiss. “Electric and Magnetic Field Probes”. In: *Am. J. Phys.* 35.11 (1967), pp. 1047–1048. DOI: 10.1119/1.1973723.

[58] R. Weiss. *Electromagnetically coupled broadband gravitational antenna.* Quarterly Report of the Research Laboratory for Electronics. MIT Report No. 105, 1972.

Other references

[6] V. Boriakoff. “Pulsar AP 2016+28 - High-frequency periodicity in the pulse microstructure”. In: *Astrophys. J. Lett.* 208 (Aug. 1976), pp. L43–L46.

[7] R. Ramaty and R. E. Lingenfelter. “Interpretations and implications of y-ray lines from solar flares, the galactic centre and y-ray transients”. In: *Phil. Trans. Roy. Soc.* 301.1462 (1981), pp. 671–686. DOI: 10.1098/rsta.1981.0151.

[8] E. N. Glass and L. Lindblom. “The radial oscillations of neutron stars”. In: *Astrophys. J. Sup.* 53 (Sept. 1983), pp. 93–103.

[9] E. N. Glass and A. Harpaz. In: *Mon. Not. R. Astron. Soc.* 202 (1983), pp. 159–171.

[10] Cecilia Chirenti, Roman Gold, and M. Coleman Miller. “Gravitational Waves from F-modes Excited by the Inspiral of Highly Eccentric Neutron Star Binaries”. In: *The Astrophysical Journal* 837.1 (2017), p. 67.

[11] K. C. Gendreau, Z. Arzoumanian, and T. Okajima. “Colloquium: Measuring the neutron star equation of state using x-ray timing”. In: *Proc. SPIE* 8443 (2012), p. 844313.

[12] A. L. Watts et al. “Colloquium: Measuring the neutron star equation of state using x-ray timing”. In: *Rev. Mod. Phys.* 88 (2 2016), p. 021001. DOI: 10.1103/RevModPhys.88.021001.

[13] P. Haensel, B. Paczynski, and P. Amsterdamski. “Gamma-ray bursts from colliding strange stars”. In: *Astrophys. J.* 375 (July 1991), pp. 209–215. DOI: 10.1086/170182.

[14] P. Haensel, J. L. Zdunik, and R. Schaeffer. “Phase transitions in dense matter and radial pulsations of neutron stars”. In: *Astron. Astrophys.* 217 (1989), pp. 137–144.

[15] S. Detweiler and L. Lindblom. “On the nonradial pulsations of general relativistic stellar models”. In: *Astrophys. J.* 292 (May 1985), pp. 12–15. DOI: 10.1086/163127.

[16] B. S. Sathyaprakash and B. F. Schutz. “Physics, Astrophysics and Cosmology with Gravitational Waves”. In: *Living Rev. Relat.* 12.1 (2009), p. 2. ISSN: 1433-8351. DOI: 10.12942/lrr-2009-2.

[17] V. Kalogera et al. “The Cosmic Coalescence Rates for Double Neutron Star Binaries”. In: *Astrophys. J. Lett.* 614 (2004), p. L137. DOI: 10.1086/425868.

[18] P. C. Peters. “Gravitational Radiation and the Motion of Two Point Masses”. In: *Phys. Rev.* 136.4B (1964), B1224–B1232. DOI: 10.1103/PhysRev.136.B1224.

[19] Antonini, F. and Perets, H. “Secular evolution of compact binaries near massive black holes: gravitational wave sources and other exotica”. In: *Astrophys. J.* 757.1 (2012), p. 27. DOI: 10.1088/0004-637x/757/1/27.

[20] S. L. Shapiro and S. A. Teukolsky. “The collapse of dense star clusters to supermassive black holes - The origin of quasars and AGNs”. In: *Astrophys. J.* 292 (May 1985), pp. 41–44. DOI: 10.1086/184469.

[21] V. Pierro and I. M. Pinto. “Gravitational-wave chirps: accumulating phase errors due to residual orbital eccentricity”. In: *I.M. Nuovo Cim B* 111.12 (1996), pp. 1517–1525. ISSN: 1826-9877. DOI: 10.1007/BF02741491.

[22] Martel, K. and Poisson, E. “Gravitational waves from eccentric compact binaries: Reduction in signal-to-noise ratio due to nonoptimal signal processing”. In: *Phys. Rev. D* 60.12 (1999), p. 124008. DOI: 10.1103/PhysRevD.60.124008.

[23] E. A. Huerta et al. “Accurate and efficient waveforms for compact binaries on eccentric orbits”. In: *Phys. Rev. D* 90.8 (Oct. 2014), p. 084016. DOI: 10.1103/PhysRevD.90.084016.

[24] N. Yunes et al. “Post-circular expansion of eccentric binary inspirals: Fourier-domain waveforms in the stationary phase approximation”. In: *Phys. Rev. D* 80.8 (Oct. 2009), p. 084001. DOI: 10.1103/PhysRevD.80.084001.

[25] C. Königsdörffer and A. Gopakumar. “Phasing of gravitational waves from inspiralling eccentric binaries at the third-and-a-half post-Newtonian order”. In: *Phys. Rev. D* 73.12 (June 2006), p. 124012. DOI: 10.1103/PhysRevD.73.124012.

[26] J. Samsing, M. MacLeod, and E. Ramirez-Ruiz. In: *Astrophys. J.* 784 (2014), p. 71.

[27] O’Leary, R. M. and Kocsis, B. and Loeb, A. In: *Mon. Not. R. Astron. Soc.* 395 (2009), p. 2127.

[28] W. H. Lee, E. Ramirez-Ruiz, and G. van de Ven. “Short Gamma-ray Bursts from Dynamically Assembled Compact Binaries in Globular Clusters: Pathways, Rates, Hydrodynamics, and Cosmological Setting”. In: *Astrophys. J.* 720 (Sept. 2010), pp. 953–975. DOI: 10.1088/0004-637X/720/1/953.

[29] D. A. Brown and P. J. Zimmerman. “Effect of eccentricity on searches for gravitational waves from coalescing compact binaries in ground-based detectors”. In: *Phys. Rev. D* 81.2 (Jan. 2010), p. 024007. DOI: 10.1103/PhysRevD.81.024007.

[30] M. Favata. “Systematic Parameter Errors in Inspiraling Neutron Star Binaries”. In: *Phys. Rev. Lett.* 112.10 (2014), p. 101101. DOI: 10.1103/PhysRevLett.112.101101.

[31] L. Bieri, D. Garfinkle, and N. Yunes. “Gravitational Waves and Their Mathematics”. In: *Notices Am. Math. Soc.* 64.7 (Aug. 2017), 673–808. DOI: 10.1090/noti/201707. arXiv: 1710.03272 [gr-qc].

[32] R. M. Wald. *General Relativity*. Chicago, USA: Chicago University Press, 1984. ISBN: 0226870332. DOI: 10.7208/chicago/9780226870373.001.0001.

[33] C. W. Misner, K. S. Thorne, and J. A. Wheeler. *Gravitation*. San Francisco, USA: W.H. Freeman and Co., 1973. ISBN: 0716703440.

[34] M. P. Hobson, G. P. Efstathiou, and A. N. Lasenby. *General Relativity: An Introduction for Physicists*. 1st ed. Cambridge: Cambridge University Press, Mar. 2006. ISBN: 0521829518. DOI: 10.1017/CBO9780511790904.

[51] P. Astone et al. “IGEC2: A 17-month search for gravitational wave bursts in 2005–2007”. In: *Phys. Rev. D* 82.2 (July 2010), pp. 022003–022012. DOI: 10.1103/PhysRevD.82.022003.

[52] E.N. Glass. “Gravitational radiation observations”. In: *Can. J. Physics* 94.12 (Dec. 2016), pp. 1251–1252. DOI: 10.1139/cjp-2016-0615.

[53] S. Boughn et al. “The use of cryogenic techniques to achieve high sensitivity in gravitational wave detectors”. In: Proceedings of the I.A.U. Conference on Gravitational Radiation and Gravitational Collapse. Warsaw, Poland, 1973.

[56] Nicolás Yunes and Xavier Siemens. “Gravitational-Wave Tests of General Relativity with Ground-Based Detectors and Pulsar-Timing Arrays”. In: *Living Rev. Relativ.* 16.1 (2013), p. 9. ISSN: 1433-8351. DOI: 10.12942/lrr-2013-9.

[60] Peter Fritschel. “Second generation instruments for the Laser Interferometer Gravitational Wave Observatory (LIGO)”. In: *Gravitational-Wave Detection*. Ed. by Peter Saulson and Adrian M. Cruise. Vol. 4856. International Society for Optics and Photonics. SPIE, 2003, pp. 282 –291. DOI: 10.1117/12.459090.

[62] M. Punturo et al. “The Einstein Telescope: a third-generation gravitational wave observatory”. In: *Class. Quant. Grav.* 27.19 (2010), p. 194002. DOI: 10.1088/0264-9381/27/19/194002.

[64] D. Blair, L. Ju, and Z. Zhu. “Gravitational wave astronomy: the current status”. In: *Sci. China-Phys. Mech. Astron.* 58.12 (Dec. 2015), p. 120401. DOI: 10.1007/s11433-015-5749-5.

[65] P. Jaranowski and A. Krolak. *Analysis of Gravitational-Wave Data*. Cambridge, UK: Cambridge University Press, 2009. ISBN: 9780511605482. DOI: 10.1017/CBO9780511605482.

[66] Yi-Ming Hu et al. “Global optimization for future gravitational wave detector sites”. In: *Class. Quantum Gravity* 32.10 (2015), p. 105010. DOI: 10.1088/0264-9381/32/10/105010.

[67] J. M. Weisberg and Y. Huang. “Relativistic Measurements from Timing the Binary Pulsar PSR B1913+16”. In: *Astrophys. J* 829.1 (2016), p. 55. DOI: 10.3847/0004-637x/829/1/55.

[68] Shibata et al. “Merger of binary neutron stars with realistic equations of state in full general relativity”. In: *Phys. Rev. D* 71 (8 2005), p. 084021. DOI: 10.1103/PhysRevD.71.084021.

[74] Theocharis A. Apostolatos et al. “Spin-induced orbital precession and its modulation of the gravitational waveforms from merging binaries”. In: *Phys. Rev. D* 49 (12 1994), pp. 6274–6297. DOI: 10.1103/PhysRevD.49.6274.

[75] L. E. Kidder. “Coalescing binary systems of compact objects to (post)$^{5/2}$-Newtonian order. V. Spin effects”. In: *Phys. Rev. D* 52.2 (1995), pp. 821–847. DOI: 10.1103/PhysRevD.52.821.

[76] Benjamin Farr et al. “A more effective coordinate system for parameter estimation of precessing compact binaries from gravitational waves”. In: *Phys. Rev. D* 90 (2 2014), p. 024018. DOI: 10.1103/PhysRevD.90.024018.

[77] Chinmay Kalaghatgi, Parameswaran Ajith, and K. G. Arun. “Template-space metric for searches for gravitational waves from the inspiral, merger, and ringdown of binary black holes”. In: *Phys. Rev. D* 91.12 (2015), p. 124042. DOI: 10.1103/PhysRevD.91.124042.

[78] Étienne Racine. “Analysis of spin precession in binary black hole systems including quadrupole-monopole interaction”. In: *Phys. Rev. D* 78 (4 2008), p. 044021. DOI: 10.1103/PhysRevD.78.044021.

[79] P. C. Peters and J. Mathews. “Gravitational Radiation from Point Masses in a Keplerian Orbit”. In: *Phys. Rev.* 131 (1 1963), pp. 435–440. DOI: 10.1103/PhysRev.131.435.

[80] Curt Cutler and Éanna E. Flanagan. “Gravitational waves from merging compact binaries: How accurately can one extract the binary’s parameters from the inspiral waveform?” In: *Phys. Rev. D* 49 (6 1994), pp. 2658–2697. DOI: 10.1103/PhysRevD.49.2658.

[81] L. Blanchet. “Gravitational Radiation from Post-Newtonian Sources and Inspiralling Compact Binaries”. In: *Living Rev. Relat.* 17 (2014), p. 2.

[82] Clifford M. Will. “The Confrontation between General Relativity and Experiment”. In: *Living Rev. Relativ.* 17.1 (2014), p. 4. ISSN: 1433-8351. DOI: 10.12942/lrr-2014-4.

[83] Douglas M. Eardley et al. “Gravitational-Wave Observations as a Tool for Testing Relativistic Gravity”. In: *Phys. Rev. Lett.* 30.18 (1973), pp. 884–886. DOI: 10.1103/PhysRevLett.30.884.

[84] Atsushi Nishizawa et al. “Probing nontensorial polarizations of stochastic gravitational-wave backgrounds with ground-based laser interferometers”. In: *Phys. Rev. D* 79 (8 2009), p. 082002. DOI: 10.1103/PhysRevD.79.082002.

[85] Alessandra Buonanno and B. S. Sathyaprakash. “Sources of Gravitational Waves: Theory and Observations”. In: *General Relativity and Gravitationn*. Ed. by Abhay Ashtekar et al. Cambridge: Cambridge University Press, 2015. Chap. 10, pp. 287–346. ISBN: 9781139583961. DOI: 10.1017/CBO9780511790904.

[86] P. Csizmadia et al. “Gravitational waves from spinning eccentric binaries”. In: *Class. Quant. Grav.* 29.24 (Nov. 2012), p. 245002. DOI: 10.1088/0264-9381/29/24/245002.

[87] Luc Blanchet. “Gravitational Radiation from Post-Newtonian Sources and Inspiralling Compact Binaries”. In: *Living Rev. Relativ.* 17.1 (2014), p. 2. ISSN: 1433-8351. DOI: 10.12942/lrr-2014-2.

[88] J. Levin, S. T. McWilliams, and H. Contreras. “Inspiral of generic black hole binaries: spin, precession and eccentricity”. In: *Class. Quant. Grav.* 28.17 (2011), p. 175001. DOI: 10.1088/0264-9381/28/17/175001.

[89] B. Allen et al. “FINDCHIRP: An algorithm for detection of gravitational waves from inspiraling compact binaries”. In: *Phys. Rev. D* 85.12 (2012), p. 122006. DOI: 10.1103/PhysRevD.85.122006.

[90] B. J. Owen. “Search templates for gravitational waves from inspiraling binaries: Choice of template spacing”. In: *Phys. Rev. D* 53.12 (1996), pp. 6749–6761. DOI: 10.1103/PhysRevD.53.6749.

[91] S. Babak, J. R. Gair, and E. K. Porter. “An algorithm for the detection of extreme mass ratio inspirals in LISA data”. In: *Class. Quant. Grav.* 26.13 (June 2009), p. 135004. DOI: 10.1088/0264-9381/26/13/135004.

[92] M. Pürrer. “Frequency domain reduced order model of aligned-spin effective-one-body waveforms with generic mass ratios and spins”. In: *Phys. Rev. D* 93.6 (Mar. 2016), p. 064041. DOI: 10.1103/PhysRevD.93.064041.

[93] B. S. Sathyaprakash and S. V. Dhurandhar. “Choice of filters for the detection of gravitational waves from coalescing binaries”. In: *Phys. Rev. D* 44.12 (1991), pp. 3819–3834. DOI: 10.1103/PhysRevD.44.3819.

[94] B. S. Sathyaprakash. “Filtering post-Newtonian gravitational waves from coalescing binaries”. In: *Phys. Rev. D* 50.12 (1994), R7111–R7115. DOI: 10.1103/PhysRevD.50.R7111.

[95] S. V. Dhurandhar and B. S. Sathyaprakash. “Choice of filters for the detection of gravitational waves from coalescing binaries. II. Detection in colored noise”. In: *Phys. Rev. D* 49.4 (1994), pp. 1707–1722. DOI: 10.1103/PhysRevD.49.1707.

[96] B. J. Owen and B. S. Sathyaprakash. “Matched filtering of gravitational waves from inspiraling compact binaries: Computational cost and template placement”. In: *Phys. Rev. D* 60.2 (June 1999), p. 022002. DOI: 10.1103/PhysRevD.60.022002.

[97] I. W. Harry, B. Allen, and B. S. Sathyaprakash. “Stochastic template placement algorithm for gravitational wave data analysis”. In: *Phys. Rev. D* 80.10 (Nov. 2009), p. 104014. DOI: 10.1103/PhysRevD.80.104014.

[98] P. Cañizares et al. “Gravitational wave parameter estimation with compressed likelihood evaluations”. In: *Phys. Rev. D* 87.12 (June 2013), p. 124005. DOI: 10.1103/PhysRevD.87.124005.

[100] A. H. Mroué et al. “Catalog of 174 Binary Black Hole Simulations for Gravitational Wave Astronomy”. In: *Phys. Rev. Lett.* 111.24 (Dec. 2013), p. 241104. DOI: 10.1103/PhysRevLett.111.241104.

[101] L. Pekowsky et al. “Comparing gravitational waves from nonprecessing and precessing black hole binaries in the corotating frame”. In: *Phys. Rev. D* 88.2 (July 2013), p. 024040. DOI: 10.1103/PhysRevD.88.024040.

[102] S. E. Field et al. “Fast Prediction and Evaluation of Gravitational Waveforms Using Surrogate Models”. In: *Phys. Rev. X* 4.3 (July 2014), p. 031006. DOI: 10.1103/PhysRevX.4.031006.

[103] S. E. Field et al. “Reduced Basis Catalogs for Gravitational Wave Templates”. In: *Phys. Rev. Lett.* 106.22 (2011), p. 221102. DOI: 10.1103/PhysRevLett.106.221102. URL: https://link.aps.org/doi/10.1103/PhysRevLett.106.221102.

[104] S. E. Field, C. R. Galley, and E. Ochsner. “Towards beating the curse of dimensionality for gravitational waves using reduced basis”. In: *Phys. Rev. D* 86.8 (2012), p. 084046. DOI: 10.1103/PhysRevD.86.084046.

[105] K. Cannon et al. “Singular value decomposition applied to compact binary coalescence gravitational-wave signals”. In: *Phys. Rev. D* 82.4 (Aug. 2010), p. 044025. DOI: 10.1103/PhysRevD.82.044025.

[106] K. Cannon, C. Hanna, and D. Keppel. “Efficiently Enclosing the Compact Binary Parameter Space by Singular-Value Decomposition”. In: *Phys. Rev. D* 84 (2011), p. 084003.

[107] Y. Maday and O. Mula. “A Generalized Empirical Interpolation Method: application of reduced basis techniques to data assimilation”. In: *NA* 4 (2013), pp. 221–235.

[108] K. Cannon, C. Hanna, and D. Keppel. “Interpolating compact binary waveforms using the singular value decomposition”. In: *Phys. Rev. D* 85 (2012), p. 081504.

[109] S. Privitera et al. “Improving the sensitivity of a search for coalescing binary black holes with nonprecessing spins in gravitational wave data”. In: *Phys. Rev. D* 89.2 (Jan. 2014), p. 024003. DOI: 10.1103/PhysRevD.89.024003.

[110] R. J. E. Smith et al. “Towards rapid parameter estimation on gravitational waves from compact binaries using interpolated waveforms”. In: *Phys. Rev. D* 87.12 (June 2013), p. 122002. DOI: 10.1103/PhysRevD.87.122002.

[111] P. Cañizares et al. “Accelerated Gravitational Wave Parameter Estimation with Reduced Order Modeling”. In: *Phys. Rev. Lett.* 114.7 (Feb. 2015), p. 071104. DOI: 10.1103/PhysRevLett.114.071104.

[112] P. Csizmadia et al. *CBwaves gravitational-waveform-template generator for compact binary objects*. 2011. URL: http://www.grid.kfki.hu/twiki/bin/view/RmiVirgo/CBwaves.

[113] L. Barack and C. Cutler. “LISA capture sources: Approximate waveforms, signal-to-noise ratios, and parameter estimation accuracy”. In: *Phys. Rev. D* 69.8 (Apr. 2004), p. 082005. DOI: 10.1103/PhysRevD.69.082005.

[114] H. P. Pfeiffer. “Numerical simulations of compact object binaries”. In: *Class. Quant. Grav.* 29.12 (June 2012), p. 124004. DOI: 10.1088/0264-9381/29/12/124004.

[115] C. Kalaghatgi, P. Ajith, and K. G. Arun. “Template-space metric for searches for gravitational waves from the inspiral, merger, and ringdown of binary black holes”. In: *Phys. Rev. D* 91.12 (June 2015), p. 124042. DOI: 10.1103/PhysRevD.91.124042.

[116] T. Cokelaer. “Gravitational waves from inspiralling compact binaries: Hexagonal template placement and its efficiency in detecting physical signals”. In: *Phys. Rev. D* 76.10 (Nov. 2007), p. 102004. DOI: 10.1103/PhysRevD.76.102004.

[117] M. Pürrer. “Frequency-domain reduced order models for gravitational waves from aligned-spin compact binaries”. In: *Classical and Quantum Gravity* 31.19 (Sept. 2014), p. 195010. DOI: 10.1088/0264-9381/31/19/195010.

[118] E. J. Candès, P. R. Charlton, and Helgason H. “Detecting highly oscillatory signals by chirplet path pursuit”. In: *Appl. Comput. Harmon. Anal.* 24.1 (2008), pp. 14 –40. ISSN: 1063-5203. DOI: https://doi.org/10.1016/j.acha.2007.04.003.

[120] C. Eckart and G. Young. “The approximation of one matrix by another of lower rank”. In: *Psychometrika* 1.3 (Sept. 1936), pp. 211–218. DOI: 10.1007/BF02288367.

[121] J. Veitch, M. Pürrer, and I. Mandel. “Measuring Intermediate-Mass Black-Hole Binaries with Advanced Gravitational Wave Detectors”. In: *Phys. Rev. Lett.* 115.14 (Sept. 2015), p. 141101. DOI: `10.1103/PhysRevLett.115.141101`.

[122] C. Cutler and L. Lindblom. In: *Astrophys. J.* 314 (1987), p. 234.

[123] K. D. Kokkotas and J. Ruoff. In: *Astron. Astrophys.* 366 (2001), pp. 565–572.

[124] Feryal Özel and Paulo Freire. “Masses, Radii, and the Equation of State of Neutron Stars”. In: *Annu. Rev. Astron. Astrophys.* 54.1 (2016), pp. 401–440. DOI: `10.1146/annurev-astro-081915-023322`.

[125] Cecilia Chirenti, Gibran H. de Souza, and Wolfgang Kastaun. “Fundamental oscillation modes of neutron stars: validity of universal relations”. In: *Phys. Rev. D* 91.4 (2015), p. 044034.

[126] J. M. Lattimer and M. Prakash. “Neutron Star Structure and the Equation of State”. In: *Astrophys. J.* 550 (Mar. 2001), pp. 426–442. eprint: `astro-ph/0002232`.

[127] Jocelyn S. Read et al. “Constraints on a phenomenologically parametrized neutron-star equation of state”. In: *Phys. Rev. D* 79 (12 2009), p. 124032.

[128] E. Fonseca et al. “The NANOGrav Nine-year Data Set: Mass and Geometric Measurements of Binary Millisecond Pulsars”. In: *Astrophys. J.* 832, 167 (Dec. 2016), p. 167.

[129] J. Antoniadis et al. “A Massive Pulsar in a Compact Relativistic Binary”. In: *Science* 340 (Apr. 2013), p. 448.

[130] M. Coleman Miller. “Astrophysical Constraints on Dense Matter in Neutron Stars”. In: (2013). arXiv: `1312.0029 [astro-ph.HE]`.

[131] M. Coleman Miller and Frederick K. Lamb. “Observational Constraints on Neutron Star Masses and Radii”. In: *Eur. Phys. J.* A52.3 (2016), p. 63.

[132] M. Feroci et al. “The Large Observatory for X-ray Timing (LOFT)”. In: *Exper. Astron.* 34 (2012), p. 415.

[133] L. Lindblom and S. L. Detweiler. “The quadrupole oscillations of neutron stars”. In: *Astrophys. J.* 53 (Sept. 1983), pp. 73–92. DOI: `10.1086/190884`.

[134] A. Shearer. *High Time Resolution Astrophysics and Pulsars.* Ed. by D. Phelan, O. Ryan, and A. Shearer. Vol. 351. Astrophysics and Space Science Library. 2008, p. 1.

[135] Shijun Yoshida and Yasufumi Kojima. “Accuracy of the relativistic Cowling approximation in slowly rotating stars”. In: *MNRAS* 289.1 (1997), pp. 117–122.

[136] Cecilia Chirenti, Jozef Skakala, and Shin’ichirou Yoshida. “Slowly rotating neutron stars with small differential rotation: equilibrium models and oscillations in the Cowling approximation”. In: *Phys. Rev.* D87.4 (2013), p. 044043.

[137] S. Chandrasekhar. In: *Astrophys. J.* 140 (1964), p. 417.

[138] S. Chandrasekhar. In: *Phys. Rev. Lett.* 12 (1964), p. 114.

[139] R. F. Tooper. “Stability of Massive Stars in General Relativity.” In: *Astrophys. J.* 140 (Aug. 1964), pp. 811–814.

[140] R. F. Tooper. "Adiabatic Fluid Spheres in General Relativity." In: *Astrophys. J.* 142 (Nov. 1965), p. 1541.

[141] J. M. Bardeen. "Stability and Dynamics of Spherically Symmetric Masses in General Relativity." PhD dissertation. Pasadena: California Institute of Technology, 1965.

[142] J. L. Friedman and B. F. Schutz. "On the stability of relativistic systems". In: *Astrophys. J.* 200 (Aug. 1975), pp. 204–220.

[143] B. K. Harrison et al. *Gravitation Theory and Gravitational Collapse.* 1st ed. Vol. 1. University of Chicago Press, June 1965. ISBN: 0226318028.

[144] G. Chanmugam. "Radial oscillations of zero-temperature white dwarfs and neutron stars below nuclear densities". In: *Astrophys. J.* 217 (Nov. 1977), pp. 799–808. DOI: `10.1086/155627`.

[145] H. M. Väth and G. Chanmugam. In: *Astron. Astrophys.* 260 (1992), pp. 250–254.

[146] D. Gondek, P. Haensel, and J. L. Zdunik. "Radial pulsations and stability of protoneutron stars." In: *Astron. Astrophys.* 325 (Sept. 1997), pp. 217–227.

[147] D. Gondek and J. L. Zdunik. "Avoided crossings in radial pulsations of neutron and strange stars". In: *Astron. Astrophys.* 344 (Apr. 1999), pp. 117–122.

[148] Z. Kopal. "The effects of viscosity and radiative braking on stellar pulsations". In: *Astrophys. Nor.* 9 (1964), p. 239.

[149] Theodore P. Higgins and Zdeněk. Kopal. "Volume Integrals of the Products of Spherical Harmonics and their Application to Viscous Dissipation Phenomena in Fluids". In: *Astrophys. Space Sci.* 2.3 (1968), pp. 352–369.

[150] D. Mihalas. "Comments on the dynamical effects of radiative viscosity". In: *Astrophys. J.* 266 (Mar. 1983), pp. 242–247.

[151] P. S. Shternin and D. G. Yakovlev. "Shear viscosity in neutron star cores". In: *Phys. Rev. D* 78 (6 2008), p. 063006. DOI: `10.1103/PhysRevD.78.063006`.

[152] P. S. Shternin, M. Baldo, and P. Haensel. "Transport coefficients of nuclear matter in neutron star cores". In: *Phys. Rev. C* 88 (6 2013), p. 065803. DOI: `10.1103/PhysRevC.88.065803`.

[153] P. S. Shternin, M Baldo, and H-J Schulze. "Transport coefficients in neutron star cores in BHF approach. Comparison of different nucleon potentials". In: *J. Phys. Conf. Ser.* 932 (1 2017), p. 012042. DOI: `10.1088/1742-6596/932/1/012042`.

[154] Laura Tolos et al. "Transport coefficients in superfluid neutron stars". In: *AIP Conference Proceedings* 1701.1 (2016), p. 080001. DOI: `10.1063/1.4938690`.

[155] Andreas Schmitt and Peter Shternin. *Reaction Rates and Transport in Neutron Stars.* Ed. by Luciano Rezzolla et al. 1st ed. Vol. 1. Springer International Publishing AG, 2018, pp. 455–574. ISBN: 978-3-319-97616-7.

[156] Benjamin D. Lackey et al. "Extracting equation of state parameters from black hole-neutron star mergers: Aligned-spin black holes and a preliminary waveform model". In: *Phys. Rev. D* 89 (4 2014), p. 043009.

[157] Benjamin D. Lackey, Mohit Nayyar, and Benjamin J. Owen. "Observational constraints on hyperons in neutron stars". In: *Phys. Rev. D* 73 (2 2006), p. 024021.

[158] Mark Alford et al. “Hybrid Stars that Masquerade as Neutron Stars”. In: *The Astrophysical Journal* 629.2 (2005), p. 969.

[159] A. Akmal, V. R. Pandharipande, and D. G. Ravenhall. “Equation of state of nucleon matter and neutron star structure”. In: *Phys. Rev. C* 58 (3 1998), pp. 1804–1828.

[160] H. Müther, M. Prakash, and T.L. Ainsworth. “The nuclear symmetry energy in relativistic Brueckner-Hartree-Fock calculations”. In: *Physics Letters B* 199.4 (1987), pp. 469 –474.

[161] Horst Müller and Brian D. Serot. “Relativistic mean field theory and the high density nuclear equation of state”. In: *Nucl. Phys.* A606 (1996), pp. 508–537.

[162] Douchin, F. and Haensel, P. “A unified equation of state of dense matter and neutron star structure”. In: *Astron. Astrophys.* 380.1 (2001), pp. 151–167. DOI: 10.1051/0004-6361:20011402.

[163] M. Prakash, J. R. Cooke, and J. M. Lattimer. “Quark-hadron phase transition in protoneutron stars”. In: *Phys. Rev. D* 52 (2 1995), pp. 661–665.

[164] Carles Bona, Carlos Palenzuela-Luque, and Carles Bona-Casas. *Elements of Numerical Relativity and Relativistic Hydrodynamics: From Einstein’ s Equations to Astrophysical Simulations*. 2nd ed. Vol. 783. Lecture Notes in Physics. Springer-Verlag, Berlin; Heidelberg, July 2009, p. 214. ISBN: 9783642011634.

[165] B. V. Ivanov. “Analytical study of anisotropic compact star models”. In: *Eur. Phys. J. C* 77.11 (2017), p. 738.

[166] Kenta Hotokezaka et al. “Mass ejection from the merger of binary neutron stars”. In: *Phys. Rev. D* 87 (2 2013), p. 024001.

[167] L. Rezzolla and O. Zanotti. *Relativistic Hydrodynamics*. 1st ed. Vol. 1. Oxford University Press, Sept. 2013. ISBN: 9780198528906.

[168] M. E. Gusakov, D. G. Yakovlev, and O. Y. Gnedin. “Thermal evolution of a pulsating neutron star”. In: *Monthly Notices of the Royal Astronomical Society* 361.4 (2005), pp. 1415–1424.

[169] Roy Maartens. “Causal Thermodynamics in Relativity”. In: *Class Quantum Grav.* 12 (Oct. 1996).

[170] C. Eckart. “The Thermodynamics of Irreversible Processes. III. Relativistic Theory of the Simple Fluid”. In: *Phys. Rev.* 58 (10 1940), pp. 919–924. DOI: 10.1103/PhysRev.58.919.

[171] E. Flowers and N. Itoh. In: *ApJ* 230 (1979), p. 847.

[172] K. S. Thorne. “The relativistic equations of stellar structure and evolution”. In: *Astrophys. J.* 212 (Mar. 1977), pp. 825–831. DOI: 10.1086/155108.

[173] Yeunhwan Lim, Chang Ho Hyun, and Chang-Hwan Lee. “Nuclear Equation of State and Neutron Star Cooling”. In: *Int. J. Mod. Phys.* E26.4 (2017), p. 1750015.

[174] L. Herrera et al. In: *Phys. Rev. D* 65 (2002), pp. 104004–10400415.

[175] Haensel, P. et al. “Keplerian frequency of uniformly rotating neutron stars and strange stars”. In: *Astron. Astrophys.* 502.2 (2009), pp. 605–610. DOI: 10.1051/0004-6361/200811605.

[176] J. L. Friedman and B. F. Schutz. In: *ApJ* 221 (1978), 937—957.

[177] R. Cornelius and A. Wiegand. In: *Phys. Rev. D* 90 (2014), p. 123503.

[178] P. Constantin. In: *JAMS* 14 (2001), pp. 263–278.

[179] S. W. Hawking. In: *Astrophys. J.* 145 (1966), p. 544.

[180] S. Weinberg. In: *Phys. Rev.* 138B (1965), p. 988.

[181] R. A. Isaacson. In: *Phys. Rev.* 166 (1968), p. 1263.

[182] A. G. Polnarev. In: *JETP* 35 (1972), p. 834.

[183] J. Madore. In: *Commun. Math. Phys.* 27 (1972), p. 291.

[184] J. Madore. In: *Commun. Math. Phys.* 30 (1973), p. 335.

[185] J. Madore. In: *Gen. Rel. Grav.* 5 (1974), p. 169.

[186] D. Chesters. In: *Phys. Rev. D* 7 (1973), p. 2863.

[187] Yu. G. Ignatyev. In: *Russian Phys. J.* 17 (1974), p. 1749.

[188] A. M. Anile and R. A Breuer. In: *Astrophys. J.* 189 (1974), p. 39.

[189] B. Carter and H. Quintana. In: *Phys. Rev. D* 16 (1977), p. 2928.

[190] A. M. Anile and V. Pirronello. In: *Il Nuovo Cimento B* 48 (1978), p. 90.

[191] S. Gayer and C. F. Kennel. In: *Phys. Rev. D* 19 (1979), p. 1070.

[192] F. Sacchetti and D. Trevese. In: *Gen. Rel. Grav.* 10 (1979), p. 947.

[193] A. Widom et al. In: *J. Phys. A* 14 (1981), p. 213.

[194] K. S. Thorne. "Gravitational Radiation: A New Window Onto the Universe". In: *Gravitational Radiation: A New Window Onto the Universe* (1994). Cambridge University Press.

[195] Z. Keresztes et al. In: *J. Cosmol. Astropart. Phys.* 11 (2015), p. 042.

[196] J. Ehlers, A. R. Prasanna, and R. A. Breuer. In: *Quantum Grav.* 4 (1987), p. 253.

[197] J. Ehlers and A. R. Prasanna. In: *Class. Quantum Grav.* 13 (1996), p. 2231.

[198] A. R. Prasanna. In: *Phys. Lett. A* 257 (1999), p. 120.

[199] O. Svítek. In: *Phys. Scr.* 79 (2009), p. 025003.

[200] Katia M. Ferrière. "The interstellar environment of our galaxy". In: *Rev. Mod. Phys.* 73 (4 2001), pp. 1031–1066. DOI: `10.1103/RevModPhys.73.1031`.

[201] Philipp Girichidis et al. "Importance of the Initial Conditions for Star Formation - I. Cloud Evolution and Morphology". In: *MNRAS* 413.4 (May 2011), pp. 2741–2759. ISSN: 0035-8711. DOI: `10.1111/j.1365-2966.2011.18348.x`.

[202] Gy. Fodor. "Generating spherically symmetric static perfect fluid solutions". In: *preprint* (2000). arXiv: `gr-qc/0011040 [gr-qc]`.

[203] J. Bohigas. "Density and pressure distribution of the warm interstellar medium andits relation to the galactic distribution of diffuse and molecular clouds." In: *Astron. Astrophys.* 205 (1988), pp. 257–266.

[204] Alexei G. Kritsuk, Michael L. Norman, and Rick Wagner. “On the density distribution in star-forming interstellar clouds”. In: *Astrophys. J.* 727.1 (2010), p. L20. DOI: 10.1088/2041-8205/727/1/l20.

[206] T.A. Apostolatos. “Construction of a template family for the detection of gravitational waves from coalescing binaries”. In: *Phys. Rev. D* 54 (1996), p. 2421.

[207] N. Murray. “Star Formation Efficiencies and Lifetimes of Giant Molecular Clouds in the Milky Way”. In: *Astrophys. J.* 729.2 (Mar. 2011), p. 133. DOI: 10.1088/0004-637X/729/2/133. arXiv: gr-qc/1007.3270 [gr-qc].

[208] Foucart et al. “Low mass binary neutron star mergers: Gravitational waves and neutrino emission”. In: *Phys. Rev. D* 93 (4 2016), p. 044019. DOI: 10.1103/PhysRevD.93.044019.

[209] A. L. Myers. “Natural units of general relativity”. In: *preprint* (2016). Provided by University of Pennsylvania. URL: https://www.seas.upenn.edu/~amyers/NaturalUnits.pdf.